

**Synthesis and studies of charge-separated
metal-organic and organic assemblies
derived from amino-P(V) scaffolds as
ferroelectric materials**

A Thesis

Submitted in Partial Fulfillment of the Requirements

for the Degree of

Doctor of Philosophy

by

Anant Kumar Srivastava

ID: 20113130



Department of Chemistry

Indian Institute of Science Education and Research, Pune

2017

Dedicated to
My Parents
&
Loved Ones...

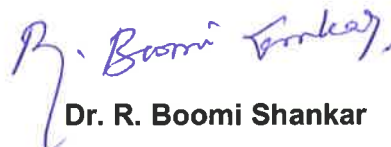


Dr. R. Boomi Shankar
Associate Professor
Department of Chemistry,
IISER Pune

CERTIFICATE

Certified that the work incorporated in the thesis entitled "***Synthesis and studies of charge-separated metal-organic and organic assemblies derived from amino-P(V) scaffolds as ferroelectric materials***" submitted by **Mr. Anant Kumar Srivastava** was carried out by the candidate, under my supervision. The work presented here or any part of it has not been included in any other thesis submitted previously for the award of any degree or diploma from any other university or institution.

Date: 14th June-2017
Place: Pune


Dr. R. Boomi Shankar
(Research Supervisor)



DECLARATION

I declare that, this written submission represents my ideas in my own words and where other's ideas have been included; I have adequately cited and referenced the original sources. I also declare that I have adhered to all principles of academic honesty and integrity and have not misrepresented or fabricated or falsified any idea/data/fact/ source in my submission. I understand that violation of the above will be cause for disciplinary action by the Institute and can also evoke penal action from the sources which have thus not been properly cited or from whom proper permission has not been taken when needed.

Anant Kumar Srivastava

Date: 14th June-2017

Place: Pune

Mr. Anant Kumar Srivastava

ID: 20113130

Acknowledgements

The past few years of my Ph.D. tenure have a significant impact on my life as I met with various persons who were there with me at every step of this journey. Their unconditional help and support have made this splendid journey of Ph.D. a mesmerising one for me.

I express my sincere gratitude to my research supervisor Dr. R. Boomi Shankar for his valuable guidance, suggestion, support and encouragements during the entire tenure of my Doctoral Research. His practical guidance and believe on my abilities have led me to derive successful results from the initial failures. He always encouraged me to have free thinking to pursue the research through my self-driven path. I acknowledge his training through which I have developed various scientific skills such as systematic execution & writing of research projects; preparation & delivery of scientific presentations at various platforms.

I am also thankful to the *Ministry of Human Resource Development (MHRD)*, Government of India, for the setup of IISERs to provide high quality teaching and research facilities within the country. It is my privilege to be a part of *Indian Institute of Science Education and Research (IISER) Pune* and I sincerely acknowledge Prof. K. N. Ganesh (Director, IISER-Pune) for providing such an outstanding campus with well-equipped research and hostel facilities within the Institute.

I would like to thank Dr. B. Praveenkumar (PZT centre, ADRE-Pune, DRDO) and his student Mrs. Pillutla Divya for performing the ferroelectric and dielectric measurements on my samples. Their constant, unstinting help and valuable inputs have played a crucial role in strengthening my understanding for ferroelectric and dielectric materials. I would like to pay my gratitude to Dr. Alexander Steiner (University of Liverpool, UK) for providing easiest solutions to the complicated issues related to crystallography.

I am grateful to the members of my Research Advisory Committee (RAC), Dr. B. Praveenkumar (ARDE, DRDO) and Dr. R. Vaidyanathan (IISER-Pune) for providing their valuable time, suggestions and expert comments to improve my research output. I would also like to express my sincere regards to all the faculty members of the Department of Chemistry, IISER-Pune for their support and making a research friendly working atmosphere. Particularly, I am thankful to Dr. Nirmalya Ballav for his support, suggestions and friendly discussions, it is very easy to approach him for any sort of professional or personal help. I am also thankful to Prof. M. Jayakannan, Dr. A. Hazra, Dr. M. Jeganmohan, and Dr. V. G. Anand for their support and research related discussions. I would like to thank Dr. M. Shanmugam (IIT Bombay) and Dr. S. N. Dhuri (Goa University) for providing me opportunity to contribute in the collaborative research projects.

I thank Dr. Umeshareddy Kacherki (Librarian) for support through library services. I would also like to acknowledge the help from the technical staff for

their support in accessing various instruments: Ms. Archana (SCXRD), Mr. Parven Nasa (SCXRD and PXRD), Mr. Prashant Kale (PXRD), Mr. Nilesh Dumbre (PXRD and SEM), Mr. Anil & Mr. Yatish (SEM), Ms. Megha (AFM), Ms. Swati M. Dixit (MALDI-TOF and CHN analysis), Ms. Swati (HRMS), Mrs. Deeplai & Mr. N. Dalvi (NMR), Mr. Mahesh Jadhav (TGA), Mr. Suresh Prajapati (UG Chemistry Lab), Mr. Ganesh Dimbar (IR). I am also thankful to the entire IT department for their support. I thank the administrative department of IISER-Pune for their support, especially Col. (Retd.) G. Raja Sekhar (Registrar, IISER-Pune), Dr. V. S. Rao, Mr. Prabhash and Mr. Mayuresh. I pay my warm acknowledgement for the support from the staff of Dean Doctoral Studies Office, specially Ms. Dipali Dalvi and Mr. Tushar.

It gives me immense pleasure to thank all the lab members. I thank the support and help provided by my senior Dr. Arvind K. Gupta during the start of my Ph.D. I am fortunate enough to share moments with Ashok, Mahesh, Vijayakanth, Rajasekar, Rishabh, Atul, Sravan, Sachin, Neetu, Meghamala, Swati and Anupriya; whose friendly discussions and support made this journey joyful and memorable. I do remember the cheerful moments shared with energetic and high-spirited juniors like Arun, Indra, and Saurabh (BS-MS alumini). I also thank the project students Suchitra (IISER, Kolkata), Hridya (IISER, Pune), Shivani (IISER, Pune), Vineet (NISER, Bhubaneswar) and Abhijeet (IISER, Pune) who worked with me although for small duration but added much to my research experience. I thank you all again for all the timely help, discussions, sharing of knowledge and research experience.

I would also like to pay my gratitude to some of the seniors from other labs specially Dr. Gopalakrishna, Dr. Santosh Gadekar, Dr. Biplab Joardar, Dr. Kiran Reddy, Mr. Neeraj Maheshwari, Dr. Ganesh and Dr. Jitendra. I thank all of my IISER colleagues and friends for their support and help.

I show my sincere gratitude to the teachers and friends from Banaras Hindu University (BHU), Varanasi, who has always encouraged me to achieve better in life. I thank all my teachers who taught me during my B.Sc. and M.Sc. degree course in BHU, Varanasi. I also thank my friends Ramesh, Nishishwari, Prabhat (now at HRI, Allahabad) and Kundan (now at NCL, Pune) for always being in touch during my failure and success.

I am thankful to all the BS-MS, Int. Ph.D. and Ph.D. students of IISER, Pune for making the campus vibrant with their involvement in extracurricular activities. I thank all the clubs of IISER, Pune for organizing wonderful events like Karavaan, IISER Premier League, Kreedajung, Cultural events and many other programmes. I thank all members of the Cricket and Football team; playing with them gave a lot of fun, relaxation and activeness. I specially thank Prabhat for making wonderful Cricket and Football teams. I also thank the catering services provided by V-square, Shivsagar and MDP. I really admire the hard work of house-keeping staffs in keeping the campus (including the working and hostel area) neat and tidy, thank you very much. I also thank the support of the Security staffs; it is because of

them I can work without worrying much about my belongings either in lab or in my hostel room.

I feel blessed to have Aparna on my side as a special friend. I appreciate the care and support provided by her in spite of her busy research schedule. She has always helped me to be a better person and I find her always besides me during all ups and downs; and I believe we will always care and support each other at all the upcoming stages of our future life. I would also like to express my earnest gratitude to Smt. Bandana Bose, Sri Devashish Banerjee & family for their overwhelming support, faith and blessings.

Words are not enough to convey my heartfelt gratitude towards the blessings, motivation, and love of my parents (Smt. Prabha Srivastava and Sri Jai Shankar Lal Srivastava) and other family members (Mr. Praveen {brother}; Mrs. Preeti {Sister}; Mrs. Anandani {sister-in-law}; Mr. Sameer {brother-in-law}; Khushi & Ani {cutie-pies}). This journey wouldn't have been possible without their unconditional emotional support, trust, encouragement, patience and sacrifice; they are the main reason and inspiration behind each and every success that I have achieved and will achieve in the future endeavors of my life.

I am thankful to IISER-Pune and Council of Scientific and Industrial Research (CSIR) for my research scholarships and requisite financial support during the course of Ph.D. I am also thankful to Department of Science and Technology (DST), Government of India, The Centre for International Co-operation in Science (CICS) and Infosys Foundation Endowment Fund for providing generous financial assistance to attend "2016 IEEE ISAF/ECAPD/PFM Conference" at Technische Universität Darmstadt, Germany. I do acknowledge the organizers of other conferences (such as NSC, ICSIC, MTIC, IICM etc.) for providing me the opportunities to present my Ph.D. research work. Furthermore, I acknowledge American Chemical Society (ACS), Royal Society of Chemistry (RSC), Elsevier Science Ltd., John Wiley & Sons, Springer etc. for publishing the research articles produced during the course of my research as well as for providing the permission and to reprint the materials under copyright.

I acknowledge to them even, whose names are unintentionally missed out, despite their unconditional help throughout my Ph.D. tenure. I always believe in following lines:

"There is no such thing as a 'self-made man'. We are made up of thousands of others. Everyone who has ever done a kind deed for us, or spoken one word of encouragement to us, has entered into the makeup of our character and of our thoughts, as well as our success. (Writer: George Matthew Adams)"

Finally, I thank the almighty God for giving this wonderful life full of opportunities.

Anant Kumar Srivastava

Contents

Contents	i
Synopsis	iv
Abbreviations	x
Rights and Permissions	xi
List of Publications	xii
Chapter 1: Introduction	1-43
1.1 Introduction to ferroelectric supramolecular assemblies	2
1.2 Dielectric materials	3
1.2.1 Electrical polarization	4
1.2.2 Mechanism of polarization in dielectric material	4
1.2.3 Effect of frequency and temperature on polarization of dielectric materials	6
1.2.4 Dielectric constant	7
1.2.5 Dielectric loss	8
1.2.6 Dielectric strength	8
1.2.7 Application of dielectric materials	9
1.3 Classification of dielectric materials	9
1.4 Piezoelectricity	10
1.5 Pyroelectricity	11
1.6 Ferroelectricity: concept and characteristics	11
1.7 Ferroelectric materials: past, present, and future	14
1.8 Application of ferroelectric materials	15
1.9 Supramolecular ferroelectrics	17
1.9.1 Ferroelectricity in crystalline organic materials	18
1.9.2 Ferroelectricity in liquid crystals	28
1.9.3 Ferroelectricity in metal-organic materials	31
1.9.4 Ferroelectricity in nonpolar supramolecular systems	34
1.10 Outline and objective of the thesis	36
1.11 References	38
Chapter 2: Anion driven $[\text{Cu}^{\text{II}}\text{L}_2]_n$ frameworks: Crystal structures, guest-encapsulation, dielectric and possible ferroelectric properties	44-65
2.1 Introduction	45



Contents

2.2	Experimental section	46
2.2.1	General remarks	46
2.2.2	Synthesis	46
2.2.3	Crystallography	49
2.2.4	Ferroelectric and dielectric measurements	51
2.3	Result and discussions	51
2.3.1	Syntheses	51
2.3.2	Crystal structures	53
2.3.3	Guest-encapsulation studies of 2	57
2.3.4	Ferroelectric and dielectric studies	58
2.4	Conclusion	62
2.5	References	63
Chapter 3: Altering polarization attributes in ferroelectric metallo-cavitands by varying hydrated alkali-metal guest cations		66-91
3.1	Introduction	67
3.2	Experimental section	68
3.2.1	General remarks	68
3.2.2	Synthesis	69
3.2.3	Crystallography	72
3.2.4	Ferroelectric and dielectric measurements	74
3.2.5	Calculation of dipole moment	74
3.3	Result and discussions	74
3.3.1	Syntheses	74
3.3.2	Crystal structure of 4 and 5	75
3.3.3	Crystal structure of the host-guest assemblies	78
3.3.4	Ferroelectric and dielectric studies on 4	80
3.3.5	Ferroelectric and dielectric studies of {[Hy-A]cM ₄ } systems	83
3.4	Conclusion	87
3.5	References	88
Chapter 4: Potentially ferroelectric {Cu^{II}L₂}_n based 2D-framework exhibiting high polarization and guest-assisted dielectric anomaly		92-113
4.1	Introduction	93
4.2	Experimental section	94
4.2.1	General remarks	94
4.2.2	Synthesis	95
4.2.3	Crystallography	96
4.2.4	Ferroelectric and dielectric measurements	98

Contents

4.3	Result and discussions	98
	4.3.1 Syntheses	98
	4.3.2 Crystal structures	99
	4.3.3 Ferroelectric and dielectric studies	103
4.4	Conclusion	109
4.5	References	110
Chapter 5: Ferroelectricity in polar organic salts stabilized by phosphonium cation		114-131
5.1	Introduction	115
5.2	Experimental section	116
	5.2.1 General remarks	116
	5.2.2 Synthesis	116
	5.2.3 Crystallography	117
	5.2.4 Ferroelectric and dielectric measurements	118
5.3	Result and discussions	119
	4.3.1 Syntheses	119
	4.3.2 Crystal structures	120
	4.3.3 Ferroelectric and dielectric studies	123
5.4	Conclusion	128
5.5	References	129
Chapter 6: Thesis conclusion and future perspectives		132-135
Appendix		136-180

Synopsis

The thesis entitled “**Synthesis and studies of charge-separated metal-organic and organic assemblies derived from amino-P(V) scaffolds as ferroelectric materials**” focuses on designing rational routes for obtaining non-centrosymmetric and polar ordered assemblies generated from amino-substituted phosphorus centered motifs and investigation of their potential ferroelectric behavior. Thus, several new metal-organic and organic polar crystalline solids, derived from neutral or cationic amino-P(V) moieties (Figure 1), have been described as part of this thesis. The structural, dielectric and ferroelectric investigations of these polar ordered materials indicate that subtle alterations in the molecular precursor components can induce drastic structural changes and marked variations in the ferroelectric properties. Hence, the structure-property interrelation has been utilized as a guiding principle to obtain ferroelectric supramolecular systems based on the amino-P(V) scaffolds. Additionally, this thesis portrays the effect of supramolecular interactions, host-guest assembly, and the role of molecular components of the organic/metal-organic systems on the overall physical characteristics particularly their ferroelectric behavior.

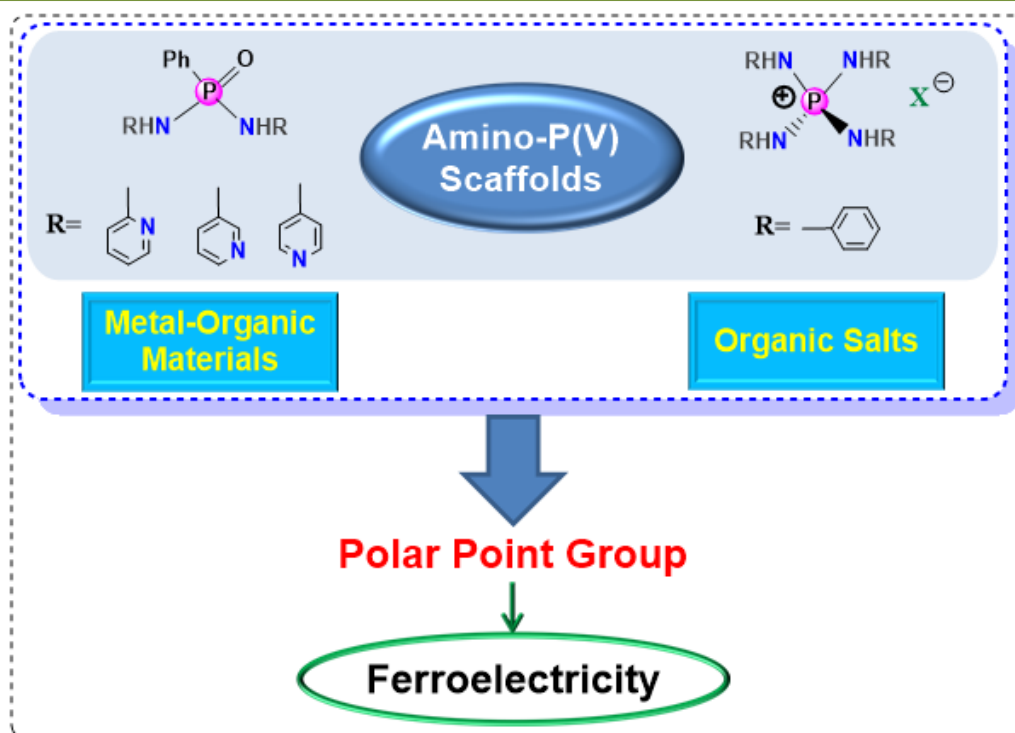


Figure 1: Outline of the Thesis.

Chapter 1: Introduction

Chapter 1 provides a brief introduction to the fundamental concepts related to the dielectric, piezoelectric, pyroelectric and ferroelectric properties of materials. Particularly, a detailed account of the ferroelectric properties, polarization mechanism and various applications of polar crystalline solids have been described. Further, this chapter provides an overview of the different families of supramolecular ferroelectrics based on hydrogen bonded crystalline organic systems, charge-transfer complexes, organic salts showing order-disorder transitions, liquid crystals, metal-organic materials and nonpolar/polar supramolecular rotators, where the supramolecular interactions assist in establishing bistable polarization. Finally, an outline of the thesis with targets specific to the use of flexible N-donor functionalized amino P(V) ligands as supports for obtaining metal-organic ferroelectric materials and the use of amino-phosphonium cations for obtaining ferroelectric organic salts have been described (Figure 1).

Chapter 2: Anion Driven $[\text{Cu}^{\text{II}}\text{L}_2]_n$ Frameworks: Crystal Structures, Guest-Encapsulation, Dielectric and Possible Ferroelectric Properties

Metal-organic ferroelectric materials have gained attention owing to their ready syntheses and tunable properties. However, synthesis of such metal-organic ferroelectric materials is still challenging due to the strict requirement of the polar crystal lattice. In that attempt, four new Cu(II) cationic coordination assemblies **1**, **1a**, **2** and **3** of composition, $\{[\text{Cu}_2(\text{L}^1)_4(\text{H}_2\text{O})_2] \cdot (\text{ClO}_4)_4 \cdot (\text{H}_2\text{O})_5 \cdot (\text{CH}_3\text{OH})\}_\infty$, $\{[\text{Cu}_3(\text{L}^1)_6(\text{H}_2\text{O})_3] \cdot (\text{ClO}_4)_5 \cdot (\text{NO}_3) \cdot (\text{H}_2\text{O})_{11}\}_\infty$, $\{[\text{Cu}_4(\text{L}^1)_8(\text{H}_2\text{O})_5] \cdot (\text{NO}_3)_8 \cdot \text{L}^1 \cdot (\text{H}_2\text{O})_9\}$ and $\{[\text{Cu}_3(\text{L}^1)_6] \cdot (\text{NO}_3)_6 \cdot (\text{H}_2\text{O})_8 \cdot (\text{CH}_3\text{OH})_2\}$, respectively, were synthesized, by employing a flexible dipodal phosphoramidate ligand L^1 , $\text{PhPO}(\text{NH}^3\text{Py})_2$ (^3Py = 3-pyridyl). The compounds **1** and **1a** having perchlorate and mixed perchlorate-nitrate anions, respectively, were obtained as non-centrosymmetric 1D-helical assemblies. On the other hand, **2** and **3** were obtained as discrete centrosymmetric assemblies of composition M_4L^1_8 and M_3L^1_6 , respectively. Interestingly, **2** can encapsulate the hydrated potassium cation $[\text{K}(\text{H}_2\text{O})_8]^+$ in its intrinsic cavity. The ferroelectric measurements of **1** and **1a** gave a well saturated ferroelectric hysteresis loop with saturation polarization (P_s) values of 1.8 and 0.55 μCcm^{-2} , respectively. This

Synopsis

indicates that the presence of nitrate anion in the packing structure has an effect in altering the asymmetry of the system which causes a change of polarization in **1a** in comparison with **1**. Furthermore, the room temperature dielectric constant values of 118.7, 27.4 and 39.2 for **1**, **1a** and **2**, respectively, suggest them to be potential candidates for high-technique applications. (Figure 2)

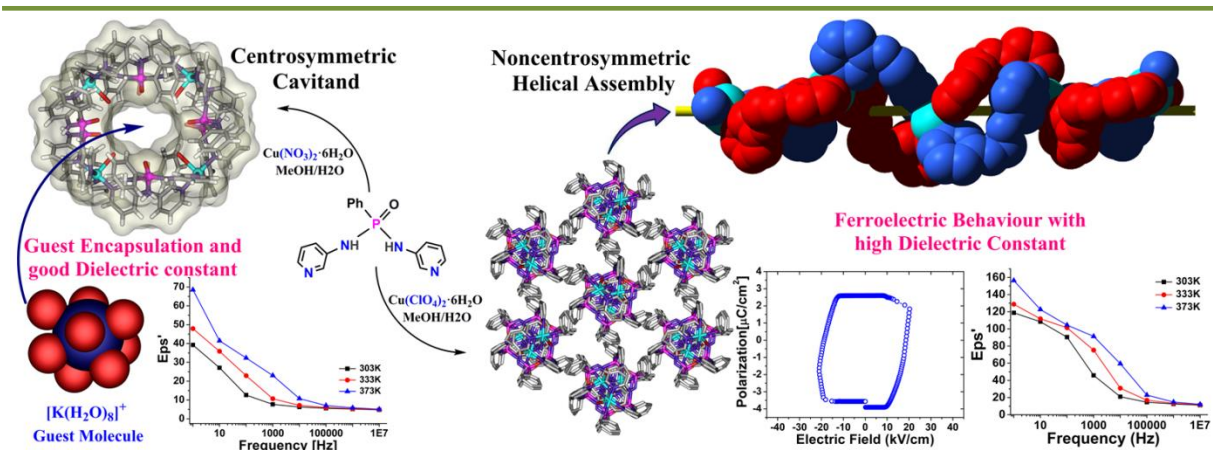


Figure 2: Anion-driven centrosymmetric and non-centrosymmetric $\{Cu^{II}L_2\}_n$ assemblies derived from flexible phosphoramidate ligand L^1 .

Chapter 3: Altering Polarization Attributes in Ferroelectric Metallo-Cavitands by Varying Hydrated Alkali-Metal Guest Cations

The host-guest supramolecular assembly has emerged as an exciting topic of research for both fundamental understanding and practical application. The host-guest interactions might create a significant influence on polar ordering and hence on the ferroelectricity in the supramolecular systems. This chapter describes the synthesis of two metallo-cavitands $[\{M_4L^1_8(H_2O)_8\}\cdot 9(H_2O)]\cdot 8(NO_3)\cdot x(H_2O)$ [$M=Ni^{2+}$ (**4**) or Co^{2+} (**5**)], utilizing the same flexible phosphoramidate ligand L^1 . Further, the solid-state host-guest behavior and ferroelectricity, in the presence of various hydrated alkali metal cations (Hy-A) at their intrinsic voids, has been demonstrated. Due to the confinement effects of the cavitands, the degree of hydration observed for these alkali metal ions are on the upper side, especially the K^+ , Rb^+ and Cs^+ ions show high hydration numbers of 8, 9 and 10, respectively. Ferroelectric studies on **4**, $[Hy-A]\subset\mathbf{4}$ and $[Hy-A]\subset\mathbf{5}$ assemblies show remnant polarization (P_r) values ranging from 27 to 30 μCcm^{-2} with concomitant variations in the coercive field (E_c) values.

Synopsis

The ferroelectricity in **4**, [Hy-A]c**4** and [Hy-A]c**5** is believed to originate from the interactions of the cavitand with the encapsulated polar solvates/ hydrated alkali metal cations. The observed features for the P-E loop characteristics of all the assemblies are reminiscent of triglycine sulfate (TGS) and certain other supramolecular ferroelectrics. Interestingly, ferroelectric fatigue measurements on all these systems show sizable variations as the cavitands with hard Li^+ ions exhibiting the maximum (fatigue) tolerance and the ones with higher polarizable Cs^+ ions show a reduction in P_r values up to 35%, after 10^5 switching cycles. The results signify the effect of encapsulated guest molecules in altering the polarization attributes (P_r , E_c and fatigue tolerance) via host-guest interactions. (Figure 3)

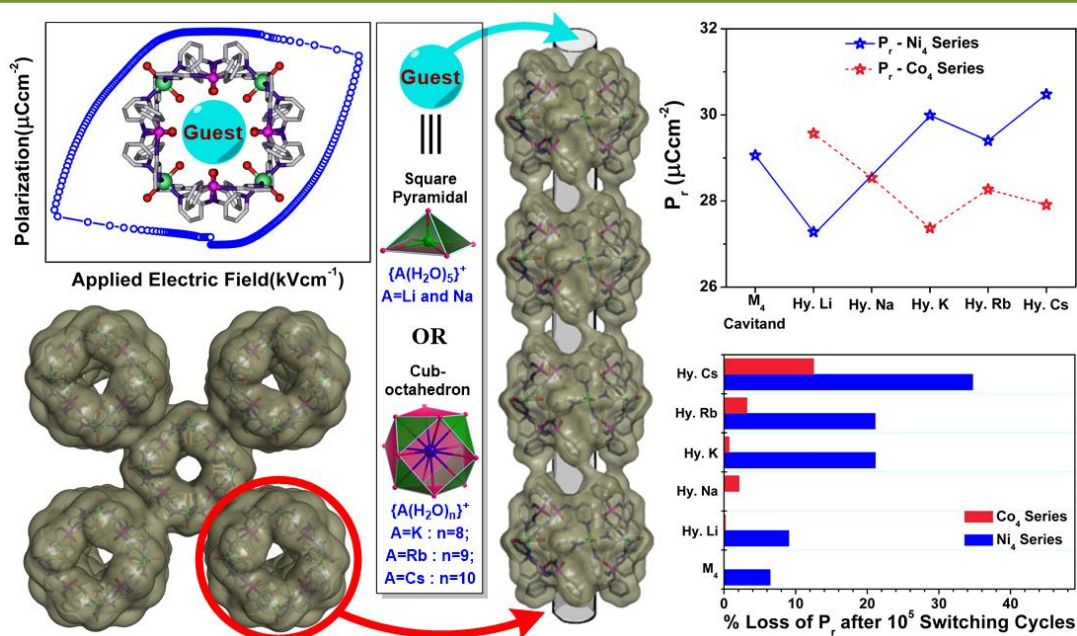


Figure 3: View of the tetrameric core of the ferroelectric $\{M_4L_8\}$ cavitand and its bcc packing leading to the formation of a central intrinsic cavity that can encapsulate hydrated alkali metal cations. Effect of hydrated alkali metal guest cations in altering the polarization attributes of ferroelectric metallo-cavitands.

Chapter 4: Potentially Ferroelectric $\{\text{Cu}^{\text{II}}L_2\}_n$ Based 2D-framework Exhibiting High Polarization and Guest-Assisted Dielectric Anomaly

Utilizing the isomeric dipodal phosphoramidate ligands, L^2 [$\text{PhPO}(\text{NH}^4\text{Py})_2$] and L^3 [$\text{PhPO}(\text{NH}^2\text{Py})_2$], two new $\text{Cu}^{\text{II}}L_2$ derivatives **6** ($\{[\text{Cu}L_2(\text{H}_2\text{O})_2] \cdot (\text{NO}_3)_2 \cdot (\text{H}_2\text{O})_{1.5} \cdot (\text{CH}_3\text{OH})\}_\infty$) and **7** ($[\text{Cu}L_3] \cdot (\text{NO}_3)_2$) were synthesized. The compound **6** crystallizes

Synopsis

in a non-centrosymmetric polar space group Cc as a 2D framework and **7** as a centrosymmetric complex. Electrical hysteresis (P-E loop) measurements on **6** at room temperature gave the remnant (P_r) and saturation (P_s) polarization values of 27.96 and 21.79 μCcm^{-2} , respectively, which are the highest among all the known metal-organic ferroelectric materials. Also, the P_r value obtained for **6** is comparable to that of barium titanate and higher than most of the organic, polymeric and inorganic ferroelectric materials. The permittivity measurements on **6** and **7** results in high dielectric constant values of 96.5 and 30.4, respectively, at 100 Hz frequency at room temperature. Temperature dependent permittivity measurement on **6** yields a dielectric anomaly peak at 40 °C due to phase transition assisted by desolvation. The existence of phase transition is further confirmed by differential scanning calorimetry, powder X-ray diffraction, and polarized light microscopy. A comparison of the P-E loops of **6**, **6**_{desolvated} and **6**_{resolvated} suggests that gasification/release of the solvate molecules from the packing structure affects the polarization in **6**. (Figure 4)

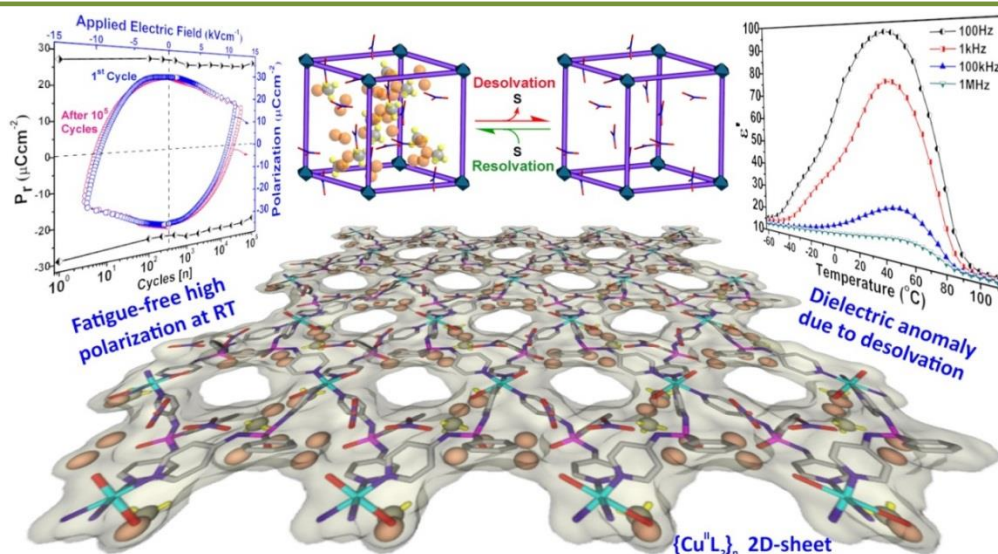


Figure 4: View of the $\{\text{Cu}^{\text{II}}\text{L}_2\}_n$ 2D-sheet structure of **6** and details of its dielectric and ferroelectric behaviour.

Chapter 5: Ferroelectricity in Polar Organic Salts Stabilized by Phosphonium Cations

The polar organic solids, formed of light-weight molecular struts, have gained tremendous attention as ferroelectric materials in the view their flexibility, non-toxicity and low-temperature fabrication techniques. Many of them can be stabilized as salts

Synopsis

where the hydrogen-bonding between the charge-separated species induces polarity. This chapter describes the syntheses of two organic salts based on tetraanilino phosphonium cations as a precursor to obtain potential molecular ferroelectric materials. This cation was found to crystallize in polar space groups in the presence of trimesate trianion and dihydrogen phosphate anion. The compounds $[\{P(NHPh)_4\}_3(C_9H_3O_6) \cdot (CH_3OH)_2]$, **8** and $[\{P(NHPh)_4\}(H_2PO_4) \cdot (CH_3OH)_{0.5}]_6$, **9** display 3D hydrogen-bonded network of phosphonium motifs and the corresponding anions that can exhibit multi-axial polar ordering in their crystal lattice. The compound **8** gave a very low polarization value ($P_r=0.035 \mu\text{Ccm}^{-2}$ at 0.1 Hz) during P-E loop measurements. Temperature dependent dielectric measurements revealed **8** as low dielectric constant material, signifying its possible use in the integration of microelectronic circuits. Remarkably, compound **9** which is referred as ^{ta}PDP (tetraanilino phosphonium dihydrogen phosphate), analogous to commercial ferroelectric material KDP (KH_2PO_4), revealed a high ferroelectric response at room temperature. The P_r value of the compound was found to be $28.88 \mu\text{Ccm}^{-2}$ at 1Hz with a high fatigue tolerance after 10^5 cycles (Figure 5). The results described in this chapter demonstrate a facile approach to obtain molecular ferroelectrics based on phosphonium cations utilizing both organic and inorganic counter anions.

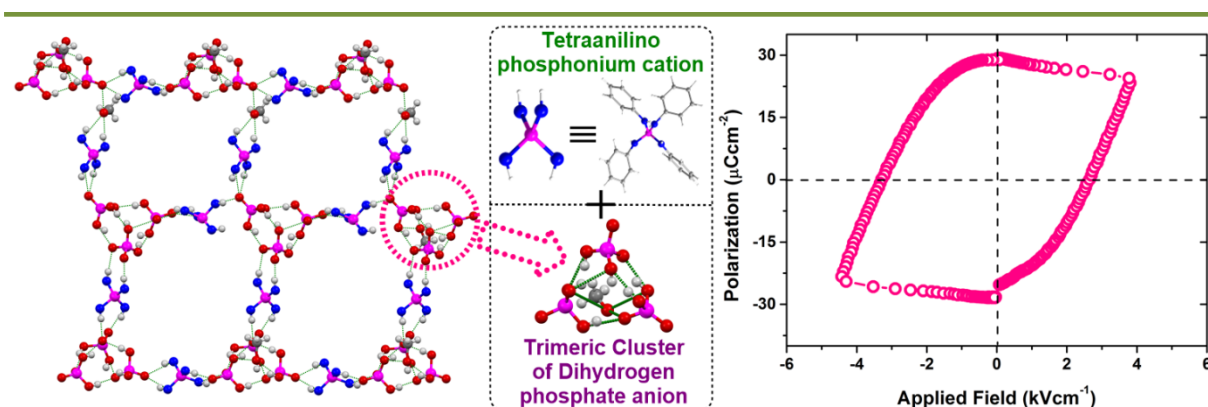


Figure 5: View of the hydrogen-bonded network in ^{ta}PDP along with its components and the room temperature P-E loop for ^{ta}PDP.

Abbreviations

Anal.	Analysis
BTO	Barium titanate
BFO	Bismuth ferrite
Calcd.	Calculated
CCDC	Cambridge Crystallographic Data Centre
DFT	Density Functional Theory
DMF	N, N-Dimethyl formamide
DMSO	Dimethyl sulphoxide
DSC	Differential Scanning Calorimetry
ESI	Electron Spray Ionization
E_c	Coercive field
FET	Field-effect transistor
FT-IR	Fourier Transform Infrared Spectroscopy
HRMS	High Resolution Mass Spectroscopy
Hz	Hertz
KDP	Potassium dihydrogen phosphate
MALDI-TOF	Matrix-Assisted Laser Desorption/Ionization – Time of Flight
MeOH	Methanol
MeCN	Acetonitrile
mg	milligram
min	minutes
μ l	microliter
ml	milliliter
mm	millimeter
mmol	millimoles
MOF	Metal-Organic Framework
M.P.	Melting point
NMR	Nuclear Magnetic Resonance
RT	Room Temperature
Ph	Phenyl
P_r	Remnant Polarization
P_s	Saturation Polarization
PVDF	Polyvinylidene difluoride
Py	Pyridyl
PZT	Lead Zirconate Titanate
PXRD	Powder X-ray Diffraction
RAM	Random Access Memory
SCXRD	Single Crystal X-ray Diffraction
T_c	Curie Temperature
TGA	Thermogravimetric Analysis
TGS	Triglycine sulphate



Chapter 2:

Reprinted (adapted) with permission from “*Chem. Mater.* **2014**, 26, 3811-3817” © 2014 American Chemical Society.

Chapter 3:

Reproduced with permission from “*J. Mater. Chem. C* **2017**, 5, 7352-7359” © 2017 The Royal Society of Chemistry.

Chapter 4:

Reprinted (adapted) with permission from “*Chem. Mater.* **2015**, 27, 5222” © 2015 American Chemical Society. This article is an open access published under an ACS AuthorChoice License, which permits copying and redistribution of the article or any adaptations for non-commercial purposes.

Contributions Included in the Thesis:

1. Anion Driven $[\text{Cu}^{\text{II}}\text{L}_2]_n$ Frameworks: Crystal Structures, Guest-Encapsulation, Dielectric, and Possible Ferroelectric Properties
Anant Kumar Srivastava, B. Praveenkumar, Indra K. Mahawar, Pillutla Divya, S. Shalini, and Ramamoorthy Boomishankar
Chem. Mater. **2014**, 26, 3811.
2. Potentially Ferroelectric $\{\text{Cu}^{\text{II}}\text{L}_2\}_n$ Based Two-Dimensional Framework Exhibiting High Polarization and Guest-Assisted Dielectric Anomaly
Anant Kumar Srivastava, Pillutla Divya, B. Praveenkumar and Ramamoorthy Boomishankar
Chem. Mater. **2015**, 27, 5222.
3. Functional Metal-organic Molecules and Materials Derived from Rigid and Flexible P-N Scaffolds
Ramamoorthy Boomishankar and **Anant Kumar Srivastava**
Phosphorus, Sulfur Silicon Relat. Elem. **2016**, 191, 618.
4. Altering Polarization Attributes in Ferroelectric Metallo-Cavitands by Varying Hydrated Alkali-Metal Guest Cations
Anant Kumar Srivastava, Thangavel Vijayakanth, Pillutla Divya, B. Praveenkumar, Alexander Steiner and Ramamoorthy Boomishankar
J. Mater. Chem. C **2017**, 5, 7352.
5. Tetraanilino Phosphonium Dihydrogen Phosphate: A Hydrogen-bonded Ferroelectric Organic Salt Exhibiting High Polarization at Room Temperature
Anant Kumar Srivastava, Thangavel Vijayakanth, Pillutla Divya, B. Praveenkumar and Ramamoorthy Boomishankar
(*Manuscript under preparation*)
6. Investigation of the Ultra-Low Dielectric Constant in a Hydrogen-bonded Tetraanilino Phosphonium Trimesate Salt
Anant Kumar Srivastava, Thangavel Vijayakanth, Pillutla Divya, B. Praveenkumar and Ramamoorthy Boomishankar
(*Manuscript under preparation*)

Contributions not included in the Thesis:

7. Discrete and Polymeric Cu(II) Complexes Derived from In Situ Generated Pyridyl-Functionalized Bis(amido)phosphate Ligands, $[\text{PO}_2(\text{NHPy})_2]^-$
Arvind K. Gupta, **Anant Kumar Srivastava**, Indra K. Mahawar and Ramamoorthy Boomishankar
Cryst. Growth Des. **2014**, 14, 1701.

Publications

8. Cationic Copper(I) Iodide Cluster MOF Exhibiting Unusual Ligand Assisted Thermochromism
Ashok Yadav, **Anant Kumar Srivastava**, A. Balamurugan and Ramamoorthy Boomishankar
Dalton Trans. **2014**, 43, 8166.
9. A Tetrakis(amido)phosphonium Cation Containing 2-pyridyl (²Py) Substituents, [P(NH²Py)₄]⁺, and its Reactivity Studies with Ag(I) Salts
Arvind K. Gupta, **Anant Kumar Srivastava** and Ramamoorthy Boomishankar
J. Chem. Sci. **2015**, 127, 619.
10. A Neutral Cluster Cage with a Tetrahedral [Pd₁₂L₆] Framework: Crystal Structures and Host–Guest Studies
Arvind K. Gupta, Ashok Yadav, **Anant Kumar Srivastava**, K. R. Ramya, Harshad Paithankar, Shyamapada Nandi, Jeetender Chugh and Ramamoorthy Boomishankar
Inorg. Chem. **2015**, 54, 3196.
11. Anion Induced Ferroelectric Polarization in a Luminescent Metal-organic Cage Compound
Ashok Yadav, **Anant Kumar Srivastava**, P. Kulkarni, Pillutla Divya, Alexander Steiner, B. Praveenkumar and Ramamoorthy Boomishankar
J. Mater. Chem. C **2017**, DOI: 10.1039/C7TC03375C.

Chapter 1



Introduction

1.1 Introduction to Ferroelectric Supramolecular Assemblies

Self-assembly techniques have emerged as a powerful tool in the domain of molecular design and functional materials.¹ Supramolecular organic and metal-organic self-assemblies have attracted immense research interest due to their facile synthesis and attractive chemical and physical properties.^{2,3} For this, molecules with proper interacting sites (ligands) can be designed which can further interact with each other, or with some other organic moieties or with metal centers resulting in the self-assembly of organic or metal-organic motifs. Moreover, these supramolecular self-assemblies utilize weak interactions (like covalent coordination, hydrogen bonding, pi-pi interactions, etc.) to provide novel crystalline structures ranging from low-dimensional clusters and cages to higher dimensional architectures such as 1D helices/chains, 2D-sheets/grids, 3D-frameworks and connected polyhedra.^{4,5} Such supramolecular self-assemblies have found applications in the fields of host-guest chemistry,⁶⁻⁸ catalytic reactions,^{9,10} gas and solvent storage,^{11,12} selective molecule trapping,¹³⁻¹⁴ and as materials for electrical,¹⁵ magnetic,^{16,17} and optical properties.¹⁸ Over the past decades, materials exhibiting ferroelectric, multiferroic, piezoelectric and magnetoelectric properties are of great interest due to their utility in modern electronics and non-linear optical devices.¹⁹⁻²⁴ Particularly, ferroelectric substances with high permittivity (dielectric constant) values are important in the development of high technology devices such as non-volatile memories.²⁵⁻³³ Ferroelectricity is an intrinsic property of polar dielectrics in which polarization can be switched between two or more stable states by the application of an electric field.³⁰ Several materials were discovered and were employed for a variety of applications. Thus, families of ferroelectric materials such as Rochelle salt and similar compounds, potassium dihydrogen phosphate (KDP) and other hydrogen-bonded ferroelectric materials, barium titanate and other perovskite structured compounds (ex. such as KNbO_3 , PbTiO_3), complex oxides such as Aurivillious compounds, triglycine sulfate and isomorphous materials (ferroelectric sulfates) have been studied due to their interesting structure and physical properties.^{30,34-42} However, the existing commercial ferroelectric materials (mostly inorganic oxides of perovskite family) possess some demerits (such as rigidity, high heavy metal content, environmental concern, high temperature processing etc.) due to which there has been an intensification of

research activities in synthesizing new families of materials with ferroelectric, pyroelectric and piezoelectric behavior.⁴³⁻⁵² In this effort, a large number of non-centrosymmetric molecules, both organic and metal-organic, have been synthesized and examined for their ferroelectric efficacy.^{15,34,53-55} Some specific examples include certain neutral organic compounds, organo-ammonium salts, metal-organic perovskites and halogenometallates.⁵⁶⁻⁶⁵ This thesis describes the synthesis and characterization of new ferroelectric materials derived from amino-P(V) scaffolds with phosphoramidate and phosphonium motifs. This chapter provides an introduction to several concepts and mechanism that provide a better understanding of the materials with dielectric, piezoelectric, pyroelectric and ferroelectric properties. A thorough literature survey has also been provided to discuss the rational approach to obtain Supramolecular ferroelectrics with enhanced performance and efficiency as compared to the known ferroelectric systems.

1.2 Dielectric materials

Dielectric materials (or Dielectrics) are electrical insulators, but are efficient supporter of an electrostatic field and can be polarized by applying an external electric field. Though they do not conduct electricity still, they are not inert to the applied electric field. The dielectric materials undergo internal charge polarization which allows them to be used for storage of an electrical charge in capacitors.⁶⁶ The application of electric field causes a limited movement of charges within the dielectric material (Figure 1.1), such that they attain a charge-separated state leading to the formation of electrical dipoles.⁶⁶ Such electrical dipoles provide dipole moment to the system and the net dipole moment per unit volume is termed as Polarization of the material.

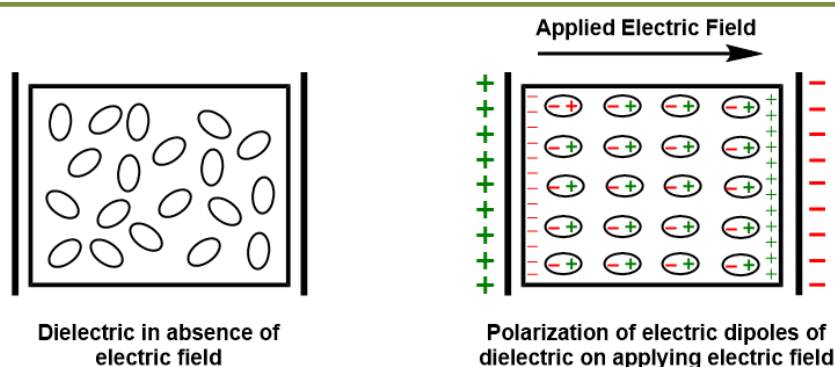


Figure 1.1: Polarization of a dielectric material in the presence of electric field.

1.2.1 Electrical polarization

Classically, the electric polarization (or polarization density or polarization) is expressed as the density of induced electric dipole moments in a dielectric material due to the application of an external electric field. The dipole moment and polarization of the material is proportional to the applied electric field, and the dipoles align in the direction of the field.⁶⁷

$$\mu = q \cdot \delta \quad \dots\dots \text{Eq 1.1}$$

Where “q” is the charge separated by a distance “ δ ” and “ μ ” is the dipole moment. Its unit is C.m.

$$P = \Sigma \mu / V \quad \dots\dots \text{Eq 1.2}$$

Here, “V” is the volume and “P” is the Polarization. The unit of P is C.m^{-2} i.e. charge per unit area.

1.2.2 Mechanism of polarization in dielectric material

The mechanism of polarization deals with the response of a molecule or atom of dielectric material to an external electric field. Simply, it can be said that it deals with the positioning of dipoles in the direction of applied field. The four polarization mechanisms^{40,66,67} of dielectric materials (Figure 1.2) are as follows:

1.2.2.1 Electronic polarization: As the name suggests, this is related to the polarization of electron cloud due to the external electric field. When an electric field, E, is applied on an individual atom, the electron cloud surrounding the heavy nucleus get slightly shifted in the direction of the positive electrode resulting in the creation of small dipole moment within the atom. The moment the electric field is removed, the electrons return to their original position around the nuclei which destroys the dipole moment, and hence the polarization disappears. However, the displacement of the electron cloud is minuscule in this case hence the magnitude of electronic polarization is quite small as compared to the other mechanisms of polarization.^{40,66,67}

1.2.2.2 Ionic polarization: As the name suggests, ionic polarization is related to the displacement of ions within the crystal structure of an ionic compound (such as NaCl) as a response to the external electric field. The application of electric field causes stretching of the bonds between the ions, which ultimately varies the dipole moment of the molecule. Depending on the structure of the ionic compound, this mechanism could cause substantial polarization effects. However, the applied electric field is not able to cause displacement of higher magnitude, due to the strong ionic bond between the charges, but is much more than the displacement of the electron cloud in case of electronic polarization.^{40,66,67}

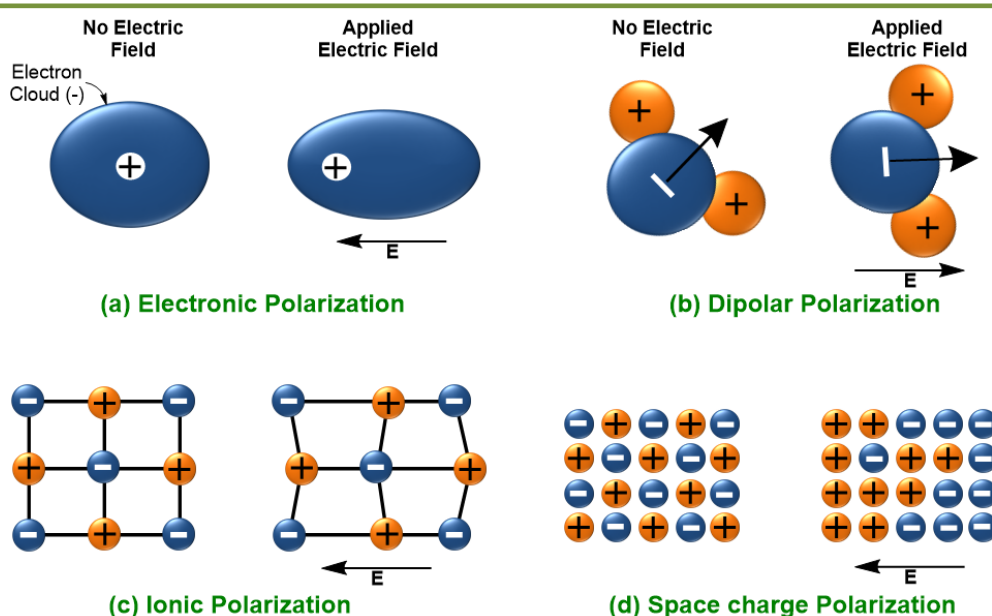


Figure 1.2: Types of Polarization mechanism in dielectrics.

1.2.2.3 Dipolar or orientation polarization: This mechanism is very common in the systems having permanent dipoles (non-centrosymmetric). Due to the thermal randomization, all the dipoles are randomly distributed, and hence the system does not have any net dipole moment (such as H₂O, HCl, etc.). However, when an external electric field is applied, it results in polarization of the randomly distributed dipoles in the direction of applied field. The dipolar polarization causes a much higher degree of polarization than the electronic or ionic polarization, because of the possibility of larger displacement of charge as compared to the spacing between the electrons and nucleus. This polarization is meaningful at lower temperature due to the decrease in the randomization because of the reduced thermal vibrations.^{40,66,67}

1.2.2.4 Interface or space charge polarization: This polarization is produced by the migration or accumulation of charge carriers (such as free ions) that can drift to some distance through the dielectric by application of an electric field. The interfaces (junction of electrode and dielectrics or junction of two different dielectrics) cease the movement of such charge carriers leading to the formation of space charge.^{40,66,67}

The electronic polarization is present in all dielectric materials. The other polarization mechanisms are additional, and most of the dielectrics exhibit more than one polarization mechanism. However, to account for the total polarization, we can consider all the polarizations except the interface/space charge polarization. This is because of the lack of methods to precisely compute the space charges, while the first three mechanisms can be easily quantified by applying mathematical methods.^{40,66}

$$\text{Total Polarization, } P = P_{\text{electronic}} + P_{\text{ionic}} + P_{\text{dipolar}} \quad \dots\dots\dots \text{Eq 1.3}$$

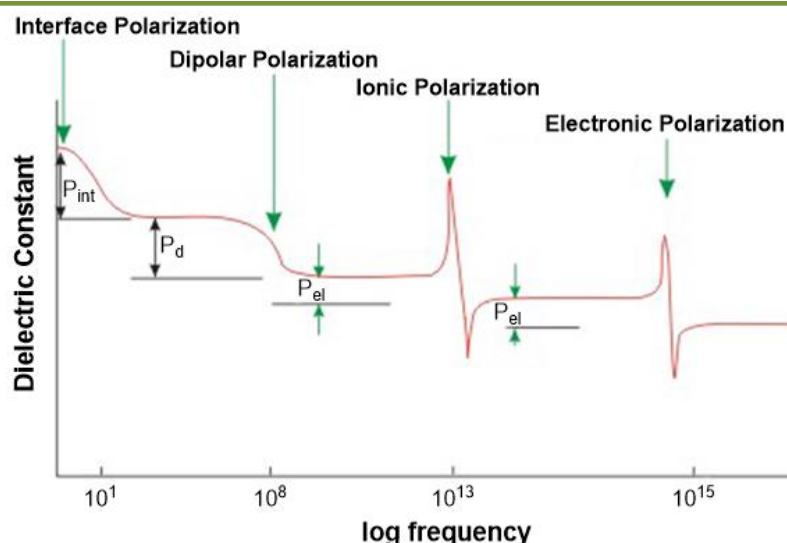


Figure 1.3: Frequency dependence of different polarization mechanisms. (Adapted with permission from “http://nptel.ac.in/courses/113104005/lecture18a/18_2.htm” Electro Ceramics Web Course (NPTEL): Module4; by Prof. Ashish Garg)⁴⁰

1.2.3 Effect of frequency and temperature on polarization of dielectric materials

The dielectric material requires time to respond or polarize when subjected to an electric field. Hence, the several polarization mechanisms which employ movement

of electrons/ions/molecules are frequency dependent. It is witnessed that the mass of the entities to be displaced are getting larger from electronic to ionic to dipolar polarization mechanisms, which is directly related to the frequency of the applied field, as the heavier entity requires more time to displace while the lighter entity will be displaced quickly. The electronic polarization occurs swiftly and usually persists at higher frequencies of $\sim 10^{13}$ - 10^{15} Hz. The other polarization mechanisms like ionic polarization (occur at frequencies between $\sim 10^9$ - 10^{13} Hz) and dipolar polarization (generally persists below 10^9 Hz) are slower than the electronic polarization. In high-frequency field, the ions/molecules do not have time to realign with each cycle. The interface or space charge polarization is the slowest mechanism and is revealed at frequencies below 10 Hz.⁴⁰

The polarization in dielectric material also shows dependence on temperature. The electronic polarization is relatively insensitive to temperature; while the ionic systems show an increase in charge carriers and ion mobility with an increase in temperature which ultimately accounts for a greater extent of polarization. In contrary, the polarization tends to decrease in dipolar systems with an increase in temperature, because higher temperature is associated with increased thermal agitation which opposes the dipolar polarization mechanism.⁴⁰

1.2.4 Dielectric constant

Dielectric constant is a quantity that measures the ability of a dielectric material to store electrical energy in the form of charge on the application of an electric field. Generally, it is referred as relative permittivity (ϵ_r). It is expressed as the ratio of absolute permittivity (ϵ) of the material to the permittivity of vacuum ($\epsilon_0 = 8.85 \times 10^{-12} \text{ Fm}^{-1}$).^{40,66,68}

$$\epsilon_r = \epsilon / \epsilon_0 \quad \dots \text{Eq 1.4}$$

The relative permittivity (ϵ_r) is a dimensionless quantity. The dielectric constant of material is a complex system and shows dependency on the frequency of the applied electric field.

$$\epsilon_r = \epsilon'_r - i\epsilon''_r \quad \dots \text{Eq 1.5}$$

Where, ϵ_r' is the real part while ϵ_r'' is the imaginary part of the complex dielectric constant and "i" is the imaginary constant ($i=\{-1\}^{1/2}$).

The relative permittivity, ϵ_r , of a dielectric material can be calculated as the ratio of the capacitance of parallel plate electrodes, in the presence of an external electric field, in the presence and absence (vacuum) of the dielectric material.

$$\epsilon_r = C_m / C_0 \quad \dots\text{Eq 1.6}$$

Here, C_0 is the capacitance of the test capacitor with a vacuum between the parallel plate electrodes separated by some distance, while C_m is the capacitance using the same capacitor and distance between its plates, with a dielectric material filling the space between the plates.^{40,66,68}

1.2.5 Dielectric loss

Dielectric loss (or dissipation factor) enumerates the inherent dissipation of energy (in the form of heat) in a dielectric material through the movement of charges, while it is subjected to an electric field. It is represented in terms of either the loss angle, δ (or lag angle), or the corresponding loss tangent, $\tan\delta$.

$$\tan\delta = \epsilon_r'' / \epsilon_r' \quad \dots\text{Eq 1.7}$$

The ϵ_r'' is called the loss factor while the $\tan\delta$ is referred as the loss tangent or the dissipation factor. A dielectric material with low loss factor is always desirable.

The possible reason for dielectric loss in materials is (a) ion migration, (b) ion vibration/deformation and (c) electronic polarization. The ion migration is most common cause found in most of the dielectric materials which are strongly affected by temperature and frequency.^{40,66,68}

1.2.6 Dielectric strength

It is the ability of a dielectric material to tolerate an applied electric field without breaking down or allowing electrical current to pass through. It is a measure of the electrical strength of a dielectric material as an insulator. Thus, the maximum electric field required to force the dielectric material to conduct electricity is referred to as

Dielectric strength of that material. It is expressed as Volts per unit thickness. It is hence advised to apply electric field less than the dielectric strength of the material for its best utilization.^{66,68}

1.2.7 Application of dielectric materials

Dielectric materials are very commonly used in capacitors, power transformers, gate dielectric, transducers, resonators, etc. Low dielectric constant materials are used as electrical insulators for integration of microelectronic circuits, while the materials having high dielectric constant are utilized in capacitors for charge storage and other functions. Most of the dielectrics employed for their (a) relative permittivity, (b) low dielectric loss, and (c) high dielectric strength. In some cases, the materials with high dielectric loss are utilized for making heating devices. Dielectric materials even find utility in many high technique applications and devices due to some of the unique properties like piezoelectricity, pyroelectricity, and ferroelectricity.^{40,66,68}

1.3 Classification of dielectric materials

The dielectric materials tend to polarize in the presence of electric field and return to their non-polarized state upon removal of the electric field. The dielectric constant (extent of polarization) of these materials increases linearly with increase in the magnitude of applied electric field. Such materials are referred as *linear dielectrics*. However, there are some special classes of dielectrics that exhibit large dielectric constant which shows nonlinearity with the applied field and may also possess non-zero polarization even in the absence of electric field. Such special dielectrics are referred as *nonlinear dielectrics*. Such nonlinear dielectrics show unusual properties where the dipoles of the materials can be polarized by mechanical stress or temperature difference even in the absence of electric field.^{34,40}

Crystallography shows a clear cut demarcation between the different types of nonlinear dielectric materials.^{34,40} Based on the crystal classes, to which their molecular crystals belong, the nonlinear dielectrics exhibit three special properties (Figure 1.4):

(a) Piezoelectricity

(b) Pyroelectricity

(c) Ferroelectricity

tetrahydrate). Piezoelectricity is a characteristic property of non-centrosymmetric crystalline materials and arises due to the coupling of mechanical strain and electric field. Piezoelectricity is a reversible process, and hence piezoelectric materials exhibit both *direct piezoelectric effect* (generation of electrical charge internally on the application of mechanical force) as well as *converse piezoelectric effect* (generation of internal mechanical strain on applying electric field). Due to this, piezoelectric materials are employed for a variety of applications such as sensors, actuators, transducers, accelerometers and sonar devices, etc.^{40,66}

1.5 Pyroelectricity

Pyroelectric materials are sub-class of piezoelectric materials, whose crystals belong to either of the 10 polar point group and possess spontaneous polarization. Pyroelectricity is the ability of materials to produce electrical potential in response to the thermal gradient (due to heating or cooling) created around them. In history, the pyroelectric effect was first noticed in 314 BC by Theophrastus but was first described (although not named as what it is known) by Louis Lemery in 1717 and named in 1824 by Sir David Brewster. Examples of pyroelectric materials include cesium nitrate (CsNO_3), gallium nitride (GaN), polyvinyl difluorides, würtzite, tourmaline, Rochelle salt, triglycine sulfate, BaTiO_3 , etc. Pyroelectric materials are employed for various applications such as power transistors, infrared detectors, energy harvesting, etc.^{40,66}

1.6 Ferroelectricity: Concept and Characteristics

Ferroelectricity is observed in certain special dielectrics which possess switchable spontaneous electric polarization that can be reversed or reoriented by application of an external electric field. The essentiality for a compound to exhibit ferroelectricity is, it must be crystalline and adopt a polar point group (C_1 , C_S , C_2 , C_{2v} , C_3 , C_{3v} , C_4 , C_{4v} , C_6 , C_{6v}). Such polar materials when subjected to an external field (E), the plot for their polarization (P) vs. electric field (E) exhibits a hysteresis loop commonly known as P-E loop (Figure 1.5). On increasing the intensity of the applied electric, the ferroelectric materials attain a saturation polarization, P_s , at the higher field strength. However, when the electric field is reduced back to zero, after attaining saturation, they retain a remnant polarization, P_r . The electric field (applied in the opposite

direction) required to reduce the remnant polarization of ferroelectric material to zero is known as coercive field, E_c . Further, by increasing the electric field strength in the opposite direction (or applying an electric field of reverse polarity), the polarization vector can be reversed, which is normally referred as switching.^{34,40,66}

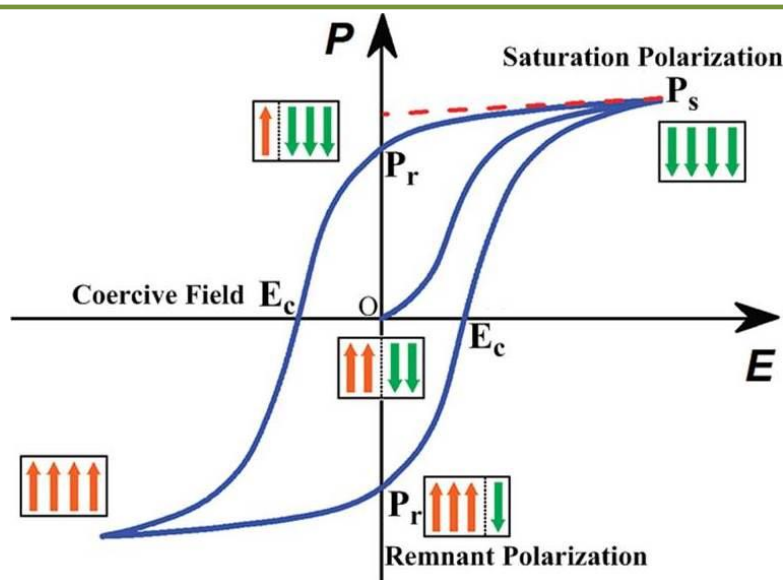


Figure 1.5: Typical Polarization (P) versus Electric field (E) hysteresis loop. (Adapted with permission from “Xiong et al. *Chem. Rev.* **2012**, 112, 1163” © 2012 American Chemical Society.)

Moreover, the observation of ferroelectricity in a material may not be possible at all temperatures. The polar arrangement in the ferroelectrics is due to the alignment of electric dipoles in the lattice. At higher temperatures, the polar alignment of dipoles is disturbed and creates a high symmetric non-polar arrangement. Hence, most of the ferroelectric crystals lose their dipole arrangement and remain non-polar (paraelectric) at elevated temperature. However, on cooling the polar arrangement is reestablished to exhibit ferroelectricity, which occurs at/below a certain temperature called Curie temperature (T_C). Thus, heating leads to a structural transition in ferroelectrics from a low-temperature, low-symmetry ferroelectric phase to a high-temperature, high symmetry paraelectric phase. The paraelectric-ferroelectric phase transition for a ferroelectric material can be determined by utilizing various characterization methods such as temperature dependent dielectric constant measurements, structure determination at different temperatures, thermal analysis, and spectroscopic measurements.^{34,40}

This paraelectric-ferroelectric phase transition may be of the following two types:

- (i) **Displacive type:** The relative displacement of the ions (as shown in Figure 1.6(i)), at temperature below the T_C , produces spontaneous polarization within the system.
- (ii) **Order-disorder type:** The reorientation of the dipolar ions (Figure 1.6(ii)) to attain polar order, below T_C , generates ferroelectricity.

Some of the ferroelectric materials may exhibit both displacive and order-disorder type mechanisms as both are not mutually exclusive, for example, KDP.^{34,40}

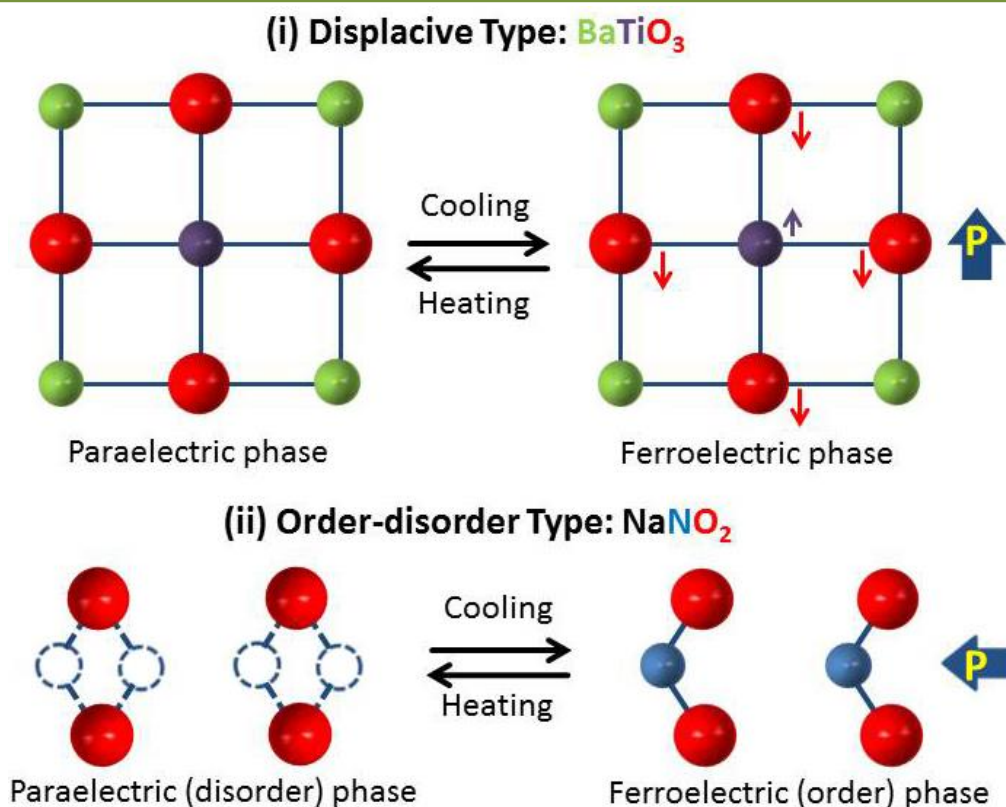


Figure 1.6: Paraelectric-ferroelectric phase transition.

Antiferroelectricity. The antiferroelectric materials are polar dielectrics, in which the electric dipoles possess an ordered crystalline array, but the neighbouring dipoles have antiparallel arrangement which cancels out the net polarization in them.³⁰ Thus, unlike ferroelectrics, the antiferroelectric materials do not possess any spontaneous polarization. However, the antiferroelectric materials exhibit double hysteresis loop when subjected to an external electric field (Appendix A1.1).

1.7 Ferroelectric materials: Past, Present, and Future

Ferroelectricity was first discovered by Valasek in the crystal of Rochelle salt in 1920.³⁵ After nearly 15 years KH_2PO_4 (KDP) was discovered by Busch and Scherrer, which have been regarded as the first example of hydrogen bonded ferroelectric materials.³⁶ Soon many other related compounds as hydrogen-bonded ferroelectrics were discovered. In the early 1940s, barium titanate (BaTiO_3 ; BTO) has been discovered as the first non-hydrogen-bonded system. After this, a lot of ceramics with perovskite structure, such as lead zirconate titanate ($\text{Pb}(\text{Zr},\text{Ti})\text{O}_3$; PZT), KNbO_3 and LiNbO_3 , etc., have been discovered that displayed excellent ferroelectric properties and thus they accelerated the application of ferroelectrics in various devices.^{30,42}

Further, the number and performance of ferroelectric compounds were significantly enhanced by the efforts of several researchers working in this area. Their contributions have revealed ferroelectricity in a wide variety of compounds such as inorganic oxides, polymers and supramolecular compounds (like organic systems, charge-transfer complexes, organic-inorganic hybrids and liquid crystals, etc.) which exhibit diverse crystal structures, chemical compositions, and polarization mechanisms.^{34,53,54}

The ceramic or inorganic oxide materials are predominantly being utilized as traditional ferroelectric materials for commercial use, owing to their high saturation polarization, large dielectric constant values, fatigue tolerance and higher T_C values. However, the difficulties related to them such as cumbersome synthesis, rigidity, heavyweight, environmental concern (due to the presence of toxic and expensive heavy metals) and high-temperature processing, has triggered the search for an alternative new age ferroelectric materials. From past few decades, more emphasis has been given for the synthesis of ferroelectric materials utilizing the polymeric, organic, metal-organic, charge-transfer and liquid crystalline systems in the view of their lightness, flexibility, non-toxicity and low-temperature fabrication techniques.^{34,53,54} There are few polymeric materials, especially PVDF (Polyvinylidene difluoride) and its copolymer, which are being commercially utilized for their piezoelectric, pyroelectric and ferroelectric properties in many sensors.⁷⁰

However, the reorientation of dipoles in such polymeric ferroelectrics demands large electric fields due to the steric influence. This results in the exceptionally large coercive field in such ferroelectric polymers as compared to other ferroelectrics.^{53,71} The supramolecular assemblies where lighter molecular systems are arranged in a polar order have gained attention in this regard. The detailed discussion about ferroelectricity in the supramolecular system has been provided in section 1.9.

Recently, attempts to harness the ferroelectric properties in mixed systems have also been initiated, and the multicomponent systems (such as composites) may dominate the contest for future ferroelectrics.⁷² Use of multicomponent composites might increase the complexity of the system, but at the same time, it also reinforces variety in the design and improvement of the ferroelectric property. By engineering the components of such composite systems (such as matrix, fillers, and dopant), it is possible to investigate and induce several desired parameters essential for the better performance of the material. More emphasis is given to generate and probe the ferroelectric properties in multifunctional composite nanomaterials. By utilizing a different kind of fillers, it is possible to produce flexible ferroelectric nanocomposites with advanced properties which are best candidates for application in various fields.

1.8 Application of Ferroelectric materials

Due to their fascinating properties, ferroelectrics have found extensive use as multifunctional electroactive polar materials for high-performance devices in diverse technological areas like electronics, electro-optics, and electromechanics (Figure 1.7).²⁹⁻³³ Most commonly, the bistable polarization of ferroelectrics makes them a worthy candidate for utility in the construction of memory elements, particularly ferroelectric random access memory (FeRAM) and ferroelectric field-effect transistors.²⁵⁻²⁸ Memory elements constructed using ferroelectric materials are non-volatile as they do not require any holding voltage, means the memory is not erased in case of power off.

Apart from this, the ferroelectric materials may also find various applications due to their other properties such as piezoelectricity, pyroelectricity, non-linear optical behavior and high dielectric constant.^{30,44-52} Due to the piezoelectric effects exhibited by ferroelectrics, they are used in actuators, transducers, ultrasonic motors,

piezoelectric elements, microsensors, micro-electro-mechanical systems (MEMS), etc. Ferroelectrics have also been employed as thermal-imaging sensor and an infrared detector, owing to their large pyroelectric effect. The ferroelectric materials with high permittivity (dielectric constant) values are employed in the development of dielectric resonators, capacitors, semiconductor chips and telecommunication signal processing units.³⁰

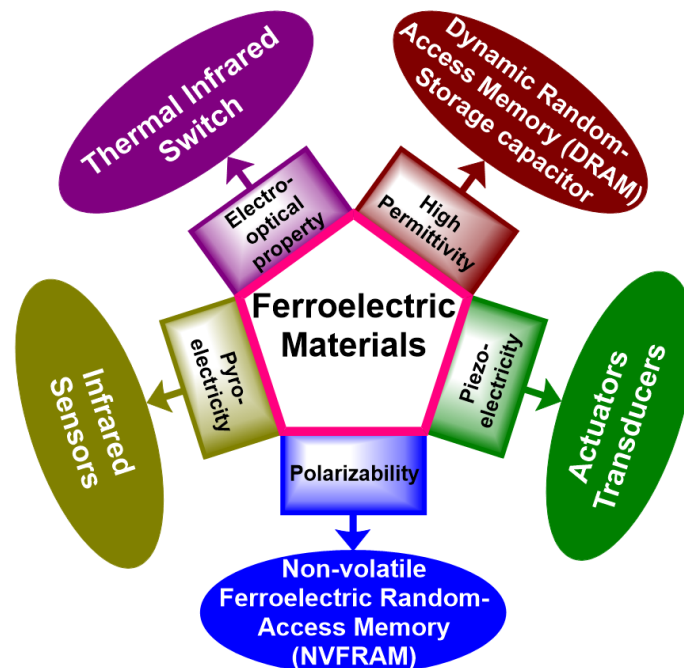


Figure 1.7: Various applications of ferroelectric materials.

In addition, due to the non-centrosymmetric crystal structure in ferroelectrics, they display nonlinear optical properties (such as second harmonic generation) and even linear electro-optic effect. Thus, the stored information in memory elements, based on ferroelectric materials, can be read/retrieved even by optical means (via electro-optic effect) rather than only electrical means. Thus the large coupling of optical and electrical properties in ferroelectrics dictates their utility as electro-optic modulators, optically read memories, light valves and even as a display.³⁰ Nowadays, ferroelectric materials are being utilized for fabricating energy harvesting devices. Ferroelectrics are envisioned to be worthwhile materials for fabricating flexible nanogenerators,⁷³ solar cells with improved efficiencies^{49,50} and as harvesters for other renewable sources of energy.⁴⁵⁻⁴⁸

1.9 Supramolecular Ferroelectrics

Supramolecular ferroelectrics utilize the non-covalent interactions that arrange the molecules into ordered assemblies. The non-covalent interactions create an asymmetry in the electron density of the interacting molecules and hence assist in generating the desired polar supramolecular dipoles. Thus, the introduction of non-covalent interactions (hydrogen bond, charge transfer, molecular rotation) in a variety of supramolecular structures (such as single-component organic crystalline lattice, organic and metal-organic salts, metal-organic coordination complexes, liquid crystals, etc.) could assist in generating ferroelectric supramolecular assemblies (Figure 1.8). The structural diversity offered by the non-covalent interactions can upsurge the yield and efficiency of self-assembled ferroelectric supramolecular systems. These interactions also assist in developing systems that can exhibit ferroelectricity at or above room temperature and mechanisms analogous to the traditional ferroelectrics.⁵⁴

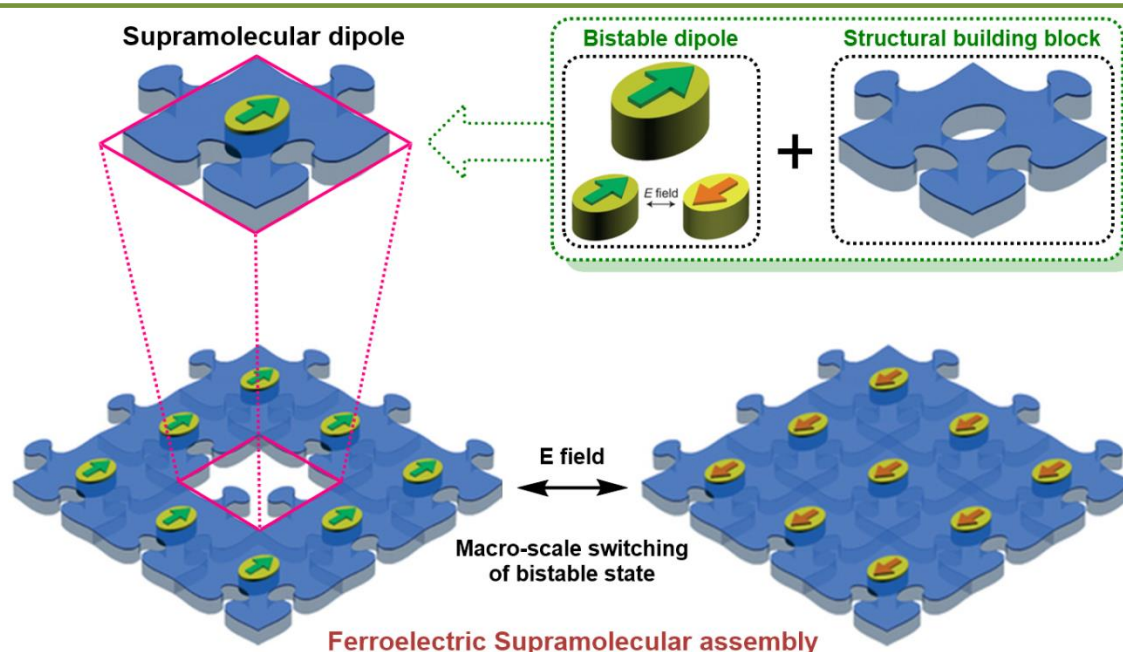


Figure 1.8: Schematic of design approach for ferroelectric supramolecular assemblies. (Adapted by permission from Macmillan Publishers Ltd: “*Nat. Chem.* **2015**, 7, 281” © 2015)

Supramolecular ferroelectrics having multicomponent molecular compounds may help in achieving molecular displacements required for displacive type mechanism. Another approach is the presence of dynamic protons on hydrogen-bonded chains,

which allows the site-to-site transfer of protons and hence switching of the spontaneous polarization. The ferroelectric materials utilizing non-covalent interactions can be broadly divided as organic and metal-organic. Further, the organic and metal-organic systems can be subdivided based on the kind of interaction/parameter involved in producing polar order such as hydrogen displacement, charge-transfer, guest encapsulation, molecular rotations, etc. Besides these, ferroelectricity has been revealed in certain nonpolar supramolecular systems too, where the applied electric field influences the non-covalently interacting constituents to align in polar order which can be retained even after removal of the field.^{53,54}

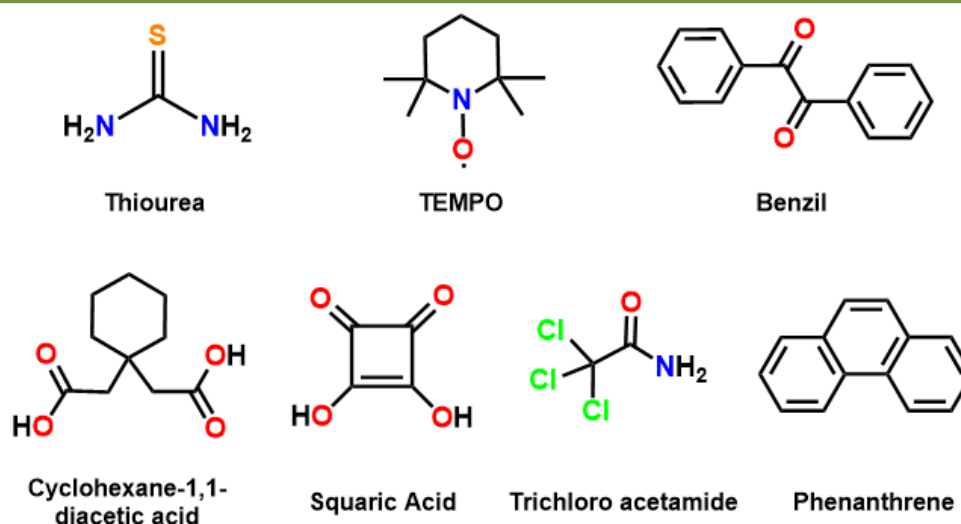


Figure 1.9: Few examples of single component organic ferroelectrics.

1.9.1 Ferroelectricity in crystalline organic materials

Thiourea is the first example of a single component organic ferroelectric, discovered in 1956, where intrinsic dipole of the molecule is the source of polarization.^{53,74,75} It received considerable interest due to its complicated multiple structural transformations between the paraelectric and ferroelectric phases. It showed good piezo-, pyro-, and ferroelectric properties below room temperature. Later on, near room temperature ferroelectricity was reported in a stable organic radical TEMPO (2,2,6,6-tetramethyl-1-piperidinyloxy; also known as “*tanane*”), however, the polarization value was quite low ($0.5 \mu\text{Ccm}^{-2}$).⁷⁶ Further, ferroelectricity has been discovered in many single component organic compounds such as Benzil,

cyclohexane-1,1-diacetic acid, squaric acid, trichloro acetamide, diacetylene-1,6-bis(2,4-dinitrophenoxy)-2,4-hexadiyne, phenanthrene, etc. (Figure 1.9),⁷⁷ where most of them exhibit low polarization values with few at room temperature. Later, ferroelectricity was explored in binary organic systems too such as phenazine-chloranilic acid, tetrathiafulvalene-chloranil, etc. The generation of bistable electrical dipoles in the organic ferroelectric materials may employ one of the three strategies: (a) correlated site-to-site proton transfer in hydrogen-bonded systems, (b) electron transfer in mixed-stack charge-transfer (CT) complexes, (c) displacive type or order-disorder transition of cations in the crystal lattice of organic salts.

1.9.1.1 Hydrogen bonded systems

Hydrogen bonding between the hydrogen donor and hydrogen acceptor molecule creates a partial negative charge on former and partial positive charge on later. The introduction of hydrogen bonding motifs in organic ferroelectrics is a very common approach as it can facilitate both the supramolecular self-assembly process and assist in the alignment of molecular dipoles. The reversibility and bistability of the parent systems turns out to be the basic design for hydrogen-bonded ferroelectrics. The motivation for the study of hydrogen bonded ferroelectrics comes from the first discovered ferroelectric systems such as Rochelle salt and KDP.^{35,36} The perchlorate salt of 1,4-diazabicyclo[2.2.2]octane (HdabcoClO₄) is an early example of N-H...N hydrogen bonded ferroelectrics that are analogous to the bistable OH...O hydrogen bonds found in KDP-type ferroelectrics (Figure 1.10a).⁷⁸ In the solid state, it crystallized in polar orthorhombic space group and exhibits room temperature polarization ($P_S \sim 4 \mu\text{Ccm}^{-2}$) perpendicular to the hydrogen-bonding direction with a T_C at 377 K. Similar properties have been found in the isostructural tetrafluoroborate salt of 1,4-diazabicyclo[2.2.2]octane (HdabcoBF₄) with T_C at 378 K.^{78,79}

This example further inspired the use of correlated hydrogen bonded systems such as two component acid-base systems. The two component crystals based on phenazine (Phz; $pK_a = 1.23$) and chloranilic acid (H₂ca; $pK_a = 0.73$) or bromanilic acid (H₂ba; $pK_a = 0.80$) are composed of alternating hydrogen-bonded chains of acid and base, where the equivalent pK_a of acid and base kept the system neutral (Figure 1.10b).⁸⁰ Here, the hydrogen bonded molecules displace collectively to produce a

polar lattice (below 253 K in Phz-H₂ca). On deuteration of the chloranilic acid, the system has shown to exhibit room temperature ferroelectricity ($T_C=304$ K). The strong isotope effect is a confirmation for the proton displacement as a key component for ferroelectricity in such systems. In systems where the difference in the pK_a is significant, hydrogen bonding produces charged species as in the case of 5,5'-dimethyl-2,2'-bipyridine (55DMBP; $pK_a = 4.2$) and iodanilic acid (H₂ia).⁸¹ As 55DMBP is more basic than Phz, one of its pyridyl units remains protonated leading to the formation of its organic salt. The salt exhibits correlated site-to-site proton transfers that induce polarization in the system (Figure 1.10c). The salt of 55DMBP with H₂ia is ferroelectric while the salts with H₂ca and H₂ba are antiferroelectric.⁸²

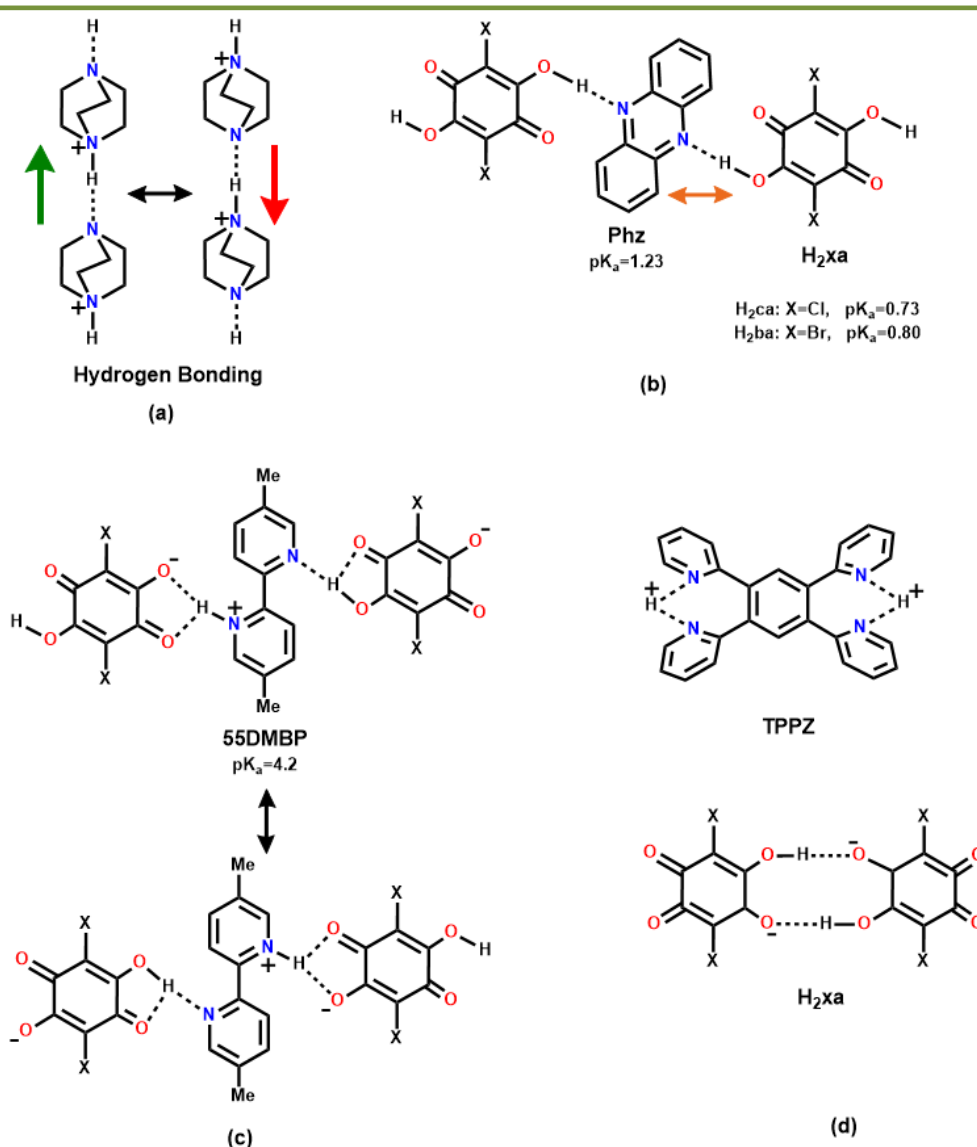


Figure 1.10: Schematic of design approach for ferroelectric supramolecular assemblies.

In continuation of this approach the use of proton sponges, such as TPPZ (2,3,5,6-tetra(2-pyridinyl)pyrazine), demonstrates another interesting class of hydrogen bonded ferroelectrics.⁸³ The TPPZ base does not interact with the anilic acid(s) through hydrogen bond; rather it captures two protons from the acid and displays intramolecular N-H...N hydrogen bond between the protonated and neutral pyridinyl rings (Figure 1.10d). The dynamic shuttling of the protons through this intramolecular N-H...N hydrogen bond generates polarization in the system.

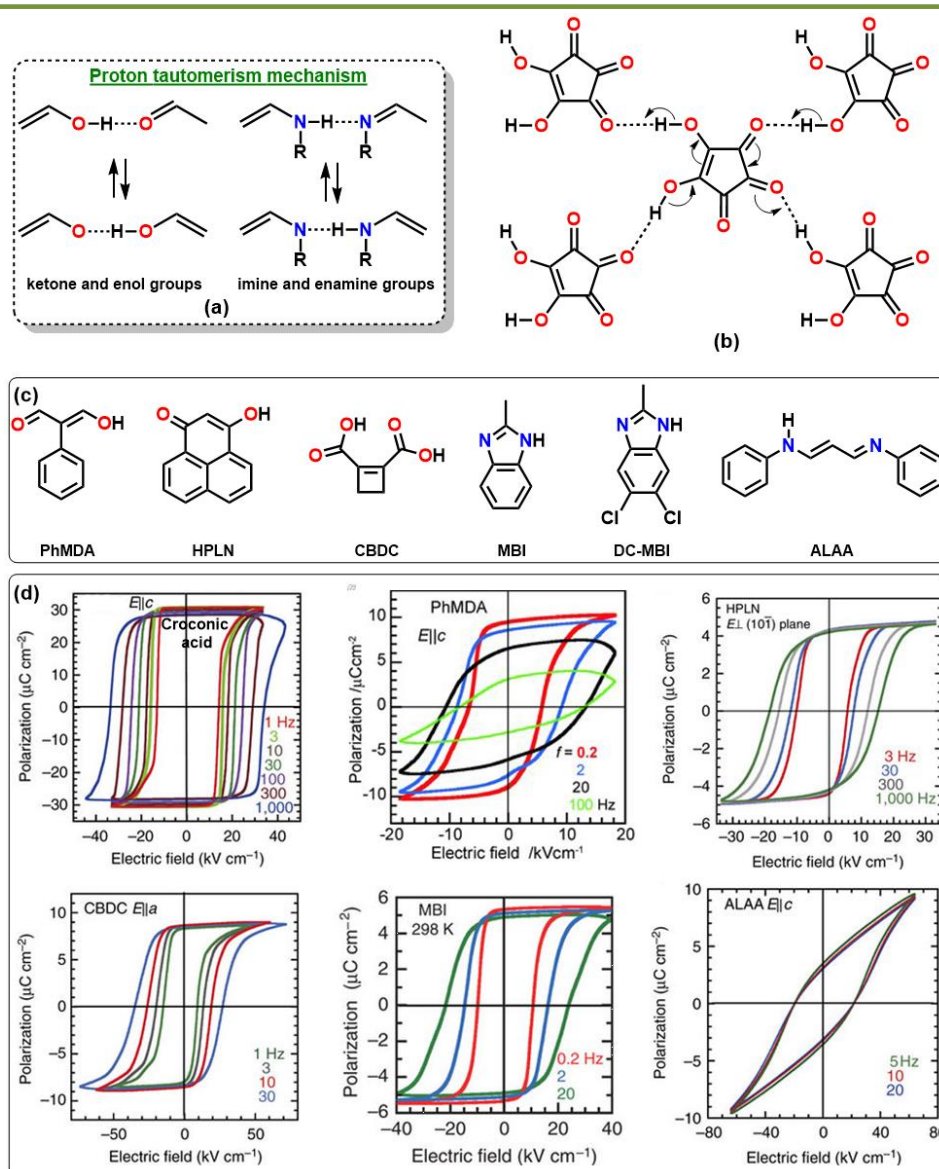


Figure 1.11: (a) Proton tautomerism mechanism in enol-ketone and imine-enamine groups. (b) Proton tautomerism in croconic acid. (c) Chemical structure of several other molecules that can self-assemble into single-component system with non-centrosymmetric polar lattice. (d) Ferroelectric hysteresis loops of representative single-component systems. (P-E loops

are adapted with permission from “Horiuchi et al. *Nat. Commun.* **2017**, *8*, 14426. © 2017 by the author” and “Tokura et al. *Nat. Commun.* **2012**, *3*, 1308. © 2012 by the author”)

The intramolecular proton migration through a cooperative proton tautomerism mechanism (PTM) has been envisioned in certain single component systems having ketone and enol groups or imine and enamine groups (Figure 1.11a).⁸⁴ Such single component tautomeric systems also exhibit intermolecular hydrogen bonding between the complementary functional groups, to generate supramolecular structures containing extended chains of resonance-assisted hydrogen bonds, which can be utilized as another approach to induce ferroelectricity. Tokura et al. have shown croconic acid as first single component organic ferroelectric where the proton migration is based on cooperative proton tautomerism (Figure 1.11b).⁵⁶ The P-E loop measurement revealed remarkably high polarization of $21 \mu\text{Ccm}^{-2}$ (recent improved value is $30 \mu\text{Ccm}^{-2}$)⁸⁴ with the reasonable coercive field (14 kVcm^{-1}) which is not only best among the organic ferroelectrics but also is highly competitive to that of polymeric and inorganic materials. However, the corrosive and air-unstable nature of croconic acid has directed the development of alternative materials to reduce the difficulty in device fabrication. Horiuchi et al. have presented his studies on a number of single component systems exhibiting cooperative proton tautomerism (Figure 1.11c).⁸⁴ They had smartly designed molecules which have β -diketo-enol or imine-enamine motifs that contain pseudo-centric symmetries to allow swift switching of dipoles. Thus they revealed ferroelectricity in 2-phenylmalondialdehyde (PhMDA), 3-hydroxyphenalenone (HPLN), cyclobutene-1,2-dicarboxylic acid (CBDC), 2-methylbenzimidazole (MBI), 5,6-dichloro-2-methylbenzimidazole (DC-MBI) and 3-anilinoacrolein anil (ALAA) systems.^{84,85} All these materials displayed above room temperature ferroelectricity with polarization values ranging from 3 to $14 \mu\text{Ccm}^{-2}$ with the workable coercive field.

1.9.1.2 Electron donor-acceptor system

The charge-transfer (CT) complex is a pair of electron donor (D) and acceptor (A) molecules which can share an electron during complexation. The electrostatic attraction resulted from the sharing of electron between the donor and acceptor offers a stabilizing force for the CT complex. The CT complexes can adopt either of

the two crystalline architectures: segregated stack or mixed stack.^{53,54} In any case the electron from the HOMO of donor molecule is partially transferred to the LUMO of acceptor, which is quantified by the ionicity, $\pm\rho$. The segregated stacks of donor and acceptor are not good for ferroelectricity as they might show metallic conduction

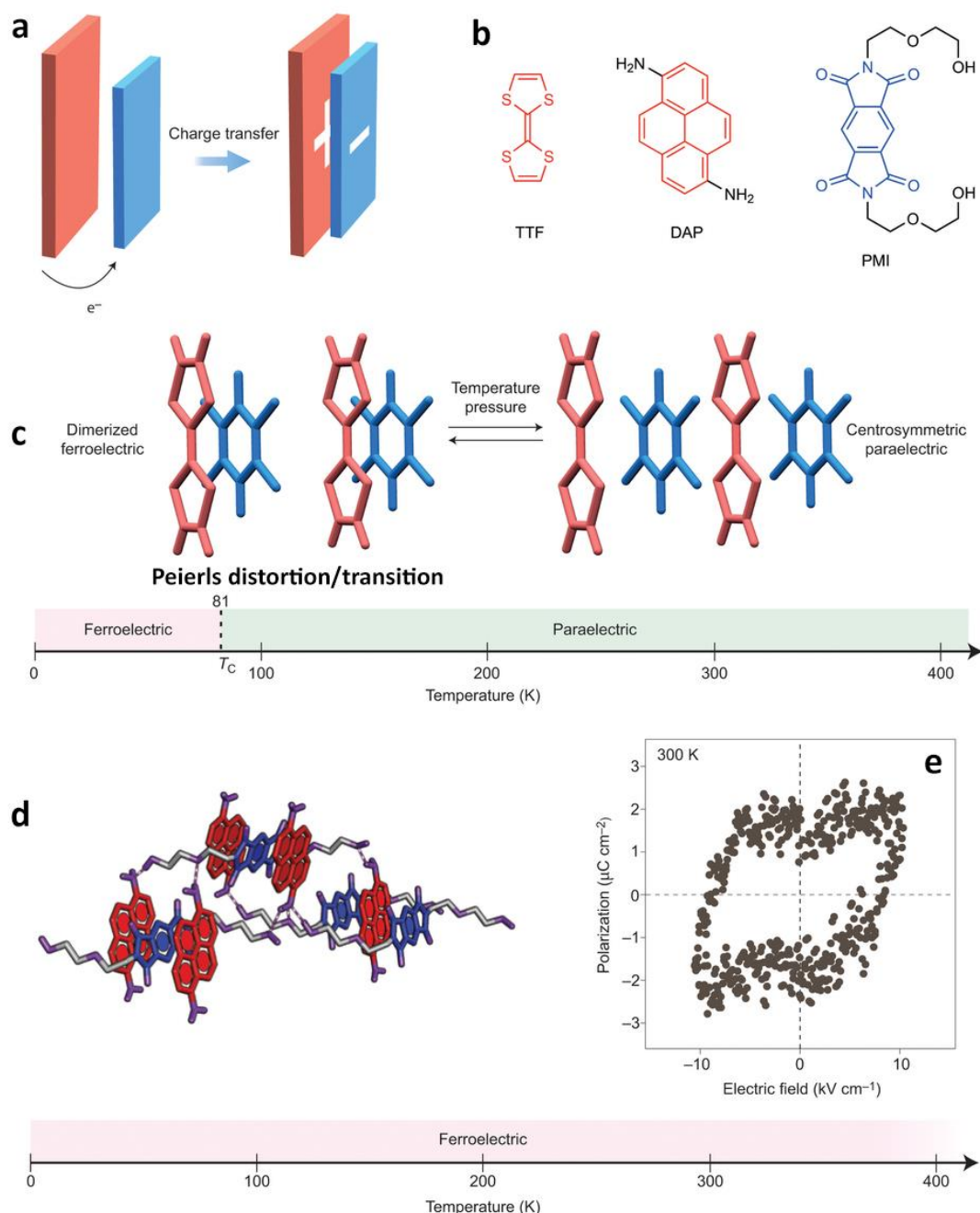


Figure 1.12: (a) Schematic of charge-transfer complex of electron donor (red) and electron acceptor (blue). (b) Chemical structure of the constituents used to form CT complexes. (c) Arrangement of the donor-acceptor pair in CT complex of TTF and chloranilic acid above and below T_c . (d) View of the supramolecular self-assembly of DAP and PMI where the

mixed stack is formed by the π - π stacking and CT between the donor-acceptor, while the hydrogen bonding through their arms forms a three-dimensional network that lock the individual stacks together. (e) The P-E loop for the DAP-PMI charge-transfer complex at room temperature. (Adapted by permission from Macmillan Publishers Ltd: "Nat. Chem. 2015, 7, 281" © 2015)

On the other hand, the mixed stack of CT complexes, that offer face-to-face alternate stacking of donor and acceptors to form one-dimensional co-crystal, may provide a route to produce displacive-type organic ferroelectrics by displacing the oppositely charged donor-acceptor molecules (Figure 1.12a). However, in most of the mixed stacks initially the donors and acceptors are equally spaced and hence form a periodic centrosymmetric arrangement. The Peierls transition, in which the donor and acceptor undergo relative molecular displacement along the axis of stack, breaks the periodic symmetry and forms a polar chain of dipolar D^+A^- dimers with macroscopic polarization. Further, on applying external electric field the donor-acceptor molecules can be swapped within the stack (e.g. the ...DA·DA·DA... can be changed to ...D·AD·AD·A...) which may ultimately cause polarization switching.^{53,54}

The CT complexes of tetrathiafulvalene (TTF) with halogenated quinones (QCl₄ and QBr₄) have been thoroughly investigated for their structure and ferroelectric properties.⁸⁶⁻⁸⁹ The TTF-QCl₄ co-crystal is centrosymmetric at room temperature and undergoes paraelectric-ferroelectric phase transition on cooling below 81 K (T_C) where the molecular displacement (Peierls transition) induces dimerization of donor and acceptor molecule (Figure 1.12c). One can also achieve such phase transition at higher pressures. The TTF-QBr₄ co-crystal is already in ionic form at room temperature but has shown to exhibit donor-acceptor dimerization (Peierls transition) at 53 K (T_C). Despite of the challenges in these systems, such as high leakage and lack of sufficient size and quality crystal, Tokura and co-workers have succeeded in performing ferroelectric hysteresis loop measurement for TTF-QCl₄, TTF-QBrCl₃ and TTF-QBr₄.^{90,91} Further, for obtaining room temperature ferroelectricity in such CT complexes, additional supramolecular interactions can be utilized to obtain polar donor-acceptor dimers as single crystal. Tayi et al. have shown a way to combine hydrogen bonding and CT to formulate an approach for disturbing centrosymmetric

packing in CT complexes.⁹² For this they used donors (based on naphthalene, pyrene and tetrathiafulvalene) and acceptors (based on pyromellitic diimide) with amine and diethylene glycol functionalized arms, such that they could form a supramolecular structure (Figure 1.12b). The hydrogen bonding between the functionalized arms of donors and acceptors formed a three-dimensional network that locks the mixed stack of donors and acceptors (Figure 1.12d). All these three supramolecular networks have shown room temperature ferroelectricity with a T_C of more than 400 K.⁹² Hence, this type of supramolecular design can provide numerous CT ferroelectrics, by employing donors and acceptors synthesized with a similar motif.

1.9.1.3 Order-disorder systems

Ferroelectricity and high T_C in dabco based organic salts (HdabcoClO_4 and HdabcoBF_4)^{78,79} have provided inspiration for the use of amine (such as dimethylamine, trimethylamine, diisopropylamine, aniline, cyclic and heterocyclic amines and their derivatives) based molecular organic salts to produce above room-temperature ferroelectrics suitable for practical applications.⁹³ However, this subsection provides discussion on few interesting polar organic salts where the ferroelectricity does not originate from hydrogen bond assisted polar order; instead it is governed by order-disorder or displacive type transition of their molecular constituents.

Recently, ferroelectricity has been discovered in two molecular salts, diisopropyl ammonium chloride (DIPAC) and diisopropyl ammonium bromide (DIPAB).^{57,58} These molecular salts exhibit excellent ferroelectric properties with high T_C values. Ferroelectricity in both salts originates from the order-disorder transition of N atoms of the diisopropyl ammonium cation (Figure 1.13a). Ferroelectric measurements revealed a spontaneous polarization of $8.2 \mu\text{Ccm}^{-2}$ for DIPAC salt (Figure 1.13b) which is higher than that of PVDF. The temperature dependent dielectric and SHG measurements gave an anomaly peak corresponding to the Curie temperature (T_C) at 440 K (Figure 1.13b,c).^{57,93} While the bromide salt, i.e., DIPAB exhibited a well-saturated hysteresis loop with a large spontaneous polarization and low coercive field just below $T_C = 426 \text{ K}$ (Figure 1.13d). The spontaneous polarization for DIPAB

was measured to be $23 \mu\text{Ccm}^{-2}$ using a pyroelectric technique (Figure 1.13e), which is comparable to that of barium titanate (BTO) and higher than many other organic and polymeric ferroelectrics.^{58,93}

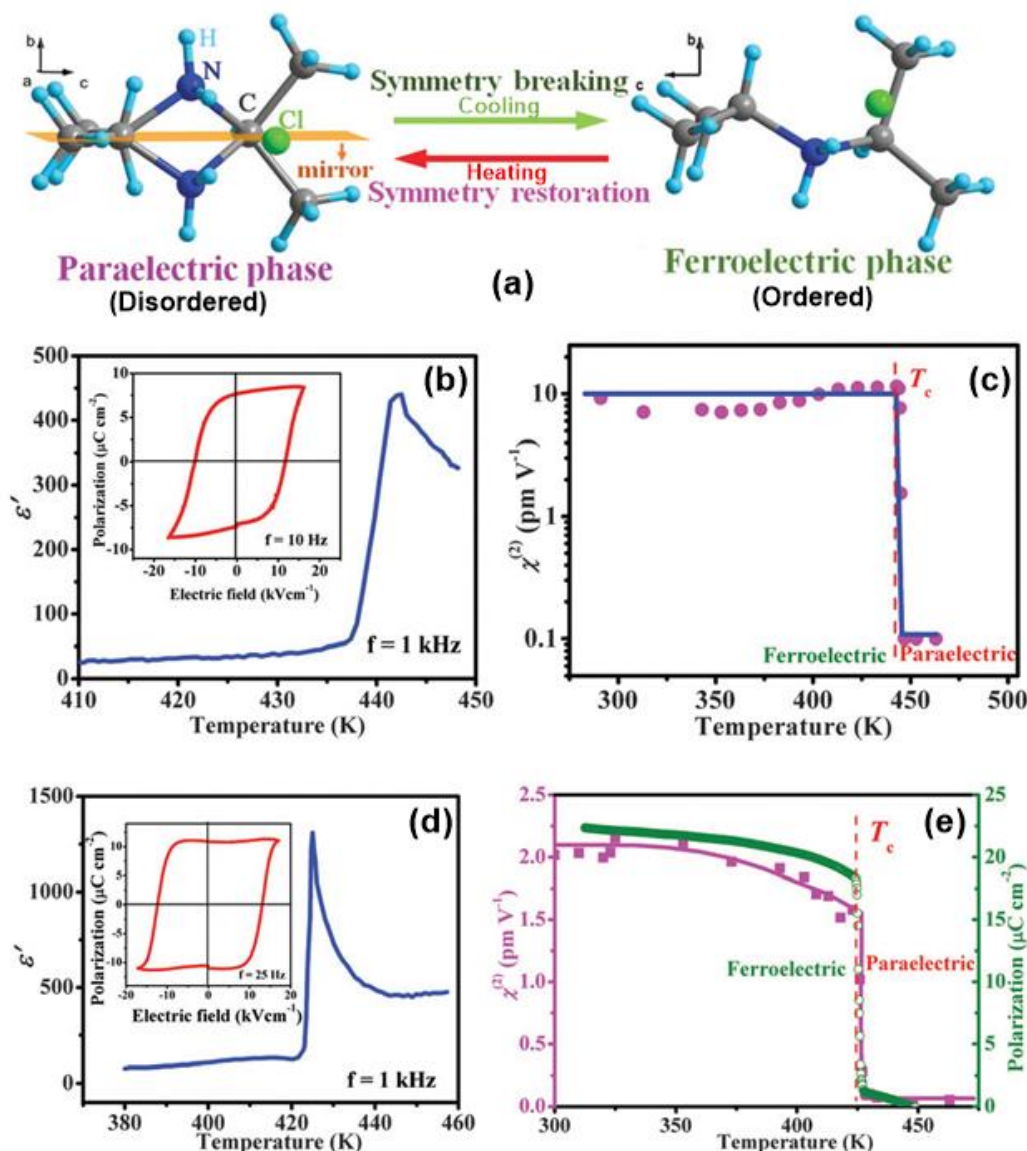


Figure 1.13: (a) Order-disorder phase transition in the diisopropyl ammonium cation. (b) Temperature dependent permittivity measurements (Inset: ferroelectric hysteresis loop recorded at 418 K) and (c) temperature dependent SHG response for diisopropyl ammonium chloride salt. (d) Temperature dependent permittivity measurements (Inset: ferroelectric hysteresis loop recorded at 416 K) and (e) temperature dependence of SHG response and spontaneous polarization (obtained through pyroelectric measurements) for diisopropyl ammonium bromide salt. (Adapted from “Xiong et al. *Chem. Soc. Rev.* **2016**, 45, 3811” with permission of The Royal Society of Chemistry)

A new simple organic salt, 4-(cyanomethyl) anilinium perchlorate ([4-NCCH₂-PhNH₃]⁺ClO₄⁻), was synthesized using an aromatic amine.⁹³ It exhibited ferroelectric properties below room temperature ($T_C = 184$ K) with low polarization values ($<1 \mu\text{Ccm}^{-2}$), however, it gave hysteresis loops even at a relatively higher frequency (10 kHz). Similarly, weak ferroelectric polarizations have also been revealed in pyridinium salts such as pyridinium perchlorate, pyridinium periodate, pyridinium perrhenate and pyridinium tetrafluoroborate.⁹⁵⁻⁹⁸ Apart from these, the salts of imidazole (Im) with anions like tetrafluoroborate (BF₄⁻),⁹⁹ perchlorate (ClO₄⁻),^{100,101} and periodate (IO₄⁻)¹⁰² have also been recently synthesized and studied for their decent ferroelectric behavior. The ferroelectric loop of imidazolium tetrafluoroborate (Im-BF₄) shows polarization value of $0.8 \mu\text{Ccm}^{-2}$ and coercive field of 3.5 kVcm^{-1} with a phase transition at 297 K (T_C).⁹⁹ However, the thin film of imidazolium perchlorate (Im-ClO₄) has been discovered to exhibit excellent ferroelectric behavior with high spontaneous polarization ($9.5 \mu\text{Ccm}^{-2}$), moderate coercive field (3.5 kVcm^{-1}) and high T_C (373 K).¹⁰¹ It also displayed exciting piezoelectric properties where the piezoelectric coefficient value was found to be on the higher side as compared to

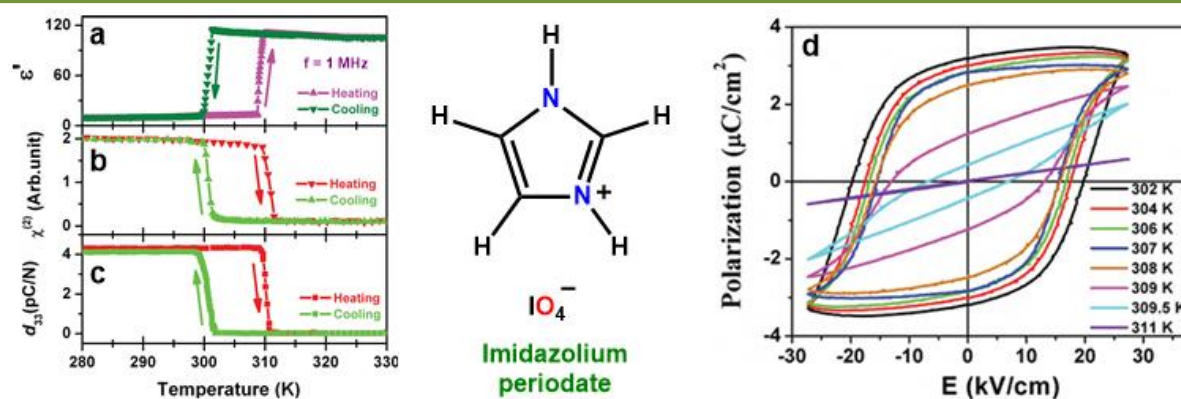


Figure 1.14: Temperature dependence of (a) dielectric, (b) SHG response ($\chi^{(2)}$) and (c) piezoelectric coefficient (d_{33}) in imidazolium periodate. (d) Ferroelectric hysteresis loop of imidazolium periodate at different temperature. (Adapted from “Xiong et al. *Adv. Mater.* **2014**, 26, 4515” © 2014 WILEY-VCH Verlag GmbH & Co. KGaA, Weinheim)

other molecular ferroelectrics. Further, ferroelectricity in a related molecular salt imidazolium periodate (Im-IO₄) have also revealed interesting features. In spite of comparatively low T_C (310 K) than its analogous ferroelectric salt Im-ClO₄, Im-IO₄ displays large thermal hysteresis and bistable properties in the dielectric,

piezoelectric and SHG behavior simultaneously (Figure 1.14a-c), which is not found in the case of Im-ClO₄. The large thermal hysteresis in Im-IO₄ corresponds to the large size of periodate anion. The ferroelectric hysteresis loop for Im-IO₄ gave P_s and E_c of about 3.5 μCcm⁻² and 20 kVcm⁻¹, respectively (Figure 1.14d). The molecular salt obtained by using all-deuterated imidazole exhibits similar electric dipole moments and phase transition temperature as that of non-deuterated Im-IO₄, suggesting that the ferroelectricity in Im-IO₄ mainly originates from the order-disorder transition of imidazolium rings and not influenced from the hydrogen-bonding.¹⁰²

1.9.2 Ferroelectricity in Liquid Crystals

Liquid crystals (or Mesogens) are another class of supramolecular systems that can be described as ordered liquids or disordered solids as they can flow like a liquid but hold some degree of ordering in its molecular arrangement. The unique combination of long range order and mobility in liquid crystals produces anisotropic physical properties that can be switched by the influence of external stimuli. In the case of ferroelectric liquid crystals, the ordered arrangement of molecules provide pseudo-rigidity which aids in establishing bistable molecular dipoles and easy switching of spontaneous polarization created by them. In most of the cases, treated device surface or additional processing are required for inducing ferroelectricity in liquid crystals. The two ways by which ferroelectricity is introduced in liquid crystals are (a) organization of chiral mesogens or (b) by the creation of intrinsic dipole within achiral molecules (Figure 1.15).⁵⁴

Meyer et al. have first demonstrated that the chiral rod-like Mesogens can possess net polarization if their smectic C phase can be changed to the tilted and layered arrangement of molecules (Figure 1.15a).¹⁰³ Similarly, Clark and Lagerwall have constructed a device that utilizes a treated substrate to provide surface mechanical forces required for the unwinding the helical structure of chiral mesogens and transforms them into a polar order.¹⁰⁴ Ferroelectric properties of such chiral smectic mesogens have been utilized for technological applications such as ferroelectric liquid crystal display. Apart from these discotic mesogens, having chiral side chains, are known to form columnar mesophases where the mesogens are arranged in a

tilted helical column. The application of electric field unwinds the helix and leaves only a tilted column of mesogens with a net polarization (Figure 1.15b).¹⁰⁵⁻¹⁰⁷ However, the mechanism of polarization switching in these systems is still unclear, but it is thought to be driven by the rotation of entire column by 180° or by the reorientation of independent molecules, which causes delay in switching as the rotation of the structure is sluggish due to the resistance offered by the neighboring column or molecule.⁵⁴

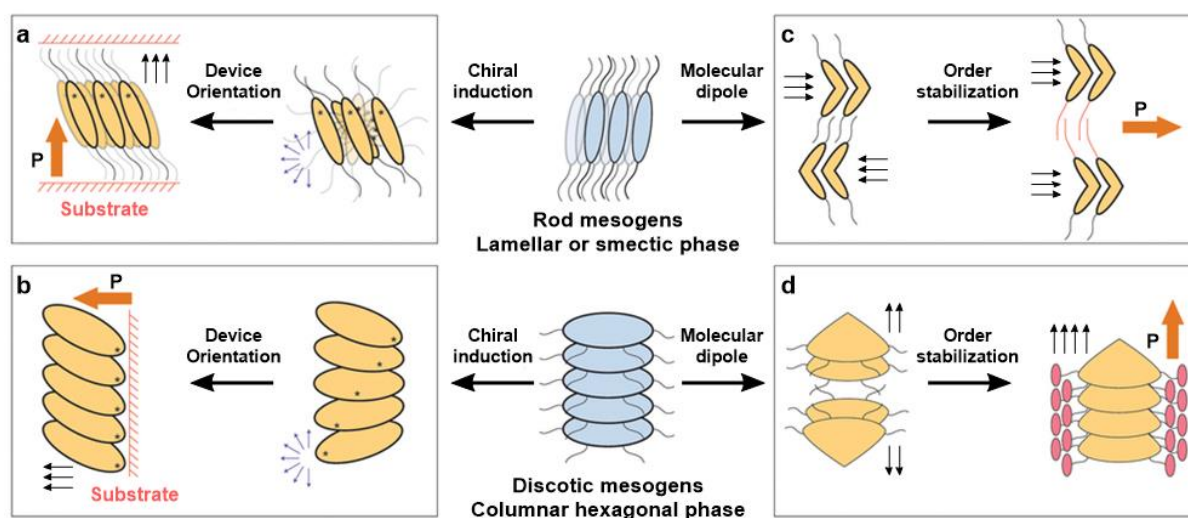


Figure 1.15: Schematic for the evolution of ferroelectric ordering in rod-shaped and discotic mesogens. (Adapted by permission from Macmillan Publishers Ltd: “*Nat. Chem.* **2015**, *7*, 281” © 2015)

Some of the mesogens containing achiral polar molecules may also exhibit ferroelectricity by self-assembling themselves into a chiral or achiral structure. Mesogens having bent-core molecules (with low C_{2v} symmetry) assemble in an ordered head-to-tail packing to form layers with the same orientation (Figure 1.15c) providing a macroscopic polarization to the system. The ferroelectricity in the bent-core liquid crystals was first reported by Takezoe and co-workers.¹⁰⁸ Sometimes the adjacent layers have an antiparallel orientation which can suppress their ferroelectric property. To address this Dantlgraber et al. demonstrated a specific design of introducing siloxane spacers in the mesogen in order to prevent the tilted packing of molecules and to promote polar dipole alignment. Liquid crystals having macrocyclic cone-shaped molecules can be utilized as another approach to obtain columnar mesogens with polarized domains.¹⁰⁹

The hexagonal columnar liquid crystals are an alternative supramolecular design for attaining intrinsic ferroelectricity, as it forms polar columns in the triangular lattice to provide macroscopic polarization parallel to the columnar axis.⁵⁴ This strategy has been utilized to attain polar order in many bowl-shaped Mesogens (Figure 1.15d). Further, Miyajima et al. have demonstrated a molecular design of stabilizing a bowl-shaped phthalonitrile derivative as a polar columnar supramolecular structure by using hydrogen bonding.^{110,111} Moreover, the phthalonitrile units construct the polarizable core and are responsible for the ferroelectric effect in such columnar liquid crystal, while the hydrogen bonding supplements to maintain the unidirectional orientation of the column (Figure 1.16). This liquid crystal is the first example of its type where the

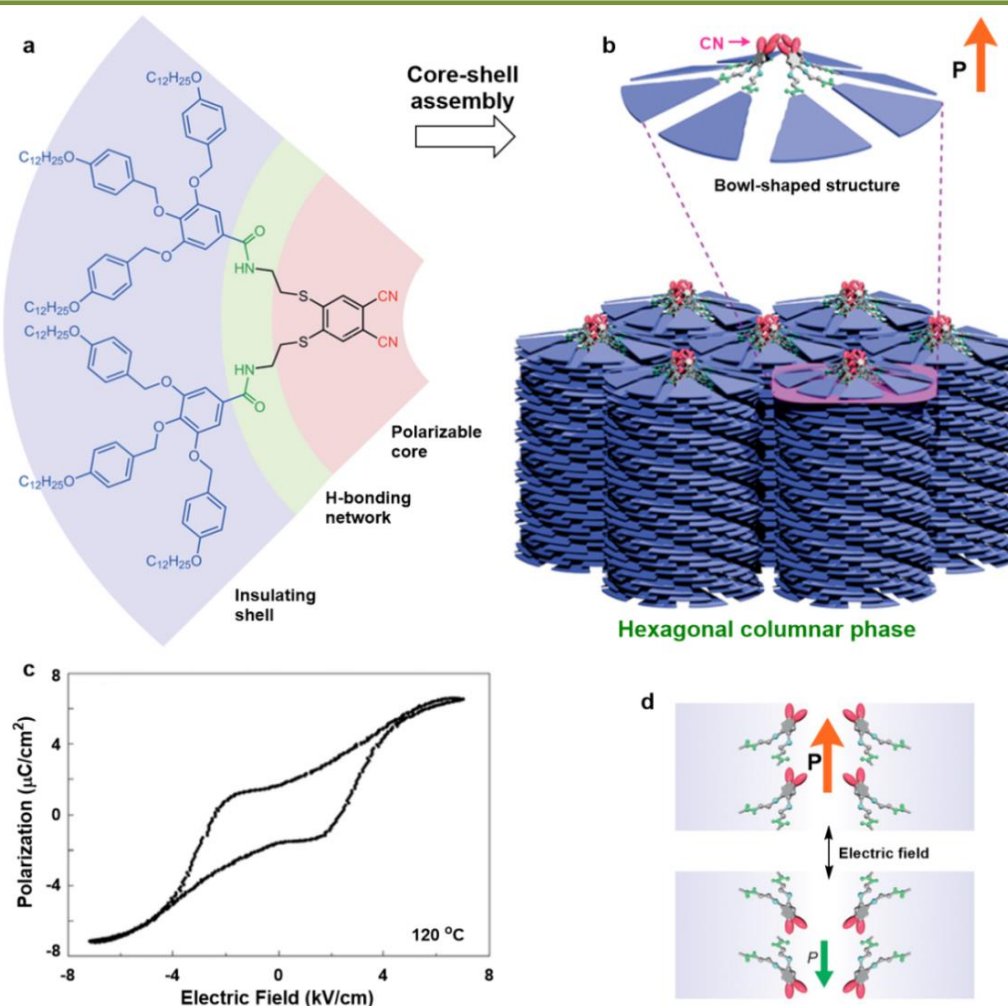


Figure 1.16: (a) The chemical structure of the mesogen that forms a columnar ferroelectric liquid crystal. (b) Schematic of the core-shell assembly of the mesogen with peripheral aliphatic side chain around the phthalonitrile units. (c) The ferroelectric hysteresis loop of the

liquid crystal at 120 °C. (d) Arrangement of cyano group within the columns leading to polar order and its switching. (Adapted by permission from Macmillan Publishers Ltd: "Nat. Chem. 2015, 7, 281" © 2015)

system exhibits intrinsic ferroelectricity, without using any device surface or further processing, and hence elucidates a new prospect for obtaining easily processable ferroelectric materials.

1.9.3 Ferroelectricity in Metal-Organic materials

Metal-organic ferroelectric materials represent a hybrid class which can bridge the trench between the inorganic and organic ferroelectrics. The inorganic and organic components (such as metal ions, linkers/ligands, solvent, anions, etc.) of the metal-organic materials provide several benefits like flexibility, tunability, and structural variability. As a result, a wide range of metal-organic materials that can exhibit ferroelectricity is possible such as ionic metal-organic salts, coordination complexes, host-guest assemblies, etc. These materials employ various interactions (such as ionic, coordination, hydrogen-bonding, etc.) between the organic struts and the metallic components (metal ions or clusters) to form zero-, one-, two-, or three-dimensional structures. Rochelle salt, which is the first ferroelectric material to be discovered, comprises of tartrate anion (organic) and K^+ and Na^+ cations (metal ions) and hence is the first metal-organic ferroelectric material.³⁵ Further, ferroelectricity has been explored in compounds analogous to Rochelle salt, commonly known as tartrate salt family, where the K^+ and/or Na^+ metal ions were replaced by other cations (such as NH_4^+ , Li^+ , Tl^+). This inspired the formation of various families of ferroelectric metal-organic salts or frameworks such as metal-organic sulfates, metal-amino acid systems, metal-propionates, metal formates, and organo-halogenometallates.³⁴ Some of the metal-organic materials having spinel structure (ABX_4) also exhibit ferroelectric properties. Kundys et al. have demonstrated ferroelectricity in a metal-organic complex compound $[C_2H_5NH_3]_2[CuCl_4]$ that have layers of ethyl-ammonium groups attached to distorted $CuCl_6$ octahedra, and the ordering of the ethyl-ammonium cation below 247 K results in a ferroelectric phase (Figure 1.17).¹¹² The P-E loop of this material showed a high remnant polarization of $37 \mu Ccm^{-2}$, however, the measurement was performed at 77K.

Some of the metal-organic assemblies have found to possess the structural features similar to those found in ceramic families of ferroelectric materials. For example, metal formates exhibit a three-dimensional perovskite lattice (ABX_3)^{34,59-61} containing

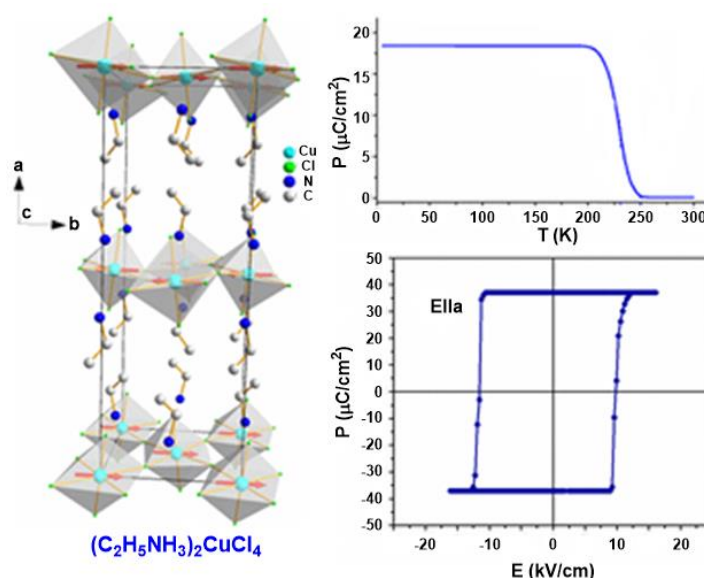


Figure 1.17: Structure and ferroelectric behavior of the ethylammonium copper chloride metal-organic compound showing very high ferroelectric polarization. (Adapted figure with permission from “Kundys et al. *Physical Review B* **2010**, 81, 224434” © 2010 by the American Physical Society)

infinite anionic metal-formate framework and organoammonium cations as interstitial guests in which the mono-cationic organoammonium ions ($[NR_4]^+$) represent the A-sites, divalent transition metal ions represent the B-sites and the formate ions as X-sites (Figure 1.18). Similar to the ceramic based ferroelectric materials, the polarization in these metal-organic materials mostly originates from order-disorder type mechanism or displacive mechanism and controlled by non-covalent interactions (such as hydrogen bonding, π - π interactions, and dipole interactions) between the host framework and the guest cation. Recent theoretical calculations by Stroppa and co-workers suggest that engineering the A-sites in metal-formate based perovskites alters the ferroelectric polarization.¹¹³ They have predicted remarkable enhancement in ferroelectric polarization values by replacing the $[NR_4]^+$ units with cationic phosphorus moieties such as alkyl/aryl phosphonium cations ($[PR'_xR_{4-x}]^+$). Notably, the largest value of the polarization, as high as $\sim 6 \mu Ccm^{-2}$, was predicted for the formate-based ABX_3 systems with a hypothetical $A = [PH_3(CH_2CF_3)]^+$ motifs.

Many articles can be found in literature focusing on the experimental and theoretical exploration of ferroelectricity in a series of metal-formate framework systems.

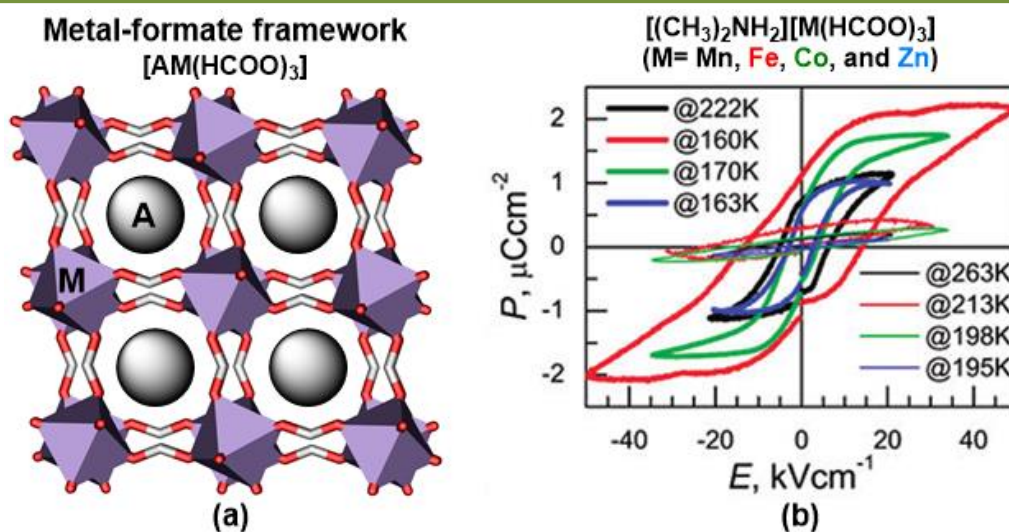


Figure 1.18: (a) A general representation of the perovskite-type metal-formate framework with organic cations (A) as intrinsic guest. (b) Ferroelectric hysteresis loops for $[(\text{CH}_3)_2\text{NH}_2][\text{M}(\text{HCOO})_3]$ frameworks ($M = \text{Mn, Fe, Co, Zn}$) at temperatures below and above their transition temperature (T_C). (Adapted with permission from “Gao et al. *J. Am. Chem. Soc.* **2011**, 133, 14948” © 2011 American Chemical Society)

Even many metal-organic salts do possess perovskite structure and exhibit ferroelectricity. Methylammonium lead halides, belonging to the organo-halogenometallate family, are well known for their application as light-harvesting layers in solar cells however recent research is focused on their ferroelectric behavior too.¹¹⁴ Similarly, many other organo-halogenometallates with perovskite structure have been discovered. Xiong and co-workers have discovered molecular pyrrolinium and pyrrolidinium manganese halide salts that can exhibit ferroelectricity in addition to other attractive properties such as photoluminescence and ferromagnetism.⁶³⁻⁶⁵ Such multifunctional compounds are very interesting and could pave the way forward for the preparation of high performance ferroelectric fluorescent displays, optoelectronic devices, and magneto-optoelectronic systems. The same research group has very recently developed a 3-dimensional molecular ferroelectric perovskite $[(3\text{-ammonio}(\text{pyrrolidinium}))\text{RbBr}_3]$ that exhibits multiaxial polarization with extremely fast polarization reversal, high T_C (440 K) and high thermal stability which is unprecedented in 3D metal-organic perovskites.⁶²

Apart from these, several ferroelectric metal-organic frameworks (MOFs), which crystallize in polar point group, have also been studied for their ferroelectric behavior.¹¹⁵ In MOFs non-centrosymmetric arrangement can be achieved by using: (a) building blocks with three-fold symmetry, (b) chiral linkers, (c) linkers with non-coordinating polar head groups, and/or (d) polar guests that interact with the host MOF through supramolecular interactions. Although there are several MOFs that crystallize in polar point group, the observed ferroelectric polarization values, and transition temperatures are far from the practical utility, except for few. Mak and co-workers have recently synthesized a Co(II) based homochiral metal-organic framework constructed by (1,3-dicarboxy-5-benzyl)carboxymethyl glycine and 1,3-bis(4-pyridyl)ethane ligands containing helical water columns.¹¹⁶ These infinite water channels provided ordered-chain of polarizable molecules which lead to solvation (on) and desolvation (off) assisted ferroelectric switching behavior (Figure 1.19). Further, in certain MOFs the free rotation of linkers has been utilized to achieve bistable orientation under the electric field.

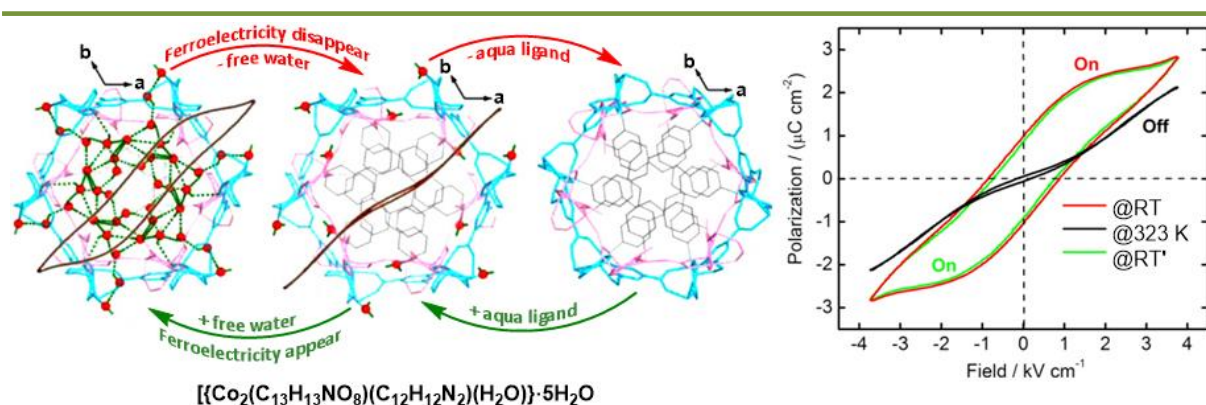


Figure 1.19: Solvent-dependent on-off switching of ferroelectric behavior in a Co(II) based metal-organic framework. (Adapted with permission from “Mak et al. *J. Am. Chem. Soc.* **2013**, *135*, 10214” © 2013 American Chemical Society)

1.9.4 Ferroelectricity in nonpolar supramolecular systems

Mostly the ferroelectric ordering results from the spatial asymmetry (polar point group) of the crystalline inorganic/organic/hybrid solids. But in few instances, the supramolecular interactions, along with some additional factors, influence permanent ferroelectric ordering even in the crystalline systems belonging to a non-polar point group. The finding of Akutagawa et al. demonstrates the control the polarity and

ferroelectricity by the rotation of meta-fluoroanilinium cation in a non-polar supramolecular rotator, $(m\text{-FAni})^+(\text{dibenzo}[18]\text{crown-6}) [\text{Ni}(\text{dmit})_2]^-$ {where, $m\text{-FAni}$ = meta-fluoroanilinium; dmit = 2-thioxo-1,3-dithiole-4,5-dithiolate} (Figure 1.20).¹¹⁷ In this case, the m -fluoroanilinium cation interacts with the dibenzo[18]crown-6 through hydrogen-bonding to form a stator-rotator assembly, while the charge-balancing $[\text{Ni}(\text{dmit})_2]^-$ anions provide steric hindrance to stabilize the rotation of cation. The m -fluoroanilinium cation undergoes an 180° flip-flop rotation and brings a centrosymmetric structure (Figure 1.20a). On application of electric field, the fluorine

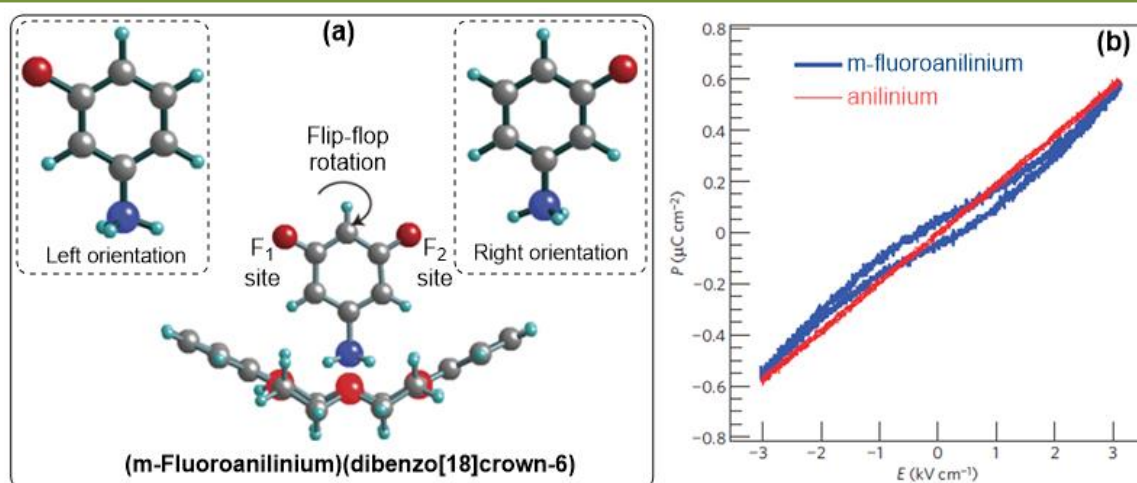


Figure 1.20: (a) Orientational disorder (F_1 and F_2 sites) for the fluorine atom of m -fluoroanilinium cation in supramolecular rotator salt, $(m\text{-FAni})^+(\text{dibenzo}[18]\text{crown-6}) [\text{Ni}(\text{dmit})_2]^-$. (b) P - E loop for the supramolecular salt having m -fluoroanilinium cation (blue; rotatory group present; ferroelectric) and anilinium cation (red; rotatory group absent; paraelectric). (Adapted by permission from Macmillan Publishers Ltd: "Nat. Mater. **2009**, 8, 342" © 2009)

atom occupies either of the F_1 or F_2 sites and creates a polar order throughout the lattice, which is responsible for the ferroelectric nature of this molecule. The role of flip-flop supramolecular rotators in controlling the ferroelectricity and polarity was further affirmed by a control experiment where the compound having anilinium cation (the rotatory group was absent) was found to be paraelectric (Figure 1.20b).

Alternately, the ordered arrangement of polar solvent within a confined environment such as carbon nanotube, nanopore membranes, and porous MOFs has also shown to induce ferroelectric polarization even in the non-polar lattice. Li and co-workers

have recently synthesized an indium 2-amino terephthalate framework in non-centrosymmetric but non-polar space group (Figure 1.21a,b).¹¹⁸ The nanochannels of the framework are filled with spiral water chains along the c-axis. The electric field controlled hydrogen bonding interaction of the water molecule with the amine-tethered nanochannels of the framework generates the polarization, which leads to a saturation polarization (P_s) of $3.8 \mu\text{Ccm}^{-2}$ during the P-E loop measurements (Figure 1.21c).

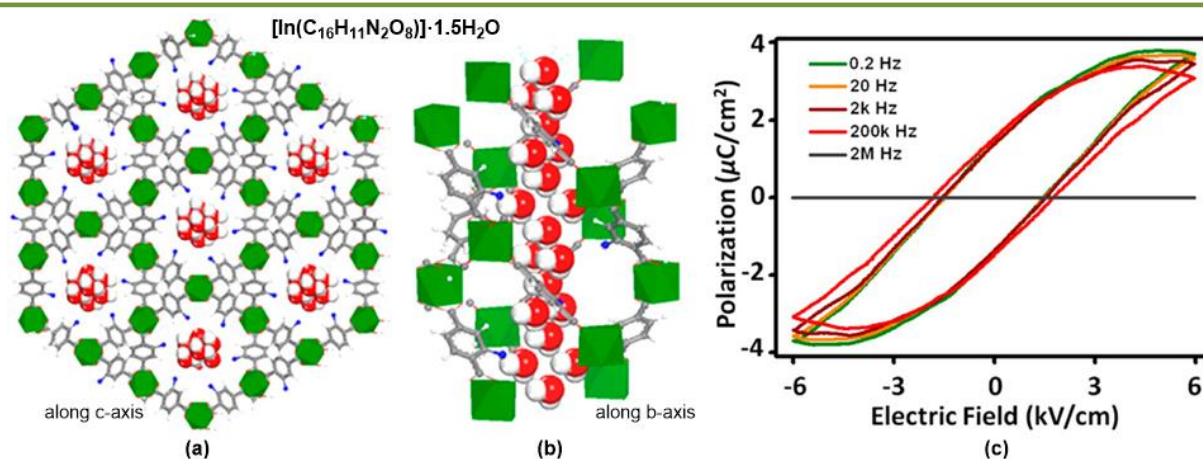


Figure 1.21: View of the Indium 2-amino terephthalate framework along (a) c-axis and (b) b-axis, showing the spiral water chains present in the nano-channels. (c) Ferroelectric hysteresis loop of the framework at different frequencies at room temperature. (Adapted with permission from “Li et al. *J. Am. Chem. Soc.* **2014**, 136, 17477” © 2014 American Chemical Society)

1.10 Outline and Objective of the Thesis

The discussions in the previous sections has highlighted the progress made in recent years for the development of organic and metal-organic supramolecular compounds that can exhibit ferroelectric behavior. However, the synthetic approaches to access such ferroelectric materials are still challenging and serendipitous because of the strict requirement of a non-centrosymmetric arrangement of the molecular constituents. Thus, there is an immense need for further efforts to systematically develop new families of metal-organic and/or organic ferroelectric materials by molecular design and crystal engineering approach. Efforts are also required to enable a better understanding of the molecular mechanism of

polarization in such supramolecules along with an aim for improved performance for practical utility.

This thesis demonstrates the efforts to obtain charge-separated supramolecular metal-organic and organic systems, derived from amino-P(V) scaffolds, in polar lattice parameters. The next four chapters will discuss a facile approach to synthesize a library of functionalized P-N scaffolds, as neutral phosphoramidate ligands or cationic phosphonium species, which assist in obtaining non-centrosymmetric metal-organic or organic assemblies and further to evaluate their ferroelectric behavior. The chapters 2, 3 and 4 will discuss the synthesis, characterization and ferroelectric properties of certain metal-organic materials that are obtained from the reaction of transition metal ions (such as Cu^{2+} , Ni^{2+} , Co^{2+}) with a dipodal flexible amino-P(V) ligand featuring peripheral pyridyl-functionalized arms, in presence of suitable counteranions and solvents. These three chapters will also elucidate the rational approach to induce required symmetry (polar point group) as well as tuning of the ferroelectric behavior in the metal-organic assemblies by a careful choice of its structural components (such as metal ions, coordinating ligands, counter anions and the guest molecules). The Chapter 5 will describe the synthesis, characterization and ferroelectric properties of polar organic salts derived from cationic phosphonium species, i.e., tetraanilino phosphonium cation.

Thus the present thesis aims:

- to synthesize new flexible amino-P(V) ligands containing peripheral N-donor functionalities and their corresponding charge separated metal-organic materials in unique structural architectures.
- to synthesize new polar organic salts stabilized by phosphonium cations.
- to assess the dielectric and ferroelectric behavior of the newly synthesized non-centrosymmetric metal-organic/organic materials having interesting structural features.

1.11 REFERENCES

- (1) Whitesides, G. M.; Boncheva M. *Proc. Natl. Acad. Sci. U.S.A.* **2002**, *99*, 4769.
- (2) Cook, T. R.; Zheng, Y.-R.; Stang, P. J. *Chem. Rev.* **2013**, *113*, 734.
- (3) Stupp, S. I.; Palmer, L. C. *Chem. Mater.* **2014**, *26*, 507.
- (4) Long, J. R.; Yaghi, O. M. *Chem. Soc. Rev.* **2009**, *38*, 1213.
- (5) Zou, X. Q.; Ren, H.; Zhu, G. S. *Chem. Commun.* **2013**, *49*, 3925.
- (6) Müller, C.; Whiteford, J. A.; Stang, P. J. *J. Am. Chem. Soc.* **1998**, *120*, 9827.
- (7) Cai, H.; Li, M.; Lin, X.-R.; Chen, W.; Chen, G.-H.; Huang, X.-C.; Li, D. *Angew. Chem. Int. Ed.* **2015**, *54*, 10454.
- (8) Yang, H.; Yuan, B.; Zhang, X. *Acc. Chem. Res.* **2014**, *47*, 2106.
- (9) Liu, J.; Chen, L.; Cui, H.; Zhang, J.; Zhang, L.; Su, C.-Y. *Chem. Soc. Rev.* **2014**, *43*, 6011.
- (10) Xia, A.-B.; Xu, D.-Q.; Wu, C.; Zhao, L.; Xu, Z.-Y. *Chem. Eur. J.* **2012**, *18*, 1055.
- (11) Ajami, D.; Rebek, J. Jr. *Angew. Chem. Int. Ed.* **2008**, *47*, 6059.
- (12) Duriska, M. B.; Neville, S. M.; Lu, J.; Iremonger, S. S.; Boas, J. F.; Kepert, C. J.; Batten, S. R. *Angew. Chem. Int. Ed.* **2009**, *48*, 8919.
- (13) Zeng, F.; Zimmerman, S. C. *Chem. Rev.* **1997**, *97*, 1681.
- (14) Huang, Y. L.; Chen, W.; Wee, A. T. S. *J. Am. Chem. Soc.* **2011**, *133*, 820.
- (15) Hang, T.; Zhang, W.; Ye, H.-Y.; Xiong, R.-G. *Chem. Soc. Rev.* **2011**, *40*, 3577.
- (16) Real, J. A.; Andrés, E.; Muñoz, M. C.; Julve, M.; Granier, T.; Bousseksou, A.; Varret, F. *Science* **1995**, *268*, 1127.
- (17) Akutagawa, T.; Nishihara, S.; Takamatsu, N.; Hasegawa, T.; Nakamura, T.; Inabe, T. *J. Phys. Chem. B* **2000**, *104*, 5871.
- (18) Papadopoulos, M. G.; Sadlej, A. J.; Leszczynski, J. *Nonlinear Optical Properties of Matter: From Molecules to Condensed Phases*; Springer: Dordrecht, The Netherlands, 2006.
- (19) Whatmore, R. *Ferroelectric Materials*. In *Springer Handbook of Electronic and Photonic Materials*, Springer: 2007; 597.
- (20) Cheong, S.-W.; Mostovoy, M. *Nat. Mater.* **2007**, *6*, 13.
- (21) Ramesh, R. *Nature* **2009**, *461*, 1218.
- (22) Eerenstein, W.; Mathur, N. D.; Scott, J. F. *Nature* **2006**, *442*, 759.
- (23) Spaldin, N. A.; Fiebig, M. *Science* **2005**, *309*, 391.
- (24) Cheetham, A. K.; Rao, C. N. R. *Science* **2007**, *318*, 58.

- (25) Das, S.; Appenzeller, J. *Nano Lett.* **2011**, *11*, 4003.
- (26) De Araujo, C. A-P.; Cuchiario, J. D.; McMillan, L. D.; Scott, M. C.; Scott, J. F. *Nature* **1995**, *374*, 627.
- (27) Han, S.-T.; Zhou, Y.; Roy, V. A. L. *Adv. Mater.* **2013**, *25*, 5425.
- (28) Scott, J. F.; De Araujo, C. A. P. *Science* **1989**, *246*, 1400.
- (29) Scott, J. F. *Ferroelectric memories* Vol. 3. Springer Science & Business Media: 2000.
- (30) Lines, M. E.; Glass, A. M. *Principles and applications of ferroelectrics and related materials*. Clarendon press Oxford: 1977.
- (31) Scott, J. F. *Science* **2007**, *315*, 954.
- (32) Uchino, K. *Ferroelectric Devices* 2nd Edition. CRC press: 2009.
- (33) Xu, Y. *Ferroelectric materials and their applications*. Elsevier: 2013.
- (34) Zhang, W.; Xiong, R.-G. *Chem. Rev.* **2012**, *112*, 1163.
- (35) Valasek, J. *Phys. Rev.* **1921**, *17*, 475-481.
- (36) Busch, G.; Scherrer, P. *Naturwissenschaften* **1935**, *23*, 737.
- (37) Samara, G. A. *Ferroelectrics* **1973**, *5*, 25.
- (38) Matthias, B. T.; Miller, C. E.; Remeika, J. P. *Phys. Rev.* **1956**, *104*, 849.
- (39) Fatuzzo, E.; Merz, W. J. *Phys. Rev.* **1959**, *116*, 61.
- (40) "http://nptel.ac.in/courses/113104005/68", Electro Ceramics Web Course (NPTEL), by Prof. Ashish Garg.
- (41) López-Juárez, R.; González, F.; Villafuerte-Castrejón, M.-E. *Lead-free ferroelectric ceramics with perovskite structure*. Ferroelectrics-Material Aspects. InTech: 2011.
- (42) Cross, L. E. *Ferroelectric Ceramics: Tailoring Properties for Specific Applications*. In: Ferroelectric Ceramics. Monte Verità (Proceedings of the Centro Stefano Franscini, Ascona). Birkhäuser Basel: 1993.
- (43) Ok, K. M.; Chi, E. O.; Halasyamani, P. S. *Chem. Soc. Rev.* **2006**, *35*, 710.
- (44) Zhang, Y.; Xie, M.; Roscow, J.; Bao, Y.; Zhou, K.; Zhang, D.; Bowen, C. R. *J. Mater. Chem. A* **2017**, *5*, 6569.
- (45) Wan, C.; Bowen, C. R. *J. Mater. Chem. A* **2017**, *5*, 3091.
- (46) Xie, M.; Dunn, S.; Boulbarac, E. L.; Bowen, C. R. *Int. J. Hydrogen Energy* **2017**. (In Press; DOI: 10.1016/j.ijhydene.2017.02.086)
- (47) Bowen, C. R.; Kim, H. A.; Weaver, P. M.; Dunn, S. *Energy Environ. Sci.* **2014**, *7*, 25.

- (48) Bowen, C. R.; Taylor, J.; LeBoulbar, E.; Zabek, D.; Chauhan, A.; Vaish, R. *Energy Environ. Sci.* **2014**, *7*, 3836.
- (49) Fan, Z.; Sun, K.; Wang, J. *J. Mater. Chem. A* **2015**, *3*, 18809.
- (50) Chen, B.; Shi, J.; Zheng, X.; Zhou, Y.; Zhuc, K.; Priya, S. *J. Mater. Chem. A* **2015**, *3*, 7699.
- (51) Bai, Y.; Siponkoski, T.; Peräntie, J.; Jantunen, H.; Juuti, J. *Appl. Phys. Lett.* **2017**, *110*, 063903.
- (52) Abdelkefi, H.; Khemakhem, H. *J. Appl. Phys.* **2007**, *102*, 114106.
- (53) Horiuchi, S.; Tokura, Y. *Nat. Mater.* **2008**, *7*, 357.
- (54) Tayi, A. S.; Kaeser, A.; Matsumoto, M.; Aida, T.; Stupp, S. I. *Nat. Chem.* **2015**, *7*, 281.
- (55) Zhang, W.; Ye, H.-Y.; Xiong, R.-G. *Coord. Chem. Rev.* **2009**, *253*, 2980.
- (56) Horiuchi, S.; Tokunaga, Y.; Giovannetti, G.; Picozzi, S.; Itoh, H.; Shimano, R.; Kumai, R.; Tokura, Y. *Nature* **2010**, *463*, 789.
- (57) Fu, D.-W.; Zhang, W.; Cai, H.-L.; Ge, J.-Z.; Zhang, Y.; Xiong, R.-G. *Adv. Mater.* **2011**, *23*, 5658.
- (58) Fu, D.-W.; Cai, H.-L.; Liu, Y.; Ye, Q.; Zhang, W.; Zhang, Y.; Chen, X.-Y.; Giovannetti, G.; Capone, M.; Li, J.; Xiong, R.-G. *Science* **2013**, *339*, 425.
- (59) Jain, P.; Dalal, N. S.; Toby, B. H.; Kroto, H. W.; Cheetham, A. K. *J. Am. Chem. Soc.* **2008**, *130*, 10450.
- (60) Xu, G.-C.; Ma, X.-M.; Zhang, L.; Wang, Z.-M.; Gao, S. *J. Am. Chem. Soc.* **2010**, *132*, 9588.
- (61) Xu, G.-C.; Zhang, W.; Ma, X.-M.; Chen, Y.-H.; Zhang, L.; Cai, H.-L.; Wang, Z.-M.; Xiong, R.-G.; Gao, S. *J. Am. Chem. Soc.* **2011**, *133*, 14948.
- (62) Pan, Q.; Liu, Z.-B.; Tang, Y.-Y.; Li, P.-F.; Ma, R.-W.; Wei, R.-Y.; Zhang, Y.; You, Y.-M.; Ye, H.-Y.; Xiong, R.-G. *J. Am. Chem. Soc.* **2017**, *139*, 3954.
- (63) Zhang, Y.; Liao, W.-Q.; Fu, D.-W.; Ye, H.-Y.; Liu, C.-M.; Chen, Z.-N.; Xiong, R.-G. *Adv. Mater.* **2015**, *27*, 3942.
- (64) Zhang, Y.; Liao, W. Q.; Fu, D. W.; Ye, H. Y.; Chen, Z. N.; Xiong, R. G. *J. Am. Chem. Soc.* **2015**, *137*, 4928.
- (65) Ye, H. Y.; Zhou, Q.; Niu, X.; Liao, W. Q.; Fu, D. W.; Zhang, Y.; You, Y. M.; Wang, J.; Chen, Z. N.; Xiong, R. G. *J. Am. Chem. Soc.* **2015**, *137*, 13148.
- (66) Richerson, D. W. *Modern ceramic engineering: properties, processing, and use in design*. CRC press: 2005.

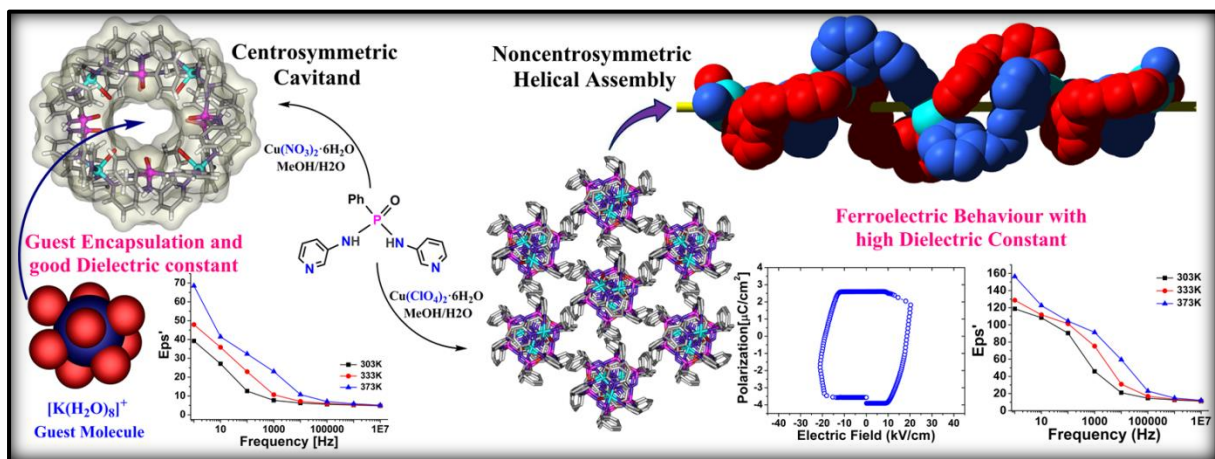
- (67) Rosenberg, H. M. *The solid state*. Oxford University Press: 1988.
- (68) Kasap, S. O. *Principles of electronic materials and devices* Vol. 784. McGraw-Hill New York: 2006.
- (69) Keppens, V. *Nat. Mater.* **2013**, *12*, 952.
- (70) Nalwa, H. S. *Ferroelectric polymers: chemistry: physics, and applications*. CRC Press: 1995.
- (71) Noda, K.; Ishida, K.; Kubono, A.; Horiuchi, T.; Yamada, H.; Matsushige, K. *J. Appl. Phys.* **2003**, *93*, 2866.
- (72) Prateek; Thakur, V. K.; Gupta, R. K. *Chem. Rev.* **2016**, *116*, 4260.
- (73) Fan, F. R.; Tang, W.; Wang, Z. L. *Adv. Mater.* **2016**, *28*, 4283.
- (74) Solomon, A. L. *Phys. Rev.* **1956**, *104*, 1191.
- (75) Goldsmith, G. J.; White, J. G. *J. Chem. Phys.* **1959**, *31*, 1175.
- (76) Bordeaux, D.; Bornarel, J.; Capiomont, A.; Lajzerowicz-Bonneteau, J. *Phys. Rev. Lett.* **1973**, *31*, 314.
- (77) Choudhury, R. R.; Chitra, R. *Cryst. Res. Technol.* **2006**, *41*, 1045.
- (78) Katrusiak, A.; Szafranski, M. *Phys. Rev. Lett.* **1999**, *82*, 576.
- (79) Shi, P.-P.; Tang, Y.-Y.; Li, P.-F.; Ye, H.-Y.; Xiong, R.-G. *J. Am. Chem. Soc.* **2017**, *139*, 1319.
- (80) Horiuchi, S.; Ishii, F.; Kumai, R.; Okimoto, Y.; Tachibana, H.; Nagaosa, N.; Tokura, Y. *Nat. Mater.* **2005**, *4*, 163.
- (81) Horiuchi, S.; Kumai, R.; Tokura, Y. *Angew. Chem. Int. Ed.* **2007**, *46*, 3497.
- (82) Kumai, R.; Horiuchi, S.; Okimoto, Y.; Tokura, Y. *J. Chem. Phys.* **2006**, *125*, 084715.
- (83) Horiuchi, S.; Kumai, R.; Tokunaga, Y.; Tokura, Y. *J. Am. Chem. Soc.* **2008**, *130*, 13382.
- (84) Horiuchi, S.; Kobayashi, K.; Kumai, R.; Ishibashi, S. *Nat. Commun.* **2017**, *8*, 14426.
- (85) Horiuchi, S.; Kagawa, F.; Hatahara, K.; Kobayashi, K.; Kumai, R.; Murakami, Y.; Tokura, Y. *Nat. Commun.* **2012**, *3*, 1308.
- (86) Collet, E.; Lemee-Cailleau, M.-H.; Buron-Le Cointe, M.; Cailleau, H.; Wulff, M.; Luty, T.; Koshihara, S.-Y.; Meyer, M.; Toupet, L.; Rabiller, P.; Techert, S. *Science* **2003**, *300*, 612.
- (87) Torrance, J. B.; Vazquez, J. E.; Mayerle, J. J.; Lee, V. Y. *Phys. Rev. Lett.* **1981**, *46*, 253.
- (88) Torrance, J.B.; Girlando, A.; Mayerle, J.J.; Crowley, J.I.; Lee, V.Y.; Batail, P.; LaPlaca, S.J. *Phys. Rev. Lett.* **1981**, *47*, 1747.

- (89) Girlando, A.; Marzola, F.; Pecile, C.; Torrance, J. B. *J. Chem. Phys.* **1983**, *79*, 1075.
- (90) Kobayashi, K.; Horiuchi, S.; Kumai, R.; Kagawa, F.; Murakami, Y.; Tokura, Y. *Phys. Rev. Lett.* **2012**, *108*, 237601.
- (91) Kagawa, F.; Horiuchi, S.; Matsui, H.; Kumai, R.; Onose, Y.; Hasegawa, T.; Tokura, Y. *Phys. Rev. Lett.* **2010**, *104*, 227602.
- (92) Tayi, A. S.; Shveyd, A. K.; Sue, A. C.-H.; Szarko, J. M.; Rolczynski, B. S.; Cao, D.; Kennedy, T. J.; Sarjeant, A. A.; Stern, C. L.; Paxton, W. F.; Wu, W.; Dey, S. K.; Fahrenbach, A. C.; Guest, J. R.; Mohseni, H.; Chen, L. X.; Wang, K. L.; Stoddart, J. F.; Stupp, S. I. *Nature* **2012**, *488*, 485.
- (93) Shi, P.-P.; Tang, Y.-Y.; Li, P.-F.; Liao, W.-Q.; Wang, Z.-X.; Xiong, R.-G. *Chem. Soc. Rev.* **2016**, *45*, 3811.
- (94) Cai, H. L.; Zhang, W.; Ge, J. Z.; Zhang, Y.; Awaga, K.; Nakamura, T.; Xiong, R.-G. *Phys. Rev. Lett.* **2011**, *107*, 147601.
- (95) Czarnecki, P.; Nawrocik, W.; Pajak, Z.; Wasicki, J. *J. Phys. Condens. Matter* **1994**, *6*, 4955.
- (96) Maluszynska, H.; Czarnecki, P.; Lewicki, S.; Wasicki, J.; Gdaniec, M. *J. Phys. Condens. Matter* **2001**, *13*, 11053.
- (97) Czarnecki, P.; Maluszynska, H. *J. Phys. Condens. Matter*, **2000**, *12*, 4881.
- (98) Czarnecki, P.; Nawrocik, W.; Pajak, Z.; Wasicki, J. *Phys. Rev. B* **1994**, *49*, 1511.
- (99) Pająk, Z.; Czarnecki, P.; Szafrńska, B.; Maluszyńska, H.; Fojud, Z. *Phys. Rev. B* **2004**, *69*, 132102.
- (100) Pająk, Z.; Czarnecki, P.; Szafrńska, B.; Maluszyńska, H.; Fojud, Z. *J. Chem. Phys.* **2006**, *124*, 144502.
- (101) Zhang, Y.; Liu, Y. M.; Ye, H. Y.; Fu, D. W.; Gao, W. X.; Ma, H.; Liu, Z. G.; Liu, Y. Y.; Zhang, W.; Li, J. Y.; Yuan, G. L.; Xiong, R.-G. *Angew. Chem. Int. Ed.* **2014**, *53*, 5064.
- (102) Zhang, Y.; Ye, H. Y.; Cai, H. L.; Fu, D. W.; Ye, Q.; Zhang, W.; Zhou, Q.; Wang, J.; Yuan, G. L.; Xiong, R.-G. *Adv. Mater.* **2014**, *26*, 4515.
- (103) Meyer, R. B.; Liebert, L.; Strzelecki, L.; Keller, P. *J. Phys. Lett.* **1975**, *36*, 69.
- (104) Clark, N. A.; Lagerwall, S. T. *Appl. Phys. Lett.* **1980**, *36*, 899.
- (105) Bock, H.; Helfrich, W. *Liq. Cryst.* **1992**, *12*, 697.
- (106) Scherowsky, G.; Chen, X. H. *J. Mater. Chem.* **1995**, *5*, 417.
- (107) Barbera, J.; Iglesias, R.; Serrano, J.L.; Sierra, T.; De La Fuente, M.R.; Palacios, B.; Perez-Jubindo, M.A.; Vazquez, J.T. *J. Am. Chem. Soc.* **1998**, *120*, 2908.

- (108) Niori, T.; Sekine, T.; Watanabe, J.; Furukawa, T.; Takezoe, H. *J. Mater. Chem.* **1996**, *6*, 1231.
- (109) Dantlgraber, G.; Eremin, A.; Diele, S.; Hauser, A.; Kresse, H.; Pelzl, G.; Tschierske, C. *Angew. Chem. Int. Ed.* **2002**, *41*, 2408.
- (110) Miyajima, D.; Araoka, F.; Takezoe, H.; Kim, J.; Kato, K.; Takata, M.; Aida, T. *J. Am. Chem. Soc.* **2010**, *132*, 8530.
- (111) Miyajima, D.; Araoka, F.; Takezoe, H.; Kim, J.; Kato, K.; Takata, M.; Aida, T. *Science* **2012**, *336*, 209.
- (112) Kundys, B.; Lappas, A.; Viret, M.; Kapustianyk, V.; Rudyk, V.; Semak, S.; Simon, C.; Bakaimi, I. *Physical Review B* **2010**, *81*, 224434.
- (113) Di Sante, D.; Stroppa, A.; Jain, P.; Picozzi, S. *J. Am. Chem. Soc.* **2013**, *135*, 18126.
- (114) Röhm, H.; Leonhard, T.; Hoffmann, M. J.; Colsmannab, A. *Energy Environ. Sci.* **2017**, *10*, 950.
- (115) Asadi, K.; Van der Veen, M. A. *Eur. J. Inorg. Chem.* **2016**, *27*, 4332.
- (116) Dong, X.-Y.; Li, B.; Ma, B.-B.; Li, S.-J.; Dong, M.-M.; Zhu, Y.-Y.; Zang, S.-Q.; Song, Y.; Hou, H.-W.; Mak, T. C. W. *J. Am. Chem. Soc.* **2013**, *135*, 10214.
- (117) Akutagawa, T.; Koshinaka, H.; Sato, D.; Takeda, S.; Noro, S. I.; Takahashi, H.; Kumai, R.; Tokura, Y.; Nakamura, T. *Nat. Mater.* **2009**, *8*, 342.
- (118) Pan, L.; Liu, G.; Li, H.; Meng, S.; Han, L.; Shang, J.; Chen, B.; Platero-Prats, A. E.; Lu, W.; Zou, X.; Li, R.-W. *J. Am. Chem. Soc.* **2014**, *136*, 17477.

End of Chapter 1

Chapter 2



**Anion Driven $[Cu^II L_2]_n$ Frameworks:
Crystal Structures, Guest-
encapsulation, Dielectric and
Possible Ferroelectric Properties**

2.1 Introduction

Over the past decades, coordination driven self-assemblies of metal-ligand ensembles have taken a crucial place in the domain of supramolecular chemistry due to their facile synthesis and novel applications.¹⁻⁴ The simplicity and the spontaneity of self-assembly methods allow the design of novel structural architectures ranging from one-dimensional helices to two-dimensional grids and sheets as well as three-dimensional frameworks and polyhedra.^{5,6} Several studies have demonstrated that these self-assemblies exhibit interesting structure dependent physical properties such as electric, magnetic and nonlinear optical properties.⁷⁻¹¹ Materials that exhibit ferroelectric properties are very important due to their utility in non-volatile computing devices, capacitors and signaling devices.¹²⁻¹⁸ Ferroelectric substances with high permittivity (dielectric constant) values are important in the development of dielectric resonators and microwave telecommunication signal processing units.¹⁹⁻²¹ Traditionally, ceramic and inorganic oxide materials have been employed for these purposes.²²⁻²⁵ Currently, organic²⁶⁻²⁹ and organic-inorganic hybrid materials³⁰⁻³⁸ are vastly explored as ferroelectric materials for their efficiency and flexibility in device fabrication. In this effort, self-assembled metal organic hybrids have gained attention owing to their ready syntheses and tunable properties.³⁹ However, syntheses of self-assembled ferroelectric materials are still challenging because of the strict requirement of a helical and non-centrosymmetric polar packing arrangement of the molecular constituents.⁴⁰ Several factors viz., coordination geometry around the metal ion, nature of the ligand, role of counter anions and solvent systems have been found to contribute towards non-centrosymmetric, chiral or polar lattice parameters.⁴¹⁻⁴² Although it is difficult to measure the role of each of these factors, a careful choice of the metal ions and counter anions in combination with a non-rigid ligand system can contribute to polar non-centrosymmetric crystal parameters which could eventually give rise to ferroelectric self-assemblies. To test this hypothesis we set out to synthesize both centrosymmetric and non-centrosymmetric structural motifs for a same metal-ligand combination depending upon the reaction conditions and counter anions. For this, a simple and flexible P-N ligand (L^1), featuring neutral pyridyl N-donor sites, was treated with Cu(II) ions (a labile metal ion) in presence of

perchlorate/nitrate anions (Scheme 2.1). These reactions yielded four new cationic coordination assemblies, of the type $\{[\text{Cu}(\text{L}^1)_2]_n[\text{A}]_{2n}\}$ (**1**: $n=\infty$, $\text{A}=(\text{ClO}_4^-)$; **1a**: $n=\infty$, $\text{A}=(\text{ClO}_4^-)_{0.835} + (\text{NO}_3^-)_{0.165}$; **2**: $n=4$, $\text{A}=(\text{NO}_3^-)$ and **3**: $n=3$, $\text{A}=(\text{NO}_3^-)$), in three unique structures. While the compounds **1** and **1a** display a non-centrosymmetric 1D-helical chain structure, the compounds **2** and **3** were obtained as centrosymmetric discrete assemblies. Permittivity measurements on **1**, **1a** and **2** show a high dielectric constant values for all of them. Further, **1** and **1a** were shown to exhibit ferroelectric behavior at room temperature.

2.2 EXPERIMENTAL SECTION

2.2.1 General Remarks

All manipulations involving phosphorus halides were performed under dry nitrogen atmosphere in standard Schlenk-glassware. Solvent toluene was dried over sodium. The 3-Aminopyridine was purchased from Aldrich and used as received. PhPOCl_2 was purchased from Acros-Organics and used as received. Tetrabutylammonium nitrate $[(^n\text{Bu}_4\text{N})\text{NO}_3]$ and Copper perchlorate salts were purchased from Aldrich, $\text{Cu}(\text{NO}_3)_2 \cdot 3\text{H}_2\text{O}$ and KNO_3 were purchased from Merck and used as received. NMR spectra were recorded on a Jeol 400 MHz spectrometer (^1H NMR: 400.13 MHz, $^{13}\text{C}\{^1\text{H}\}$ NMR: 100.62 MHz, $^{31}\text{P}\{^1\text{H}\}$ NMR: 161.97 MHz) at room temperature using SiMe_4 (^1H , ^{13}C) and 85% H_3PO_4 (^{31}P). The MALDI-TOF spectra were obtained on an Applied Biosystem MALDI-TOF/TOF spectrometer. The powder X-ray diffraction (PXRD) data were obtained from a Bruker-D8 Advance diffractometer. Thermal analysis (TGA) data has been obtained from a Perkin-Elmer STA-6000 thermogravimetric analyzer. Elemental analyses were performed on a Vario-EL cube elemental analyzer. FT-IR spectra were taken on a Perkin Elmer spectrophotometer with samples prepared as KBr pellets. Melting points were obtained using an Electro thermal melting point apparatus and were uncorrected.

2.2.2 Synthesis

2.2.2.1 Synthesis of ligand $[\text{PhPO}(\text{NH}^3\text{Py})_2]$ (L^1): To a stirred solution of 3-Aminopyridine (11.756 g, 125 mmol) in toluene (~200 ml) at 0°C , PhPOCl_2 (2.5 ml, 3.475 g, 17.82 mmol) in 10 ml of toluene was added drop wise through a pressure

equalizer funnel under inert atmosphere and the reaction mixture was refluxed for 4 hrs. The residue was filtered and washed 3-4 times with distilled water to get a white solid, which was then dried and collected. Colourless crystalline needles suitable for single crystal X-ray diffraction (SCXRD) analysis were obtained from its methanolic solution after 2 days. Yield: 4.92 g (89%), based on P. M.P.: 223-225 °C. $^1\text{H-NMR}$ (400 MHz, $(\text{CD}_3)_2\text{SO}$): δ 2.05 (s, 2H, NH), 7.16 (m, 2H, CH), 7.52 (m, 3H, CH), 7.82 (m, 2H, CH), 8.01 (s, 2H, CH), 8.35 (m, 4H, CH). $^{31}\text{P-NMR}$ (161 MHz, $\{(\text{CD}_3)_2\text{SO}\}$): δ 10.04. FT-IR data in KBr pellet (cm^{-1}): 3464, 1587, 1477, 1386, 1197, 1120, 1061, 938, 810, 699 and 514. ESI-MS = 311.1049 $[\{\text{PhPO}(\text{NH}^3\text{Py})_2\}+\text{H}]^+$; 217.0522 $[\text{PhPO}(\text{NH}^3\text{Py})]^+$. Anal. Calcd. for $\text{C}_{16}\text{H}_{15}\text{N}_4\text{OP}$: C, 61.93; H, 4.87; N, 18.06. Found: C, 62.01; H, 4.84; N, 17.97.

2.2.2.2 Synthesis of compound ($\{[\text{Cu}_2(\text{L}^1)_4(\text{H}_2\text{O})_2] \cdot (\text{ClO}_4)_4 \cdot (\text{H}_2\text{O})_5 \cdot (\text{CH}_3\text{OH})\}_\infty$) (1):

To a stirred solution of L^1 (62 mg, 0.2 mmol) in MeOH (3 ml), $\text{Cu}(\text{ClO}_4)_2 \cdot 6\text{H}_2\text{O}$ (37 mg, 0.1 mmol) in H_2O (3 ml) was added. To this mixture, 5 drops of DMF was added and the stirring was continued for four hours. The solution was then filtered through a thick pad of celite and left for crystallization. Large blue crystals of **1** suitable for SCXRD analysis were obtained after 2-3 weeks. Yield: 53% (51 mg), based on Cu. FT-IR data in KBr pellet (cm^{-1}): 3440, 1607, 1584, 1499, 1391, 1335, 1275, 1194, 1120, 1087, 946, 809, 696, 624 and 521. Anal. Calcd. for $\text{C}_{65}\text{H}_{78}\text{N}_{16}\text{O}_{28}\text{P}_4\text{Cu}_2\text{Cl}_4$: C, 40.57; H, 4.09; N, 11.65. Found: C, 40.43; H, 4.11; N, 11.52.

2.2.2.3 Synthesis of compound ($\{[\text{Cu}_3(\text{L}^1)_6(\text{H}_2\text{O})_3] \cdot (\text{ClO}_4)_5 \cdot (\text{NO}_3) \cdot (\text{H}_2\text{O})_{11}\}_\infty$) (1a):

To a stirred solution of L^1 (62 mg, 0.2 mmol) in MeOH (3 ml), a solution of $\text{Cu}(\text{ClO}_4)_2 \cdot 6\text{H}_2\text{O}$ (37 mg, 0.1 mmol) and tetrabutylammonium nitrate $[\{(\text{C}_4\text{H}_9)_4\text{N}\}\text{NO}_3]$ (30 mg, 0.1 mmol) in H_2O (3 ml) was added. To this mixture, 5 drops of DMF was added and the stirring was continued for another four hours. The solution was then filtered through a thick pad of celite and left for crystallization. Blue crystals of **1a** suitable for SCXRD analysis were obtained after 2-3 weeks. Yield: 57% (54 mg), based on Cu. FT-IR data in KBr pellet (cm^{-1}): 3489, 1608, 1584, 1499, 1390, 1336, 1275, 1194, 1121, 1092, 942, 808, 696, 622, and 521. Anal. Calcd. for $\text{C}_{96}\text{H}_{118}\text{N}_{25}\text{O}_{43}\text{P}_6\text{Cu}_3\text{Cl}_5$: C, 40.26; H, 4.15; N, 12.23. Found: C, 40.12; H, 4.03; N, 12.12.

2.2.2.4 Synthesis of compound ($\{[\text{Cu}_4(\text{L}^1)_8(\text{H}_2\text{O})_5] \cdot (\text{NO}_3)_8 \cdot \text{L}^1 \cdot (\text{H}_2\text{O})_9\}$) (2**):** To a stirred solution of L^1 (62 mg, 0.2 mmol) in MeOH (3 ml), $\text{Cu}(\text{NO}_3)_2 \cdot 3\text{H}_2\text{O}$ (24 mg, 0.1 mmol) in H_2O (3 ml) was added and the stirring was continued for another four hours. The solution was then filtered through a thick pad of celite and left for crystallization. Blue crystals of **2** suitable for SCXRD analysis were obtained after 2 weeks. Yield: 61% (52 mg), based on Cu. FT-IR data in KBr pellet (cm^{-1}): 3474, 1607, 1584, 1503, 1478, 1384, 1273, 1192, 1121, 1064, 1028, 943, 807, 695, 623, 521, and 503. Anal. Calcd. For $\text{C}_{144}\text{H}_{163}\text{N}_{44}\text{O}_{47}\text{P}_9\text{Cu}_4$: C, 45.57; H, 4.33; N, 16.24. Found: C, 45.38; H, 4.22; N, 16.09.

2.2.2.5 Synthesis of compound ($\{[\text{Cu}_4(\text{L}^1)_8(\text{H}_2\text{O})_5] \cdot (\text{NO}_3)_8 \cdot (\text{H}_2\text{O})_9\}$) (2a**):** To a stirred solution of L^1 (62 mg, 0.2 mmol) in MeOH (3 ml), a solution of $\text{Cu}(\text{NO}_3)_2 \cdot 3\text{H}_2\text{O}$ (24 mg, 0.1 mmol) and tetrabutylammonium nitrate (100 mg, 0.3 mmol) in H_2O (3 ml) was added and the stirring was continued for another four hours. The solution was then filtered through a thick pad of celite and left for crystallization. Large blue crystals of **2a** suitable for SCXRD analysis were obtained after 3-4 weeks. Yield: 58% (50 mg), based on Cu. FT-IR data in KBr pellet (cm^{-1}): 3454, 1608, 1584, 1502, 1479, 1385, 1272, 1191, 1122, 1064, 1028, 947, 809, 690, 652 and 509. Anal. Calcd. for $\text{C}_{128}\text{H}_{148}\text{N}_{40}\text{O}_{46}\text{P}_8\text{Cu}_4$: C, 44.12; H, 4.28; N, 16.08. Found: C, 43.96; H, 4.17; N, 16.20.

2.2.2.6 Synthesis of compound ($\{[\text{Cu}_4(\text{L}^1)_8(\text{H}_2\text{O})_4] \supset [\text{K}(\text{H}_2\text{O})_8] \cdot (\text{NO}_3)_9 \cdot (\text{H}_2\text{O})_9\}$) (2** \supset $[\text{K}(\text{H}_2\text{O})_8]$):** (a) To a solution of KNO_3 (101 mg, 1 mmol) in methanol and water (10 ml), crystals of **2** (20 mg) were added and stirred for 24 hours. The solution was then filtered through a thick pad of celite and left for crystallization. Rectangular-rod like blue crystals of **2** \supset $[\text{K}(\text{H}_2\text{O})_8]$ suitable for SCXRD analysis were obtained after a week. Yield: 43% (8.4 mg), based on Cu. (b) To a stirred solution of L^1 (62 mg, 0.2 mmol) in MeOH (5 ml), $\text{Cu}(\text{NO}_3)_2 \cdot 3\text{H}_2\text{O}$ (24 mg, 0.1 mmol) and KNO_3 (50 mg, 0.5 mmol) in H_2O (3 ml) was added and stirred further. The solution was then filtered through a thick pad of celite and left for crystallization. Rectangular-rod like blue crystals of **2** \supset $[\text{K}(\text{H}_2\text{O})_8]$ suitable for SCXRD analysis were obtained after a week. Yield: 49% (43 mg), based on Cu. FT-IR data in KBr pellet (cm^{-1}): 3484, 3144, 3060, 1607, 1584, 1503, 1479, 1384, 1272, 1192, 1122, 1064, 1028, 942, 807, 695, 521

and 503. Anal.Calcd. for $\text{C}_{128}\text{H}_{162}\text{N}_{41}\text{O}_{56}\text{P}_8\text{Cu}_4$: C, 41.42; H, 4.40; N, 15.47. Found: C, 41.55; H, 4.48; N, 15.60.

2.2.2.7 Synthesis of compound ($\{[\text{Cu}_3(\text{L}^1)_6] \cdot (\text{NO}_3)_6 \cdot (\text{H}_2\text{O})_8 \cdot (\text{CH}_3\text{OH})_2\}$) (3): To the solution of tetrabutylammonium nitrate (100 mg, 0.33 mmol) in MeOH (10 mL), crushed crystals of **1** (20 mg, 0.01 mmol) was added with slow stirring. After 4-5 hours, formation of a greenish-blue precipitate was observed. The slow stirring was continued for 48 hours and then the solution was filtered and the filtrate was kept at RT for crystallization. Blue crystals of **3** suitable for analysis by SCXRD technique were obtained after a week. Yield: 4% (3.5 mg), based on Cu. FT-IR data in KBr pellet (cm^{-1}): 3450, 1597, 1460, 1384, 1299, 1269, 1152, 1054, 926, 771, 644, 587, 498 and 483. Anal.Calcd. for $\text{C}_{98}\text{H}_{114}\text{N}_{30}\text{O}_{34}\text{P}_6\text{Cu}_3$: C, 44.69; H, 4.32; N, 15.42. Found: C, 44.52; H, 4.24; N, 15.57.

2.2.3 Crystallography

Reflections were collected on a Bruker Smart Apex Duo diffractometer at 100 K using $\text{MoK}\alpha$ radiation ($\lambda = 0.71073 \text{ \AA}$) for L^1 , **1**, **1a**, **2a**, **3** and $2 \rightarrow [\text{K}(\text{H}_2\text{O})_8]$. For **2**, the data was collected on a Bruker D8 Venture fitted with a microfocus source at 150 K using $\text{CuK}\alpha$ radiation ($\lambda = 1.54178 \text{ \AA}$). Structures were refined by full-matrix least-squares against F^2 using all data (SHELX).⁴³ Crystallographic data for all these compounds are listed in Table 2.1. All non-hydrogen atoms were refined anisotropically if not stated otherwise. Hydrogen atoms were constrained in geometric positions to their parent atoms. Crystals of L^1 , **1**, and **3** were weakly diffracting at higher angles and hence a $2\theta=50^\circ$ cutoff was applied. Four perchlorate ions in **1** and one perchlorate ion in **1a** were disordered. Similarly some of the nitrate ions, phenyl rings and phosphoryl oxygen atoms in **2**, **2a**, $2 \rightarrow [\text{K}(\text{H}_2\text{O})_8]$ and **3** were thermally disordered. Atom positions of the disordered groups were freely refined isotropically over two positions using similar distances and similar U-restraints. Some of the nitrate ions in these structures were disordered along with the solvate water molecules. Hence these were treated as diffuse contributions to the overall scattering and removed by the SQUEEZE/PLATON for a better refinement data.⁴⁴ The exact amount of the solvate water molecules were further confirmed by TGA data (Appendix A2.1). The refinement parameters in **2** and **2a** were slightly higher

owing to the diffuse nature of these highly solvated crystals as well as to a large number of unique atoms in the asymmetric unit.

Table 2.1: Details of crystallographic data collection and structure refinements for L¹, 1, 1a, 2, 2a, 2⇨[K(H₂O)₈] and 3.

Compound	L ¹	1	1a	2_sq
Chemical formula	C ₁₆ H ₁₅ N ₄ OP	C ₆₅ H ₇₈ Cl ₄ Cu ₂ N ₁₆ O ₂₈ P ₄	C ₉₆ H ₁₁₈ Cl ₅ Cu ₃ N ₂₅ O ₄₃ P ₆	C ₁₄₄ H ₁₆₃ Cu ₄ N ₄₄ O ₄₇ P ₉
Formula weight	310.29	1924.19	2863.84	3795.06
Temperature	100(2)K	100(2) K	100(2)	150(2)
Crystal system	Monoclinic	Trigonal	Trigonal	Monoclinic
Space group	P2(1)/n	R3	R3	P2(1)/n
a (Å); α (°)	10.300(6); 90	20.565(2); 90	20.3990(18); 90	20.842(11); 90
b (Å); β (°)	6.107(4); 93.104(12)	20.565(2); 90	20.3990(18); 90	23.706(12); 103.819(3)
c (Å); γ (°)	22.774(13); 90	50.106(4); 120	24.969(2); 120	38.839(2); 90
V (Å ³); Z	1430.4(15); 4	18352(3); 9	8997.9(14); 3	18634.1(17); 4
ρ (calc.) mg m ⁻³	1.441	1.567	1.586	1.353
μ mm ⁻¹	0.200 (Mo K _α)	0.821 (Mo K _α)	0.815 (Mo K _α)	1.970 (Cu K _α)
2θ _{max} (°)	50	50	58	136
R(int)	0.1042	0.0381	0.0837	0.1145
Completeness to θ	99.3 %	99.6 %	99.7 %	98.3 %
Data / param.	2516 / 199	13396 / 1105	9311 / 533	33662 / 1907
GOF	1.098	1.035	1.012	1.375
R1 [F>4σ(F)]	0.0697	0.0599	0.0607	0.1434
wR2 (all data)	0.1880	0.1687	0.1543	0.4299
max. peak/hole (e.Å ⁻³)	1.190 / -0.526	1.502 / -1.033	0.809 / -0.886	1.194 / -1.084

Compound	2a_sq	2⇨[K(H ₂ O) ₈] _{sq}	3
Chemical formula	C ₁₂₈ H ₁₄₈ Cu ₄ N ₄₀ O ₄₆ P ₈	C ₁₂₈ H ₁₆₂ Cu ₄ N ₄₁ O ₅₆ P ₈ K	C ₉₈ H ₁₁₄ Cu ₃ N ₃₀ O ₃₄ P ₆
Formula weight	3484.78	3712.00	2632.63
Temperature	100(2)	100(2)	100(2)
Crystal system	Monoclinic	Tetragonal	Monoclinic
Space group	P2(1)/n	I-4	C2/c
a (Å); α (°)	21.364(3); 90	42.390(2); 90	21.231(4); 90
b (Å); β (°)	22.855(3); 91.641(3)	42.390(2); 90	23.026(5); 94.949(4)
c (Å); γ (°)	33.322(5); 90	19.197(10); 90	24.026(5); 90
V (Å ³); Z	16263(4); 4	34495(4); 4	11702(4); 4
ρ (calc.) mg m ⁻³	1.423	0.715	1.494
μ mm ⁻¹	0.685 (Mo K _α)	0.339 (Mo K _α)	0.714 (Mo K _α)
2θ _{max} (°)	56	56	50
R(int)	0.1442	0.0678	0.1865
Completeness to θ	99.5 %	99.6 %	99.5 %
Data / param.	40201 / 1568	42628 / 1881	10299 / 812
GOF	0.933	0.992	1.031
R1 [F>4σ(F)]	0.1156	0.0778	0.0930
wR2 (all data)	0.3633	0.2244	0.2868
max. peak/hole (e.Å ⁻³)	1.150 / -0.771	1.405 / -0.983	1.462 / -0.737

2.2.4 Ferroelectric and Dielectric measurements

In order to determine the dielectric and ferroelectric properties, the powdered samples of these compounds were compacted in the form of discs (of approximately 10 mm diameter and 1 mm thickness). The compacted discs were subsequently attached to aluminum adhesive foils which act as electrodes for both ferroelectric and dielectric measurements. The frequency dependent dielectric characteristics for **1**, **1a** and **2** at various temperatures were measured using the Novocontrol dielectric spectrometer. The ferroelectric hysteresis loop in **1** and **1a** were measured by using Sawyer-Tower circuit. Both polarizations and fatigue studies were recorded using hysteresis loop analyser (TF Analyser 2000, aixACCT Germany). Time dependent leakage current was measured dynamically during the hysteresis loop measurements. It was recorded for various applied voltage steps using the TF analyser. The P-E loop results show that remnant polarization in the positive direction is slightly lower than that in negative direction for the sample **1**, and a reverse of this trend was observed in case of **1a**. The asymmetries of hysteresis loop in the two opposite directions can be related to the electrode asymmetry (adhesive aluminium foils) which is attributed to the variations in the air gap between the electrode and the sample at the top and bottom surfaces. The asymmetric reversal of loop in sample **1a** in comparison with **1** is due to the switch in electric field direction and different leakage currents under a positive and negative bias. The gap observed at the start and end points of the P-E hysteresis is due to the delay period between the (i) preset loop and the start of the measurement loop, (ii) space charge formed from the lattice distortion and (iii) energy traps at the electrode interfaces.

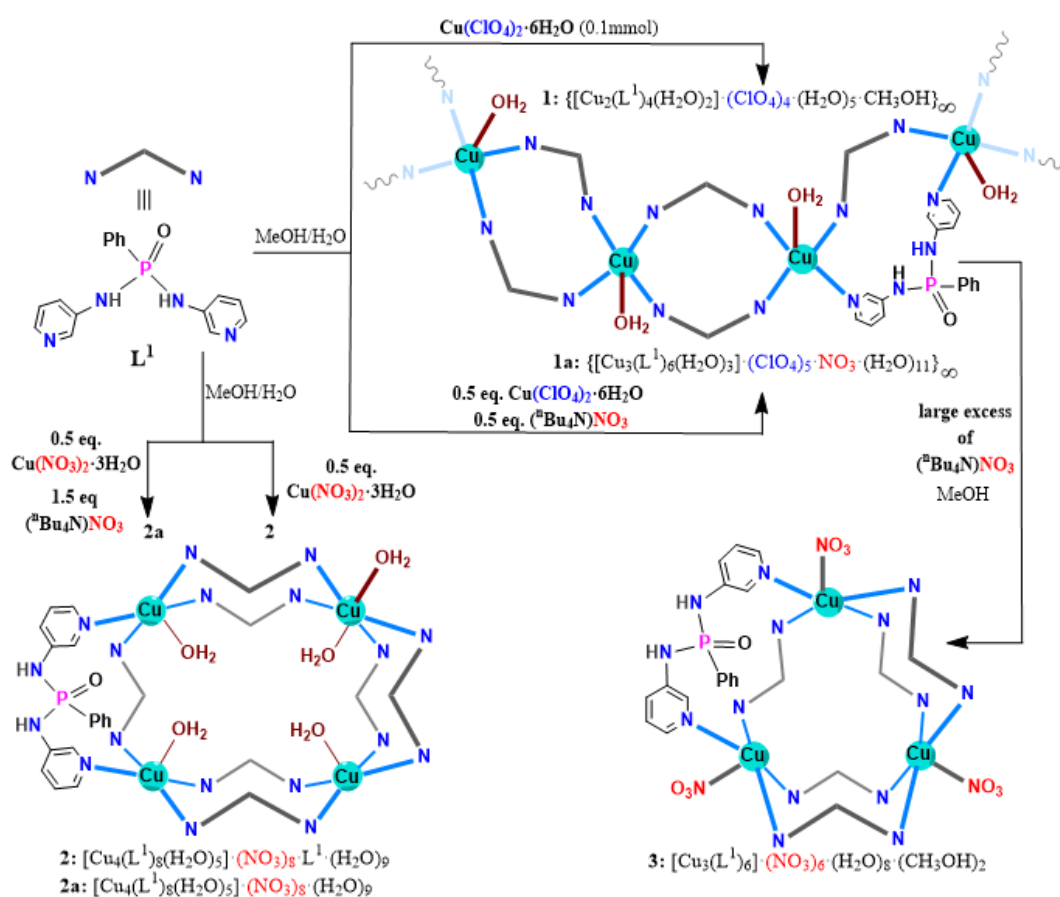
2.3 RESULTS AND DISCUSSION

2.3.1 Syntheses

The precursor ligand L^1 was synthesized from PhPOCl_2 and excess 3-aminopyridine in refluxing toluene (Appendix A2.2 and A2.3). The 1D-helical assembly of **1** was isolated as blue crystals in a 2:1 reaction mixture involving L^1 and $\text{Cu}(\text{ClO}_4)_2$ in $\text{MeOH}/\text{H}_2\text{O}$ medium at room temperature (Scheme 2.1). Conversely, treatment of L^1 with $\text{Cu}(\text{NO}_3)_2$ gave the Cu_4L_8 cavitand complex **2** (an uncoordinated free ligand was found in its packing cavity). In order to obtain the helical assembly of **1** with only

nitrate anions, L^1 was treated with $\text{Cu}(\text{ClO}_4)_2$ and $(^n\text{Bu}_4\text{N})\text{NO}_3$ in 2:1:1 ratio. However, the obtained blue crystals indicated the formation of **1a** with mixed perchlorate/nitrate combination.

Scheme 2.1: Schematic Diagram Showing the Anion Driven Assemblies of the $[\text{Cu}^{\text{II}}\text{L}_2]_n$ Frameworks



In another attempt, treatment of **1** with excess $(^n\text{Bu}_4\text{N})\text{NO}_3$ in methanol gave a new discrete trinuclear M_3L_6 complex **3** in low yields along with the quantitatively precipitated sample of **1a** admixed with unreacted $(^n\text{Bu}_4\text{N})\text{NO}_3$. In order to see whether **3** can be obtained in a direct reaction, we treated L^1 with $\text{Cu}(\text{NO}_3)_2$ and $(^n\text{Bu}_4\text{N})\text{NO}_3$ in methanol. However, the obtained crystals showed the formation of the same tetranuclear Cu_4L_8 assembly **2a**, with a slightly different packing composition, instead of **3**. The MALDI-TOF mass spectra of all these compounds exhibit similarity in the peaks suggesting that all these assemblies are built from the same set of repeating units in their solution, which associate to form distinct assemblies under different conditions (Appendix A2.4).

2.3.2 Crystal Structures

The molecular structure of L^1 was solved in the monoclinic space group $P2_1/n$. It consists of two amino pyridyl moieties, one phenyl group and one phosphoryl oxygen around the central P-atom (Figure 2.1a). The ligand L^1 shows rich intermolecular hydrogen bonding. Figure 2.1b displays the formation of a 1D-double chain structure mediated by $\text{N-H}\dots\text{N}_{\text{pyridyl}}$ and $\text{N-H}\dots\text{O}_{\text{phosphoryl}}$ hydrogen bonding interactions. One of the pyridyl N-donor sites in L^1 doesn't have an H-bonding partner and hence remains non-interacting.

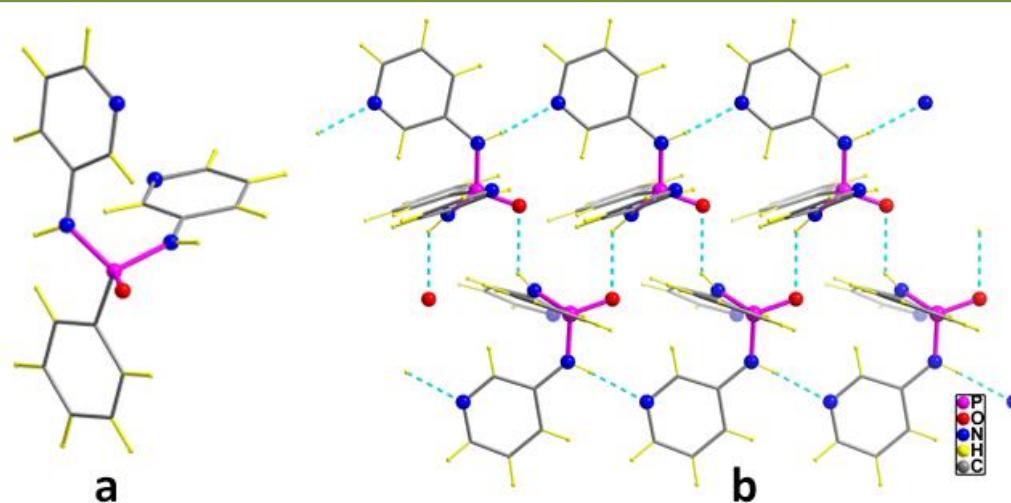


Figure 2.1: (a) Crystal Structure of ligand L^1 . (b) View of the H-Bonding in L^1 .

The molecular structures of all these assemblies consists of $[\text{Cu}^{\text{II}}\text{L}_2]_n$ (**1**, $n=\infty$; **1a**, $n=\infty$; **2**, $n=4$; and **3**, $n=3$) repeat units having corner-shared 20-membered Cu_2L_2 macrocycles. The coordination environment at the $\text{Cu}(\text{II})$ centers in all of them contains four equatorial $\text{N}_{\text{pyridyl}}$ sites and an apical coordination from either water molecules (**1**, **1a**, **2**, and **2a**) or nitrate ions (**3**). Thus, the coordination geometry in all of these assemblies can best be described as distorted square pyramidal (sp) except for one of the four $\text{Cu}(\text{II})$ atoms in **2** and **2a** which exhibits an octahedral coordination with two axial water molecules.

The molecular structures of **1** and **1a** were solved in the trigonal non-centric polar space group R_3 (polar point group of C_3). The repeating unit of the helical assembly of **1** consists of two $\text{Cu}(\text{II})$ ions, four ligand motifs, and two coordinated water molecules on each $\text{Cu}(\text{II})$ atom. The charge balance is restored by the presence of

four perchlorate ions. The molecular structure can be viewed as a left-handed helical double chain consisting of an infinite array of Cu_2L_2 macrocyclic segments (Figure 2.2a).

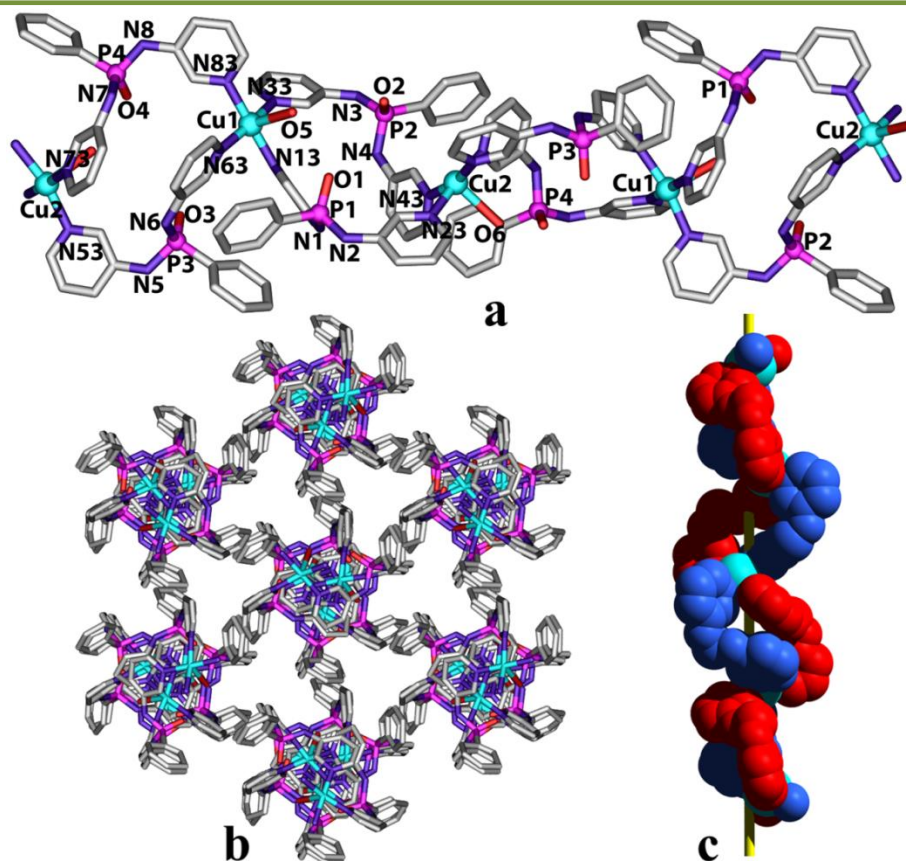


Figure 2.2: (a) View of the 1D-helical cationic assembly in **1**. (b) Packing diagram of **1** depicting the trigonal channels along the *c*-axis. (c) View of the two left-handed strands shown in red and blue colored spheres; the Cu(II) atoms are shown as cyan colored spheres (phenyl rings and phosphoryl oxygen atoms are omitted).

The two coordinated $\text{N}_{\text{pyridyl}}$ sites of the ligand are mutually positioned to give an arrangement that is in between the *syn* and *anti*-conformations with respect to the P=O groups. Every fourth macrocyclic segment is in the replicating position of the first one contributing to an approximate 120° rotation. Each ligand motif within the Cu_2L_2 segments could be considered as part of a distinct chain which upon propagation gives rise to two fused left-handed strands (Figure 2.2c). The pitch of the helical chain was found to be around 25.5 \AA , and the width of the helix is approximately 10 \AA . The packing diagram of the molecule shows the presence of trigonal channel structures (Figure 2.2b) which are occupied by the disordered

perchlorate ions and solvate molecules. The cationic assembly in **1a** resembles to that of **1** with closely related metric parameters (Table 2.1) except that the asymmetric unit in **1a** consists of one-half of the segments found in **1** (Appendix A2.5).

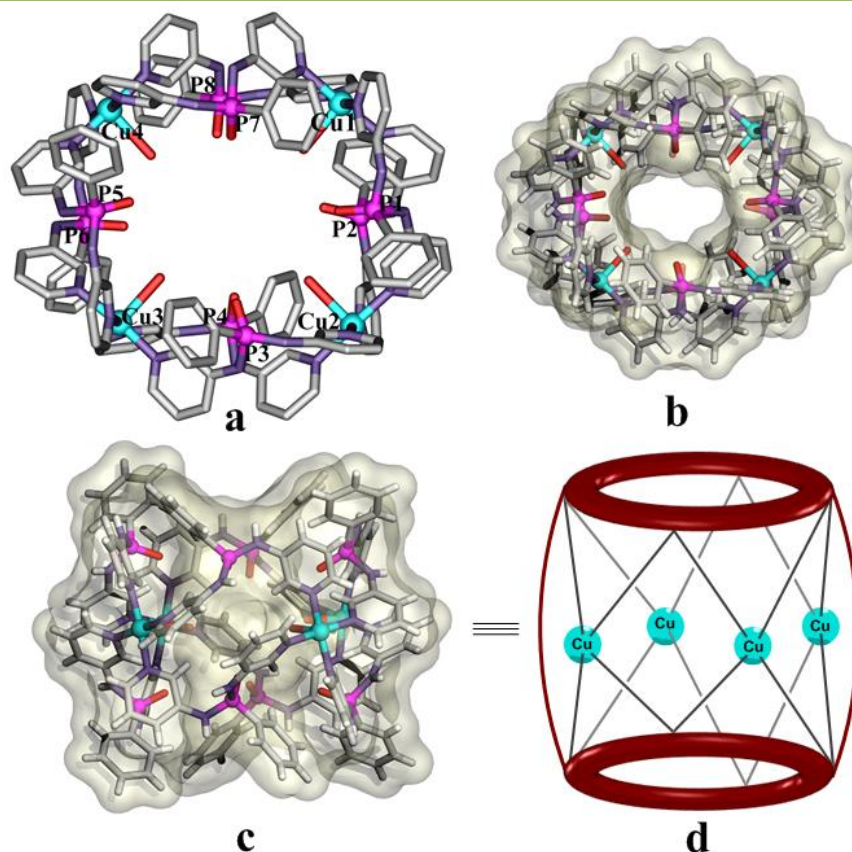


Figure 2.3: (a) View of the tetrameric cavitand core in **2**. Surface overlay view of the tetramer along (b) '1,1,0' plane and (c) '0,0,1' plane. (d) Cartoon diagram representing the barrel shaped cavitand structure of **2** along the c-axis.

The crystal structures of **2** and **2a** were solved in the monoclinic centrosymmetric space group $P2_1/n$. The molecular core in both of them consists of a tetranuclear cationic Cu_4L_8 rectangular-cavitand with the approximate point group symmetry of D_4 (Figures 2.3a-c). The cavitand structure in **2** can be viewed as a planar array of four $\text{Cu}(\text{II})$ atoms which are connected by four bidentate ligand pairs above and below the Cu_4 plane. Thus, the Cu_4L_8 moiety consists of four Cu_2L_2 segments similar to those found in **1**. The charge balance is restored by the presence of eight nitrate anions. Further, two coordinated $\text{N}_{\text{pyridyl}}$ sites of the ligands in **2** are mutually positioned in *syn* conformations with the $\text{P}=\text{O}$ groups pointing inward in an *endo* orientation. The

cationic ensemble in **2** (and in **2a**) can be viewed as a metal–ligand analogue of cucurbiturils (CBs)⁴⁵⁻⁴⁶ consisting of symmetrical apertures at the top and bottom ends, except that the M-H₂O groups in **2** are located inside the cavity (in the case of CBs, the hydroxyl groups are located above and below the internal cavity). The cavity diameters in **2** (and **2a**) are measured to be at approximately 6.5 and 8.1 Å, and the outer dimensions are in the range between CB[6] and CB[8] (Figure 2.3d). The contact surface volume of the cavity is approximately 153 Å³ as calculated by the mercury software.⁴⁷ The intrinsic pores in **2** and **2a** were filled with disordered solvate water molecules (Appendix A2.6).

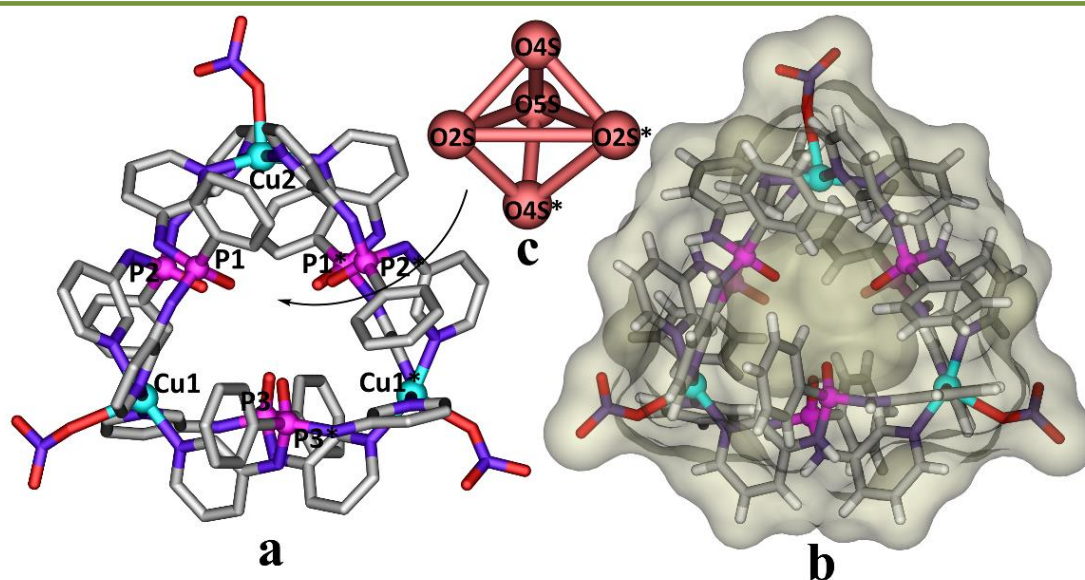


Figure 2.4: (a) Molecular structure of **3** showing the trinuclear cage assembly. The disordered and uncoordinated nitrate ions, solvate molecules, and H atoms are omitted for clarity. (b) Surface overlay view of the trimer along the c-axis. (c) Disordered water molecules (4.25 molecules) encapsulated inside the cage over five positions in a TBP fashion.

The crystal structure of **3** was solved in the monoclinic centrosymmetric space group $P2_1/c$. The asymmetric unit consists of one and a half Cu(II) ions, three ligand motifs, three nitrate ions located over four positions with two of them coordinated (with Cu(II) ions) and two of them uncoordinated, two methanol molecules, and four H₂O molecules. The molecular core consists of a cationic M₃L₆ cage-like framework (D_3 symmetry) having three corner-shared Cu₂L₂ segments (Figure 2.4a-b). The Cu2 atom is located on a mirror plane, and hence, the nitrate ion attached to it is

positionally disordered on either side of the plane. The formation of the discrete cage assembly of **3** from **1** can be envisioned via the cleavage of two of the six Cu–N bonds at either ends of the helical turn followed by the ring closure at the terminal metal sites. In **3**, the angle between the two Cu-centers was nearly 60° to give an overall angle of 179.97° (58.52 , 58.52 , and 62.96°). Whereas, in **1** the twist angle between the three successive Cu-centers is approximately 155° . Moreover, the two coordinated $\text{N}_{\text{pyridyl}}$ sites of the ligands in **3** are oriented in *syn* conformation with respect to the P=O groups as observed for **2** and **2a**. As computed from MSROLL software calculations, the intrinsic void space in **3** was found to be 65 \AA^3 with a fixed probe radius of 1.4 \AA .⁴⁸ Further, the cavity was found to be occupied by 4.25 disordered water molecules over five positions in trigonal bipyramidal geometry (Figure 2.4c).

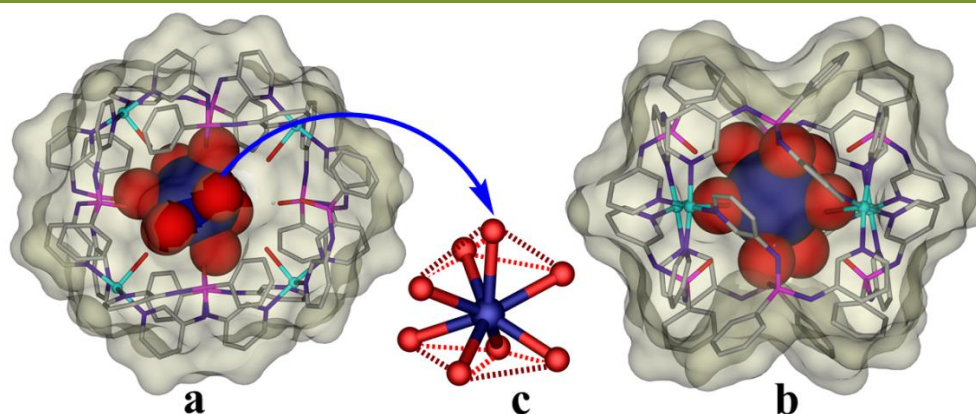


Figure 2.5: Crystal structure of **2** $[\text{K}(\text{H}_2\text{O})_8]$ along the (a) '1,1,0' plane and the (b) '0,0,1' plane. (c) The dodecahedral geometry of the $[\text{K}(\text{H}_2\text{O})_8]^+$ guest shown in a ball and stick model.

2.3.3 Guest-Encapsulation Studies of **2**

Gas adsorption studies performed on the activated sample of **2** (and **2a**) did not show any appreciable uptake characteristics for CO_2 and N_2 gas. This could be attributed to the hindered access for the gas molecules in the intrinsic cavity of **2** caused by its solid-state packing structure (Appendix A2.7). Nevertheless, the cavity dimensions in **2** are suitable for the host–guest chemistry in solution. Thus, the reaction of **2** with excess KNO_3 in water/methanol gave the complex **2** $[\text{K}(\text{H}_2\text{O})_8]$, which encapsulated the K^+ ion in the hydrated form (Figure 2.5). The molecular

structure of $2\supset[\text{K}(\text{H}_2\text{O})_8]$ shows that the tetrameric structure of **2** was retained in the solid state with marginal changes in its inner diameters ranging from 6.2 to 9.2 Å caused by the guest encapsulation (Figure 2.6). The coordination geometry around the K^+ ion in its primary hydration sphere can be described as distorted dodecahedral (Figure 2.5c). The four coordinated molecules on each Cu^{2+} ion and the phosphoryl oxygen atoms provide the second sphere coordination to the encapsulated K^+ ion. However, similar attempts with NaNO_3 and CsF did not result in any guest encapsulation exemplifying that the cavity space in **2** is specific only for the hydrated K^+ ion.

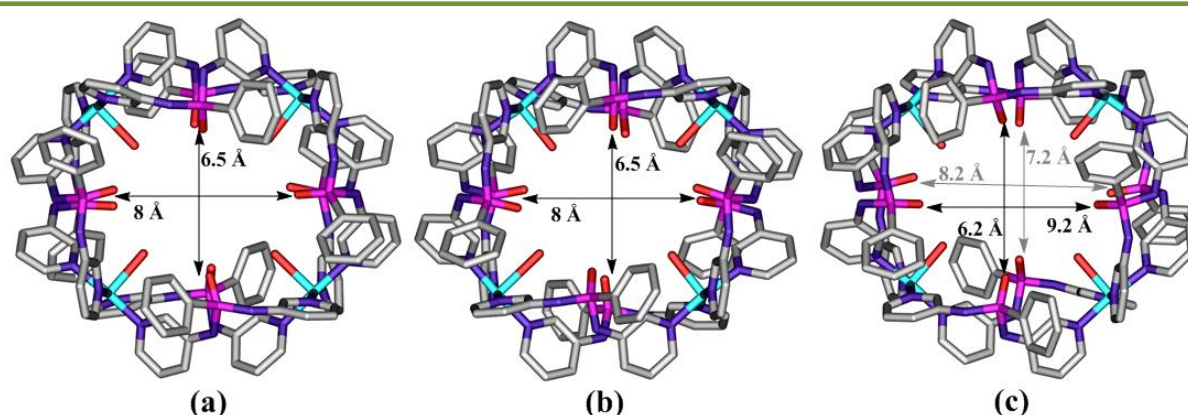


Figure 2.6: Comparison of cavity diameter in (a) **2**, (b) **2a** and (c) $2\supset[\text{K}(\text{H}_2\text{O})_8]$.

2.3.4 Ferroelectric and Dielectric Studies

As **1** and **1a** belong to one of the 10 polar point groups (C_1 , C_s , C_2 , C_{2v} , C_3 , C_{3v} , C_4 , C_{4v} , C_6 and C_{6v}) that are associated with ferroelectric behavior,⁴⁰ the ferroelectric measurements were performed on their samples. The saturated polarization (P) vs. electric field (E) hysteresis loop was obtained for both **1** and **1a** at room temperature, confirming the occurrence of ferroelectricity in them (Figure 2.7). Further, the extremely low leakage (10^{-5} to 10^{-6} A) currents demonstrate that observed hysteresis loops are clearly due to ferroelectricity. The saturated polarization (P_s) value of **1** is seen to be $1.8 \mu\text{Ccm}^{-2}$, which is higher than that of Rochelle salt ($0.25 \mu\text{Ccm}^{-2}$) and several recently reported metal organic materials, and slightly smaller than that of potassium dihydrogen phosphate ($5 \mu\text{Ccm}^{-2}$).^{28,34-38} Whereas, a lower P_s value of $0.55 \mu\text{Ccm}^{-2}$ has been observed for **1a**. The coercive field (E_c) of **1** and **1a** were

observed at 16 kVcm^{-1} and 30 kVcm^{-1} , respectively, which are smaller than those of several polymeric ferroelectrics.²⁸ However, the saturation polarization and the rectangularity of the loop decreases for both **1** and **1a** with increase in frequency. Preliminary ferroelectric fatigue studies on these compounds show that the remnant polarization (P_r) remains unchanged after several switching operations. This confirms the presence of switchable ferroelectric domains in them even after several cycles.

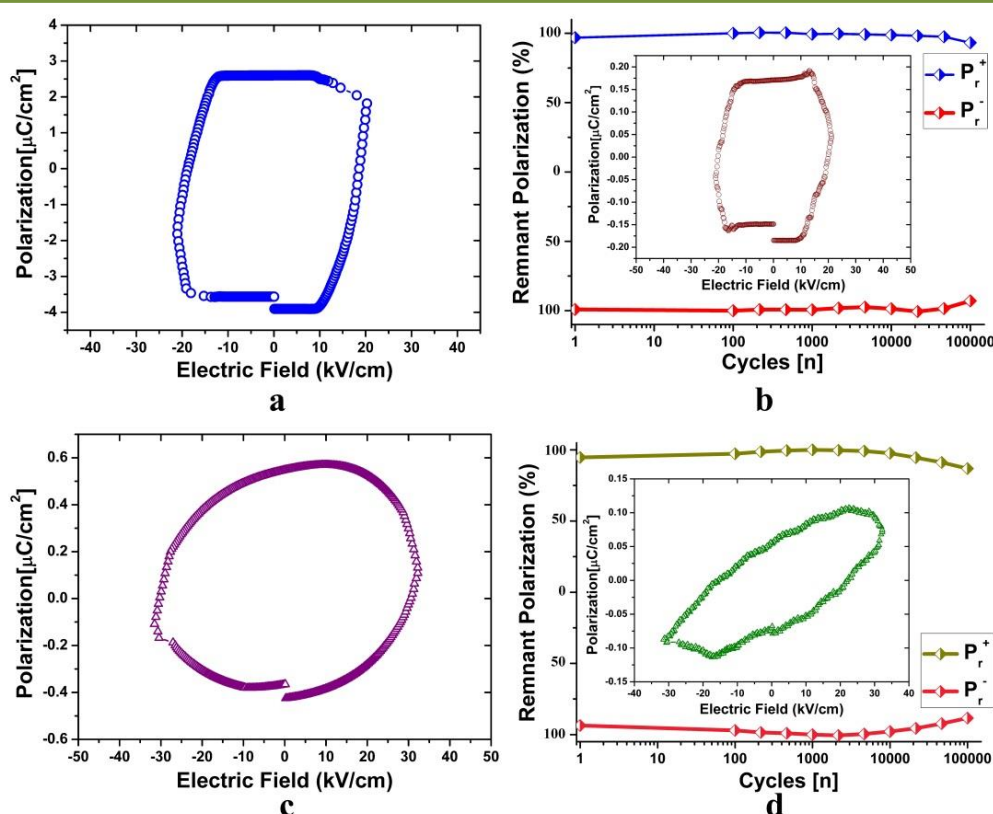


Figure 2.7: Dielectric P - E hysteresis loop of (a) **1** and (c) **1a** at a 0.1 Hz frequency. Ferroelectric fatigue studies on (b) **1** and (d) **1a** at 1 Hz frequency; the insets show the respective P - E loops at the same frequency.

As observed with most ferroelectric materials, the polarization in **1** and **1a** originates from the spatial asymmetry of these cationic helical assemblies, in addition to the contributions from the polarizable free counter anions ($\text{ClO}_4^-/\text{NO}_3^-$). Further, the anion induced polarization in them originates from two distinct kinds of guest (anions and solvents) arrangements found in the trigonal channels present in their unit-cell packing (Figure 2.8). The high saturation polarization and rectangularity obtained for

1 is primarily attributed to its polar packing arrangements. Thus, the addition of nitrate ion has an effect in altering the asymmetry of the system, which causes a change of polarization in **1a**. This is evidenced by the higher coercive field (30 kVcm^{-1}) that is required for its ferroelectric switching operations. Moreover, the electrical fatigue is reduced to 10^4 cycles in **1a** in comparison with 10^5 cycles in **1**. Such a behavior is normally attributed to decrease in polarizability of the system, movement of space charges (similar to n-p hopping charges and oxygen vacancies observed in metal-oxides),⁴⁹ and the orientation of switchable ferroelectric domains.

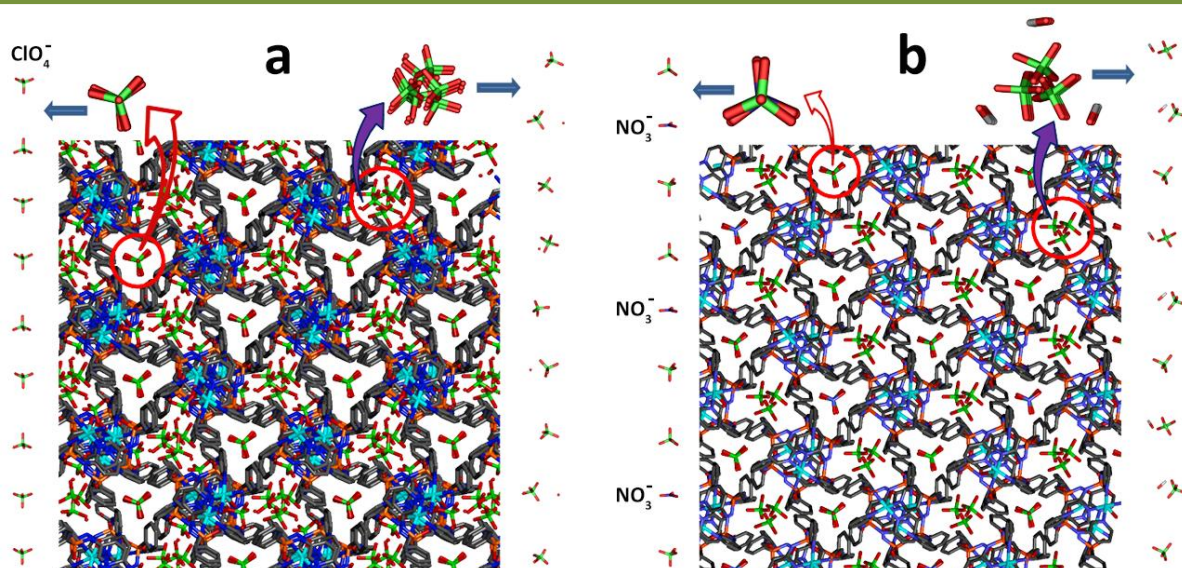


Figure 2.8: The 2x2x2 super-cell structure of (a) **1** and (b) **1a** having two distinct packing for the guest anions and solvents in either linear or helical arrangements in their unique trigonal channels. The nitrate ions in **1a** were present only in the linear arrangement of the guest anions.

Furthermore, studies on behavior of the real part of the dielectric constant and the dielectric loss factor as a function of frequency at various temperatures on **1**, **1a**, and **2** were performed (Figure 2.9). The room temperature dielectric constant values at 1 Hz for **1**, **1a**, and **2** are 118.7, 27.4, and 39.2, respectively, suggesting them as high dielectric constant materials.⁵⁰ The ferroelectric nature of sample **1** is evident from its large dielectric constant (~ 120) at room temperature. The observed decrease in dielectric constant in **1a** is again due to the distortions in polar arrangements causing a break in the long-range interactions within the helical assembly. In fact, it is interesting to observe a significant dielectric constant for **2** despite its

centrosymmetric nature. Also, as observed from Figure 2.9, all of these three materials show very low dielectric loss factors.

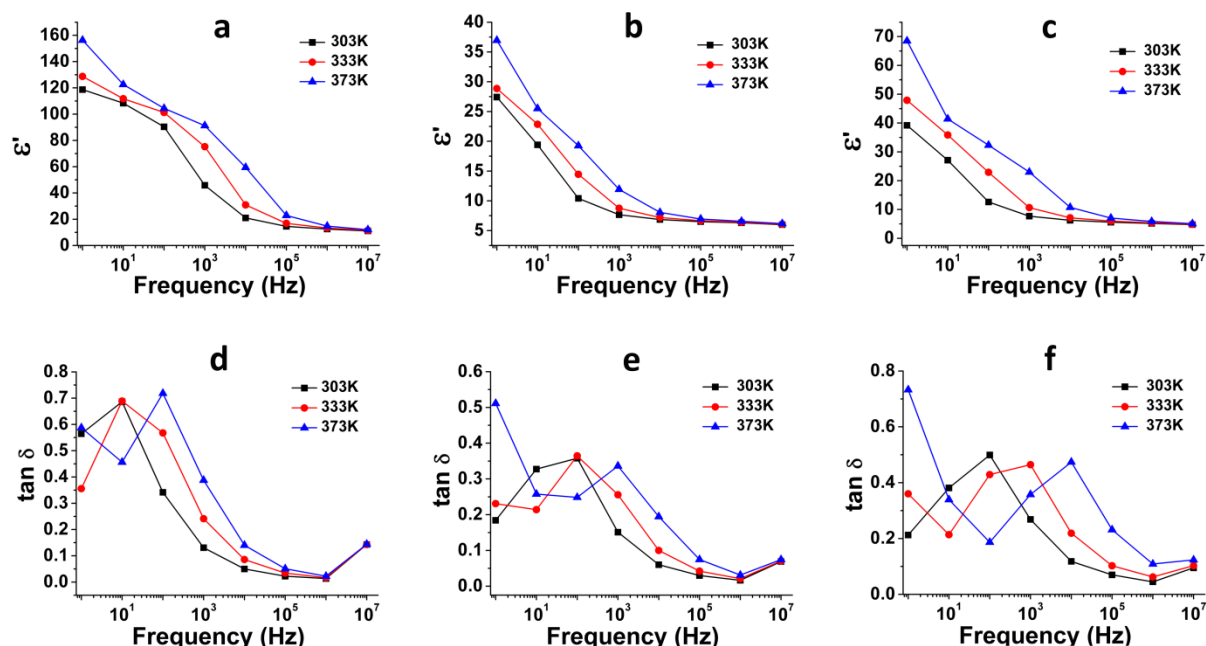


Figure 2.9: Frequency dependence of the real part of the dielectric constants for (a) **1**, (b) **1a**, and (c) **2** at different temperature. The plot of dielectric loss as a function of frequency for (d) **1**, (e) **1a**, and (f) **2** at different temperatures.

As with most dielectric materials, the dielectric constant of all of these three compounds increases with increase in temperature and decrease in frequency (Figure 2.9 and Appendices A2.8–A2.10). The increasing trend of dielectric constant with decrease in frequency is due to the contribution of all of the polarization (space-charge, orientation, ionic, and electronic) mechanisms at lower frequencies (<100 Hz).¹⁷ As frequency increases, space charge, ionic, and electronic polarizations become inoperative in that order. The same behavioral trend has also been observed in many ferroelectric materials.⁵¹⁻⁵³ The increase in dielectric constant with temperature is due to the increase in dominance of interfacial polarization compared to dipolar polarization.⁵⁴

2.4 CONCLUSION

In conclusion, the present work shows that counter anions such as perchlorate or nitrate ions can not only control the structural architectures in the same metal–ligand combination but also alter the physical properties associated with them. Thus, the iso-structural 1D-helical assemblies of **1** and **1a** exhibit large variations for ferroelectric saturation polarization (P_s) and dielectric constant values as the higher values are observed for the former one. Also, the tetrameric cavitand **2** shows a significant dielectric constant despite having a centrosymmetric structure. In addition, the hydrophilic nature of the central cavity in **2** was confirmed by the encapsulation of a hydrated potassium cation. Similarly, **3** can host a water cluster in its intrinsic cavity. These results demonstrate that anion driven self-assembly is a facile approach for tuning the behavior of metal–organic ferroelectrics and pave the way for the synthesis of new practical materials.

2.5 REFERENCES

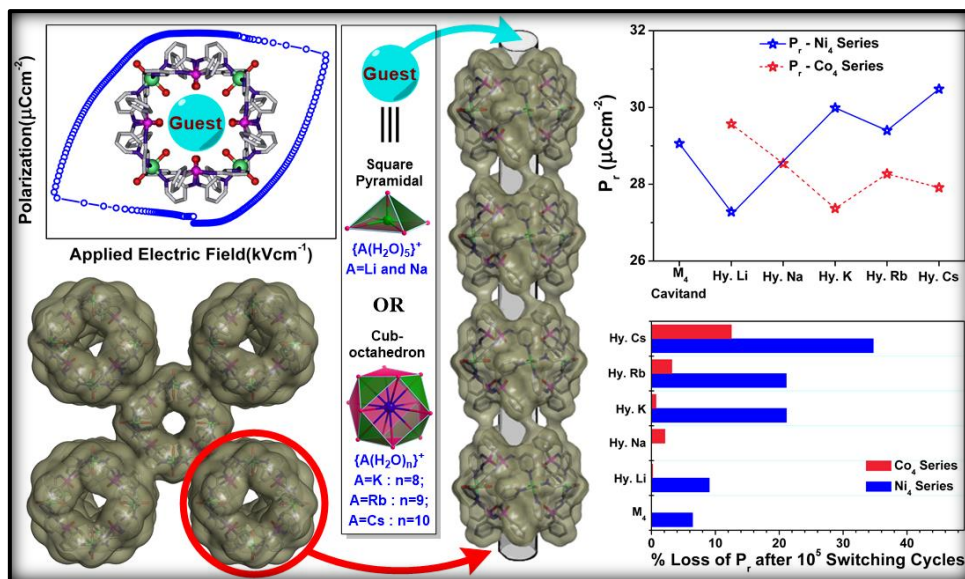
- (1) Cariati, E.; Macchi, R.; Roberto, D.; Ugo, R.; Galli, S.; Casati, N.; Macchi, P.; Sironi, A.; Bogani, L.; Caneschi, A. *J. Am. Chem. Soc.* **2007**, *129*, 9410.
- (2) Horcajada, P.; Serre, C.; Vallet-Regí, M.; Sebban, M.; Taulelle, F.; Férey, G. *Angew. Chem. Int. Ed.* **2006**, *45*, 5974.
- (3) Ma, L.; Falkowski, J. M.; Abney, C.; Lin, W. *Nat. Chem.* **2010**, *2*, 838.
- (4) Wang, M.-S.; Guo, S.-P.; Li, Y.; Cai, L.-Z.; Zou, J.-P.; Xu, G.; Zhou, W.-W.; Zheng, F.-K.; Guo, G.-C. *J. Am. Chem. Soc.* **2009**, *131*, 13572.
- (5) Furukawa, H.; Cordova, K. E.; O'Keeffe, M.; Yaghi, O. M. *Science* **2013**, *341*, 974.
- (6) Long, J. R.; Yaghi, O. M. *Chem. Soc. Rev.* **2009**, *38*, 1213-1214. (c) Zou, X. Q.; Ren, H.; Zhu, G. S. *Chem. Commun.* **2013**, *49*, 3925.
- (7) Batten, S. R.; Murray, K. S. *Coordin. Chem. Rev.* **2003**, *246*, 103.
- (8) Noveron, J. C.; Lah, M. S.; Del Sesto, R. E.; Arif, A. M.; Miller, J. S.; Stang, P. J. *J. Am. Chem. Soc.* **2002**, *124*, 6613.
- (9) Papadopoulos, M. G.; Sadlej, A. J.; Leszczynski, J. *Non-linear optical properties of matter*, Springer: 2006.
- (10) Ren, Z.-G.; Li, H.-X.; Liu, G.-F.; Zhang, W.-H.; Lang, J.-P.; Zhang, Y.; Song, Y.-L. *Organometallics* **2006**, *25*, 4351.
- (11) Wang, X.-Y.; Wang, Z.-M.; Gao, S. *Chem. Commun.* **2007**, 1127.
- (12) Dawber, M.; Rabe, K. M.; Scott, J. F. *Rev. Mod. Phys.* **2005**, *77*, 1083.
- (13) Dearaujo, C. A. P.; Cuchiaro, J. D.; Mcmillan, L. D.; Scott, M. C.; Scott, J. F. *Nature* **1995**, *374*, 627.
- (14) Lee, H. N.; Christen, H. M.; Chisholm, M. F.; Rouleau, C. M.; Lowndes, D. H. *Nature* **2005**, *433*, 395.
- (15) Rijnders, G.; Blank, D. H. A. *Nature* **2005**, *433*, 369.
- (16) Scott, J. F.; Dearaujo, C. A. P. *Science* **1989**, *246*, 1400.
- (17) M. E. Lines, A. M. *Glass Principles and Applications of Ferroelectrics and Related Materials*; Oxford University Press: New York, 1977.
- (18) K. Uchino *Ferroelectric Devices*, Marcel Dekker: New York, 2000.
- (19) Homes, C. C.; Vogt, T.; Shapiro, S. M.; Wakimoto, S.; Ramirez, A. P. *Science* **2001**, *293*, 673.

- (20) Hughes, H.; Allix, M. M. B.; Bridges, C. A.; Claridge, J. B.; Kuang, X. J.; Niu, H. J.; Taylor, S.; Song, W. H.; Rosseinsky, M. J. *J. Am. Chem. Soc.* **2005**, *127*, 13790.
- (21) Vanderah, T. A. *Science* **2002**, *298*, 1182.
- (22) Long, X. F.; Ye, Z. G. *Chem. Mater.* **2007**, *19*, 1285.
- (23) Park, B. H.; Kang, B. S.; Bu, S. D.; Noh, T. W.; Lee, J.; Jo, W. *Nature* **1999**, *401*, 682.
- (24) Ramesh, R.; Lee, J.; Sands, T.; Keramidas, V. G.; Auciello, O. *Appl. Phys. Lett.* **1994**, *64*, 2511.
- (25) Zylberberg, J.; Belik, A. A.; Takayama-Muromachi, E.; Ye, Z. G. *Chem. Mater.* **2007**, *19*, 6385.
- (26) Horiuchi, S.; Ishii, F.; Kumai, R.; Okimoto, Y.; Tachibana, H.; Nagaosa, N.; Tokura, Y. *Nat. Mater.* **2005**, *4*, 163.
- (27) Horiuchi, S.; Kumai, R.; Tokura, Y. *Chem. Commun.* **2007**, 2321.
- (28) Horiuchi, S.; Tokura, Y. *Nat. Mater.* **2008**, *7*, 357.
- (29) Tayi, A. S.; Shveyd, A. K.; Sue, A. C. H.; Szarko, J. M.; Rolczynski, B. S.; Cao, D.; Kennedy, T. J.; Sarjeant, A. A.; Stern, C. L.; Paxton, W. F.; Wu, W.; Dey, S. K.; Fahrenbach, A. C.; Guest, J. R.; Mohseni, H.; Chen, L. X.; Wang, K. L.; Stoddart, J. F.; Stupp, S. I. *Nature* **2012**, *488*, 485.
- (30) Fu, D. W.; Cai, H. L.; Liu, Y. M.; Ye, Q.; Zhang, W.; Zhang, Y.; Chen, X. Y.; Giovannetti, G.; Capone, M.; Li, J. Y.; Xiong, R. G. *Science* **2013**, *339*, 425.
- (31) Fu, D. W.; Zhang, W.; Cai, H. L.; Ge, J. Z.; Zhang, Y.; Xiong, R. G. *Adv. Mater.* **2011**, *23*, 5658.
- (32) Ye, H. Y.; Fu, D. W.; Zhang, Y.; Zhang, W.; Xiong, R. G.; Huang, S. D. *J. Am. Chem. Soc.* **2009**, *131*, 42.
- (33) Zhao, H.; Qu, Z. R.; Ye, H. Y.; Xiong, R. G. *Chem. Soc. Rev.* **2008**, *37*, 84.
- (34) Ye, Q.; Song, Y. M.; Wang, G. X.; Chen, K.; Fu, D. W.; Chan, P. W. H.; Zhu, J. S.; Huang, S. D.; Xiong, R. G. *J. Am. Chem. Soc.* **2006**, *128*, 6554.
- (35) Zhao, H. X.; Zhuang, G. L.; Wu, S. T.; Long, L. S.; Guo, H. Y.; Ye, Z. G.; Huang, R. B.; Zheng, L. S. *Chem. Commun.* **2009**, 1644.
- (36) Duan, X. Y.; Meng, Q. J.; Su, Y.; Li, Y. Z.; Duan, C. Y.; Ren, X. M.; Lu, C. S. *Chem. Eur. J.* **2011**, *17*, 9936.
- (37) Wen, L.; Zhou, L.; Zhang, B.; Meng, X.; Qu, H.; Li, D. *J. Mater. Chem.* **2012**, *22*, 22603.
- (38) Tang, Y. Z.; Zhou, M.; Huang, J.; Tan, Y. H.; Wu, J. S.; Wen, H. R. *Inorg. Chem.* **2013**, *52*, 1679.

- (39) Hang, T.; Zhang, W.; Ye, H.-Y.; Xiong, R.-G. *Chem. Soc. Rev.* **2011**, *40*, 3577.
- (40) Li, Y.-H.; Qu, Z.-R.; Zhao, H.; Ye, Q.; Xing, L.-X.; Wang, X.-S.; Xiong, R.-G.; You, X.-Z. *Inorg. Chem.* **2004**, *43*, 3768.
- (41) Xu, G. C.; Ma, X. M.; Zhang, L.; Wang, Z. M.; Gao, S. *J. Am. Chem. Soc.* **2010**, *132*, 9588.
- (42) Zhang, W.; Xiong, R. G. *Chem. Rev.* **2012**, *112*, 1163.
- (43) Sheldrick, G. M. *Acta Crystallogr.* **2008**, *A64*, 112.
- (44) Spek, A. L. *Acta Cryst. C* **2015**, *C71*, 9.
- (45) Lagona, J.; Mukhopadhyay, P.; Chakrabarti, S.; Isaacs, L. *Angew. Chem. Int. Ed.* **2005**, *44*, 4844.
- (46) Kim, K.; Selvapalam, N.; Ko, Y. H.; Park, K. M.; Kim, D.; Kim, J. *Chem. Soc. Rev.* **2007**, *36*, 267.
- (47) Macrae, C. F.; Edgington, P. R.; McCabe, P.; Pidcock, E.; Shields, G. P.; Taylor, R.; Towler, M.; Streek, J. v. d. *J. Appl. Cryst.* **2006**, *39*, 453.
- (48) Connolly, M. L. *J. Mol. Graph.* **1993**, *11*, 139.
- (49) Zhang, M. F.; Wang, T.; Wang, K. F.; Zh, J. S.; Liu, J. M. *J. Appl. Phys.* **2009**, *105*, 61639.
- (50) Compounds having dielectric constant value greater than that of silicon nitride ($\epsilon_r > 7.0$) are classified as high dielectric constant materials.
- (51) Mal, J.; Choudhary, R. N. P. *Phase Transit.* **1997**, *62*, 119.
- (52) Misra, N. K.; Sati, R.; Choudhary, R. N. P. *Mater. Lett.* **1995**, *24*, 313.
- (53) Rai, R.; Sharma, S. *Solid state Commun.* **2005**, *133*, 635.
- (54) Rai, R.; Sharma, S.; Soni, N. C.; Choudhary, R. N. P. *Physica B* **2006**, *382*, 252.

End of Chapter 2

Chapter 3



**Altering Polarization Attributes in
Ferroelectric Metallo-Cavitands by
Varying Hydrated Alkali-Metal Guest
Cations**

3.1 Introduction

Ferroelectric substances are characterized by spontaneous electric polarization that can be reversed by the inversion of the applied electric field.¹ Ferroelectrics, owing to their electric switchable nature, are widely used as multifunctional electroactive polar materials for high-performance devices.²⁻⁸ In addition to their great potential as memory elements, ferroelectric materials are actively being pursued for energy harvesting applications due to their piezoelectric and pyroelectric properties.⁹⁻¹⁶ Ferroelectricity was first discovered in Rochelle salt,¹⁷ but since then inorganic oxides (BTO and PZT, etc.) and polymers (PVDF and its copolymers) have been the desired choice of materials for ferroelectric applications.¹⁸⁻²¹ Ferroelectricity has also been observed in certain supramolecular systems based on organic, liquid crystalline, charge-transfer and metal-organic scaffolds as they can possess specific advantages such as facile synthesis, low density, flexibility, and easy fabrication over the traditional ferroelectric inorganic oxides.²²⁻²⁵ In most of these systems, supramolecular interactions that facilitate hydrogen displacement, coaxed charge-transfer complexation and dipole encapsulation etc. have contributed to their polar order. Nevertheless, inducing non-centrosymmetric polar packing arrangements in these systems is still challenging and serendipitous.

Recently, ferroelectric metal-organic and hybrid organic-inorganic materials have gained tremendous attention as the non-centrosymmetric arrangement of dipoles in these assemblies can be efficiently invoked by simple chemical modifications like nature of metal-ligand interactions, choice of cations and anions and the extra-framework molecules present in them.²⁶⁻³⁴ In some instances, charge-balanced MOFs and molecular motion systems have been shown to exhibit ferroelectric ordering under the influence of an applied electric field.^{35,36} In this effort, our group has synthesized a family of $\{\text{Cu}^{\text{II}}\text{L}_2\}_n$ based assemblies, derived from flexible dipodal ligands of the type $[\text{PhPO}(\text{NHPy})_2]$, (Py = 2-pyridyl (²Py) or 3-pyridyl (³Py) or 4-pyridyl(⁴Py)), which showed non-centrosymmetric structure and subsequent ferroelectric responses depending on the counter anions, dimensionality of the framework and solvate molecules present in them.^{37,39} These findings prompted us to

look for a robust $\{M^{\text{II}}L_2\}_n$ system based on these ligands in which the ferroelectric polarization attributes can be systematically altered by using certain chemically tunable functions. Specifically, we paid attention to obtain discrete ferroelectric metal-ligand cages and cavitands and to get insights on certain supramolecular interactions or host-guest behavior that influences the overall polarization in them.

Herein, we report the synthesis of two non-centrosymmetric cavitands of formula $[\{Ni_4L^1_8(H_2O)_8\}\supset 9(H_2O)]\cdot 8(NO_3)\cdot 25(H_2O)$ (**4**; Ni₄-cavitand) and $[\{Co_4L^1_8(H_2O)_8\}\supset 9(H_2O)]\cdot 8(NO_3)\cdot 27(H_2O)$ (**5**; Co₄-cavitand), built on the phosphoramidate ligand L¹, PhPO(NH³Py)₂. Owing to the presence of large intrinsic cavities, host-guest systems based on hydrated alkali metal cations (Hy-A), ranging from Li⁺ to Cs⁺ ions has been synthesized for both **4** and **5**. Structural analyses revealed that the hydration spheres around the alkali metal ions were found to be on the higher side, especially the K⁺, Rb⁺ and Cs⁺ ions were exclusively coordinated with 8, 9 and 10 molecules of water, respectively. Ferroelectric hysteresis measurements on **4** gave a well-saturated loop with high remnant polarization (P_r) value of 29.50 μCcm^{-2} (at 0.1 Hz). The P-E loop measurements on all the (Hy-A)_c**4** and (Hy-A)_c**5** systems show excellent ferroelectric responses with notable variations in their polarization attributes, which are consistent with the polarizability of the alkali metal cations. Interestingly, the ferroelectric fatigue measurements on (Hy-A)_c**4** and (Hy-A)_c**5** systems show exceptional fatigue resistant behavior albeit with a prominent reduction in P_r for the Cs-encapsulated systems at higher switching cycles. These observations suggest the effect of intrinsic-guest molecules in the overall polarization of the $\{M_4L_8\}^{8+}$ cavitand systems. To the best of our knowledge, the present study is unique of its kind for the systematic investigation on a family of supramolecular host-guest systems.

3.2 EXPERIMENTAL SECTION

3.2.1 General Remarks

All manipulations involving phosphorus halides were performed under a dry nitrogen atmosphere in standard Schlenk-glassware; toluene was dried over

sodium. The ligand L^1 was synthesized as per the procedure reported in chapter 2.³⁸ $Ni(NO_3)_2 \cdot 6H_2O$ and $Co(NO_3)_2 \cdot 6H_2O$ were purchased from Merck and used as received. KNO_3 , $NaNO_3$, and $RbNO_3$ were purchased from Sigma-Aldrich, while $LiNO_3$ and $CsNO_3$ were locally purchased and used as received. The X-ray powder diffraction (PXRD) data were obtained from a Bruker-D8 Advance diffractometer. FT-IR in attenuated total reflectance (ATR) mode was taken on neat samples on a Bruker Alpha spectrophotometer. Elemental analyses were performed on a Vario-EL cube elemental analyzer.

3.2.2 Synthesis

3.2.2.1 Synthesis of compound $[Ni_4L^1_8(H_2O)_8] \cdot 9(H_2O) \cdot 8(NO_3) \cdot 25(H_2O)$ (4): To a stirred solution of L^1 (62 mg, 0.2 mmol) in MeOH (4 ml), $Ni(NO_3)_2 \cdot 6H_2O$ (30 mg, 0.1 mmol) in H_2O (2 ml) was added. The mixture was subjected to continuous stirring for an hour. Then the solution was filtered through a thick pad of celite, and the filtrate was left undisturbed at room temperature for crystallization. The blue coloured single crystals of **1** suitable for SCXRD analysis were obtained after 2-3 weeks. Yield: 61% (61 mg), based on Ni. FT-IR data (cm^{-1}): 3744, 3124, 2961, 1646, 1582, 1504, 1476, 1394, 1327, 1268, 1184, 1117, 1058, 1031, 945, 806, 748, 694. Anal. Calcd. for $C_{128}H_{204}N_{40}O_{74}P_8Ni_4$: C, 38.73; H, 5.18; N, 14.11. Found: C, 39.01; H, 4.95; N, 14.12.

3.2.2.2 Synthesis of compound $[Co_4L^1_8(H_2O)_8] \cdot 9(H_2O) \cdot 8(NO_3) \cdot 27(H_2O)$ (5): The similar procedure, as stated above for **1**, was adopted by using $Co(NO_3)_2 \cdot 6H_2O$ (29 mg, 0.1 mmol) in place of $Ni(NO_3)_2 \cdot 6H_2O$. The orange coloured single crystals of **2** suitable for SCXRD analysis were obtained after 2-3 weeks. Yield: 9% (9 mg), based on Co. FT-IR data (cm^{-1}): 3746, 3132, 2959, 1648, 1580, 1506, 1475, 1391, 1326, 1268, 1180, 1117, 1050, 1029, 949, 808, 749, 694. Anal. Calcd. for $C_{128}H_{208}N_{40}O_{76}P_8Co_4$: C, 38.37; H, 5.23; N, 13.98. Found: C, 38.59; H, 4.91; N, 14.15.

3.2.2.3 Synthesis of $[Hy-A]_c4$ and $[Hy-A]_c5$ host-guest systems (where $A = Li^+$, Na^+ , K^+ , Rb^+ , Cs^+ ions): The $[Hy-A]_c4$ and $[Hy-A]_c5$ systems were synthesized by adopting the following procedure:

(a) To a stirred solution of L^1 (62 mg, 0.2 mmol) in MeOH (5 ml), $Ni(NO_3)_2 \cdot 6H_2O/Co(NO_3)_2 \cdot 6H_2O$ (0.1 mmol) and ANO_3 (0.1 mmol) in H_2O (3 ml) were added and stirred further. The solution was then filtered through a thick pad of celite and left for crystallization. Definite shaped crystals of $[Hy-A]c4$ or $[Hy-A]c5$ suitable for SCXRD analysis were obtained after 10-15 days.

(b) To a solution of ANO_3 (1 mmol) in methanol (4 ml) and water (4 ml), crystals of **4** or **5** (20 mg) were added and stirred for 24 hours. The solution was then filtered through a thick pad of celite and left for crystallization. Definite shaped single crystals suitable for SCXRD analysis were obtained after 2-3 weeks.

3.2.2.4 Characterization data for $[Hy-A]c4$ and $[Hy-A]c5$ systems (reported yields are based on method a):

3.2.2.4.1 $\{[Ni_4L^1_8(H_2O)_8] \supset Li(H_2O)_5 \cdot (H_2O)_2\} \cdot 9(NO_3) \cdot 16.5(H_2O)$ ($[Hy-Li]c4$): Yield: 68% (65 mg), based on Ni. FT-IR data (cm^{-1}): 3859, 3743, 3152, 2959, 1646, 1581, 1508, 1477, 1392, 1327, 1269, 1174, 1116, 1056, 1030, 949, 807, 748, 694. Anal. Calcd. for $C_{128}H_{183}N_{41}O_{66.5}LiP_8Ni_4$: C, 39.94; H, 4.79; N, 14.92. Found: C, 40.12; H, 4.65; N, 14.80.

3.2.2.4.2 $\{[Ni_4L^1_8(H_2O)_8] \supset 0.25[Na(H_2O)_5] \cdot (H_2O)_{5.5}\} \cdot 8.25(NO_3) \cdot 20(H_2O)$ ($[Hy-Na]c4$): Yield: 61% (59 mg), based on Ni. FT-IR data (cm^{-1}): 3860, 3744, 3146, 2959, 1646, 1581, 1508, 1477, 1392, 1328, 1269, 1181, 1117, 1058, 1030, 949, 808, 748, 694. Anal. Calcd. for $C_{128}H_{189.5}N_{40.25}O_{67.5}Na_{0.25}P_8Ni_4$: C, 39.82; H, 4.95; N, 14.60. Found: C, 40.03; H, 4.72; N, 14.57.

3.2.2.4.3 $\{[Ni_4L^1_8(H_2O)_8] \supset K(H_2O)_8\} \cdot 9(NO_3) \cdot 17(H_2O)$ ($[Hy-K]c4$): Yield: 72% (70 mg), based on Ni. FT-IR data (cm^{-1}): 3860, 3744, 3143, 2958, 1646, 1581, 1510, 1477, 1394, 1328, 1269, 1180, 1117, 1058, 1028, 949, 807, 749, 694. Anal. Calcd. for $C_{128}H_{186}N_{41}O_{68}KP_8Ni_4$: C, 39.33; H, 4.80; N, 14.69. Found: C, 39.22; H, 5.01; N, 14.54.

3.2.2.4.4 $\{[Ni_4L^1_8(H_2O)_8] \supset Rb(H_2O)_9\} \cdot 9(NO_3) \cdot 20(H_2O)$ ($[Hy-Rb]c4$): Yield: 70% (71 mg), based on Ni. FT-IR data (cm^{-1}): 3861, 3745, 3153, 2963, 1646, 1581, 1511, 1477, 1394, 1327, 1269, 1175, 1118, 1058, 1028, 950, 808, 748,

694. Anal. Calcd. for $C_{128}H_{194}N_{41}O_{72}RbP_8Ni_4$: C, 38.18; H, 4.86; N, 14.26. Found: C, 38.37; H, 4.75; N, 13.98.

3.2.2.4.5 $[Ni_4L^1_8(H_2O)_8] \cdot Cs(H_2O)_{10} \cdot 9(NO_3) \cdot 17(H_2O)$ ([Hy-Cs]c4): Yield: 69% (70 mg), based on Ni. FT-IR data (cm^{-1}): 3861, 3744, 3145, 2961, 1646, 1578, 1511, 1466, 1394, 1328, 1268, 1176, 1117, 1057, 1028, 950, 807, 748, 694. Anal. Calcd. for $C_{128}H_{190}N_{41}O_{70}CsP_8Ni_4$: C, 38.07; H, 4.74; N, 14.22. Found: C, 37.83; H, 4.77; N, 14.27.

3.2.2.4.6 $[Co_4L^1_8(H_2O)_8] \cdot Li(H_2O)_5 \cdot (H_2O)_2 \cdot 9(NO_3) \cdot 25(H_2O)$ ([Hy-Li]c5): Yield: 52% (52 mg), based on Co. FT-IR data (cm^{-1}): 3860, 3742, 3152, 2959, 1647, 1580, 1508, 1477, 1391, 1325, 1269, 1176, 1116, 1059, 1029, 949, 807, 749, 694. Anal. Calcd. for $C_{128}H_{200}N_{41}O_{75}LiP_8Co_4$: C, 38.40; H, 5.04; N, 14.34. Found: C, 38.63; H, 4.89; N, 14.23.

3.2.2.4.7 $[Co_4L^1_8(H_2O)_8] \cdot 0.25Na(H_2O)_5 \cdot (H_2O)_5 \cdot 8.25(NO_3) \cdot 27(H_2O)$ ([Hy-Na]c5): Yield: 51% (49 mg), based on Co. FT-IR data (cm^{-1}): 3860, 3743, 3146, 2960, 1647, 1580, 1510, 1476, 1392, 1328, 1269, 1180, 1117, 1059, 1030, 949, 807, 748, 694. Anal. Calcd. for $C_{128}H_{189.5}N_{40.25}O_{67.5}Na_{0.25}P_8Co_4$: C, 39.81; H, 4.95; N, 14.60. Found: C, 39.60; H, 4.83; N, 14.43.

3.2.2.4.8 $[Co_4L^1_8(H_2O)_8] \cdot K(H_2O)_8 \cdot 9(NO_3) \cdot 23(H_2O)$ ([Hy-K]c5): Yield: 69% (69 mg), based on Co. FT-IR data (cm^{-1}): 3861, 3742, 3144, 2958, 1646, 1580, 1510, 1476, 1394, 1329, 1269, 1180, 1117, 1059, 1029, 949, 807, 749, 694. Anal. Calcd. for $C_{128}H_{198}N_{41}O_{74}KP_8Co_4$: C, 38.26; H, 4.97; N, 14.29. Found: C, 38.41; H, 4.70; N, 14.35.

3.2.2.4.9 $[Co_4L^1_8(H_2O)_8] \cdot Rb(H_2O)_9 \cdot 9(NO_3) \cdot 27(H_2O)$ ([Hy-Rb]c5): Yield: 65% (67 mg), based on Co. FT-IR data (cm^{-1}): 3860, 3745, 3149, 2960, 1648, 1580, 1510, 1477, 1394, 1327, 1268, 1175, 1118, 1058, 1028, 949, 808, 749, 694. Anal. Calcd. for $C_{128}H_{208}N_{41}O_{79}RbP_8Co_4$: C, 37.01; H, 5.05; N, 13.82. Found: C, 37.13; H, 4.96; N, 14.03.

3.2.2.4.10 $[Co_4L^1_8(H_2O)_8] \cdot Cs(H_2O)_{10} \cdot 9(NO_3) \cdot 25(H_2O)$ ([Hy-Cs]c5): Yield: 66% (69 mg), based on Co. FT-IR data (cm^{-1}): 3860, 3746, 3146, 2959, 1649,

1581, 1510, 1472, 1394, 1328, 1269, 1175, 1117, 1058, 1028, 949, 807, 748, 694. Anal. Calcd. for $C_{128}H_{206}N_{41}O_{78}CsP_8Co_4$: C, 36.75; H, 4.96; N, 13.73. Found: C, 36.92; H, 4.87; N, 14.00.

3.2.3 Crystallography

Reflections were collected on a Bruker Smart Apex Duo diffractometer at 100 K using MoK α radiation ($\lambda = 0.71073 \text{ \AA}$) for the crystals of **4**, **5**, [Hy-A]c**1** and [Hy-A]c**5**. Structures were refined by full matrix least squares against F^2 using all data (SHELX).⁴⁰ Crystallographic data for all these compounds are listed in Table 3.1. All non-hydrogen atoms were refined anisotropically, if not stated otherwise. Hydrogen atoms were constrained in geometric positions to their parent atoms. The phenyl rings were thermally disordered in all the cases, hence the atom positions of the disordered groups were freely refined isotropically over two positions using similar

Table 3.1: Details of crystallographic data collection and structure refinements for **4, **5**, [Hy-A]c**4** and [Hy-A]c**5** systems.**

Compound	4	[Hy-Li]c 4	[Hy-Na]c 4	[Hy-K]c 4
Chemical formula	$C_{128}H_{204}N_{40}O_{74}P_8Ni_4$	$C_{128}H_{183}LiN_{41}O_{66.5}P_8Ni_4$	$C_{128}H_{189.50}Na_{0.25}N_{40.25}O_{67.50}P_8Ni_4$	$C_{128}H_{186}KN_{41}O_{68}P_8Ni_4$
Formula weight	3969.90	3849.68	3860.53	3908.87
Temperature	100(2)	100(2)	100 (2)	100(2)
Crystal system	Tetragonal	Tetragonal	Tetragonal	Tetragonal
Space group	I422	I422	I422	I422
a (\AA); α ($^\circ$)	24.810(2); 90	24.222(7); 90	24.399(7); 90	24.382(2); 90
b (\AA); β ($^\circ$)	24.810(2); 90	24.222(7); 90	24.399(7); 90	24.382(2); 90
c (\AA); γ ($^\circ$)	17.809(15); 90	17.620(4); 90	17.576(5); 90	17.522(3); 90
V (\AA^3); Z	10963(2); 2	10337(6); 2	10463(6); 2	10417(3); 2
ρ (calc.) mg m^{-3}	1.203	1.237	1.225	1.246
μ mm^{-1}	0.481 (Mo K_α)	0.505 (Mo K_α)	0.500 (Mo K_α)	0.522 (Mo K_α)
$2\theta_{\text{max}}$ ($^\circ$)	56	56	45	56
R(int)	0.0822	0.1493	0.0471	0.0795
Completeness to θ	100 %	99.9 %	99.7 %	100 %
Data / param.	6848 / 218	6535 / 220	3427 / 220	6531 / 224
GOF	1.066	0.996	1.081	1.036
R1 [$F > 4\sigma(F)$]	0.0668	0.0693	0.0520	0.0495
wR2 (all data)	0.2478	0.2468	0.1664	0.1602
max. peak/hole ($\text{e.}\text{\AA}^{-3}$)	0.455 / -0.260	0.544 / -0.290	0.636 / -0.253	0.747 / -0.228

Compound	[Hy-Rb]c4	[Hy-Cs]c4	5	[Hy-Li]c5
Chemical formula	C ₁₂₈ H ₁₉₄ RbN ₄₁ O ₇₂ P ₈ Ni ₄	C ₁₂₈ H ₁₉₀ CsN ₄₁ O ₇₀ P ₈ Ni ₄	C ₁₂₈ H ₂₀₈ Co ₄ N ₄₀ O ₇₆ P ₈	C ₁₂₈ H ₂₀₀ LiN ₄₁ O ₇₅ P ₈ Co ₄
Formula weight	4027.30	4038.71	4006.81	4003.70
Temperature	100(2)	100(2)	100(2)	100(2)
Crystal system	Tetragonal	Tetragonal	Tetragonal	Tetragonal
Space group	I422	I422	I422	I422
a (Å); α (°)	24.570(8); 90	24.462(6); 90	24.556(4); 90	24.507(6); 90
b (Å); β (°)	24.570(8); 90	24.462(6); 90	24.556(4); 90	24.507(6); 90
c (Å); γ (°)	17.699(7); 90	17.608(5); 90	17.680(3); 90	17.716(6); 90
V (Å ³); Z	10685(8); 2	10537(6); 2	10661(4); 2	10640(6); 2
ρ (calc.) mg m ⁻³	1.252	1.273	1.248	1.250
μ mm ⁻¹	0.719 (Mo K _α)	0.668 (Mo K _α)	0.454 (Mo K _α)	0.454 (Mo K _α)
2θ _{max} (°)	56	56	56	56
R(int)	0.1900	0.0844	0.0860	0.2162
Completeness to θ	99.9 %	99.9 %	100 %	100 %
Data / param.	6634 / 224	6711 / 224	6641 / 195	6661 / 173
GOF	0.963	1.032	1.058	0.964
R1 [F>4σ(F)]	0.0618	0.0446	0.0861	0.0876
wR2 (all data)	0.1943	0.1368	0.3228	0.3234
max. peak/hole (e.Å ⁻³)	0.286 /-0.320	0.442 /-0.502	0.765 /-0.354	0.594 /-0.396

Compound	[Hy-Na]c5	[Hy-K]c5	[Hy-Rb]c5	[Hy-Cs]c5
Chemical formula	C ₁₂₈ H _{202.5} Na _{0.25} N _{40.25} O ₇₄ P ₈ Co ₄	C ₁₂₈ H ₁₉₈ KN ₄₁ O ₇₄ P ₈ Co ₄	C ₁₂₈ H ₂₀₈ RbN ₄₁ O ₇₉ P ₈ Co ₄	C ₁₂₈ H ₂₀₆ CsN ₄₁ O ₇₈ P ₈ Co ₄
Formula weight	3978.52	4017.84	4154.29	4183.72
Temperature	100(2)	100(2)	100(2)	100(2)
Crystal system	Tetragonal	Tetragonal	Tetragonal	Tetragonal
Space group	I422	I422	I422	I422
a (Å); α (°)	24.524(12); 90	24.404(4); 90	24.651(3); 90	24.580(3); 90
b (Å); β (°)	24.524(12); 90	24.404(4); 90	24.651(3); 90	24.580(3); 90
c (Å); γ (°)	17.661(8); 90	17.589(3); 90	17.773(2); 90	17.611(3); 90
V (Å ³); Z	10622(12); 2	10476(4); 2	10801(3); 2	10640(3); 2
ρ (calc.) mg m ⁻³	1.244	1.274	1.277	1.306
μ mm ⁻¹	0.455 (Mo K _α)	0.481 (Mo K _α)	0.674 (Mo K _α)	0.625 (Mo K _α)
2θ _{max} (°)	50	56	56	56
R(int)	0.2054	0.1837	0.0623	0.0444
Completeness to θ	99.9 %	100 %	99.9 %	99.9 %
Data / param.	4705 / 172	6564 / 201	6750 / 201	6612 / 201
GOF	0.947	0.977	1.044	1.028
R1 [F>4σ(F)]	0.0879	0.0692	0.0503	0.0375
wR2 (all data)	0.3072	0.2402	0.1623	0.1133
max. peak/hole (e.Å ⁻³)	0.781/-0.298	0.322 /-0.262	0.391 /-0.307	0.411 /-0.266

distances and similar U-restraints. The water molecules encapsulated within the **4**, **5**, [Hy-A]c4 and [Hy-A]c5 were also disordered. Hence their occupancies and numbers were fixed using the SUMP command. The nitrate ions in all these structures were disordered along with the solvated molecules

at the packing cavities. Hence, these were treated as diffuse contributions to the overall scattering and removed by the SQUEEZE/PLATON. In case of [Hy-Li]c4, [Hy-Rb]c4, [Hy-Cs]c4, [Hy-Rb]c5 and [Hy-Cs]c5, the most disagreeable reflection outliers were removed using OMIT command.

3.2.4 Ferroelectric and Dielectric measurements

To determine the dielectric and ferroelectric properties, the powdered samples of all the compounds were compacted in the form of discs (of approximately 10 mm diameter and 1 mm thickness). The compacted discs were subsequently electroded using aluminium adhesive foils for both ferroelectric and dielectric measurements. The frequency dependent dielectric characteristics for **4**, **5**, [Hy-A]c4 and [Hy-A]c5 at various temperatures were measured using the Novocontrol, Dielectric Spectrometer. The ferroelectric hysteresis loop in **4**, [Hy-A]c4 and [Hy-A]c5 were measured by using Sawyer-Tower circuit. Both polarizations and fatigue studies were recorded using hysteresis loop analyser (TF Analyser 2000, aixACCT Germany). Time-dependent leakage current was measured dynamically during the hysteresis loop measurements. It was recorded for various applied voltage steps using the TF analyser.

3.2.5 Calculation of Dipole Moment

The dipole moment of **4** was obtained by performing single-point ONIOM calculations by using the Gaussian 09 program.⁴¹ The cationic cage segment was considered as low layer while the encapsulated H₂O, solvates and nitrate anions were selected as high layer to perform ONIOM calculation. The high layer was optimized by DFT methods (B3LYP/6-31g) and semi-empirical method (PM6) was used for the lower layer.

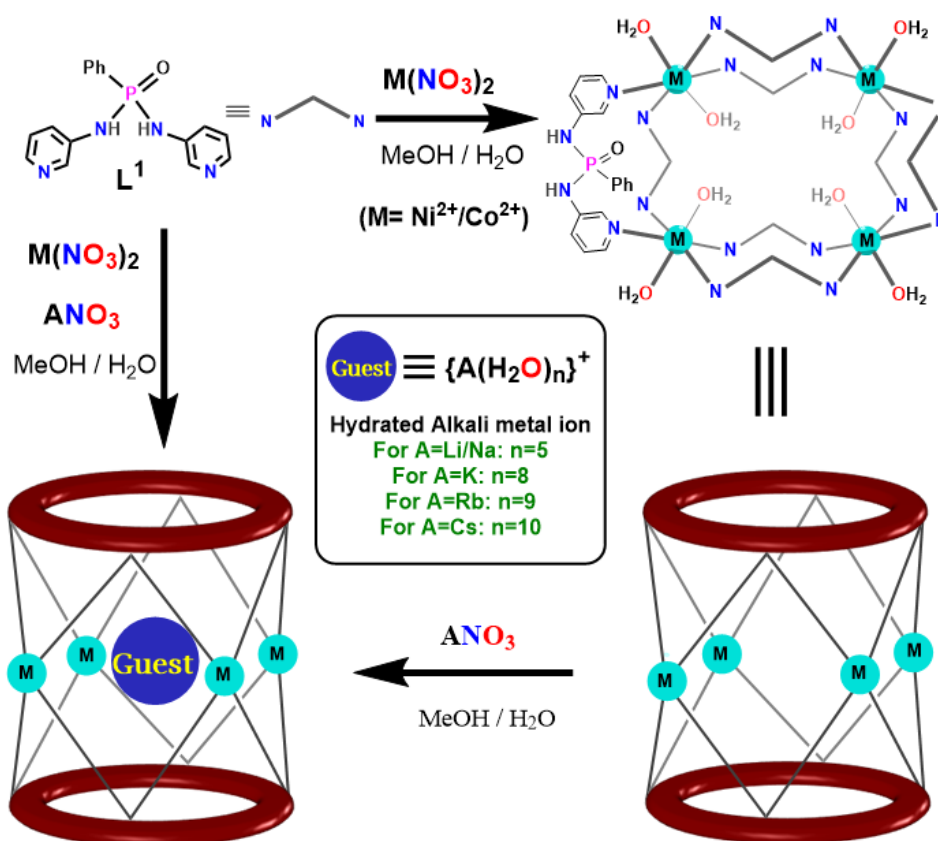
3.3 RESULTS AND DISCUSSION

3.3.1 Syntheses

The Ni₄-cavitand **4** was isolated as blue coloured crystals in a 2:1 reaction mixture involving L¹ and Ni(NO₃)₂·6H₂O in MeOH/H₂O medium at room temperature

(Scheme 3.1). Performing the reaction in the presence of alkali metal cations (A^+), employed as their corresponding nitrate salts, results in the formation of the host-guest systems $[Hy-A]c4$ and $[Hy-A]c5$ (where $[Hy-A] = [A(H_2O)_n]^+$; for $A = Li/Na$ $n = 5$; for $A = K/Rb/Cs$: $n = 8/9/10$). A similar reaction of L^1 with $Co(NO_3)_2 \cdot 6H_2O$ in $MeOH/H_2O$ results in the corresponding the Co_4 -cavitand **5**, in low yields. However, the yields of the $\{[Hy-A]c5\}$ systems drastically increase when the reaction was performed in the presence of alkali metal nitrate salts (Scheme 3.1). Phase purity for all the $[Hy-A]c4$ and $[Hy-A]c5$ systems were confirmed by powder X-ray diffraction analysis (Appendices A3.1 and A3.2).

Scheme 3.1: Schematic diagram for obtaining the tetrameric Ni/Co-cavitands and their hydrated alkali metal ion encapsulated systems.



3.3.2 Crystal Structure of **4** and **5**

The crystal structures of **4** and **5** were solved in the tetragonal space group $I422$ (symmetry D_4). The molecular structures of both **4** and **5** consist of a cationic metal-ligand core, disordered nitrate ions and encapsulated solvate

molecules. The metal ions in them were located in a distorted octahedral geometry, consisting of four N_{pyridyl} planar contacts and two axially coordinated water molecules. The structures can be described as tetranuclear $M_4L^1_8$ cavitands built from four edge-shared 20-membered macrocyclic $M_2L^1_2$ segments (Figure 3.1a). The metal ions were found to be located at the corners of a square plane and each of the four bidentate ligand pairs sit above

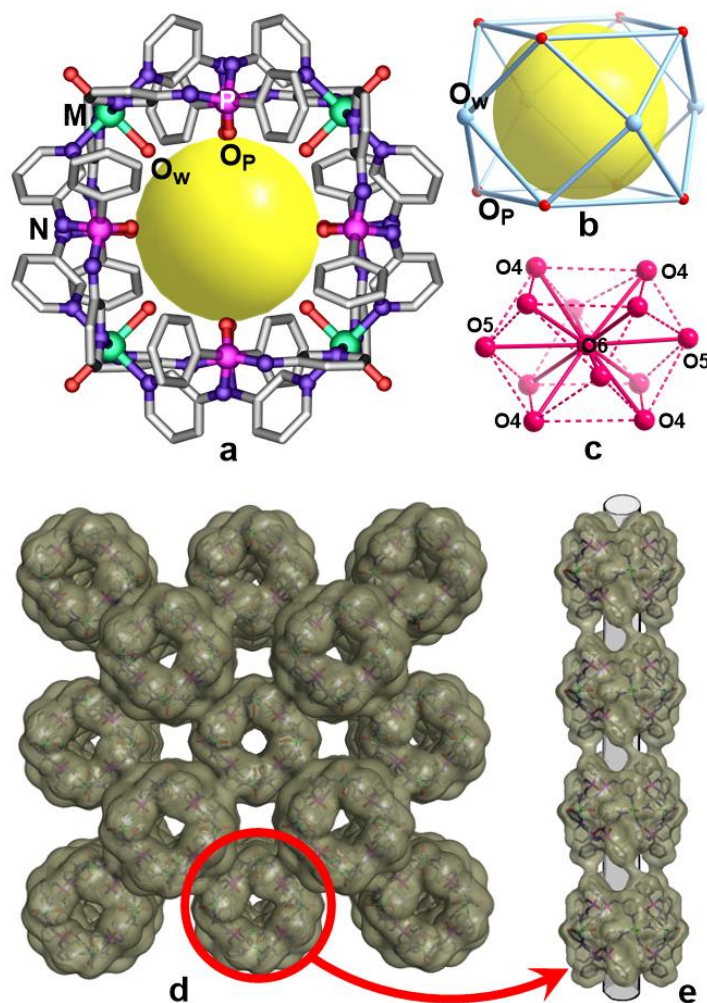


Figure 3.1: (a) View of the tetrameric core in **4** and **5**. (b) The cuboctahedral cavity and (c) the cuboctahedral arrangement of the solvate molecule in them. (d) The bcc packing along the *c*-axis. (e) View of a 1D-channel like structure that connects the intrinsic cavities.

and below the M_4 -plane. The two N_{pyridyl} functionalities in each of the ligand motifs were aligned in *syn*-conformation with respect to the endo oriented $P=O$ groups. The inner surfaces of the cavitands were lined with O-atoms from eight phosphoramidate ligands (O_P) and four Ni-bound water molecules (O_W)

that are arranged at the corners of a putative distorted cuboctahedron (Figure 3.1b and Appendix A3.3). These intrinsic voids were filled with nine disordered water molecules. One of them (O6) is unique and is located at the centre of the cage. The remaining ones, O4 and O5 (disordered) occupy the peripheral positions giving rise to another H-bonded cuboctahedron (Figure 3.1c).

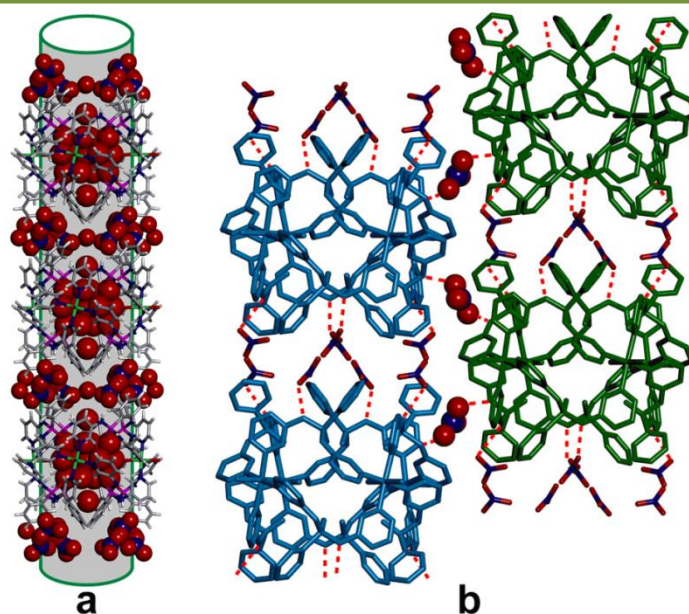


Figure 3.2: (a) View of the contiguous 1D-channel like structure in **4** along the *c*-axis showing the eclipsed arrangement of the Ni_4 -cavitand; connection between the cages along the 1d-channel structure were provided by disordered nitrate anions and extrinsic solvates via H-bonding. (b) Linkage between the adjacent 1D-channels via the interaction of the additional nitrate ions (shown in the space filled representation).

The unit-cell diagrams of both **4** and **5** show the presence of solvent accessible extrinsic voids (in addition to the intrinsic voids) that are lined up with nitrate anions and bulk of solvate molecules (Figure 3.1d and Appendix A3.4). In both **4** and **5**, the tetragonal body-centered packing facilitates the stacking of the cavitands one below the other in an eclipsed manner. This arrangement leads to the formation of a contiguous one-dimensional pore resembling a nano-channel like structure that runs parallel to the long *c*-axis (Figures 3.1e and 3.2). In case of the $Cu_4L^1_8$ cavitand (compound **2**; discussed in chapter 2), the adjacent layers as well as the one below other are orthogonally arranged with respect to each other (Appendix A3.5).³⁸ Such an

arrangement precludes the extension of their voids as 1D-channels in the Cu_4L^1_8 cavitand **2**.

3.3.3 Crystal Structure of the Host-Guest Assemblies

The single crystal X-ray diffraction (SCXRD) analysis on the $\{[\text{Hy-A}]_4\}$ and $\{[\text{Hy-A}]_5\}$ assemblies confirmed the encapsulation of corresponding $[\text{A}(\text{H}_2\text{O})_n]^+$ motifs in all of them while retaining the parent tetrameric structures (Figure 3.3a). Since both the $\{[\text{Hy-A}]_4\}$ and $\{[\text{Hy-A}]_5\}$ assemblies are iso-structural in most instances, henceforth all the molecular structure descriptions are presented only with respect to the $\{[\text{Hy-A}]_4\}$ systems for the sake of simplicity. All the $[\text{Hy-A}]$ encapsulated structures contain a large electron density peak at the central position of the cage (Wyckoff site 2a) except that of $\{[\text{Hy-Na}]_5\}$. In cases of $\{[\text{Hy-Li}]_4\}$, and $\{[\text{Hy-Na}]_4\}$, this peak can be attributed to a water molecule as found in **4** (O6). In these assemblies, the Li^+ and Na^+ ions are located along the four-fold axes away from the central position of O6 and generate meaningful distances to O4 (aqua ligands). As a result, Li and Na atoms would have to be disordered over the two equivalent positions along the 4-fold axis. The metal ions have square-pyramidal environments (Figures 3.3c and 3.3d); the water molecule at their apex may be the one that occupies the equivalent site (O7 in case of Na) or the one at the central position (O6 in case of Li) (Appendices A3.6 and A3.7). Considering the low occupancy factors of Na (1/4) in $\{[\text{Hy-Na}]_4\}$, the scenario of the hosted metal ion (Appendix A3.7a) may co-exist with the one that features no metal ion but only a water molecule at the center of the cage (Appendix A3.7b). Observation of such $\text{A}(\text{H}_2\text{O})_5$ motifs are unprecedented in the family of hydrated Li^+ and Na^+ ions. In fact for the Li^+ ions, the tetrahedral $[\text{Li}(\text{H}_2\text{O})_4]$ coordination has been shown to be energetically favoured over the $[\text{Li}(\text{H}_2\text{O})_5]$ geometry.⁴² In this regard, these findings indicate that the M_4 -cavitands not only efficiently encapsulate Li^+ ion but also stabilizes the energetically less favoured $[\text{Li}(\text{H}_2\text{O})_5]^+$ system.

The heavier alkali metal ions K^+ , Rb^+ and Cs^+ occupy the center of the cage (in place of O6 at the Wyckoff site 2a); their coordination environment is determined by the relative occupancy of positions of the water shell. Altogether there are twelve positions for O4 and O5 in a cuboctahedral

arrangement around the center of the cage (Figure 3.3g). The disordered state produces a 24 vertex truncated cube as the positions of O4 are also disordered in these structures in addition to the disorder of the O5 positions as observed before (Appendix A3.8). Since O_P atoms are exclusively H-acceptors and O_M sites are H-donors, there are only a few arrangements possible which would generate an appropriate H-bonded network such as the cuboctahedral one observed for **4**.

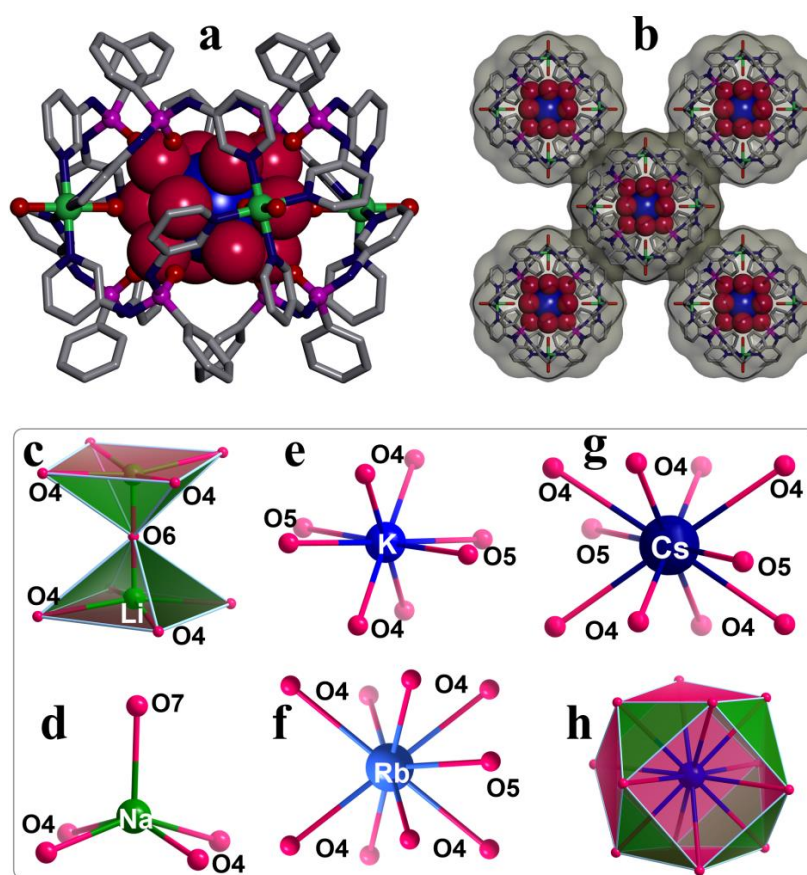


Figure 3.3: (a) Molecular structure of $[Hy-K]c4$. (b) The packing view of $[Hy-K]c4$ along the c -axis. (c) The disordered $[Li(H_2O)_5]^+$ fragments in the square pyramidal geometry. (d)-(g) View of the respective idealized core geometries of $[Na(H_2O)_5]^+$, $[K(H_2O)_8]^+$, $[Rb(H_2O)_9]^+$ and $[Cs(H_2O)_{10}]^+$ ions. (h) The cuboctahedral arrangement of the O4 and O5 atoms around $K^+/Rb^+/Cs^+$ ions.

In order to extract the exact hydration number for these $K^+/Rb^+/Cs^+$ ions, refinements for their corresponding structures were performed with varying hydration numbers ranging from 6 to 12. From these refinement data, coordination numbers of 8, 9 and

10 for K^+ , Rb^+ and Cs^+ ions, respectively (Figure 3.32e-g), appear to be in good agreement with the listed values (Appendices A3.9 and A3.10). While the most favoured coordination for these heavier cations is only seven (for K) or eight (for Rb and Cs) in bulk aqueous systems,⁴³ the higher hydration spheres observed for the $K^+/Rb^+/Cs^+$ assemblies is a consequence of the confinement effects. Moreover, there is a very little information available on the hydration spheres of Rb^+ and Cs^+ ions because of their low charge densities.^{44,45} Furthermore, the A-O distance between $O_{hydrated}$ (O4 and O5) and the alkali metal ions show a slight increase from K to Cs. However, the O-O distances pertaining to $O_{hydrated}$ and O_P or O_W are fairly similar for all of them, and are in the appropriate range for hydrogen bonding (Appendix A3.11). The packing diagrams of all the $\{[Hy-A] \subset \mathbf{4}\}$ and assemblies closely resemble to that of **4** and the guest encapsulated tetrameric cores in them were again stacked in an eclipsed manner along the 4-fold axis (Figure 3.3b). This arrangement results in a one-dimensional array of H-bonded alkali metal framework inside the non-covalent channels of **4**.

3.3.4 Ferroelectric and Dielectric Studies on **4**

The ferroelectric hysteresis measurements on **4** gave a well saturated polarization vs. electric field (P-E) loop at low frequencies (Figure 3.4a and Appendix A3.12). A remnant polarization (P_r) value of $29.50 \mu\text{Ccm}^{-2}$ has been observed at a lower frequency of 0.1 Hz ($29.06 \mu\text{Ccm}^{-2}$ at 1 Hz). Also, the coercive fields (E_c) were obtained at 8.60 (0.1 Hz) and 12.35 kVcm^{-1} (1 Hz) which are much smaller than many commercial ferroelectric materials such as PVDF. This is attributed to the facile switching of the polarizable domains in **4**, a desired property for many practical applications. Further, from the obtained leakage current densities (ranges between 10^{-4} and 10^{-9} Acm^{-2}) and the frequency dependent conductivity plots (ranges between 10^{-4} and $10^{-12} \text{ Scm}^{-1}$), the ferroelectric origin of the hysteresis loops in **4** can be confirmed (Appendices A3.13 and A3.14). Also, the ferroelectric fatigue studies were performed on **4** to verify the retention of polarization after several bipolar switching cycles. These studies show a remarkable fatigue resistant behavior as its P_r values (at 1 Hz) remained almost same even after 10^5 cycles (Figure 3.4b). This suggests the absence of space charge accumulation (or movement) and reduction in the pinning of domain walls, which ultimately aids in the facile switching of its

polarizable domains and confirms the ferroelectric origin of the obtained loop.⁴⁶ Furthermore, the stability of the compound **4** during P-E loop measurements was confirmed by the PXRD analysis which gave similar peak profiles for the sample before and after ferroelectric measurements (Appendix A3.15).

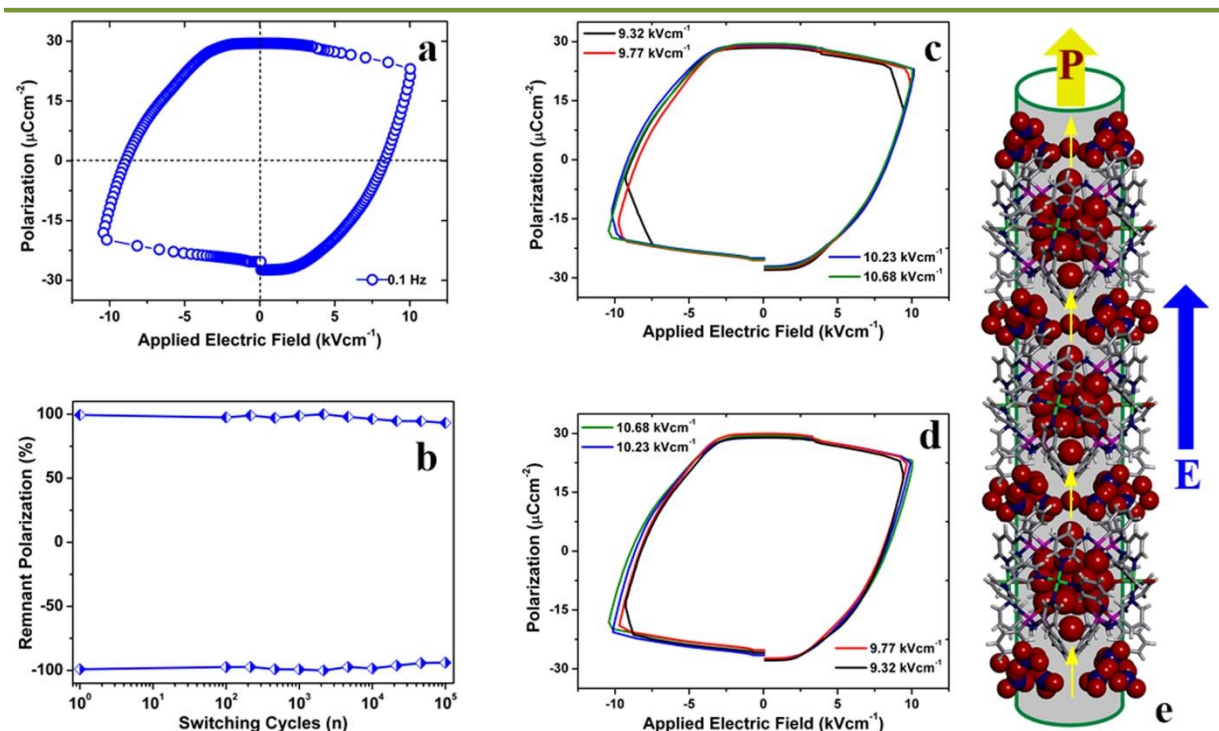


Figure 3.4: (a) Ferroelectric hysteresis loop of **4** and (b) its fatigue data up to 10^5 cycles at 1 Hz. (c) and (d) Evolution of the P-E loops of **4** at the various fields in the forward and backward sweeps, respectively. (e) Schematic depicting the ordering of the confined guest molecules under the external field.

Since the tetrameric cavitands in **4** and **5** exhibit a crystallographic ‘422’ nonpolar point group, the observed P-E loop hysteresis for **4** is thus believed to originate from the array of the encapsulated solvates at the intrinsic nano-channels (Figure 3.4e).⁴⁷ This observation can be supported by earlier studies on the ordered arrangement of polar solvents within the nanosized ensembles such as carbon nanotube, nanopore membranes and porous framework solids which have shown to induce ferroelectric polarization in presence of an external field.⁴⁸⁻⁵¹ This was verified by subjecting the sample of **4** to a forward electric field from 0.1 to 15 kVcm^{-1} which gave the P-E loops with a progressively improved shape and saturation polarization. A closer look at the P-E loops in the forward sweep between 9.32 and 10.68 kVcm^{-1} indicates that

the threshold field with which the dipoles in **4** can be completely aligned is attained at 10.68 kVcm^{-1} (Figure 3.4c). However, the shape and the polarization values of the P-E loops were retained in the backward sweep of the field until 9.32 kVcm^{-1} (Figure 3.4d). This implies that once the dipoles are fully aligned (at the threshold field), the maximum P_r and P_s values along with the shapes of the loops can be retained even at certain lower electric fields. Thus **4** exhibits electric field induced realignment of the dipoles that originates from the ordering of the polar guest-molecules. Such a behavior has been observed in certain ceramic and supramolecular ferroelectric materials as well.^{35,52,53} Dipole moment (ONIOM) calculations performed on the assembly of **4** show that almost 60% of the polarizable dipoles in **4** originates from the intrinsic guest solvates (Appendix A3.16). Similar P-E loop measurements could not be performed on **5** owing to the poor yields of its crystals in the absence of template guest molecules (vide infra). The reported P_r and E_c values of **4** are the best among the class of supramolecular compounds.^{23,54-60} The observed trend in the P_r and P_s values and the shape of the loops in **4** are reminiscent to that of TGS (though these values are much higher for **4**). This can be attributed to higher relaxation time necessary for the alignment of dipoles that are held together by weak interactions such as H-bonding. Such behavior is found to be common among several supramolecular ferroelectrics.⁶¹

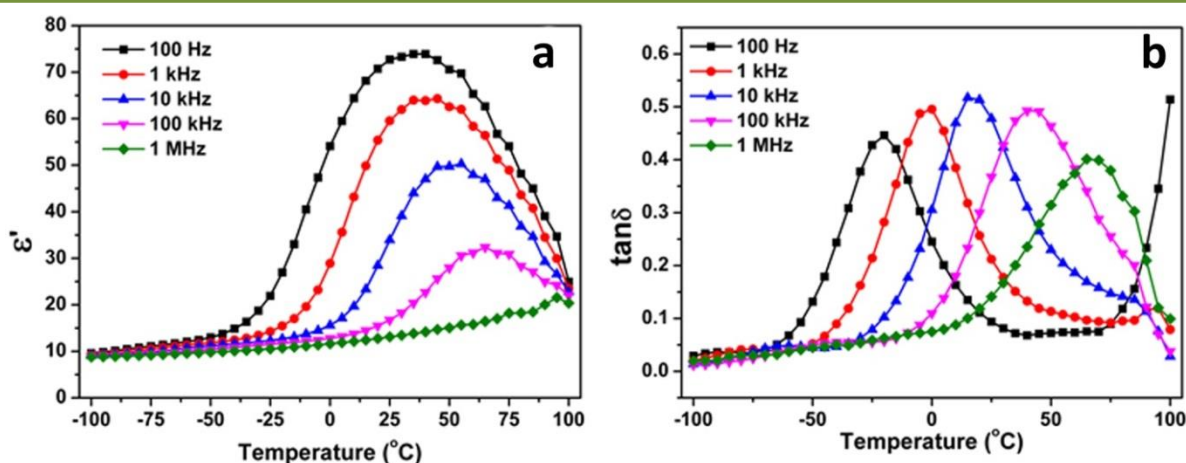


Figure 3.5: Temperature dependence of (a) the real part of dielectric constant and (b) dielectric loss of **4** at various frequencies showing the dielectric relaxation phenomenon.

The temperature dependent dielectric measurement on **4** at various frequencies gave an anomalous peak at 40 $^{\circ}\text{C}$ with a maximum ϵ' (real part of permittivity) value

of 73.9 at 100 Hz (Figure 3.5a). The broad feature of the anomaly peaks, at a relatively low-temperature, indicates the presence of desolvation-assisted phase transition in **4**. At higher frequencies, the broad anomalous peak was found to be slightly shifted to higher temperatures along with a decrease in the maxima of its ϵ' values. Such shift in peak intensities were observed for both ϵ'' (imaginary part of permittivity) and $\tan\delta$ (dielectric loss) parts as well with an opposite shift in its intensity maxima (Figure 3.5b and Appendix A3.18). These observations can be compared to the trend observed for typical relaxor materials^{62,63} and in the present instance it can be attributed to the desolvation assisted dielectric relaxation phenomenon. The differential scanning calorimetry (DSC) measurements on **4** gave no peaks in the temperature range of -50 to 100 °C which suggests that the observed broad dielectric anomaly peak does not corresponds to any phase (structural) transition, rather is associated with the release of solvates from **4**.

3.3.5 Ferroelectric and Dielectric Studies of {[Hy-A]cM₄} systems

Subsequent ferroelectric measurements on both {[Hy-A]c**4**} and {[Hy-A]c**5**} systems resulted in a well saturated rectangular P-E loops for almost all the host-guest assemblies (except for {[Hy-Na]c**4**})⁶⁴ with slight variation in their P_r and E_c values at 1 Hz (Figure 3.6a,b). From Figure 3.6a, it can be observed that there is a marginal decrease and increase in the P_r values for {[Hy-Li]c**4**} and {[Hy-Cs]c**4**}, respectively, whereas the E_c values were found to be showing values in an opposite trend for these two systems. The {[Hy-K]c**4**} and {[Hy-Rb]c**4**} systems show a nearly similar P_r and E_c values and lies in-between those of {[Hy-Li]c**4**} and {[Hy-Cs]c**4**} (Figure 3.6c). This signifies that the hardness and softness of the alkali-metal ions, which is related to the size and strength of their polarizability, plays a vital role in the alignment of their dipoles. Thus, the comparably higher E_c value for {[Hy-Li]c**4**} over **4** and other {[Hy-A]c**4**} systems can be attributed to the hardness of the Li^+ ion, which requires relatively higher fields to achieve the maximum polarization. However, the presence of softer K, Rb and Cs cations in **4** facilitates a swift polarization switching at relatively lower electric fields compared to [Hy-Li]c**4**. A similar trend can be observed for the {[Hy-A]c**5**} assemblies as well, albeit with a slightly less prominent shifts in their P_r and E_c values (Figure 3.6b,c). All these

observations corroborate the role of alkali-metal guest cations on the overall polarization of these systems.

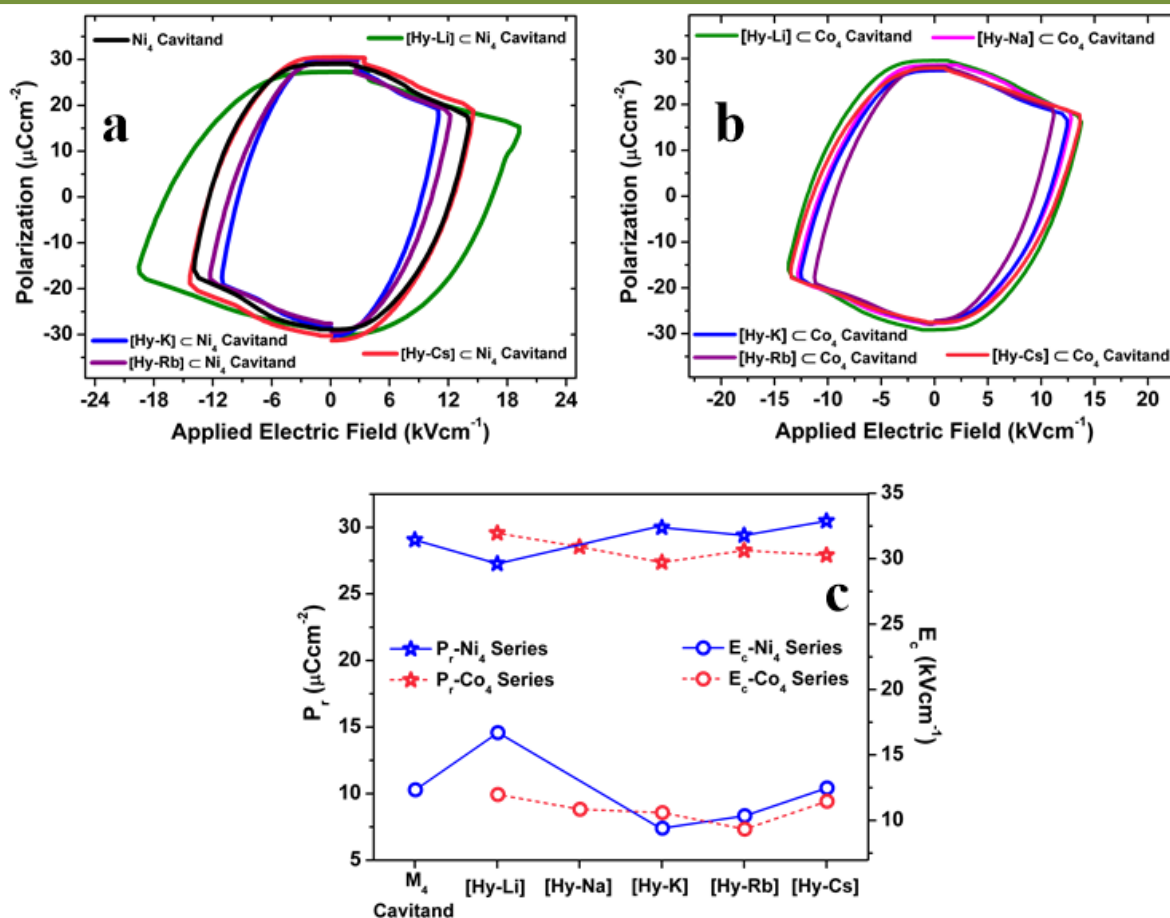


Figure 3.6: Ferroelectric P-E loops of (a) {[Hy-A]c₄} and (b) {[Hy-A]c₅} systems at 1 Hz and (c) the comparison of their P_r and E_c values.

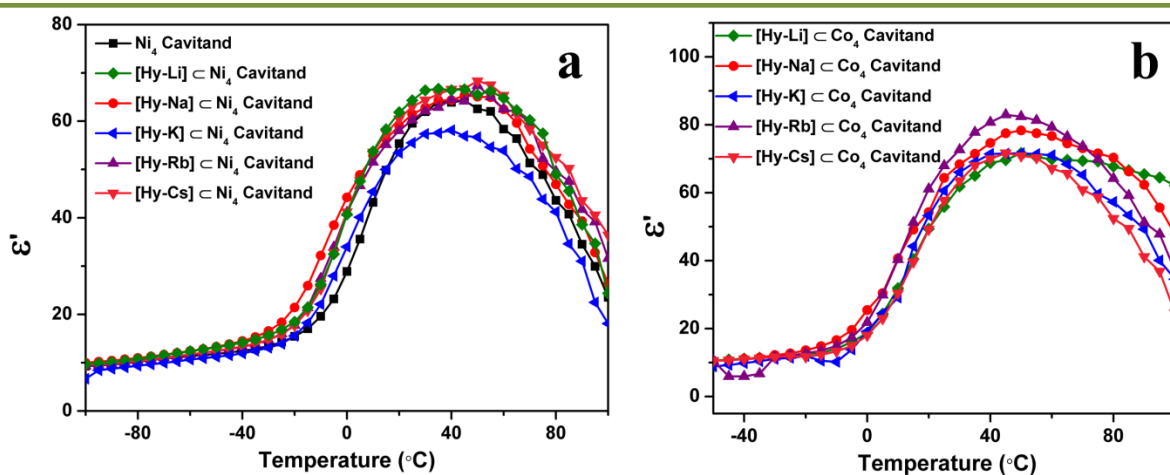


Figure 3.7: Temperature dependent real part of dielectric constants for (a) {[Hy-A]c_{Ni₄}} and (b) {[Hy-A]c_{Co₄}} systems at 1kHz.

To further check the effect of guest encapsulation on the polarization properties of the host-guest systems, the temperature dependent dielectric permittivity measurements were performed on all the {[Hy-A]c4} and {[Hy-A]c5} systems (Figure 3.7a,b and Appendix A3.19). Thus, all the guest-encapsulated systems of the Ni₄- and Co₄-series show nearly similar ε' values (within their series) at all the measured frequencies and the obtained values are comparable with that of 4. The dielectric anomaly peaks for the Ni₄- and Co₄-series were comparable to each other and ranges from 35 to 40 °C and their ε' values were ranging between 60 and 75 at 1 kHz.

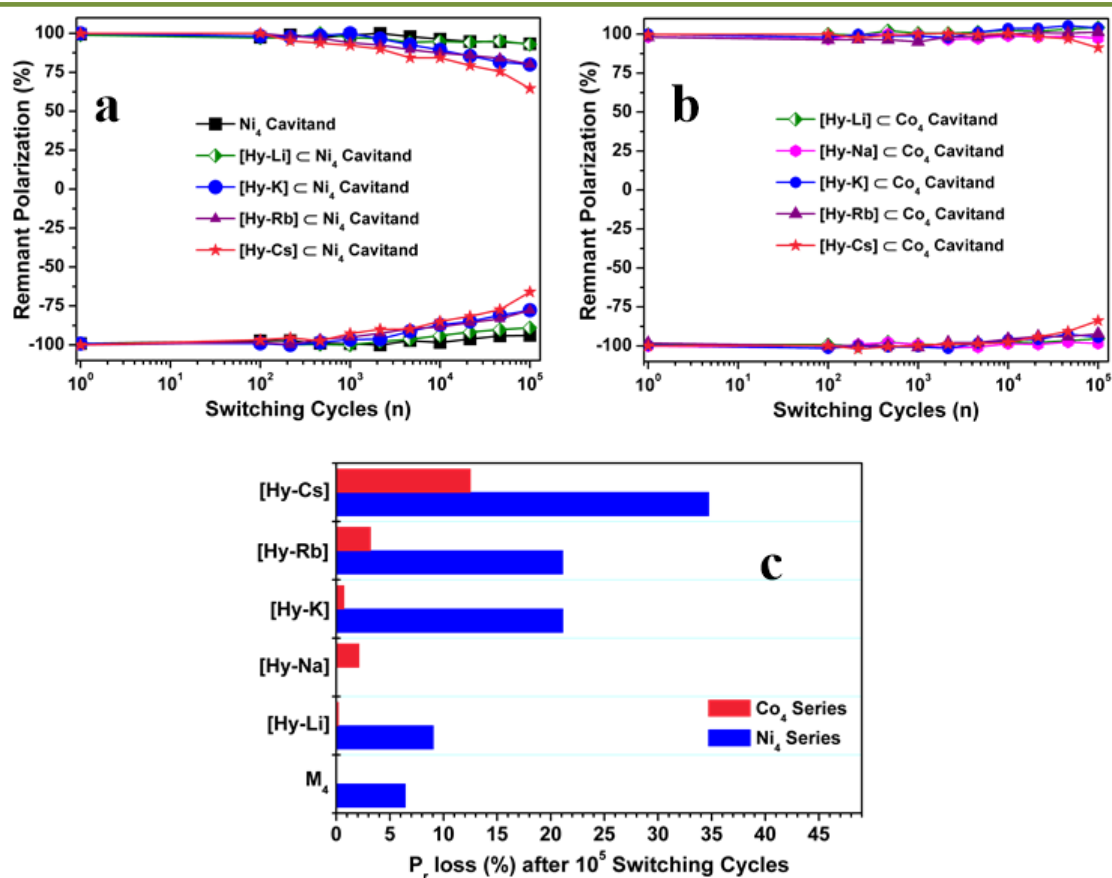


Figure 3.8: Ferroelectric fatigue data for all the (a) {[Hy-A]cNi₄} and (b) {[Hy-A]cCo₄} systems at 1 Hz and (c) the averaged P_r reduction values (%) after 10⁵ switching cycles.

The fatigue measurements showed an interesting trend, yet with a high P_r after 10⁵ cycles, for all these host-guest assemblies. Notably, for the Ni₄-series, the fatigue tolerance of the guest-encapsulated systems (except that of Li⁺), was found to decrease beyond 10⁴ cycles as the size of the alkali metal cation increases. The

fatigue studies of the Co_4 -series also show a very similar trend but with a less pronounced reduction in P_r at higher switching cycles. Interestingly from the Figure 3.8a and 3.8b, it can be observed that the Li^+ encapsulated systems, $\{[\text{Hy-Li}]<4\}$ and $\{[\text{Hy-Li}]<5\}$, exhibited the best fatigue resistant behavior among all of them. This shows that these assemblies can exhibit a longer polarization memory, once the smaller and hard Li^+ ions are polarized under an external electric field. The guest assemblies with the bigger (and soft) Cs^+ ions, $\{[\text{Hy-Cs}]<4\}$ and $\{[\text{Hy-Cs}]<5\}$, were the most fatigue prone systems as their respective P_r at 1 Hz have been pruned to 65% and 87% of the original values, after 10^5 cycles (Figure 3.8c). The reduction of polarization for the $[\text{Hy-Cs}]$ systems at higher cycles, despite the presence of polarizable Cs^+ ions, can be attributed to its size and compact fitting within the cavitand structure.

Thus the $[\text{Hy-Cs}]$ moieties, owing to their efficient host-guest complexation, may exhibit a restricted orientation for the switchable domains during the bipolar cycles. The other K^+ and Rb^+ encapsulated systems showed an intermediate fatigue tolerance among their series and again the Co_4 -derived systems showing a better retention of P_r in comparison with the Ni_4 -based systems (Figure 3.8c and Appendix A3.20). All these results suggest that the encapsulation of hydrated alkali metal ions at the intrinsic cavities exhibits a clear influence on the polarization attributes of the M_4 -cavitands. Also, from the shapes of the P-E loops and from the fatigue studies it can be gleaned that the Co_4 -cavitand of **5** provides a better and efficient platform over the Ni_4 -cavitand of **4** for an overall and robust polarization. In this context, it can be noted that change of metal ions have shown to alter the ferroelectric polarization in metal-formate based 3D-frameworks.⁶⁵ Thus, it is reasonable to visualize that the change of metal ions (both host and guest) has a clear influence on the overall polarization attributes of the $\{[\text{Hy-A}]<\mathbf{M}_4\}$ systems.

3.4 CONCLUSION

This work presents a comprehensive study on the ferroelectric behavior of a family of Ni_4L^1_8 and Co_4L^1_8 cavitands that are crystallized in the tetragonal symmetry. These cavitands are packed in a body-centered crystal lattice and show a non-covalently stacked 1D-columnar like structure for their intrinsic cavities. The inner space of these cavitands provides cuboctahedral pockets that host a series of hydrated alkali metal cations. The lighter Li^+ and Na^+ ions were disordered and exist as pentahydrates in distorted square pyramidal geometry. Also, this is the first instance for the observation of thermodynamically less favourable $[\text{Li}(\text{H}_2\text{O})_5]^+$ motifs. The heavier K^+ , Rb^+ and Cs^+ ions take up the general position and have highest hydration spheres of 8, 9 and 10 molecules of water, respectively. The observed highest coordination for these heavier cations can be attributed to the hydrophilic as well as the confinement effects of the voids. Ferroelectric measurement on **4** shows an excellent ferroelectric P-E hysteresis loop with a remnant polarization of $29.50 \mu\text{Ccm}^{-2}$. Remarkably, all the $\{[\text{Hy-A}]\subset\mathbf{M}_4\}$ systems were shown to retain the high polarization due to **4** with some variations in the P_r and E_c values. However, ferroelectric fatigue data obtained on all the $\{[\text{Hy-A}]\subset\mathbf{M}_4\}$ show sizable variations among these assemblies for the P_r values, after 10^5 switching cycles, that can be related to the differences in polarizability and size of the encapsulated cations. Thus, the $\{[\text{Hy-Li}]\subset\mathbf{5}\}$ assembly containing the least polarizable Li^+ ion exhibits the highest fatigue resistance while the $\{[\text{Hy-Cs}]\subset\mathbf{4}\}$ showing a drop of about 35% in the P_r value. These observations highlight the prominence of host-guest systems in the domain of ferroelectric materials and signify the effect of supramolecular interactions on the polarization attributes such as spontaneous polarization, coercive fields and fatigue tolerance. Ferroelectric supramolecules, owing to their facile synthesis, solution viability and low temperature processability, has an excellent prospect as a new class of materials for high-tech applications in the years to come. Such supramolecular ferroelectrics are envisioned to be worthwhile materials for fabricating flexible nanogenerators⁶⁶ and other energy harvesting systems.

3.5 REFERENCES

- (1) Lines, M. E.; Glass, A. M. *Principles and Applications of Ferroelectrics and Related Materials*; Oxford University Press: New York, **1977**.
- (2) Scott, J. F. *Ferroelectric memories*, Vol. 3; Springer Science & Business Media: Heidelberg, Germany, **2000**.
- (3) Uchino, K. *Ferroelectric Devices*, 2nd ed.; CRC Press: Boca Raton, FL, USA, **2009**.
- (4) Xu, Y. *Ferroelectric materials and their applications*; Elsevier: Amsterdam, **2013**.
- (5) Das, S.; Appenzeller, J. *Nano Lett.* **2011**, *11*, 4003-4007.
- (6) Whatmore, R. Ferroelectric Materials. In *Springer Handbook of Electronic and Photonic Materials*, Springer: **2007**; pp 597-623.
- (7) Scott, J. F. *Science* **2007**, *315*, 954-959.
- (8) Smolenskii, G. A.; Bokov, V. A.; Isupov, V. A.; Krainik, N. N.; Pasinkov, R. E.; Sokolov, I. A. *Ferroelectrics and Related Materials*; Gordon and Breach Science Publishers: New York, **1984**.
- (9) Ok, K. M.; Chi, E. O.; Halasyamani, P. S. *Chem. Soc. Rev.* **2006**, *35*, 710-717.
- (10) Zhang, Y.; Xie, M.; Roscow, J.; Bao, Y.; Zhou, K.; Zhang, D.; Bowen, C. R. *J. Mater. Chem. A* **2017**, *5*, 6569-6580.
- (11) Wan, C.; Bowen, C. R. *J. Mater. Chem. A* **2017**, *5*, 3091-3128.
- (12) Xie, M.; Dunn, S.; Boulbar, E. L.; Bowen, C. R. *Int. J. Hydrogen Energy* **2017** (In Press; DOI: 10.1016/j.ijhydene.2017.02.086).
- (13) Roscow, J.; Zhang, Y.; Taylor, J.; Bowen, C.R. *Eur. Phys. J. Special Topics* **2015**, *224*, 2949–2966.
- (14) Bowen, C. R.; Taylor, J.; LeBoulbar, E.; Zabek, D.; Chauhan, A.; Vaish, R. *Energy Environ. Sci.* **2014**, *7*, 3836–3856.
- (15) Chen, B.; Shi, J.; Zheng, X.; Zhou, Y.; Zhuc, K.; Priya, S. *J. Mater. Chem. A* **2015**, *3*, 7699-7705.
- (16) Fan, Z.; Sun, K.; Wang, J. *J. Mater. Chem. A* **2015**, *3*, 18809–18828.
- (17) Valasek, J. *Phys. Rev.* **1921**, *17*, 475-481.
- (18) Haertling, G. H. *J. Am. Ceram. Soc.* **1999**, *82*, 797-818.
- (19) Vanderah, T. A. *Science* **2002**, *298*, 1182-1184.
- (20) Furukawa, T., Date, M.; Fukada, E. *J. Appl. Phys.* **1980**, *51*, 1135–1141.
- (21) Furukawa, T. *Phase Trans.* **1989**, *18*, 143–211.

- (22) Tayi, A. S.; Kaeser, A.; Matsumoto, M.; Aida, T.; Stupp, S. I. *Nat. Chem.* **2015**, *7*, 281-294.
- (23) Horiuchi, S.; Tokura, Y. *Nat. Mater.* **2008**, *7*, 357-366.
- (24) Ghosh, S.; Sante, D. D.; Stroppa, A. *J. Phys. Chem. Lett.*, **2015**, *6*, 4553-4559.
- (25) Jain, P.; Ramachandran, V.; Clark, R. J.; Zhou, H. D.; Toby, B. H.; Dalal, N. S.; Kroto, H. W.; Cheetham, A. K. *J. Am. Chem. Soc.* **2009**, *131*, 13625-13627.
- (26) Zhang, W.; Xiong, R.-G. *Chem. Rev.* **2012**, *112*, 1163-1195.
- (27) Hang, T.; Zhang, W.; Ye, H.-Y.; Xiong, R.-G. *Chem. Soc. Rev.* **2011**, *40*, 3577-3598.
- (28) Zhang, W.; Ye, H.-Y.; Xiong, R.-G. *Coord. Chem. Rev.* **2009**, *253*, 2980-2997.
- (29) Li, P.-F.; Tang, Y.-Y.; Wang, Z.-X.; Ye, H.-Y.; You, Y.-M.; Xiong, R.-G. *Nat. Commun.* **2016**, *7*, 13635-366.
- (30) Shi, P.-P.; Tang, Y.-Y.; Li, P.-F.; Ye, H.-Y.; Xiong, R.-G. *J. Am. Chem. Soc.* **2017**, *139*, 1319-1324.
- (31) Tang, Y.-Y.; Zhang, W.-Y.; Li, P.-F.; Ye, H.-Y.; You, Y.-M.; Xiong, R.-G. *J. Am. Chem. Soc.* **2016**, *138*, 15784-15789.
- (32) Ye, H.-Y.; Ge, J.-Z.; Tang, Y.-Y.; Li, P.-F.; Zhang, Y.; You, Y.-M.; Xiong, R.-G. *J. Am. Chem. Soc.* **2016**, *138*, 13175-13178.
- (33) Di Sante, D.; Stroppa, A.; Jain, P.; Picozzi, S. *J. Am. Chem. Soc.* **2013**, *135*, 18126-18130.
- (34) Stroppa, A.; Sante, D. D.; Barone, P.; Bokdam, M.; Kresse, G.; Franchini, C.; Whangbo, M.-H.; Picozzi, S. *Nat. Commun.* **2014**, *5*, 5900.
- (35) Akutagawa, T.; Koshinaka, H.; Sato, D.; Takeda, S.; Noro, S.-I.; Takahashi, H.; Kumai, R.; Tokura, Y.; Nakamura, T. *Nat. Mater.* **2009**, *8*, 342-347.
- (36) Fu, D.-W.; Zhang, W.; Cai, H.-L.; Zhang, Y.; Ge, J.-Z.; Xiong, R.-G.; Huang, S. D. *J. Am. Chem. Soc.* **2011**, *133*, 12780-12786.
- (37) Srivastava, A. K.; Divya, P.; Praveenkumar, B.; Boomishankar, R. *Chem. Mater.* **2015**, *27*, 5222-5229.
- (38) Srivastava, A. K.; Praveenkumar, B.; Mahawar, I. K.; Divya, P.; Shalini, S.; Boomishankar, R. *Chem. Mater.* **2014**, *26*, 3811-3817.
- (39) Boomishankar, R.; Srivastava, A. K. *Phosphorus, Sulfur, and Silicon and the Related Elements* **2016**, *191*, 618-623.
- (40) Sheldrick, G. M. *Acta Crystallogr. C* **2015**, *71*, 3-8.

- (41) Frisch, M.; Trucks, G.; Schlegel, H. *GAUSSIAN 03, Revision B. 05*, Gaussian Inc., Wallingford, CT, **2004**.
- (42) Pye, C. C. *Int. J. Quantum Chem.* **2000**, *76*, 62-76.
- (43) Mähler, J.; Persson, I. *Inorg. Chem.* **2012**, *51*, 425-438.
- (44) Ikeda, T.; Boero, M. *J. Chem. Phys.* **2012**, *137*, 041101.
- (45) Pichierri, F. *Dalton. Trans.* **2013**, *42*, 6083-6091.
- (46) Law, C. W.; Tong, K. Y.; Li, J. H.; Li, K. *Solid-State Electron.* **2000**, *44*, 1569-1571.
- (47) Pan, L.; Liu, G.; Li, H.; Meng, S.; Han, L.; Shang, J.; Chen, B.; Platero-Prats, A. E.; Lu, W.; Zou X.; Li, R.-W. *J. Am. Chem. Soc.* **2014**, *136*, 17477-17483.
- (48) Zhao, H.-X.; Kong, X.-J.; Li, H.; Jin, Y.-C.; Long, L.-S.; Zeng, X. C.; Huang, R.-B.; Zheng, L.-S. *Proc. Natl. Acad. Sci. U.S.A.* **2011**, *108*, 3481-3486.
- (49) Menzl, G.; Köfinger, J.; Dellago, C. *Phys. Rev. Lett.* **2012**, *109*, 020602.
- (50) Luo, C.-F.; Fa, W.; Zhou, J.; Dong, J.-M.; Zeng, X.-C. *Nano Lett.* **2008**, *8*, 2607-2612.
- (51) Dong, X.-Y.; Li, B.; Ma, B.-B.; Li, S.-J.; Dong, M.-M.; Zhu, Y.-Y.; Zang, S.-Q.; Song, Y.; Hou, H.-W.; Mak, T. C. W. *J. Am. Chem. Soc.* **2013**, *135*, 10214-10217.
- (52) Harada, J.; Shimojo, T.; Oyamaguchi, H.; Hasegawa, H.; Takahashi, Y.; Satomi, K.; Suzuki, Y.; Kawamata, J.; Inabe, T. *Nat. Chem.* **2016**, *8*, 946-952.
- (53) Ke, Q.; Lu, W.; Huang, X.; Wang, J. *J. Electrochem. Soc.* **2012**, *159*, G11-G14.
- (54) Horiuchi, S.; Tokunaga, Y.; Giovannetti, G.; Picozzi, S.; Itoh, H.; Shimano, R.; Kumai, R.; Tokura, Y. *Nature* **2010**, *463*, 789-792.
- (55) Noda, K.; Ishida, K.; Kubono, A.; Horiuchi, T.; Yamada, H.; Matsushige, K. *J. Appl. Phys.* **2003**, *93*, 2866-2870.
- (56) Szafranski, M.; Katrusiak, A.; McIntyre, G. J. *Phys. Rev. Lett.* **2002**, *89*, 215507.
- (57) Hoshino, S.; Mitsui, T.; Jona, F.; Pepinsky, R. *Phy. Rev.* **1957**, *107*, 1255.
- (58) Szafranski, M. *J. Phys. Chem. B* **2011**, *115*, 8755-8762.
- (59) Fu, D.-W.; Cai, H.-L.; Liu, Y.; Ye, Q.; Zhang, W.; Zhang, Y.; Chen, X.-Y.; Giovannetti, G.; Capone, M.; Li, J.; Xiong, R. G. *Science* **2013**, *339*, 425-428.
- (60) Fu, D. W.; Zhang, W.; Cai, H. L.; Ge, J. Z.; Zhang, Y.; Xiong, R. G. *Adv. Mater.* **2011**, *23*, 5658-5662.
- (61) Ma, H.; Gao, W.; Wang, J.; Wu, T.; Yuan, G.; Liu, J.; Liu, Z. *Adv. Electron. Mater.* **2016**, *2*, 1600038.
- (62) Cross, L. E. Relaxor Ferroelctrics. In *Piezoelectricity: evolution and future of a technology*. Vol. 114; Springer Science & Business Media: **2008**; pp 131-155.

(63) Bokov, A. A.; Ye, Z.-G. *J. Adv. Dielectr.* **2012**, *2*, 1241010–1-24.

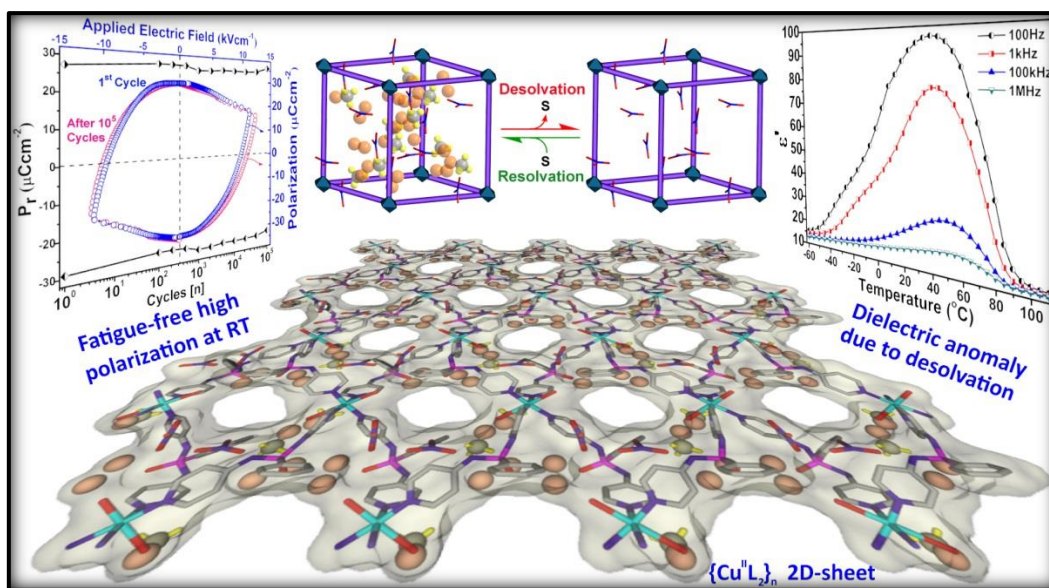
(64) The [[Hy-Na]₄] did not give a well-saturated loop and hence it is not included in any of the ferroelectric related discussions.

(65) Xu, G.-C.; Zhang, W.; Ma, X.-M.; Chen, Y.-H.; Zhang, L.; Cai, H.-L.; Wang, Z.-M.; Xiong, R.-G.; Gao, S. *J. Am. Chem. Soc.* **2011**, *133*, 14948–14951.

(66) Fan, F. R.; Tang, W.; Wang, Z. L. *Adv. Mater.* **2016**, *28*, 4283–4305.

End of Chapter 3

Chapter 4



**Potentially Ferroelectric $\{Cu^{II}L_2\}_n$
Based 2D-Framework Exhibiting
High Polarization and Guest-
Assisted Dielectric Anomaly**

4.1 Introduction

Materials having ferroelectric, multi-ferroic and magnetoelectric properties are of tremendous research interest owing to their application in high-technique devices.¹⁻⁷ Particularly ferroelectric materials, characterized by switchable electric polarization, are very attractive for their utility in non-volatile computing devices, capacitors, micro-electro mechanical systems (MEMS), semi-conductor chips, field-effect transistors (FETs), tele-communication signal processing units, ultra-sonic medical imaging devices and nonlinear optical devices.⁸⁻²¹ Traditionally, ceramic materials of perovskite family, for example barium titanate (BTO) and lead zirconate titanate (PZT) are used as commercial ferroelectrics.²²⁻²⁷ However, certain limitations such as high temperature processing, higher molecular weight, high content of toxic and expensive heavier metals etc. triggered the search for alternate sources of ferroelectric materials.²⁸ In this effort, a range of new age materials viz., polymers, organic-inorganic hybrids, small molecules and liquid crystals have been explored for ferroelectric and multi-ferroic applications.²⁹⁻⁵⁰ Currently, ferroelectric behavior in metal-organic materials are widely been examined due to their simple synthesis, flexibility and low-temperature fabrication techniques.^{51,52} Moreover, the structural components of the metal-organic assemblies namely, metal ions, coordinating ligands, counter anions and the guest molecules provide a handle in imparting the required symmetry (polar point group) as well as tuning their ferroelectric behavior.^{53,54} As discussed in chapter 1, we have synthesized a family of anion driven $[\text{Cu}^{\text{II}}\text{L}_2]_n$ coordination assemblies in discrete (centrosymmetric) and helical 1D-polymeric (noncentrosymmetric) structures, starting from a flexible phosphoramidate ligand ($\text{L}^1 = \text{PhPO}(\text{NH}^3\text{Py})_2$; $^3\text{Py} = 3\text{-pyridyl}$). Interestingly, the presence of perchlorate or nitrate anions in the packing cavities of the 1D-helical assemblies played a major role in tuning their ferroelectric behavior.⁵⁵ Inspired by these observations, we set out to explore the family of ferroelectric materials based on $[\text{Cu}^{\text{II}}\text{L}_2]_n$ assemblies by tuning various parameters. Specifically, I aimed at monitoring the change in structural topologies of $[\text{Cu}^{\text{II}}\text{L}_2]_n$ frameworks with subtle variations in the peripheral N-donor functionalities in phenyl phosphoric diamide backbone. Herein, I report the synthesis of two new assemblies, **6** ($\{[\text{CuL}_2^2(\text{H}_2\text{O})_2] \cdot (\text{NO}_3)_2 \cdot (\text{H}_2\text{O})_{1.5} \cdot (\text{CH}_3\text{OH})\}_\infty$) and **7** ($[\text{CuL}_2^3] \cdot (\text{NO}_3)_2$) based on the

phosphoramidate ligands $[PhPO(NH^4Py)_2]$ (L^2) and $[PhPO(NH^2Py)_2]$ (L^3), respectively. The compound **6** exhibits a noncentrosymmetric 2D-polymeric structure, while **7** was obtained as a centrosymmetric discrete mononuclear complex. Ferroelectric measurements on **6** gave a high remnant polarization (P_r) value of $\sim 28 \mu Ccm^{-2}$ at room temperature, which is the highest among all known metal-organic ferroelectric materials and is closely comparable with BTO. Temperature dependent dielectric measurements on **6** show an interesting dielectric anomaly peak $\sim 40^\circ C$ due to desolvation indicating that the solvated molecules in the packing structure affects its overall polarization.

4.2 EXPERIMENTAL SECTION

4.2.1 General Remarks

All manipulations involving phosphorus halides were performed under dry nitrogen atmosphere in standard Schlenk-glassware; toluene was dried over sodium. The 4-Aminopyridine and 2-Aminopyridine were purchased from Aldrich and used as received. $PhPOCl_2$ and $Cu(NO_3)_2 \cdot 3H_2O$ were purchased from Acros-Organics and Merck, respectively, and used as received. NMR spectra were recorded on a Jeol 400 MHz spectrometer (1H NMR: 400.13 MHz, $^{13}C\{^1H\}$ NMR: 100.62 MHz, $^{31}P\{^1H\}$ NMR: 161.97 MHz) at room temperature using $SiMe_4$ (1H , ^{13}C) and 85% H_3PO_4 (^{31}P). The MALDI-TOF spectra were obtained on an Applied Biosystem MALDI-TOF/TOF spectrometer. The powder X-ray diffraction (PXRD) data were obtained from a Bruker-D8 Advance diffractometer. Thermal gravimetric analysis (TGA) data has been obtained from a Perkin-Elmer STA-6000 thermogravimetric analyzer. Polarized light microscope images of the crystals were recorded by using a LEICA DM2500P microscope equipped with Linkam TMS 94 heating stage. Elemental analyses were performed on a Vario-EL cube elemental analyzer. FT-IR spectra were taken on a Perkin Elmer spectrophotometer with samples prepared as KBr pellets. FT-IR in Attenuated total reflectance (ATR) mode was taken on neat samples on Bruker Alpha Spectrophotometer. Melting points were obtained using an Electro thermal melting point apparatus and were uncorrected.

4.2.2 Synthesis

4.2.2.1 Synthesis of ligand [PhPO(NH⁴Py)₂] (L²): To a well stirred suspension of 4-Aminopyridine (11.756 g, 125 mmol) in chloroform (~200 ml) at 0 °C, PhPOCl₂ (2.5 ml, 3.475 g, 17.82 mmol) in 10 ml chloroform was added drop wise. The reaction mixture was refluxed for 6 h and the obtained residue was filtered and washed 3 times with water. This was then dried in a vacuum desiccator and collected. Rod-like colorless crystals suitable for single crystal X-ray diffraction (SCXRD) analysis were obtained from its MeCN solution after 4-5 days. Yield: 84% (4.66 g), based on P. M.P.: 195-200 °C. ¹H-NMR (400 MHz, (CD₃)₂SO): δ 3.28 (m, 2H, NH), 7.14 (m, 4H, CH(pyridyl)), 7.61 (m, 3H, CH(phenyl)), 7.91 (m, 2H, CH(phenyl)), 8.2 (m, 4H, CH(pyridyl)). ¹³C-NMR (100 MHz, (CD₃)₂SO): δ 112.97, 129.18, 132.08, 133.11, 149.48, 150.59. ³¹P-NMR (162 MHz, {(CD₃)₂SO}): δ 11.79. FT-IR data in KBr pellet (cm⁻¹): 3485, 1611, 1571, 1506, 1467, 1409, 1332, 1274, 1180, 1120, 1067, 926, 827, 756, 689, 661, and 520. ESI-MS = 311.1057 [{PhPO(NH⁴Py)₂]+H]⁺; 217.0527 [PhPO(NH⁴Py)]⁺. Anal. Calcd. for C₁₆H₁₅N₄OP: C, 61.93; H, 4.87; N, 18.06. Found: C, 61.75; H, 4.91; N, 17.99.

4.2.2.2 Synthesis of ligand [PhPO(NH²Py)₂] (L³): To a stirred solution of 2-Aminopyridine (11.756 g, 125 mmol) in toluene (~200 ml) at 0 °C, PhPOCl₂ (2.5 ml, 3.475 g, 17.82 mmol) in 10 ml toluene was added drop wise. The reaction mixture was refluxed for 4 h and the obtained residue was filtered and washed 3-4 times with water. This was then dried in a vacuum desiccator and collected. Regular shaped colorless crystals suitable for SC-XRD analysis were obtained from its solution in MeOH/MeCN after 2-3 days. Yield: 92% (5.08 g), based on P. M.P.: 220°C. ¹H-NMR (400 MHz, (CD₃)₂SO): δ 6.86 (m, 2H, CH(pyridyl)), 7.06 (m, 2H, CH(pyridyl)), 7.48 (m, 2H, CH(phenyl)), 7.54 (m, 1H, CH(phenyl)), 7.59 (m, 2H, CH(phenyl)), 7.91 (m, 2H, CH(pyridyl)), 8.12 (m, 2H, CH(pyridyl)), 8.67 (s, 2H, NH). ¹³C-NMR (100 MHz, (CD₃)₂SO): δ 111.77, 116.80, 128.71, 132.06, 134.40, 138.32, 148.13, 155.08. ³¹P-NMR (162 MHz, {(CD₃)₂SO}): δ 8.62. FT-IR data in KBr pellet (cm⁻¹): 3467, 1589, 1481, 1379, 1201, 1129, 1057, 939, 824, 721, 685, 659, and 514. ESI-MS = 311.1049 [{PhPO(NH²Py)₂]+H]⁺; 217.0522 [PhPO(NH²Py)]⁺. Anal. Calcd. for C₁₆H₁₅N₄OP: C, 61.93; H, 4.87; N, 18.06. Found: C, 62.03; H, 4.87; N, 17.87.

4.2.2.3 Synthesis of compound ($\{[\text{Cu}(\text{L}^2)_2(\text{H}_2\text{O})_2] \cdot (\text{NO}_3)_2 \cdot (\text{H}_2\text{O})_{1.5} \cdot (\text{CH}_3\text{OH})\}_\infty$) (6):

To a stirred and filtered solution of L^2 (62 mg, 0.2 mmol) in MeOH (3 ml), water (3 ml) was layered carefully, followed by a careful layer of solution of $\text{Cu}(\text{NO}_3)_2 \cdot 3\text{H}_2\text{O}$ (24.5 mg, 0.1 mmol) in MeOH (3 ml). The resultant mixture was then kept undisturbed at RT in a screw capped vial. Blue crystals of **6** suitable for SCXRD analysis were recovered after 4-5 weeks. Yield: 41% (37 mg), based on Cu. FT-IR data in KBr pellet (cm^{-1}): 3488, 1615, 1577, 1509, 1384, 1333, 1293, 1214, 1124, 1066, 1024, 933, 838, 756, 694, 662, and 521. Anal. Calcd. for $\text{C}_{33}\text{H}_{41}\text{N}_{10}\text{O}_{12.5}\text{P}_2\text{Cu}$: C, 43.88; H, 4.58; N, 15.51. Found: C, 43.75; H, 4.71; N, 15.52.

4.2.2.4 Synthesis of compound ($\{[\text{Cu}(\text{L}^3)_2] \cdot (\text{NO}_3)_2$ (7):

To a gently heated stirred solution of L^3 (62 mg, 0.2 mmol) in MeOH (3 ml) and MeCN (2 ml), $\text{Cu}(\text{NO}_3)_2 \cdot 3\text{H}_2\text{O}$ (24.1 mg, 0.1 mmol) in MeOH (5 ml) was added. The blue solution was then filtered through a thick pad of celite and left for crystallization at RT. Blue crystals of **7** suitable for SCXRD analysis were obtained within 2-3 weeks. Yield: 52% (21 mg), based on Cu. FT-IR data in KBr pellet (cm^{-1}): 1607, 1581, 1507, 1468, 1383, 1270, 1193, 1125, 1061, 1025, 945, 805, 691, 621, 519 and 501. Anal. Calcd. for $\text{C}_{32}\text{H}_{30}\text{CuN}_{10}\text{O}_8\text{P}_2$: C, 47.56; H, 3.74; N, 17.33. Found: C, 47.49; H, 3.69; N, 17.27.

4.2.2.5 Synthesis of compound $6_{\text{desolvated}}$: This was obtained by heating **6** at 60 °C under vacuum for 12 hours. The formation of the desolvated phase of **6** was confirmed by PXRD and TGA analysis.

4.2.2.6 Synthesis of compound $6_{\text{resolvated}}$: This was obtained by the exposure of $6_{\text{desolvated}}$ to the mixture of MeOH and water vapours inside a screw-capped vial. Rapid formation of $6_{\text{resolvated}}$ can be observed upon adding few drops of the mother liquor of **6** to a sample of $6_{\text{desolvated}}$.

4.2.3 Crystallography

Reflections were collected on a Bruker Smart Apex Duo diffractometer at 100 K using $\text{MoK}\alpha$ radiation ($\lambda = 0.71073 \text{ \AA}$) for L^2 , L^3 , **6**, **6_sq** and **7**. Structures were refined by full-matrix least-squares against F^2 using all data (SHELX).⁵⁶ Crystallographic data for all these compounds are listed in Table 4.1. All non-hydrogen atoms were refined anisotropically if not stated otherwise. Hydrogen atoms

were constrained in geometric positions to their parent atoms. Crystals of L^2 was weakly diffracting at higher angles and hence a $2\theta = 50^\circ$ cutoff was applied. Two nitrate anions and two phenyl rings in **6** was thermally disordered.

Table 4.1: Details of crystallographic data collection and structure refinements for L^2 , L^3 , **1_sq, **1** and **2****

Compound	$\text{L}^2 \cdot \text{H}_2\text{O}$	L^3	6_sq
Chemical formula	$\text{C}_{16}\text{H}_{17}\text{N}_4\text{O}_2\text{P}$	$\text{C}_{16}\text{H}_{15}\text{N}_4\text{OP}$	$\text{C}_{32}\text{H}_{34}\text{CuN}_{10}\text{O}_{10}\text{P}_2$
Formula weight	328.31	310.29	844.17
Temperature	100(2)K	100(2) K	100(2) K
Crystal system	Monoclinic	Triclinic	Monoclinic
Space group	C2/c	P-1	Cc
a (Å); α (°)	19.594(10); 90	8.433(3); 80.921(7)	25.688(5); 90
b (Å); β (°)	8.739(4); 99.234(12)	9.174(4); 80.814(7)	12.212(3); 127.862(3)
c (Å); γ (°)	18.853(10); 90	10.074(4); 89.836(8)	17.076(7); 90
V (Å ³); Z	3186(3); 8	759.6(5); 2	4229(2); 4
ρ (calc.) mg m ⁻³	1.369	1.357	1.326
μ mm ⁻¹	0.188 (Mo K α)	0.188 (Mo K α)	0.654 (Mo K α)
$2\theta_{\text{max}}$ (°)	50	57	56
R(int)	0.0397	0.0284	0.1005
Completeness to θ	99.6 %	99.0 %	99.6 %
Data / param.	2825 / 214	3862 / 199	9555 / 406
GOF	1.052	1.058	0.894
R1 [F>4 σ (F)]	0.0320	0.0383	0.0992
wR2 (all data)	0.0854	0.1072	0.2980
max. peak/hole (e.Å ⁻³)	0.308 / -0.386	0.357 / -0.492	1.315 / -0.823

Compound	6	7
Chemical formula	$\text{C}_{33}\text{H}_{41}\text{CuN}_{10}\text{O}_{12.5}\text{P}_2$	$\text{C}_{32}\text{H}_{30}\text{CuN}_{10}\text{O}_8\text{P}_2$
Formula weight	903.24	808.14
Temperature	100(2) K	100(2)K
Crystal system	Monoclinic	Tetragonal
Space group	Cc	I4(1)/a
a (Å); α (°)	25.688(5); 90	23.781(5); 90
b (Å); β (°)	12.212(3); 127.862(3)	23.781(5); 90
c (Å); γ (°)	17.076(7); 90	11.844(3); 90
V (Å ³); Z	4229(2); 4	6698(4); 8
ρ (calc.) mg m ⁻³	1.419	1.603
μ mm ⁻¹	0.663 (Mo K α)	0.817 (Cu K α)
$2\theta_{\text{max}}$ (°)	56	57
R(int)	0.1154	0.1293
Completeness to θ	99.6 %	100 %
Data / param.	9555 / 435	4181 / 241
GOF	1.044	1.005
R1 [F>4 σ (F)]	0.1103	0.0436
wR2 (all data)	0.3448	0.1003
max. peak/hole (e.Å ⁻³)	1.450 / -1.082	0.413 / -0.476

Atom positions of the disordered groups were freely refined isotropically over two positions using similar distances and similar U-restraints. The solvate methanol and water molecules in **6** were disordered, hence were treated as diffuse contributions to the overall scattering and removed by the SQUEEZE/PLATON for a better refinement data (in case of **6_sq**). The exact amount of the solvate water molecules were further confirmed by TGA data. The refinement parameter in **6** was slightly higher owing to the diffuse nature of the solvated crystals. Unit cell parameters for **6** at 40 °C were obtained on a Bruker D8 Venture diffractometer with Microfocus X-ray source and photon detector after heating the single crystal under hot N₂ flow for 24h. However, the weak reflections were not sufficient enough to yield an acceptable structure.

4.2.4 Ferroelectric and Dielectric measurements

In order to determine the dielectric and ferroelectric properties, the powdered samples of **6** and **7** were compacted in the form of discs (of approximately 10 mm diameter and 1 mm thickness). The compacted discs were subsequently electroded using aluminium adhesive foils for both ferroelectric and dielectric measurements. The dielectric characteristics for **6** and **7** were measured using the Novocontrol, Dielectric Spectrometer.

The ferroelectric hysteresis loops in **6** were measured by using Sawyer-Tower circuit. The measurements pertaining to polarization and fatigue cycles were recorded using hysteresis loop analyser (TF Analyser 2000, aixACCT Germany). Leakage current was measured dynamically for various voltage steps during the hysteresis loop measurements.

4.3 RESULTS AND DISCUSSION

4.3.1 Syntheses

The phosphoric diamide Ligands L² and L³ were synthesized by reacting PhPOCl₂ with 4- and 2-aminopyridine, respectively. The ligands L² and L³ were characterized by mass spectra, ¹H-, ¹³C- and ³¹P-NMR spectroscopy and single crystal X-ray diffraction techniques (Figures 4.1-4.2 and Appendices A4.1-A4.6). The 2D-

coordination polymer **6** ($\{[Cu(L^2)_2(H_2O)_2] \cdot (NO_3)_2 \cdot (H_2O)_{1.5} \cdot (CH_3OH)\}_\infty$) was isolated as blue colored crystals in a 2:1 reaction mixture involving L^2 and $Cu(NO_3)_2$ in MeOH/ H_2O medium at room temperature. The mononuclear complex **7** was prepared in a similar 2:1 reaction of L^3 with $Cu(NO_3)_2$ in MeOH/MeCN medium at room temperature (Scheme 4.1).

Scheme 4.1: Synthesis of compound **6** and **7**.

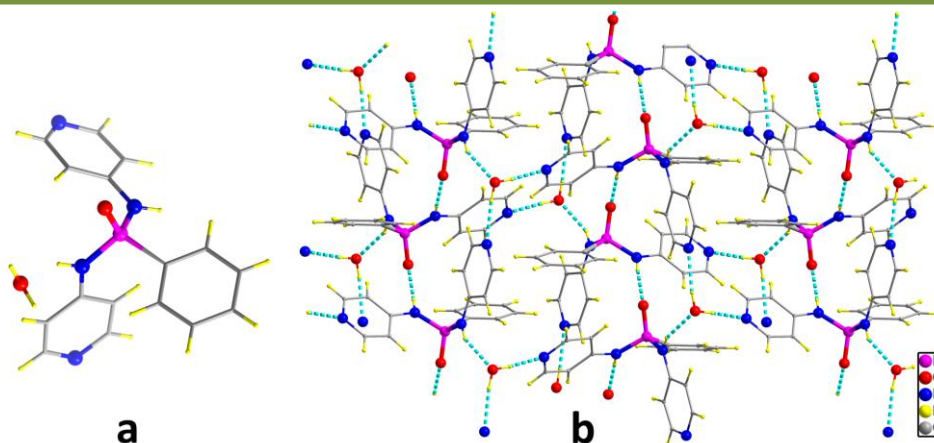
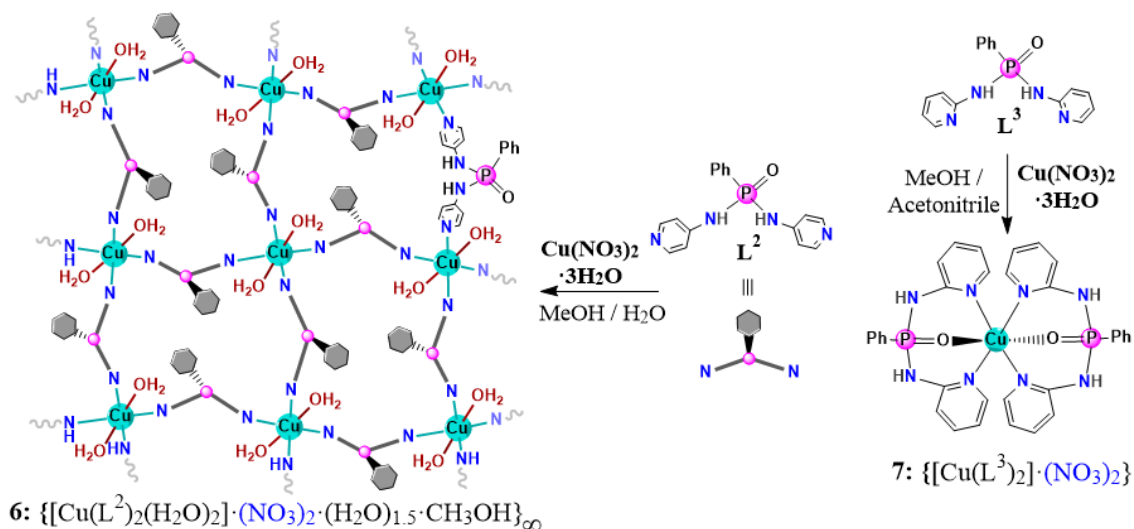


Figure 4.1: a) Crystal Structure of ligand L^2 . (b) View of the Hydrogen-bonding in L^2 .

4.3.2 Crystal Structures

The molecular structure of L^2 was solved in the monoclinic space group $C2/c$. It consists of two amino pyridyl moieties, one phenyl group and one phosphoryl oxygen around the central P-atom (Figure 4.1a). The ligand L^2 exhibits 2D-structure mediated by $N-H \dots N_{pyridyl}$ and $N-H \dots O_{phosphoryl}$ hydrogen bonding interactions, where

both the pyridyl N-donor sites and the phosphoryl oxygen participate in hydrogen bonding (Figure 4.1b).

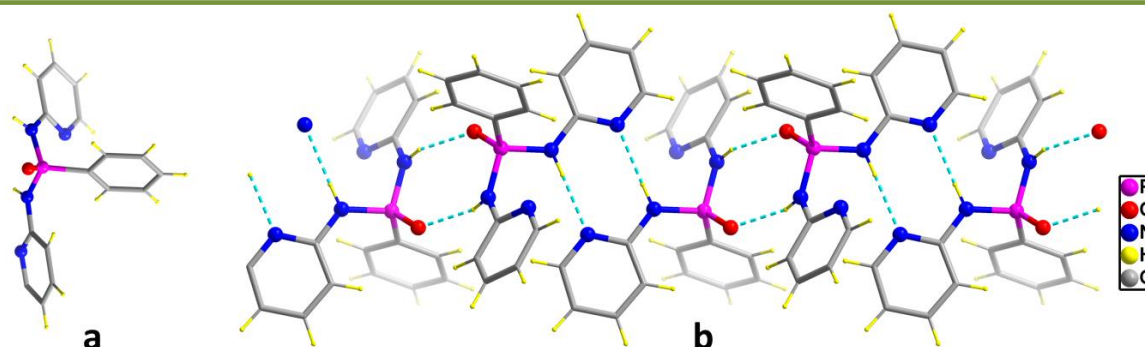


Figure 4.2: a) Crystal Structure of ligand L^3 . (b) View of the Hydrogen-bonding in L^3 .

The molecular structure of L^3 was solved in the monoclinic space group $P-1$. It consists of two amino pyridyl moieties, one phenyl group and one phosphoryl oxygen around the central P-atom (Figure 4.2a). The ligand L^3 shows rich intermolecular hydrogen bonding. Figure 4.2b displays the formation of a zig-zag 1D-chain structure mediated by $\text{N-H}\dots\text{N}_{\text{pyridyl}}$ and $\text{N-H}\dots\text{O}_{\text{phosphoryl}}$ hydrogen bonding interactions. One of the pyridyl N-donor sites in L^3 doesn't have an H-bonding partner and hence remains non-interacting.

The crystal structure of **6** was solved in the monoclinic non-centric polar space group Cc , point group 'm' and point group symmetry ' C_s ' (Table 4.1). The asymmetric unit consists of a Cu(II) ion, two ligand motifs, two charge-balancing (non-coordinating) nitrate ions disordered over four positions, two coordinated water molecules and solvated molecules of methanol and water (Appendix A4.7). The molecular structure of **6** consists of a cationic 2D-polymeric structure of composition $\{[\text{Cu}^{\text{II}}(\text{L}^2)_2(\text{H}_2\text{O})_2]^{2+}\}_n$ (Figure 4.3a). The Cu(II) ions are located in a distorted octahedral environment with four $\text{N}_{\text{pyridyl}}$ contacts from four different ligand units and two coordinated water molecules. Each ligand motif acts as a bridge between two Cu(II) centers and is part of two 48-membered Cu_4L^2_4 macrocycles. Thus, the cationic $[\text{Cu}^{\text{II}}(\text{L}^2)_2]_n$ network in **6** consists of a contiguous array of Cu_4L^2_4 edge-shared macrocycles in which the Cu(II) ions acts as the corner atoms (Figure 4.3b). Two unique Cu...Cu distances have been found within each macrocycle, 12.107 and 11.617 Å, owing to two crystallographically unique ligand scaffolds. The diagonal Cu...Cu distances in these

macrocycles vary by a large margin with the longer one having a distance of 20.32(4) Å and the shorter one is at 12.21(2) Å. The inter-layer distance in **6** is in the range between 8.51(3) and 9.04(5) Å (Appendix A4.8).

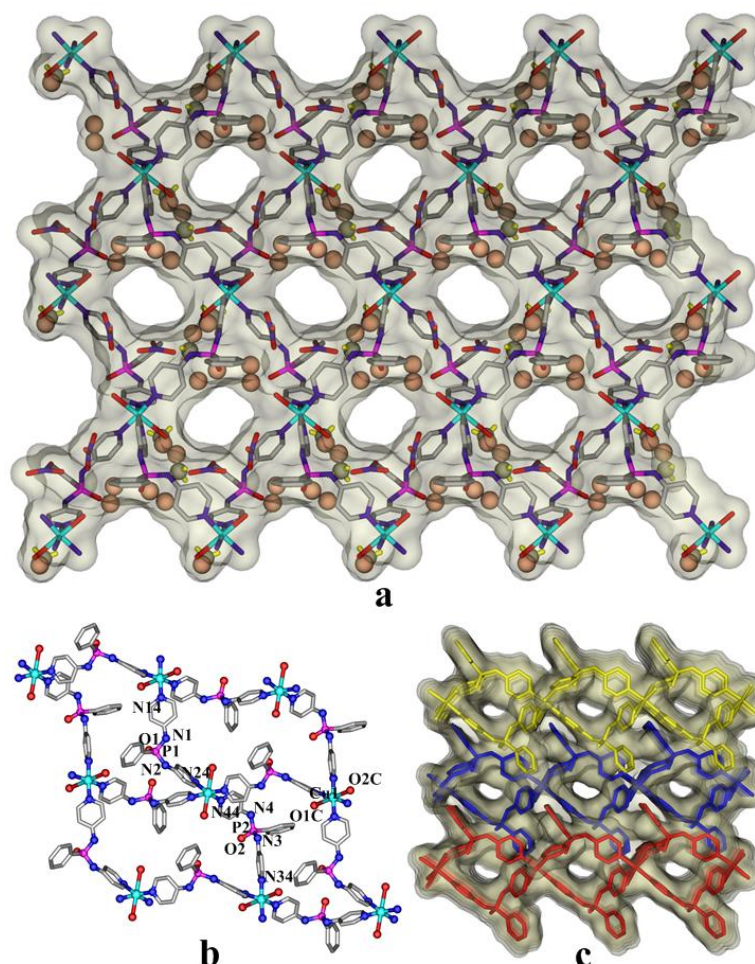


Figure 4.3: (a) View of the 2D framework in **6**. The “C” and “O” atoms of the solvate molecules are depicted as gray and beige colored spheres, respectively and “H” atoms as yellow straws. (b) Segment of the 2D assembly showing the crisscross orientation of the adjoined macrocycles. (c) Packing diagram of the cationic assembly in **6** along the *b*-axis showing the presence of intrinsic and extrinsic cavities. The individual 2D layers are colored differently for clarity.

TOPOS analysis^{57,58} for **6** gave a 4-connected uninodal sql/Shubnikov tetragonal plane net represented by the Schläfli symbol $\{4^4.6^2\}$ (Appendix A4.9).^{59,60} The packing diagram of **6** shows the presence of both intrinsic and extrinsic cavities which are filled with nitrate anions and solvate molecules (Figure 4.3c). While the extrinsic cavity partially contains the solvated methanol, the intrinsic cavity contains

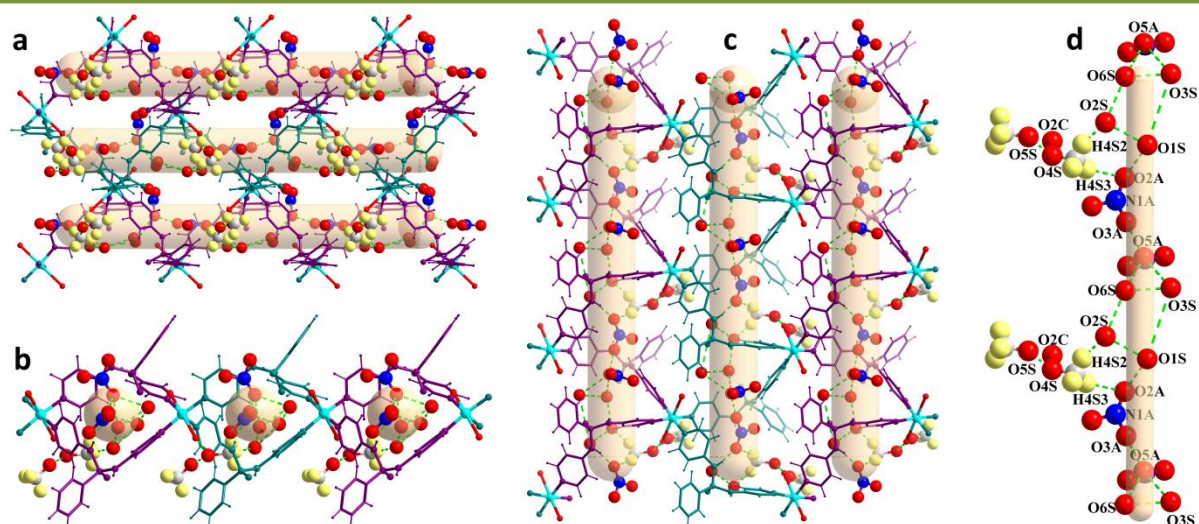


Figure 4.4: View of the single layer of **6** with anions and solvents in its intrinsic cavity along (a) *a*-axis, (b) *b*-axis and (c) *c*-axis. (d) View (along *c*-axis) of the H-bonded wire of nitrate anions and the polar solvent (methanol and water) molecules in the intrinsic cavity of **1**. (Color Code: blue- N; red- O; cyan- Cu; yellow- H; Grey- C. The whole ligand L^2 is shown in purple and dark green color, creating alternate 1D intrinsic cavity).

the solvated water, part of methanol and nitrate anions. However, all the solvated molecules and anions form Hydrogen-bonded 1D-wires which interact with the host framework through the coordinated water molecules (Figure 4.4). The TGA trace of **6** infers a 10% weight loss in temperature range between 40 and 100 °C, which corresponds to the loss of 3.5 molecules of water (both coordinated and solvated) and a molecule of methanol (Appendix A4.10).

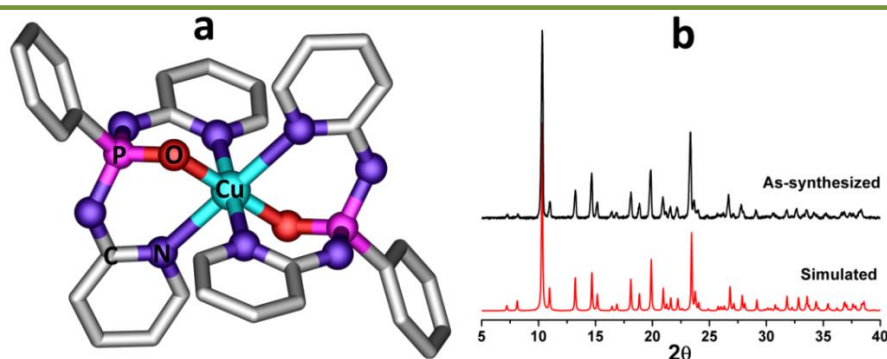


Figure 4.5: (a) Crystal structure of showing the cationic $[\text{Cu}^{\text{II}}(\text{L}^3)_2]$ core of the mononuclear complex **7**. (b) Powder X-ray diffraction pattern for **7**.

The crystal structure of **7** was solved as a mononuclear complex in the tetragonal centrosymmetric space group $I4_1/a$ (point group '4/m' and point group symmetry

' C_{4h} '). The asymmetric unit of **7** contains a Cu(II) ion with one-half occupancy, one phosphoramidate ligand and a nitrate anion for charge balance. The Cu(II) ion is located in an octahedral coordination with four N_{pyridyl} and two $O_{\text{phosphoryl}}$ contacts in which each L^3 moiety acts as a cis-directed N,N,O-coordinating ligand (Figure 4.5).

4.3.3 Ferroelectric and Dielectric Studies

An important characteristic of ferroelectric materials is the observation of a ferroelectric hysteresis loop. Hence the ferroelectric measurements were performed on the sample of **6**, as it is noncentrosymmetric and belongs to one of the 10 polar point groups (1, m, 2, mm2, 3, 3m, 4, 4mm, 6, and 6mm) essential for the ferroelectric behavior.^{61,62} The measurements show a well-defined rectangular polarization (P) vs. electric field (E) loop at 0.1 and 1 Hz frequencies. Remarkably high remnant polarization (P_r) values of 27.95 (0.1 Hz) and 28.53 (1 Hz) μCcm^{-2} are obtained for **6**. The saturation polarization (P_s) values for the P-E loops are found to be 21.79 (0.1 Hz) and 18.35 (1 Hz) μCcm^{-2} ; the coercive fields obtained in these measurements (E_c) are 5.9 and 9.7 kVcm^{-1} at 0.1 and 1 Hz frequencies, respectively (Figure 4.6a,b). The leakage current densities are in the range between 10^{-4} and 10^{-8} Acm^{-2} indicating that the observed hysteresis loops are clearly due to ferroelectricity (Figure 4.6c). To the best of our knowledge, the polarization values obtained for **6** is the highest among all the ferroelectric metal-organic self-assemblies known so far, higher than several organic, molecular and polymeric ferroelectric materials and is closely comparable with BTO (26 μCcm^{-2}).^{33,34} Also, it is significantly higher in comparison with commercial ferroelectrics like KDP, TGS and NaNO_2 .

The retention of ferroelectric polarization for **6** was probed by fatigue studies (loss of remnant polarization during bipolar switching cycles) at 1 Hz frequency. From Figure 4.6b it is clearly evident that the P_r value and the rectangular shape of the hysteresis loop is completely retained after 10^5 switching cycles. This is attributed to a facile reversal of domain switching and absence of accumulation of space charge that pins the domain walls,⁶³ confirming the fatigue-free ferroelectric behavior in **6**. The fatigue resistance of **6** may be attributed to its dense charge-separated MOF structure, along with guest solvents, which provides a steady polarization even for higher switching cycles. The PXRD data obtained on the compacted disc, both before and

after measurements, remained unchanged and matched with that of the as-synthesized **6** confirming the stability of the framework during disc formation as well as P-E loop measurements (Figure 4.6d).

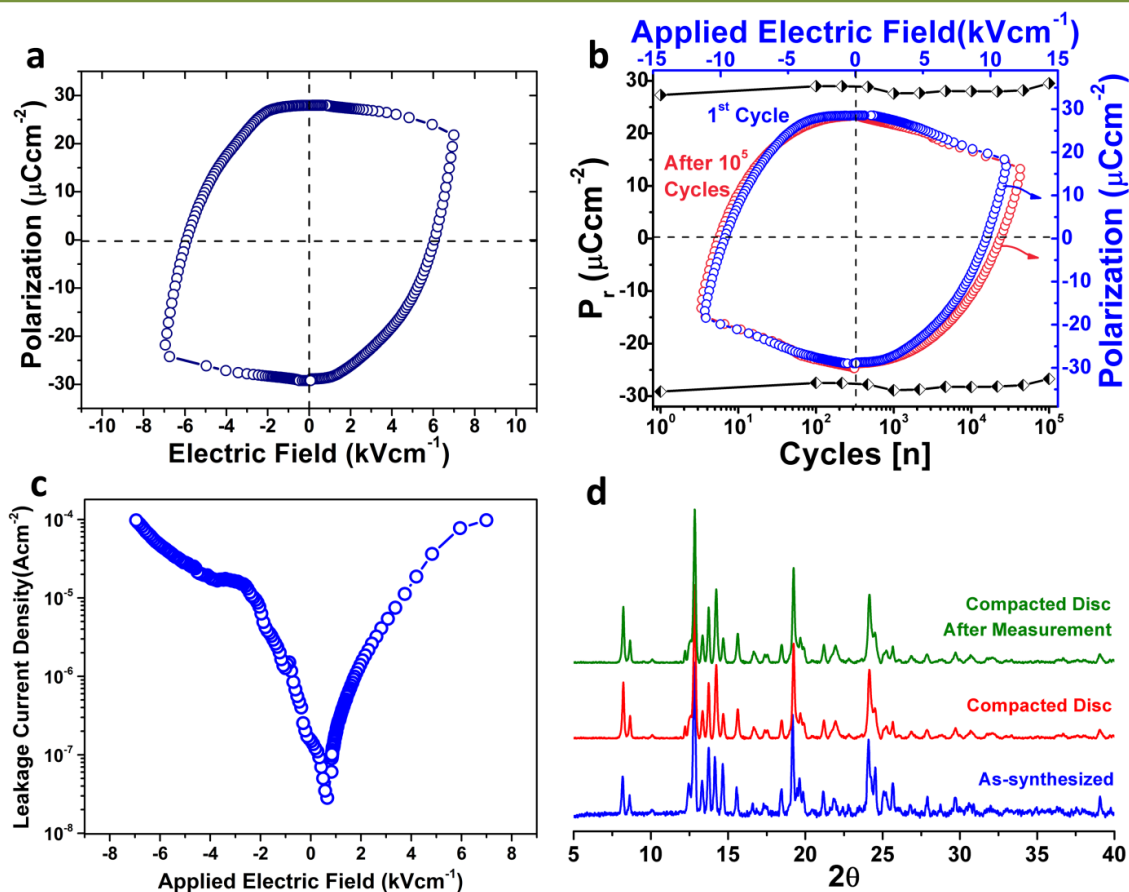


Figure 4.6: Dielectric hysteresis measurement of **6**: (a) P–E loop at 0.1 Hz. (b) Ferroelectric fatigue studies and P–E loop before (blue) and after (pink) fatigue measurements at 1 Hz. (c) Leakage current density plot as a function of applied electric field for **6** (at 0.1 Hz). (d) Comparison of the PXRD patterns of the compacted disc of **6** before and after P–E loop measurements with that of as-synthesized phase.

It is interesting to note that the anions and the polar solvent molecules form H-bonded wire-like structures which are located at the intrinsic channels present within the 2D-sheet of **6** (Figure 4.4). These H-bonded wires further interact with the coordinated water molecules positioned along the walls of the cavities and ensure an effective long-range interaction between the ionic pairs. Although it is difficult to predict the precise origin of ferroelectricity in **6** and in metal-organic materials in general (owing to their complex structure), the spatial asymmetry (polar point group) and ordered arrangement of polar solvent, in the form of wire or cluster restricted in a

confined environment such as carbon nanotube, nanopore membranes and porous MOFs, have been shown to induce ferroelectric polarization.⁶⁴⁻⁶⁶ Thus, the H-bonded wires of polar solvents and anions in a confined region of lower symmetry could be the reason for the enhanced polarization in **6**.

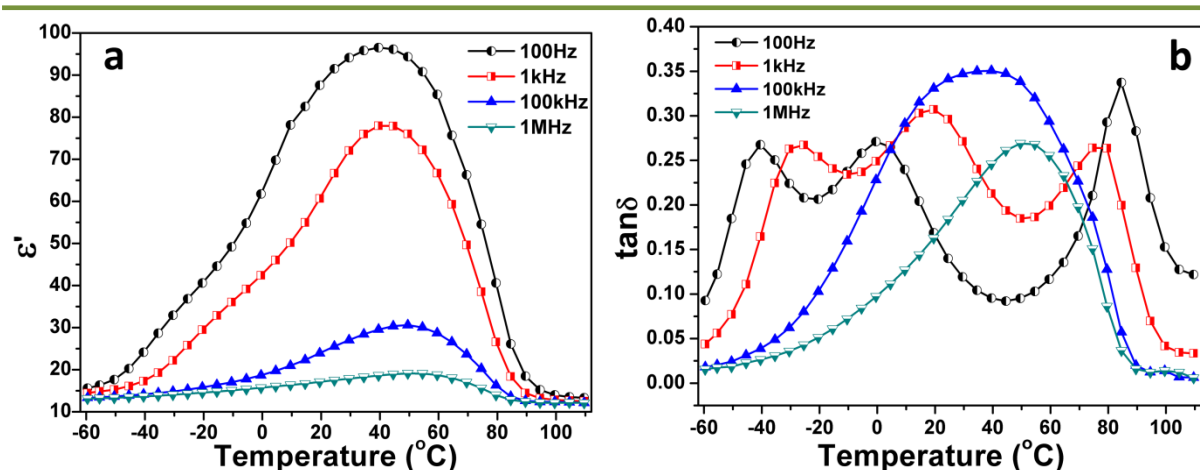


Figure 4.7: (a) Temperature dependence of the real part of dielectric constant (ϵ') for **6** measured at various frequencies showing the presence of a broad dielectric anomaly peak at around 40 $^{\circ}C$. (b) Temperature dependence of dielectric loss for **6**.

The temperature and frequency dependent dielectric permittivity (ϵ) studies were performed on **6**. The plot of the real part of dielectric permittivity as a function of frequency showed a maximum ϵ' value of 96.5 at 40 $^{\circ}C$ at 100 Hz frequency (Appendix A4.11). The observed ϵ' values at room temperature (30 $^{\circ}C$) are found to be 186.3 and 94.7 at 1 Hz and 100 Hz frequencies, respectively. The high room temperature dielectric permittivity value of **6** also supports its ferroelectric nature. Permittivity measurements on **7** (Appendix A4.12) shows a reasonable ϵ' value of ~ 31 at 30 $^{\circ}C$ in 100 Hz frequency. The observed decrease in ϵ' with increase in frequency is attributed to the contribution of all polarization mechanisms at lower frequencies.⁵⁵ Furthermore, the temperature dependence of dielectric constant of **6** was measured at various frequencies between 10^2 and 10^6 Hz (Figure 4.7). An initial increase in the ϵ' values of **6** with increase in temperature is found starting from -60 $^{\circ}C$ up to 40 $^{\circ}C$. Beyond this point a gradual decrease in ϵ' values are observed. As a result, an anomalous dielectric peak is observed at 40 $^{\circ}C$ with a maximum ϵ' value of 96.5 at 100 Hz indicating the presence of phase transition due to desolvation (Figure 4.7a). This may be attributed to the break in long-range interaction within the

structural components of **6** during the desolvation. The anomaly peak gradually decreases in intensity with marginal shift in the dielectric maxima to higher temperatures upon increasing the frequency of measurement. This can be attributed to the dielectric relaxation phenomenon assisted by desolvation.⁵³ However, the measured dielectric loss factors and conductivity are invariably low in both **6** and **7** suggesting them as a good dielectric material for practical utility (Appendices A4.13-A4.16).⁶⁷

The existence of desolvation assisted dielectric anomaly peak in **6** is also evident from the differential scanning calorimetry (DSC) analysis which displays an endothermic peak at around 55 °C associated with an irreversible phase transition (Appendix A4.17).⁶⁸ The variable temperature powder X-ray diffraction (PXRD) analysis also exhibits change in peak patterns above 40 °C (Figure 4.8a and Appendix A4.18). The PXRD obtained in the temperature range between 50 and 270 °C remained almost same and match very well with the desolvated sample of **6**. The single crystal X-ray diffraction patterns of **6** at various temperatures between -173 and 40 °C (on a Bruker Smart Apex Duo diffractometer) indicates the weakening of the diffraction spots at higher temperatures (Appendix A4.19). Performing the Data collection on a Bruker D8 Venture diffractometer with Microfocus X-ray source, gave satisfactory unit cell parameters for **6** at 40 °C. A change in cell parameters along all the three axes was observed at 40 °C (Figure 4.8b-c and Appendix A4.20). These unit cell parameters agree well with those extracted from indexing the PXRD of **6**_{desolvated} (Appendix A4.21). This suggests changes in both in-plane structure and inter-layer distances with no abrupt changes in the parent metal-ligand assembly in **6** during desolvation. The FT-IR spectra in ATR mode for the neat samples of **6**, **6**_{desolvated} and **6**_{resolvated} gave almost identical peak patterns except for **6**_{desolvated}, where the -OH (water and methanol) stretching frequency peaks were absent (Figure 4.8d). The polarized light microscope (PLM) images in the temperature range between 30 and 100 °C show that the transparent crystals **6** turned opaque above 40 °C during the desolvation process (Figure 4.8e-h). However, the original state of the crystals has been recovered upon addition of few drops of the mother liquor (Figure 4.8i). In fact the broad dielectric anomaly peak can be related to the change in polarizability of **6** due to gasification or release of solvated molecules of water and methanol at that temperature (Figure 4.8b-c).

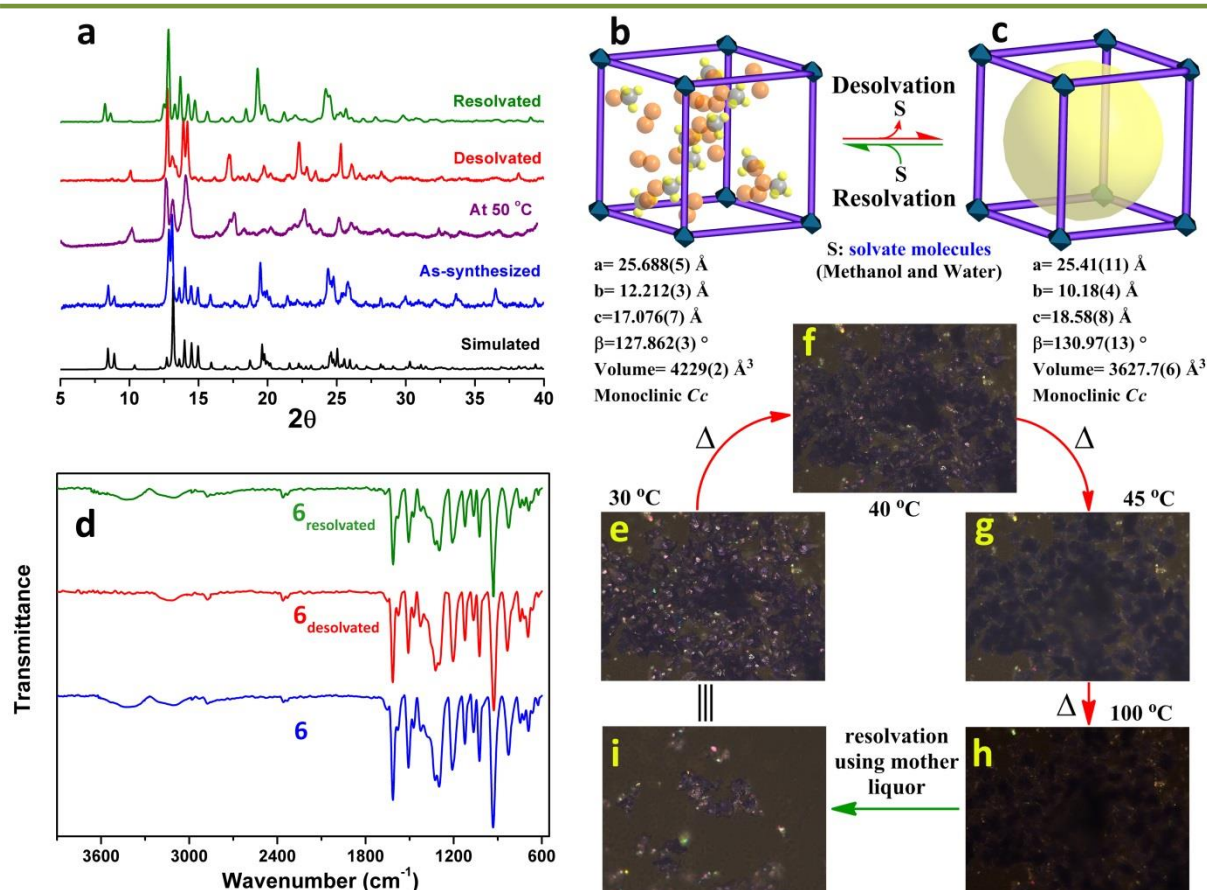


Figure 4.8: (a) Powder X-ray diffraction (PXRD) profiles of various samples of **6**. (b) Unit cell box of **6** showing the location of solvate molecules. The cationic $[Cu^{II}(L^2)]_n$ framework and nitrate anions have been removed for clarity. (c) Unit cell box obtained from the 40 °C data indicating the structural changes due to desolvation. (d) FT-IR spectra of **6**, **6**_{desolvated} and **6**_{resolvated} in ATR mode. Hot-stage PLM images of crystals of **6** during desolvation (e–h) and resolution (i).

In order to study the role of solvated molecules on the ferroelectric behavior of **6**, the ferroelectric hysteresis measurements were performed on desolvated and resolvated samples of **6**. The P-E loop of **6**_{desolvated} shows the behavior of a resistor-like material.⁶⁹ However, **6**_{resolvated} gave a similar P-E loop as well as polarization values as that of as made **6** (Figure 4.9a). In a related report, Mak and coworkers observed a reversible switching of ferroelectric and paraelectric states in a 3D framework induced by solvate molecules.⁶⁶ The leakage current density of **6**_{resolvated} (10^{-4} - 10^{-8} Acm^{-2}) measured as a function of voltage also shows a close resemblance to that of **6**, while **6**_{desolvated} shows a much lower leakage current density of 10^{-7} - $10^{-10} \text{ Acm}^{-2}$ (Figure 4.9b). Thus, the increased leakage current density for **6**, vis-à-vis **6**_{resolvated}, in

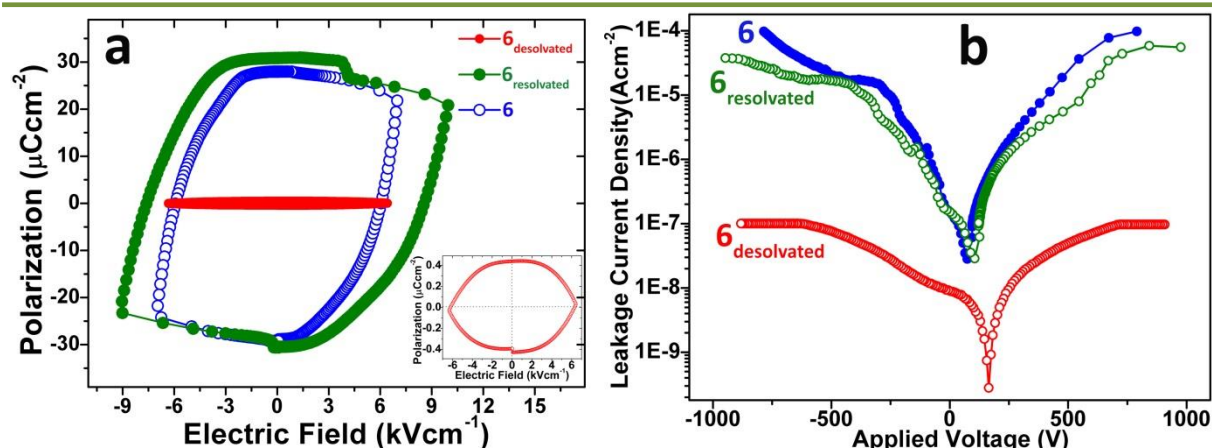


Figure 4.9: (a) Dielectric hysteresis loops of the as-synthesized, desolvated, and resolvated samples of **6**. Inset: closer view of the P - E loop of 1desolvated showing a resistor-type behavior. (b) Plots of leakage current density as a function of applied voltage for the as-synthesized, desolvated, and resolvated samples of **6**.

comparison with that of $\mathbf{6}_{\text{desolvated}}$ illustrate the extrinsic effects caused by solvate molecules towards the polarization.⁷⁰ This implies that resolution restores the long-range interaction between the ionic pairs (cationic and anionic components of the framework) that are responsible for the polarization. In addition, there is no significant change in leakage current of all the samples when the voltage polarity is reversed. Subsequently, in the intermediate electric field region a space-charge limited current conduction behavior is observed. This is due to the electric charge, in dielectrics, is considered as a continuum of charge distributed over a region of space.⁷¹ It is noteworthy to mention that such type of solvent assisted dielectric transition and high ferroelectric polarization may not originate solely from the 1D-arrangement of the polar solvents, H_2O and MeOH .⁷²⁻⁷⁴ Nevertheless, in **6** the polarization is due to the collective contributions from the H-bonded chain-like arrangement of the solvate molecules and nitrate anions and their cumulative interactions with the cationic $\{[\text{Cu}(\text{L}^2)_2(\text{H}_2\text{O})_2]^{2+}\}_n$ host framework.

4.4 CONCLUSION

The present study demonstrates the tunable nature of ferroelectric behavior in metal-ligand assemblies, such as $[Cu^{II}L_2]_n$ frameworks, via ligand driven dimensionality control. The cationic two-dimensional $[Cu^{II}(L^2)_2]_n$ framework **6** shows a very high remnant polarization, P_r , which is the highest among all the reported metal-organic ferroelectric materials. While there is a ten-fold increase in the P_r value of **6** in comparison with the previously reported $[Cu^{II}L^1_2]_n$ based 1D-helical framework, the monomeric $[Cu^{II}(L^3)_2]$ assembly of **7** is centrosymmetric and exhibits no ferroelectric behavior. However, both **6** and **7** shows high dielectric permittivity values. A dielectric anomaly peak at 40 °C was obtained in the temperature dependent permittivity measurements for **6**, attributed to the loss of solvate molecules. The P-E measurements done on the desolvated and resolvated samples of **6** indicate that the solvated molecules in the packing structure of **6** affects the polarization of the framework.

4.5 REFERENCES

- (1) Cheetham, A. K.; Rao, C. N. R. *Science* **2007**, *318*, 58.
- (2) Whatmore, R. Ferroelectric Materials. In *Springer Handbook of Electronic and Photonic Materials*, Springer: 2007; 597.
- (3) Cheong, S.-W.; Mostovoy, M. *Nat. Mater.* **2007**, *6*, 13.
- (4) Ramesh, R. *Nature* **2009**, *461*, 1218.
- (5) Ramesh, R.; Spaldin, N. A. *Nat. Mater.* **2007**, *6*, 21.
- (6) Eerenstein, W.; Mathur, N. D.; Scott, J. F. *Nature* **2006**, *442*, 759.
- (7) Spaldin, N. A.; Fiebig, M. *Science* **2005**, *309*, 391.
- (8) Das, S.; Appenzeller, J. FETRAM. *Nano Lett.* **2011**, *11*, 4003.
- (9) Dawber, M.; Rabe, K. M.; Scott, J. F. *Rev. Mod. Phys.* **2005**, *77*, 1083.
- (10) De Araujo, C. A-P.; Cuchiaro, J. D.; McMillan, L. D.; Scott, M. C.; Scott, J. F. *Nature* **1995**, *374*, 627.
- (11) Han, S.-T.; Zhou, Y.; Roy, V. A. L. *Adv. Mater.* **2013**, *25*, 5425.
- (12) Lee, H. N.; Christen, H. M.; Chisholm, M. F.; Rouleau, C. M.; Lowndes, D. H. *Nature* **2005**, *433*, 395.
- (13) Rijnders, G.; Blank, D. H. A. *Nature* **2005**, *433*, 369.
- (14) Salje, E. K. H.; Scott, J. F. *Appl. Phys. Lett.* **2014**, *105*, 252904.
- (15) Scott, J. F. *Science* **2007**, *315*, 954.
- (16) Scott, J. F.; De Araujo, C. A. P. *Science* **1989**, *246*, 1400.
- (17) Vanderah, T. A. *Science* **2002**, *298*, 1182.
- (18) Lines, M. E.; Glass, A. M. *Principles and applications of ferroelectrics and related materials*. Clarendon press Oxford: 1977.
- (19) Scott, J. F. *Ferroelectric memories*. Springer Science & Business Media: 2000; Vol. 3.
- (20) Uchino, K. *Ferroelectric Devices 2nd Edition*. CRC press: 2009.
- (21) Xu, Y. *Ferroelectric materials and their applications*. Elsevier: 2013.
- (22) Haertling, G. H. *J. Am. Ceram. Soc.* **1999**, *82*, 797.
- (23) Long, X.; Ye, Z.-G. *Chem. Mater.* **2007**, *19*, 1285.
- (24) Park, B. H.; Kang, B. S.; Bu, S. D.; Noh, T. W.; Lee, J.; Jo, W. *Nature* **1999**, *401*, 682.
- (25) Ramesh, R.; Lee, J.; Sands, T.; Keramidas, V. G.; Auciello, O. *Appl. Phys. Lett.* **1994**, *64*, 2511.

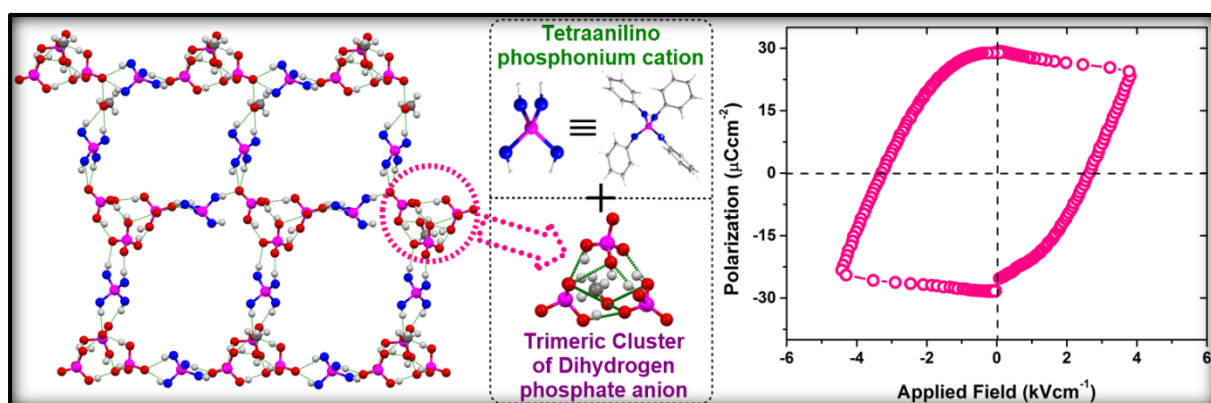
- (26) Saito, Y.; Takao, H.; Tani, T.; Nonoyama, T.; Takatori, K.; Homma, T.; Nagaya, T.; Nakamura, M. *Nature* **2004**, *432*, 84.
- (27) Zylberberg, J.; Belik, A. A.; Takayama-Muromachi, E.; Ye, Z.-G. *Chem. Mater.* **2007**, *19*, 6385.
- (28) Ye, H.-Y.; Zhang, Y.; Fu, D.-W.; Xiong, R.-G. *Angew. Chem. Int. Ed.* **2014**, *53*, 6724.
- (29) Fu, D.-W.; Zhang, W.; Cai, H.-L.; Ge, J.-Z.; Zhang, Y.; Xiong, R.-G. *Adv. Mater.* **2011**, *23*, 5658.
- (30) Fu, D.-W.; Cai, H.-L.; Liu, Y.; Ye, Q.; Zhang, W.; Zhang, Y.; Chen, X.-Y.; Giovannetti, G.; Capone, M.; Li, J.; Xiong, R.-G. *Science* **2013**, *339*, 425.
- (31) Horiuchi, S.; Ishii, F.; Kumai, R.; Okimoto, Y.; Tachibana, H.; Nagaosa, N.; Tokura, Y. *Nat. Mater.* **2005**, *4*, 163.
- (32) Horiuchi, S.; Kumai, R.; Tokura, Y. *Chem. Commun.* **2007**, 2321.
- (33) Horiuchi, S.; Tokunaga, Y.; Giovannetti, G.; Picozzi, S.; Itoh, H.; Shimano, R.; Kumai, R.; Tokura, Y. *Nature* **2010**, *463*, 789.
- (34) Horiuchi, S.; Tokura, Y. *Nat. Mater.* **2008**, *7*, 357.
- (35) Jain, P.; Dalal, N. S.; Toby, B. H.; Kroto, H. W.; Cheetham, A. K. *J. Am. Chem. Soc.* **2008**, *130*, 10450.
- (36) Tayi, A. S.; Shveyd, A. K.; Sue, A. C.-H.; Szarko, J. M.; Rolczynski, B. S.; Cao, D.; Kennedy, T. J.; Sarjeant, A. A.; Stern, C. L.; Paxton, W. F.; Wu, W.; Dey, S. K.; Fahrenbach, A. C.; Guest, J. R.; Mohseni, H.; Chen, L. X.; Wang, K. L.; Stoddart, J. F.; Stupp, S. I. *Nature* **2012**, *488*, 485.
- (37) Xu, G.-C.; Ma, X.-M.; Zhang, L.; Wang, Z.-M.; Gao, S. *J. Am. Chem. Soc.* **2010**, *132*, 9588.
- (38) Ye, H.-Y.; Fu, D.-W.; Zhang, Y.; Zhang, W.; Xiong, R.-G.; Huang, S. D. *J. Am. Chem. Soc.* **2009**, *131*, 42.
- (39) Ye, Q.; Song, Y.-M.; Wang, G.-X.; Chen, K.; Fu, D.-W.; Hong Chan, P. W.; Zhu, J.-S.; Huang, S. D.; Xiong, R.-G. *J. Am. Chem. Soc.* **2006**, *128*, 6554.
- (40) Zhao, H.; Qu, Z.-R.; Ye, H.-Y.; Xiong, R.-G. *Chem. Soc. Rev.* **2008**, *37*, 84.
- (41) Zhao, H.-X.; Zhuang, G.-L.; Wu, S.-T.; Long, L.-S.; Guo, H.-Y.; Ye, Z.-G.; Huang, R.-B.; Zheng, L.-S. *Chem. Commun.* **2009**, 1644.
- (42) Zhang, Y.; Ye, H.-Y.; Cai, H.-L.; Fu, D.-W.; Ye, Q.; Zhang, W.; Zhou, Q.; Wang, J.; Yuan, G.-L.; Xiong, R.-G. *Adv. Mater.* **2014**, *26*, 4515.
- (43) Cui, H.; Wang, Z.; Takahashi, K.; Okano, Y.; Kobayashi, H.; Kobayashi, A. *J. Am. Chem. Soc.* **2006**, *128*, 15074.

- (44) Di Sante, D.; Stroppa, A.; Jain, P.; Picozzi, S. *J. Am. Chem. Soc.* **2013**, *135*, 18126.
- (45) Jain, P.; Ramachandran, V.; Clark, R. J.; Zhou, H. D.; Toby, B. H.; Dalal, N. S.; Kroto, H. W.; Cheetham, A. K. *J. Am. Chem. Soc.* **2009**, *131*, 13625.
- (46) Ohkoshi, S.-i.; Tokoro, H.; Matsuda, T.; Takahashi, H.; Irie, H.; Hashimoto, K. *Angew. Chem. Int. Ed.* **2007**, *46*, 3238.
- (47) Rogez, G.; Viart, N.; Drillon, M. *Angew. Chem. Int. Ed.* **2010**, *49*, 1921.
- (48) Stroppa, A.; Barone, P.; Jain, P.; Perez-Mato, J. M.; Picozzi, S. *Adv. Mater.* **2013**, *25*, 2284.
- (49) Stroppa, A.; Jain, P.; Barone, P.; Marsman, M.; Perez-Mato, J. M.; Cheetham, A. K.; Kroto, H. W.; Picozzi, S. *Angew. Chem. Int. Ed.* **2011**, *50*, 5847.
- (50) Thomson, R. I.; Jain, P.; Cheetham, A. K.; Carpenter, M.A. *Phys. Rev. B* **2012**, *86*, 214304.
- (51) Hang, T.; Zhang, W.; Ye, H.-Y.; Xiong, R.-G. *Chem. Soc. Rev.* **2011**, *40*, 3577.
- (52) Zhang, Y.; Ye, H.-Y.; Fu, D.-W.; Xiong, R.-G. *Angew. Chem. Int. Ed.* **2014**, *53*, 2114.
- (53) Zhang, W.; Xiong, R.-G. *Chem. Rev.* **2012**, *112*, 1163.
- (54) Zhang, W.; Ye, H.-Y.; Xiong, R.-G. *Coord. Chem. Rev.* **2009**, *253*, 2980.
- (55) Srivastava, A. K.; Praveenkumar, B.; Mahawar, I. K.; Divya, P.; Shalini, S.; Boomishankar, R. *Chem. Mater.* **2014**, *26*, 3811.
- (56) Sheldrick, G. M. *Acta Crystallogr. A* **2008**, *64*, 112.
- (57) Blatov, V. A.; Shevchenko, A. P.; Proserpio, D. M. *Cryst. Growth Des.* **2014**, *14*, 3576.
- (58) Blatov, V. A.; Shevchenko, A. P.; Serezhkin, V. N. *J. Appl. Crystallogr.* **2000**, *33*, 1193.
- (59) O'Keeffe, M.; Yaghi, O. M. *Chem. Rev.* **2012**, *112*, 675.
- (60) Thirumurugan, A.; Li, W.; Cheetham, A. K. *Dalton Trans.* **2012**, *41*, 4126.
- (61) Ok, K. M.; Chi, E. O.; Halasyamani, P. S. *Chem. Soc. Rev.* **2006**, *35*, 710.
- (62) Li, Y.-H.; Qu, Z.-R.; Zhao, H.; Ye, Q.; Xing, L.-X.; Wang, X.-S.; Xiong, R.-G.; You, X.-Z. *Inorg. Chem.* **2004**, *43*, 3768.
- (63) Law, C. W.; Tong, K. Y.; Li, J. H.; Li, K. *Solid-State Electronics* **2000**, *44*, 1569.
- (64) Menzl, G.; Köfinger, J.; Dellago, C. *Phys. Rev. Lett.* **2012**, *109*, 020602.
- (65) Luo, C.-F.; Fa, W.; Zhou, J.; Dong, J.-M.; Zeng, X.-C. *Nano Lett.* **2008**, *8*, 2607.
- (66) Dong, X.-Y.; Li, B.; Ma, B.-B.; Li, S.-J.; Dong, M.-M.; Zhu, Y.-Y.; Zang, S.-Q.; Song, Y.; Hou, H.-W.; Mak, T. C. W. *J. Am. Chem. Soc.* **2013**, *135*, 10214.
- (67) Compounds having dielectric constant value greater than that of silicon nitride ($\epsilon_r > 7.0$) are classified as high dielectric constant materials.

- (68) The TGA and DSC profile of $\mathbf{1}_{\text{desolvated}}$ shows no weight loss until 270 °C. However, the TGA and DSC graphs of $\mathbf{1}_{\text{resolvated}}$ closely resembles to that of $\mathbf{1}$.
- (69) Jin, L.; Li, F.; Zhang, S. *J. Am. Ceram. Soc.* **2014**, *97*, 1.
- (70) Chen, J.I.; Chen, H.m.; Lee, J. Y. *Appl. Phys. Lett.* **1996**, *69*, 4011.
- (71) Yang, J.-K.; Kim, W. S.; Park, H.-H. *Appl. Surf. Sci.* **2001**, *169*, 544.
- (72) Cui, H.; Zhou, B.; Long, L.-S.; Okano, Y.; Kobayashi, H.; Kobayashi, A. *Angew. Chem. Int. Ed.* **2008**, *47*, 3376.
- (73) Cui, H.-B.; Takahashi, K.; Okano, Y.; Kobayashi, H.; Wang, Z.; Kobayashi, A. *Angew. Chem. Int. Ed.* **2005**, *44*, 6508.
- (74) Wang, Z. M.; Hu, K.; Gao, S.; Kobayashi, H. *Adv. Mater.* **2010**, *22*, 1526.

End of Chapter 4

Chapter 5



Ferroelectricity in Polar Organic Salts Stabilized by Phosphonium Cations

5.1 Introduction

Earlier research on ferroelectric materials have demonstrated the utility of inorganic oxide materials like BTO (barium titanate), PZT (lead zirconate titanate), KNbO₃ (potassium niobate), BFO (bismuth ferrite) as potential commercial ferroelectric materials especially in the domain of materials for non-volatile memories.¹⁻¹⁰ However, such materials also exhibit certain limitations owing to their high content of toxic and expensive heavier metals and difficulties in fabrication processes which require more time, high-cost and high temperature.¹¹⁻¹³ On the other hand, discovery of ferroelectricity based on small molecules and self-assembled supramolecules such as charge transfer complexes, molecular crystals with high spontaneous polarization, thin films based on molecular ferroelectrics with multiaxial polarization and certain molecular rotators have shown the potential of these systems as alternate choices of materials for this application.¹⁴⁻²⁸ Further, these molecule based ferroelectric systems having the organic struts, can be efficiently synthesized under mild conditions in high purity and can be employed in solution based methods for device fabrication which promises their utility in the development of economically viable high-performance devices.^{28,29} As a result, a number of molecular ferroelectrics, as neutral organic moieties or organic salts, with excellent ferroelectric properties have been developed.³⁰⁻³⁴ Rochelle salt, KDP (potassium dihydrogen phosphate) and TGS (triglycine sulphate) are commercial molecular ferroelectrics known since long time, where hydrogen bonding between the individual constituents induce polar order.³⁵⁻³⁸ Some polar organic compounds (such as croconic acid, cyclobutene-1,2-dicarboxylic acid, 5,6-dichloro-2-methylbenzimidazole etc.) have shown attractive ferroelectric properties through the proton tautomerism mechanism, facilitated by site-to-site proton transfer in hydrogen bonds.³⁰⁻³² Apart from this, many ammonium based organic salts have been found to exhibit ferroelectric properties with good polarization values.^{21-25,28,33,34,39} Several organic and organic-inorganic hybrids have found to exhibit perovskite structure and display very good ferroelectric behavior along with some additional properties like luminescence.⁴⁰⁻⁴³ The chloride and bromide salts of diisopropyl amine (DIPA) are one of the well-known order-disorder type above room temperature molecular ferroelectrics that display high curie temperature (T_c) and high polarization values.^{33,34} Particularly, the diisopropyl

ammonium bromide (DIPAB) has a very large polarization of $23 \mu\text{Ccm}^{-2}$, comparable to that of barium titanate.³⁴ The exciting ferroelectric properties of these molecules, especially croconic acid and DIPAB, have attracted the interest of researchers working in this topic with a view of achieving the performances exhibited by traditional ferroelectric materials. In this chapter, we describe our efforts to develop a rational route for obtaining molecular ferroelectric materials based phosphonium cations. These investigations have resulted in the formation of two polar molecular salts $[\{\text{P}(\text{NHPH})_4\}_3(\text{C}_9\text{H}_3\text{O}_6) \cdot (\text{CH}_3\text{OH})_2]$, **8** and $[\{\text{P}(\text{NHPH})_4\}(\text{H}_2\text{PO}_4) \cdot (\text{CH}_3\text{OH})_{0.5}]_6$, **9** based on the tetraanilino phosphonium cations.

5.2 EXPERIMENTAL SECTION

5.2.1 General Remarks

All manipulations involving phosphorus halides were performed under dry nitrogen atmosphere in standard Schlenk-glassware; toluene was dried over sodium. Aniline and Trimesic acid were purchased from Aldrich and used as received. Orthophosphoric acid (85%) was purchased locally from SDFCL and used as received. NMR spectra were recorded on a Jeol 400 MHz spectrometer (^1H NMR: 400.13 MHz, $^{13}\text{C}\{^1\text{H}\}$ NMR: 100.62 MHz, $^{31}\text{P}\{^1\text{H}\}$ NMR: 161.97 MHz) at room temperature using SiMe_4 (^1H , ^{13}C) and 85% H_3PO_4 (^{31}P). The MALDI-TOF spectra were obtained on an Applied Biosystem MALDI-TOF/TOF spectrometer. The powder X-ray diffraction (PXRD) data were obtained from a Bruker-D8 Advance diffractometer. Thermal gravimetric analysis (TGA) data has been obtained from a Perkin-Elmer STA-6000 thermogravimetric analyzer. Elemental analyses were performed on a Vario-EL cube elemental analyzer. FT-IR in Attenuated total reflectance (ATR) mode was taken on neat samples on Bruker Alpha Spectrophotometer. Melting points were obtained using an Electro thermal melting point apparatus and were uncorrected.

5.2.2 Synthesis

The phosphonium salt $[\{\text{P}(\text{NHPH})_4\}\text{Cl}]$ (L^4) and $[\text{P}(\text{NPh})(\text{NHPH})_3]$ (L^5) were synthesized by employing a modified reported procedure.^{44,45}

5.2.2.1 Synthesis of Tetraanilino phosphonium trimesate $[\{P(NHPh)_4\}_3(C_9H_3O_6) \cdot (CH_3OH)_2]$ (8**):** To a well stirred solution of L^5 (50 mg, 0.125 mmol) in methanol (~5 ml), a solution of trimesic acid (8.50 mg, 0.041 mmol) in methanol (2 ml) was slowly added with continuous stirring. The mixing leads to formation of a suspension. Further, 10 ml of methanol was added to the mixture and then stirred overnight to dissolve most of the precipitate. The solution was filtered after overnight stirring and the filtrate was kept undisturbed for evaporation of solvent at room temperature. This gave colorless crystals suitable for single crystal X-ray diffraction (SCXRD) analysis after 4-6 days. Yield: 70% (40 mg), based on P. M.P.: >250 °C. 1H -NMR (400 MHz, $(CD_3)_2SO$: δ 2.04 (s, 6H, methyl), 3.76 (br, 12 H, NH), 6.78 (m, 12 H, *p*-CH), 7.17 (m, 24 H, *m*-CH), 7.37 (m, 24 H, *o*-CH), 8.58 (m, 3 H, CH, trimesic). ^{13}C -NMR (100 MHz, $(CD_3)_2SO$: δ 48.63, 116.98, 121.93, 129.19, 132.18, 134.48, 139.59. ^{31}P -NMR (162 MHz, $\{(CD_3)_2SO\}$): δ 4.78. FT-IR data in KBr pellet (cm^{-1}): 3599, 3062, 1597, 1548, 1489, 1413, 1347, 1280, 1217, 1028, 951, 816, 746, 686. Anal. Calcd. for $C_{83}H_{83}N_{12}O_8P_3$: C, 67.84; H, 5.69; N, 11.44. Found: C, 67.95; H, 5.61; N, 11.59.

5.2.2.2 Synthesis of Tetraanilino phosphonium dihydrogen phosphate $[\{P(NHPh)_4\}(H_2PO_4) \cdot (CH_3OH)_{0.5}]_6$ (9**):** To a well stirred solution of L^5 (20 mg, 0.05 mmol) in methanol (~3 ml), an excess of 85% solution of orthophosphoric acid (100 μ l) was added with constant stirring. The clear solution was stirred for an hour and was then filtered through a thick pad of celite. The filtrate was left for crystallization at RT. The colourless crystals suitable for single crystal X-ray diffraction (SCXRD) analysis were obtained in 2-3 days. Yield: 70% (18 mg), based on P. M.P.: >250 °C. 1H -NMR (400 MHz, $(CD_3)_2SO$: δ 2.04 (s, 3H, methyl), 2.76 (s, 8 H, NH), 6.81 (m, 24 H, *o*- and *p*-CH), 7.12 (m, 16 H, *m*-CH). ^{13}C -NMR (100 MHz, $(CD_3)_2SO$: δ 31.23, 119.30, 122.05, 129.55, 140.46. ^{31}P -NMR (162 MHz, $\{(CD_3)_2SO\}$): δ 1.53, 1.60. FT-IR data in KBr pellet (cm^{-1}): 3596, 3208, 1598, 1492, 1403, 1282, 1220, 1127, 1082, 1054, 1031, 966, 746, 689. Anal. Calcd. for $C_{147}H_{168}N_{24}O_{27}P_{12}$: C, 57.42; H, 5.51; N, 10.93. Found: C, 57.35; H, 5.41; N, 10.99.

5.2.3 Crystallography

Reflections were collected on a Bruker Smart Apex Duo diffractometer at 100 K using MoK α radiation ($\lambda = 0.71073 \text{ \AA}$) for **8** and **9**. Structures were refined by full-

matrix least-squares against F^2 using all data (SHELX).⁴⁶ Crystallographic data for all these compounds are listed in Table 5.1. All non-hydrogen atoms were refined anisotropically if not stated otherwise. Hydrogen atoms were constrained in geometric positions to their parent atoms. Three phenyl rings in **9** are disordered over two positions. Atom positions of the disordered groups in **9** were split over two positions and refined isotropically using similar-distance U-restraints. Crystals of **8** and **9** were weakly diffracting at higher angles and hence a $2\theta = 50^\circ$ cutoff was applied. The refinement parameter in **9** was slightly higher owing to the diffuse nature of the solvated crystals.

Table 5.1: Details of crystallographic data collection and structure refinements for 8 and 9

Compound	8	9
Chemical formula	C ₈₃ H ₈₃ N ₁₂ O ₈ P ₃	C ₁₄₇ H ₁₆₈ N ₂₄ O ₂₇ P ₁₂
Formula weight	1469.52	3074.68
Temperature	100(2)K	100(2) K
Crystal system	Orthorhombic	Monoclinic
Space group	Pca2 ₁	P2 ₁
a (Å); α (°)	19.19(3); 90	13.240(2); 90
b (Å); β (°)	18.48(4); 90	23.700(4); 97.866(5)
c (Å); γ (°)	21.86(4); 90	24.808(4); 90
V (Å ³); Z	7753(25); 4	7711(2); 2
ρ (calc.) mg m ⁻³	1.259	1.324
μ mm ⁻¹	0.141 (Mo K _α)	0.209 (Mo K _α)
2θ _{max} (°)	50	50
R(int)	0.2810	0.0836
Completeness to θ	99.90 %	99.8 %
Data / param.	11702 / 962	23489 / 1610
GOF	1.011	1.213
R1 [F > 4σ(F)]	0.0891	0.1032
wR2 (all data)	0.2229	0.2489
max. peak/hole (e.Å ⁻³)	0.457 / -0.326	1.653 / -0.658

5.2.4 Ferroelectric and Dielectric measurements

In order to determine the dielectric and ferroelectric properties, the crystals of **8** and **9** were crushed and the crystalline powdered samples were compacted in the form of discs (of approximately 10 mm diameter and 1mm thickness). The compacted discs were subsequently electroded using aluminium adhesive foils for both ferroelectric

and dielectric measurements. The dielectric characteristics for **8** and **9** were measured using the Novocontrol, Dielectric Spectrometer.

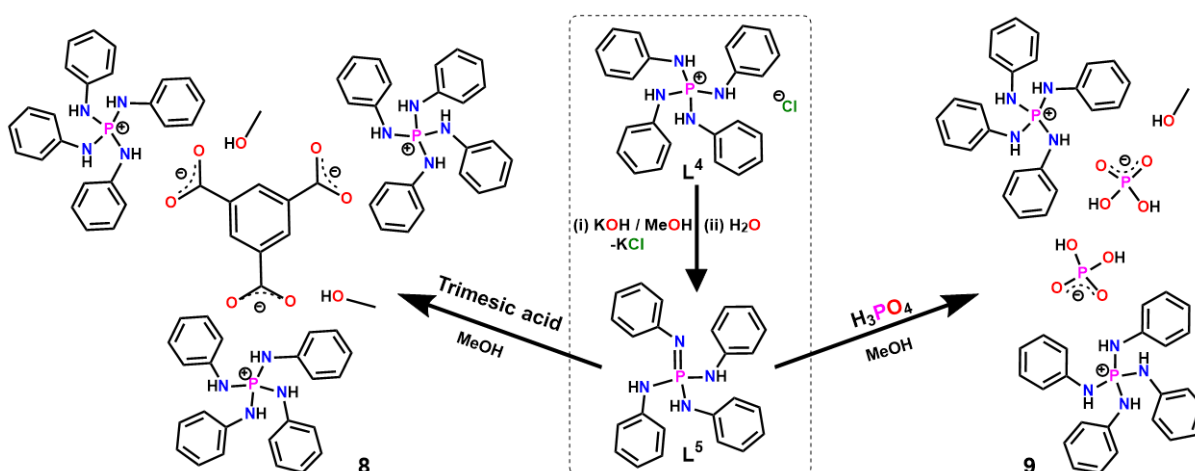
The ferroelectric hysteresis loops in **8** and **9** were measured by using Sawyer-Tower circuit. The measurements pertaining to polarization and fatigue cycles were recorded using hysteresis loop analyser (TF Analyser 2000, aixACCT Germany). Leakage current was measured dynamically for various voltage steps during the hysteresis loop measurements.

5.3 RESULTS AND DISCUSSION

5.3.1 Syntheses

The tetraanilino phosphonium cation, $[\text{P}(\text{NPh})_4]\text{Cl}$ (L^4), was synthesized as described earlier by reacting PCl_5 with excess of aniline in toluene and reflux under inert atmosphere.^{44,45} Further, L^4 was treated with KOH to yield the neutral phosphine imine $[\text{P}(\text{NPh})(\text{NHP})_3]$ (L^5).⁴⁷ The polar H-bonded phosphonium salts **8** and **9** were obtained by protonation of L^5 in methanol with trimesic acid and orthophosphoric acid, respectively (Scheme 1). The phosphonium salt **8** was prepared by a 3:1 reaction of L^5 with trimesic acid in methanol at room temperature. While, the phosphonium salt **9** (*taPDP*), analogous to KDP, was synthesized by the 1:1 reaction of L^5 with orthophosphoric acid in methanol at room temperature.

Scheme 5.1: Schematic for the synthesis of 8 and 9



5.3.2 Crystal Structures

The molecular structure of **8** having tetraanilino phosphonium cation and 1,3,5-benzene tricarboxylate (trimesate) trianion was crystallized in the polar orthorhombic space group $Pca2_1$. The asymmetric unit of **8** consists of a trimesate trianion, three tetraanilino phosphonium cations, and two solvate methanol molecules (Figure 5.1a). Compound **8** is a polymorph of an already published solvent free salt of formula $[(P(NHPh)_4)_6(C_9H_3O_6)_2]$ obtained in the P_c space group.⁴⁷ The crystal lattice of **8** reveals a rich hydrogen bonding interactions between trimesate anions and phosphonium cations. Out of the three carboxylate ends of the trimesate anion, one is hydrogen bonded to two phosphonium units while the other two are hydrogen bonded to one phosphonium unit and one methanol solvent (Figure 5.1b). Out of the three distinct phosphonium motifs, two of them (P1 and P3) exhibit similar hydrogen bonding interactions and bonded to only the $O_{\text{carboxylate}}$ of trimesate anion, while the third one (P2) is primarily hydrogen bonded to solvated methanol which further interacts with the $O_{\text{carboxylate}}$ of the trimesate anion (Figures 5.1c-e).

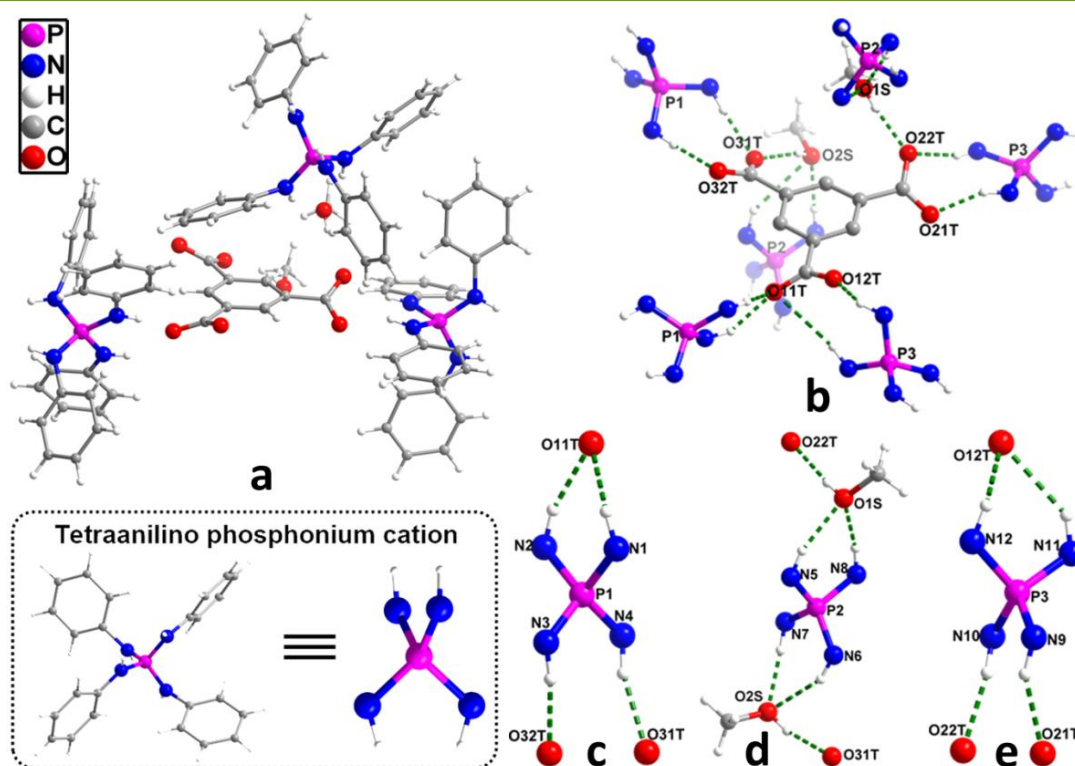


Figure 5.1: (a) Crystal Structure of **8**. (b-e) View of hydrogen bonding pattern for the individual trimesate anion and phosphonium cations.

In return, the trimesate anion is involved in a direct H-bonding with four phosphonium cations (labelled P1 and P3) forming a 2D-sheet like structure (Figure 5.2). These hydrogen bonded 2D-sheets were further pillared by two other phosphonium motif (labelled P2) in which the donor-acceptor type interaction of the methanol molecules acts as glue between the two individual sheets and the phosphonium pillars leading to a 3D- hydrogen bonded network (Figure 5.2).

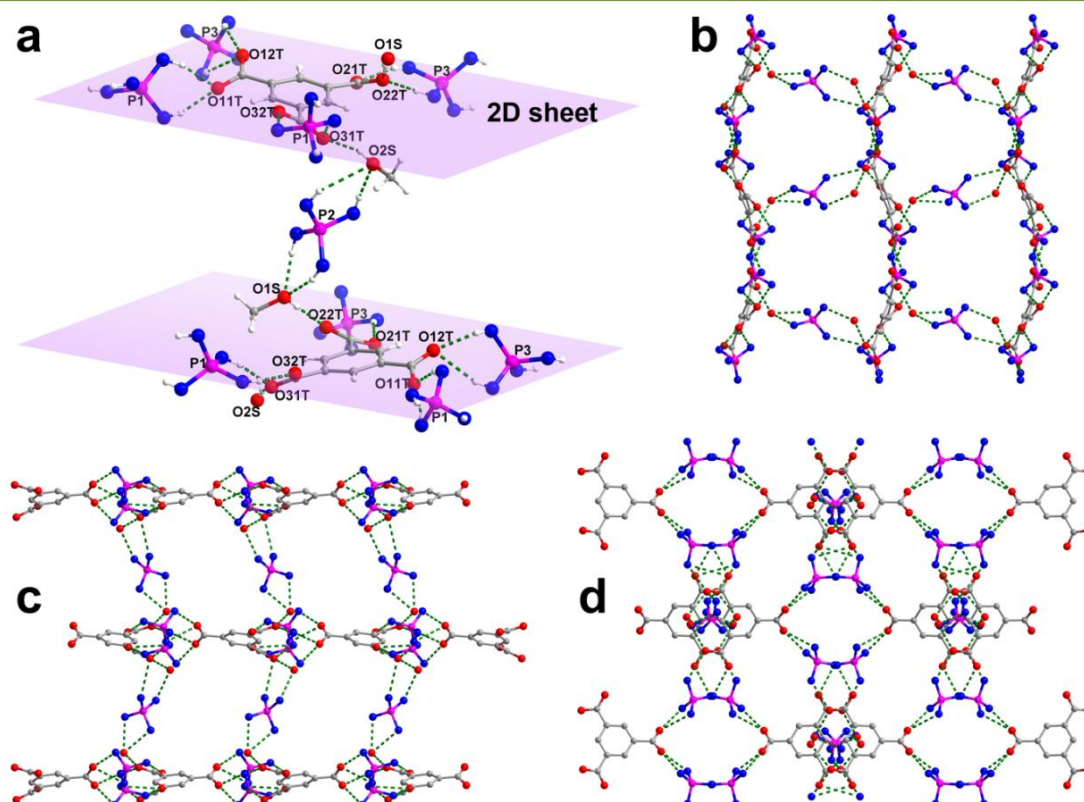


Figure 5.2: (a) View of the hydrogen bonding interactions leading to 3D network in **8**. View of the 2x2x2 hydrogen bonded packing structure in **8** along (b) a-axis, (c) b-axis and (d) c-axis (Phenyl rings on the phosphonium cations have been removed for clarity).

Furthermore, the N-H...O bond distances and angles in **8** are found to be comparable to the carboxylate salts of protonated amines.⁴⁸⁻⁵⁰ The details of the hydrogen bonds associated with the compound **8** is provided in Appendix A5.2. Owing to the chelating hydrogen-bonding N-H...O interactions in **8**, the N-P-N bond angles in **8** deviates from the ideal tetrahedral angle. As a result, acute angles of around 100° are found for the N-P-N segments (N1-P1-N2, N3-P1-N4, N6-P2-N7, N5-P2-N8, N9-P3-N10, and N11-P3-N12) involved in chelating interactions (Appendix A5.1).

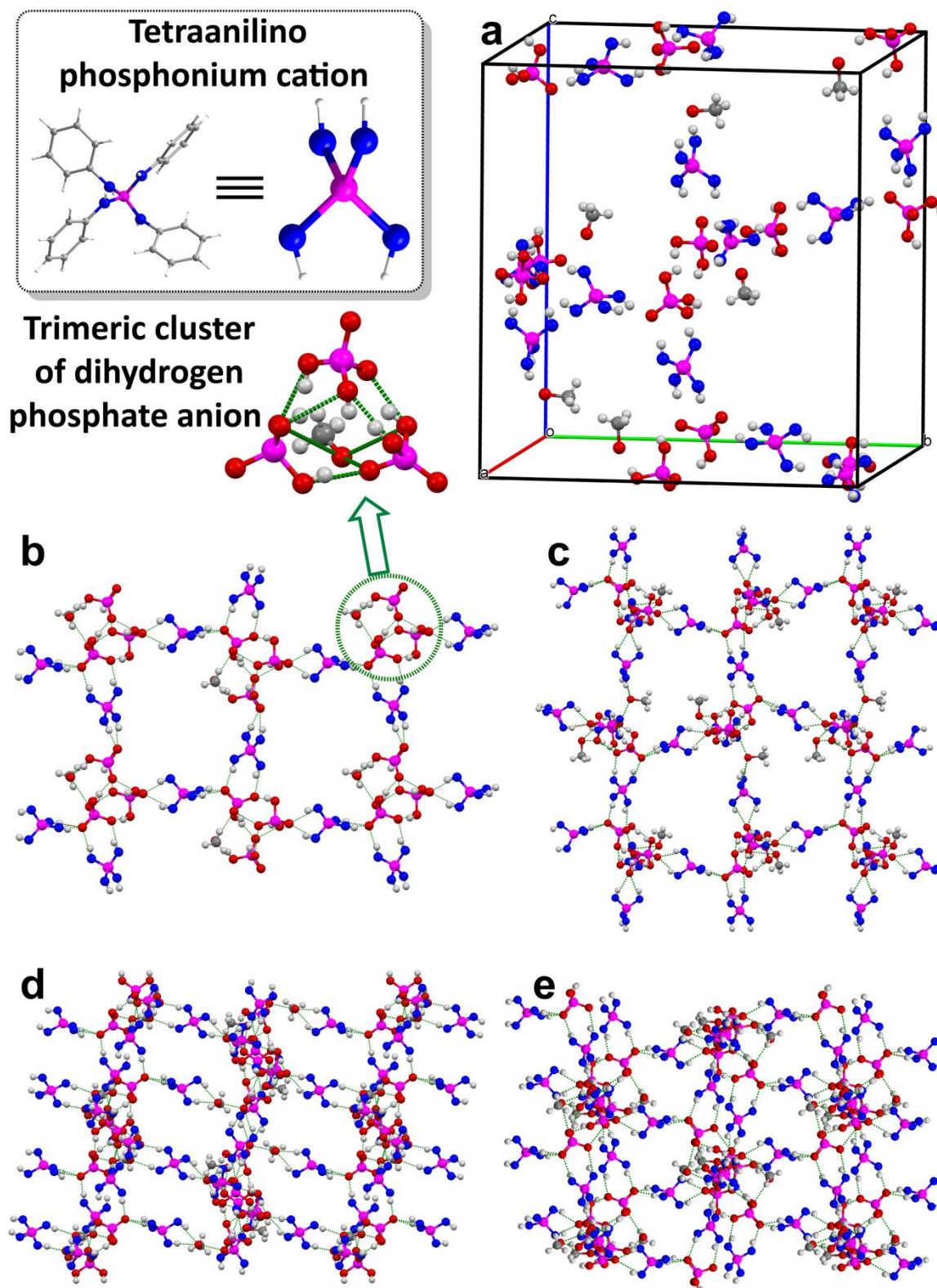


Figure 5.3: Crystal Structure of **9** (a) Unit cell box. (b) View of the 2D-sheet showing hydrogen bonding between phosphonium motifs and trimeric clusters of the dihydrogen phosphate trianion. View of the packing structure of hydrogen bonded 3D network in **9** along (c) a-axis, (d) b-axis and (e) c-axis.

The molecular structure of **9** having tetraanilino phosphonium cations and dihydrogen phosphate anions ($[\text{H}_2\text{PO}_4]^-$) was solved in the polar monoclinic space group $P2_1$. The asymmetric unit consists of six tetraanilino phosphonium cations, six dihydrogen phosphate anions, and three solvated methanol molecules. As anticipated, compound **9** displays a rich hydrogen bonding interactions between the dihydrogen phosphate anions and the phosphonium cations leading to the formation of an intricate 3D-framework structure (Figure 5.3). The 3D network in **9** can be understood as follows. First, a trimeric cluster is formed by the donor-acceptor type hydrogen-bonding interactions within three dihydrogen phosphate anions. This cluster further accepts H-bonding interactions from six phosphonium cations and three methanol solvates. Of the six phosphonium cations, four of them, along with the trimeric cluster of dihydrogen phosphate anions, were involved in the 2D sheet formation via a distorted 4,4-grid type hydrogen-bonded network along the *ab*-plane (Figure 5.3b). These 2D-sheets are further pillared by the remaining two phosphonium motifs along the *ac*-plane. Among the three solvate methanol, one is primarily attached to the trimeric cluster and the remaining two are acting as glue between the trimeric clusters and alternate phosphonium pillars (Figure 5.3c-e).

The N-H...O bond distances and angles in **9** are found in the range normally observed for hydrogen bonding (Appendix A5.3). Some of the phosphonium moieties offer a chelating hydrogen bond interaction which causes marginal deviation in the N-P-N bond angles from the ideal tetrahedral angle. As a result some N-P-N segments show acute angles of around 100° as they are involved in chelating interactions (Appendix A5.1). The O-P-O segments of the dihydrogen phosphate anions also exhibit slight variation from the ideal tetrahedral angle due to their involvement in hydrogen bonding (Appendix A5.1).

5.3.3 Ferroelectric and Dielectric Studies

The compound **8** was crystallized in $Pca2_1$ space group (point group “ $mm2$ ”) while compounds **9** was crystallized in $P2_1$ space group (point group “ 2 ”). Both these space groups are noncentrosymmetric and belongs to the 10 polar point groups (1, m , 2 , $mm2$, 3 , $3m$, 4 , $4mm$, 6 , and $6mm$) essential for the ferroelectric behavior.^{51,52}

Hence, electrical measurements were performed on the samples of **8** and **9** to probe their ferroelectric behaviour.

5.3.3.1 Ferroelectric and Dielectric Studies of 8. The compacted disc of **8** was subjected for the ferroelectric measurements which gave a polarization (P) vs electric field (E) hysteresis loop at room temperature (Figure 5.4a). The P-E loop obtained at 0.1 Hz gave a P_r of about $0.035 \mu\text{Ccm}^{-2}$ with an E_c at 20 kVcm^{-1} . Further, the leakage current densities are in the range between 10^{-5} and 10^{-9} Acm^{-2} indicating that the observed hysteresis loops are clearly due to ferroelectricity (Appendix A5.4). Despite the presence of a rectangular hysteresis loop in **8**, the observed value of remnant polarization (P_r) was very low and the coercive field (E_c) was a bit on the higher side. This indicates that the nature of dipoles in **8** is rather weak and responds very poorly against the applied electric field.

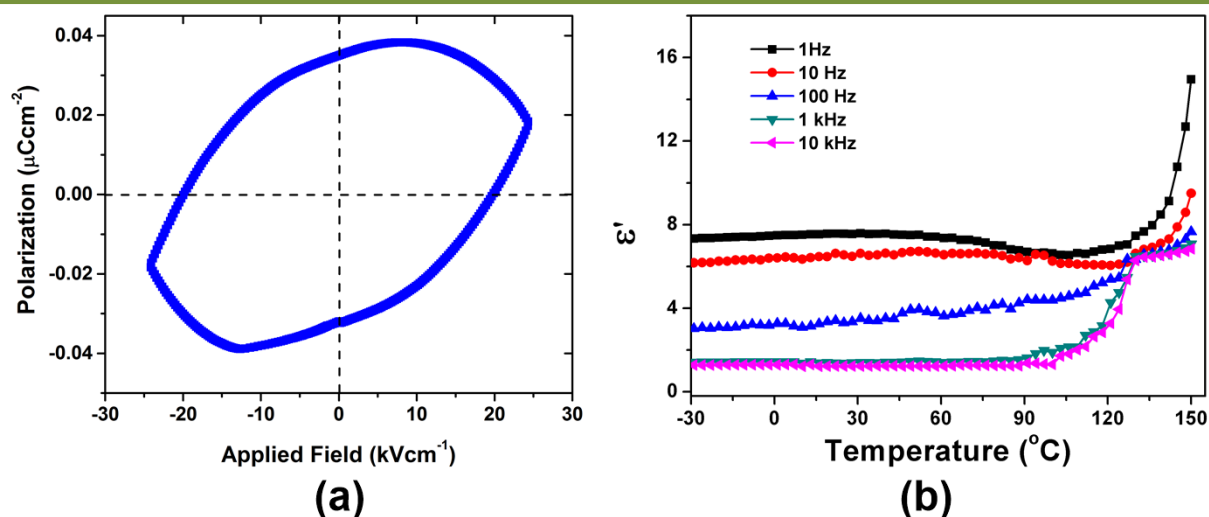


Figure 5.4: Dielectric measurements on **8**: (a) P-E loop at 0.1 Hz. (b) Temperature dependence of the real part of dielectric constant measured at various frequencies.

Further, the temperature dependence of dielectric constant of **8**, measured at various frequencies (between 1 and 10^5 Hz) in the temperature range of -50 $^{\circ}\text{C}$ to 150 $^{\circ}\text{C}$, gave quite low dielectric constant values (ϵ' value of 3.5 and 1.4 at 100 Hz and 1 kHz, respectively) suggesting it to be a low-dielectric constant material (Figure 5.4b and Appendix A5.5). Also, the plot of real part of permittivity against temperature exhibits no anomalous dielectric peak which suggests the absence of structural phase transition in **8**. These observations are again consistent with the obtained P-E

loop characteristics of **8**. Nevertheless, the very low dielectric constant values coupled with the presence of weak polarizations promises its utility as potential material for the integration of microelectronic circuits.⁵³

5.3.3.2 Ferroelectric and Dielectric Studies in **9**.

On subjecting the sample of compound **9** for ferroelectric measurements at room temperature, a well-defined polarization (P) vs electric field (E) hysteresis loop was observed at 1 Hz frequency. The remnant polarization (P_r) value for **9** was found to be $28.88 \mu\text{Ccm}^{-2}$ with a low coercive field (E_c) of 3.3 kVcm^{-1} at 1 Hz frequency (Figure 5.5a). The leakage current densities are in the range between 10^{-5} and 10^{-7} Acm^{-2} indicating that the observed hysteresis loops are clearly due to ferroelectricity (Figure 5.5b). It is very interesting to note that the observed P-E loop in **9** shows improved ferroelectric characteristics than Rochelle salt, KDP, TGS and various other well-known molecular/organic ferroelectrics. Particularly, the compound **9**, which is referred here as *ta*PDP, shows higher polarization value than that of KDP ($5 \mu\text{Ccm}^{-2}$). However, the coercive field for **9** is higher than that of KDP (0.1 kVcm^{-1}), but still is lower in comparison with certain commercial (such as PVDF and its copolymers) and molecular ferroelectrics.^{14,15}

Further, it is interesting to look at the structural analogy between the *ta*PDP (**9**) and KDP. As described earlier, *ta*PDP (**9**) displays rich hydrogen bonding interactions between the phosphonium motifs and the trimeric cluster of dihydrogen phosphate anions which creates polar hydrogen bonded 3D network. On the other hand, the structure of KDP (KH_2PO_4) is quite complicated, where the polar order and ferroelectric polarization is prompted from the displacement of K^+ and PO_4^{-3} ions along the polar axis, with additional contribution from the ordering of protons in the lattice.³

Further, the ferroelectric fatigue measurements were performed on the sample of **9** to check the retention of polarization after several bipolar switching cycles. It was observed that the P_r value and the shape of the hysteresis loop in **9** was completely retained even after 10^5 switching cycles at 1Hz frequency (Figure 5.5c-d). This remarkable fatigue resistant behaviour indicates the facile switching of polarizable

domains in **9** and also suggests the absence of space charge accumulation (or movement) and reduction in the pinning of domain walls.^{54,55} The analysis of the PXRD data obtained on the compacted disc, both before and after measurements, confirms the stability of the material during disc formation as well as P-E loop measurements as the PXRD plots remained unchanged and matched with that of the as-synthesized **9** (Appendix A5.6).

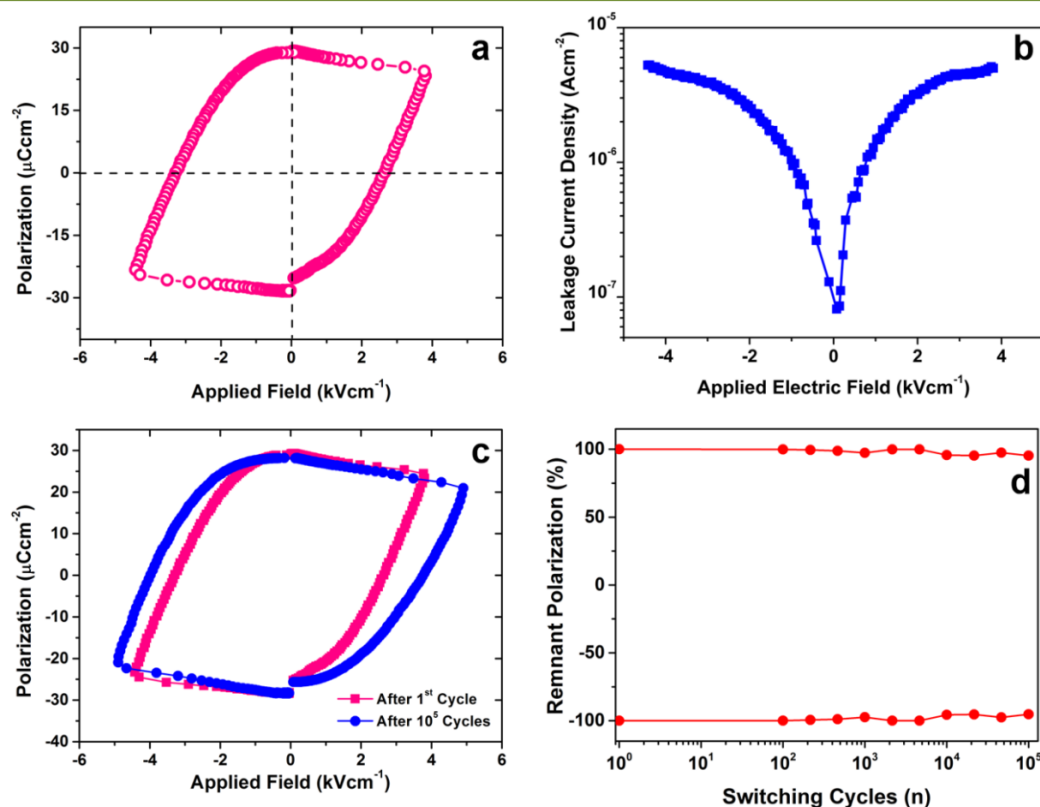


Figure 5.5: Dielectric hysteresis measurement on **9**: (a) P–E loop at 1 Hz. (b) Plot of the leakage current density versus applied electric field. (c) P–E loop before (pink) and after (blue) fatigue measurements at 1 Hz. (d) Ferroelectric fatigue study showing the retention of P_r after 10^5 switching cycles.

The temperature dependent permittivity measurements were performed on the sample of **9** at various frequencies ranging from 10^2 and 10^6 Hz in the temperature range of -50 °C to 120 °C (Figure 5.6). The real part of dielectric permittivity (ϵ') was found to increase with increase in temperature from -50 °C to 40 °C, after which a gradual decrease in ϵ' values are observed (Figure 5.6a). This gave an anomalous dielectric peak at 40 °C with a maximum ϵ' value of 228.5 and 88 at 100 Hz and 1 kHz, respectively. This anomaly peak does not corresponds to any ferroelectric-

paraelectric phase transition, rather is an indicative of phase transition due to onset of evaporation of solvated methanol.^{56,57}

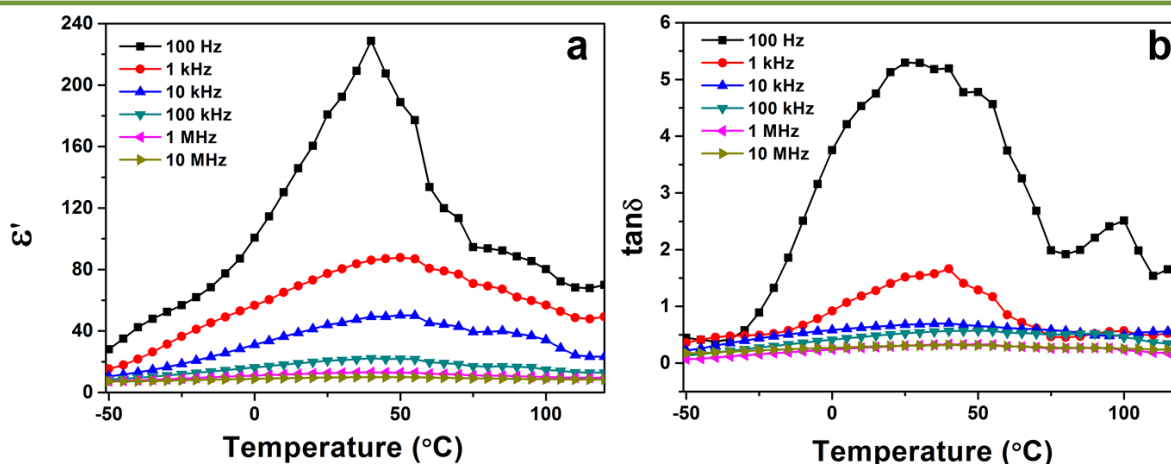


Figure 5.6: Temperature dependence of the (a) real part of dielectric constants and (b) dielectric loss of **9** measured at various frequencies.

This was further substantiated by PXRD analysis and also from unit cell measurement at different temperatures above room temperature. The PXRD obtained in the temperature range between 30 and 125 °C (Figure 5.7a) shows that the profile patterns match well with the simulated pattern up to 50 °C. However, it changes at 70 °C and above showing a slight deviation from the as-synthesized phase but matches very well with the PXRD pattern of the desolvated sample of **9**. Unit cell parameters obtained on a single crystal of **9** at higher temperatures (beyond 50 °C) shows a slight variation in the lattice distances consistent with the loss of solvates but yet with the retention of the polar $P2_1$ space group (Appendix A5.7). This suggests that even after desolvation the polar arrangement of cations and anions is retained in **9**. However, we were unable to solve the structure of **9** beyond 50 °C due to the presence of weak diffraction spots at higher angles. The TGA-DSC plot shows a weight loss of about 3% up to 100 °C, due to the loss of solvated methanol molecules. But this loss is not associated with any phase transition as the DSC data obtained on **9** does not show any endothermic/exothermic anomaly peak between 30 and 160 °C (Figure 5.7b). All these observations evidence that the dielectric anomaly peak in **9**, obtained in the temperature dependent permittivity measurements, was due to the gasification or release of solvated methanol. Furthermore, the low dielectric loss factor coupled with the high ϵ' values suggests

that **9** is a good dielectric material and could be of use for dielectric related applications (Figure 5.6b).

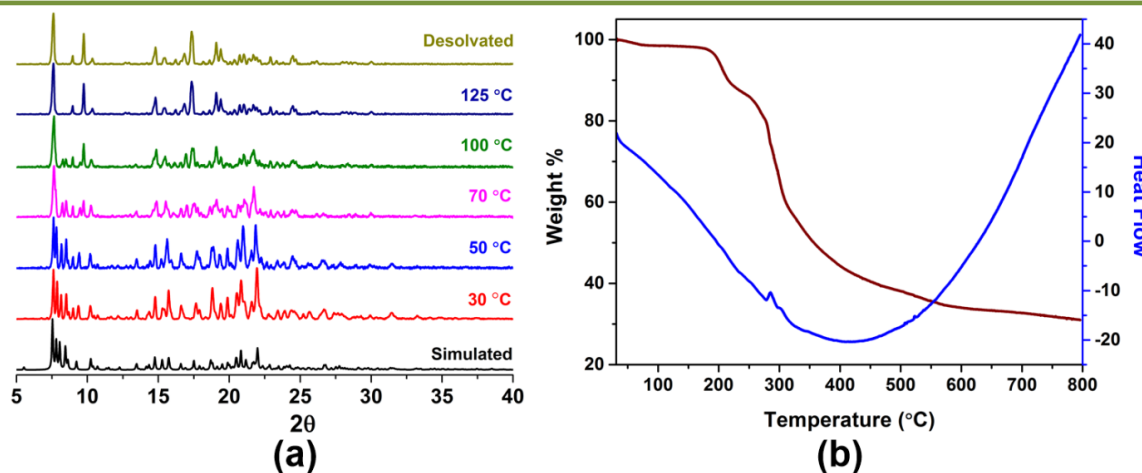


Figure 5.7: (a) Powder X-ray diffraction (PXRD) profiles of **9** at different temperatures. (b) TGA-DSC plot for **9**.

5.4 CONCLUSION

In conclusion, the present work demonstrates our approach to obtain polar organic salts based on phosphonium cations and suitable anions. We utilized the monophosphazene base L^5 , obtained from the deprotonation of tetraanilino phosphonium chloride (L^4), to obtain the polar organic salts **8** and **9** upon reaction with the trimesic and orthophosphoric acids, respectively. Both these salts exhibit polar space groups and exhibit interesting hydrogen bonded 3D network. The ferroelectric and dielectric measurements on a compressed pellet of **8** gave low polarization as well as very low dielectric constant values. On the other hand, the ferroelectric measurements on **9** (structural analogue of KDP) gave a well saturated P-E loop with a high polarization value of $28.88 \mu\text{Ccm}^{-2}$ at 1 Hz frequency, which is higher than most of the typical hydrogen bonded ferroelectrics (such as KDP, TGS, Rochelle salt). Furthermore, compound **9** was found to possess high fatigue tolerance and low coercive field (E_c) of 3.3 kVcm^{-1} , which indicates the swift switching of polarizable domains. Thus, the results described in this chapter demonstrate a facile approach to obtain polar molecular compounds with attractive ferroelectric and dielectric properties and will pave the way for the development of new practical ferroelectric materials.

5.5 REFERENCES

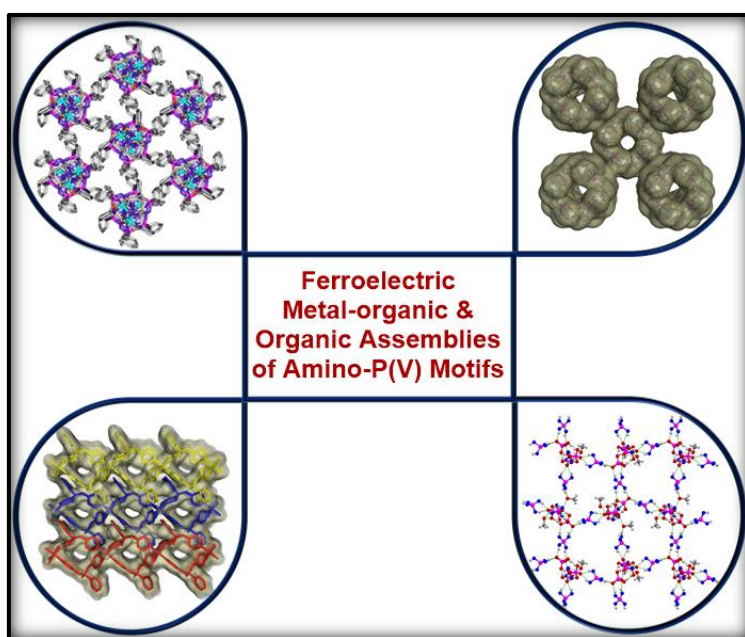
- (1) Haertling, G. H. *J. Am. Ceram. Soc.* **1999**, *82*, 797.
- (2) Scott, J. F.; De Araujo, C. A. P. *Science* **1989**, *246*, 1400.
- (3) Lines, M. E.; Glass, A. M. *Principles and applications of ferroelectrics and related materials*. Clarendon press Oxford: 1977.
- (4) Scott, J. F. *Ferroelectric memories*. Springer Science & Business Media: 2000; Vol. 3.
- (5) Xu, Y. *Ferroelectric materials and their applications*. Elsevier: 2013.
- (6) Uchino, K. *Ferroelectric Devices 2nd Edition*. CRC press: 2009.
- (7) Dawber, M.; Rabe, K. M.; Scott, J. F. *Rev. Mod. Phys.* **2005**, *77*, 1083.
- (8) Long, X.; Ye, Z.-G. *Chem. Mater.* **2007**, *19*, 1285.
- (9) Park, B. H.; Kang, B. S.; Bu, S. D.; Noh, T. W.; Lee, J.; Jo, W. *Nature* **1999**, *401*, 682.
- (10) Ramesh, R.; Lee, J.; Sands, T.; Keramidas, V. G.; Auciello, O. *Appl. Phys. Lett.* **1994**, *64*, 2511.
- (11) Saito, Y.; Takao, H.; Tani, T.; Nonoyama, T.; Takatori, K.; Homma, T.; Nagaya, T.; Nakamura, M. *Nature* **2004**, *432*, 84.
- (12) Zylberberg, J.; Belik, A. A.; Takayama-Muromachi, E.; Ye, Z.-G. *Chem. Mater.* **2007**, *19*, 6385.
- (13) Ye, H.-Y.; Zhang, Y.; Fu, D.-W.; Xiong, R.-G. *Angew. Chem. Int. Ed.* **2014**, *53*, 6724.
- (14) Tayi, A. S.; Kaeser, A.; Matsumoto, M.; Aida, T.; Stupp, S. I. *Nat. Chem.* **2015**, *7*, 281.
- (15) Horiuchi, S.; Tokura, Y. *Nat. Mater.* **2008**, *7*, 357.
- (16) Tayi, A. S.; Shveyd, A. K.; Sue, A. C.-H.; Szarko, J. M.; Rolczynski, B. S.; Cao, D.; Kennedy, T. J.; Sarjeant, A. A.; Stern, C. L.; Paxton, W. F.; Wu, W.; Dey, S. K.; Fahrenbach, A. C.; Guest, J. R.; Mohseni, H.; Chen, L. X.; Wang, K. L.; Stoddart, J. F.; Stupp, S. I. *Nature* **2012**, *488*, 485.
- (17) Shi, P.-P.; Tang, Y.-Y.; Li, P.-F.; Liao, W.-Q.; Wang, Z.-X.; Ye, Q.; Xiong, R.-G. *Chem. Soc. Rev.* **2016**, *45*, 3811.
- (18) Sato, M. *Nat. Chem.* **2016**, *8*, 644.
- (19) Horiuchi, S.; Ishii, F.; Kumai, R.; Okimoto, Y.; Tachibana, H.; Nagaosa, N.; Tokura, Y. *Nat. Mater.* **2005**, *4*, 163.
- (20) Horiuchi, S.; Kumai, R.; Tokura, Y. *Chem. Commun.* **2007**, 2321.
- (21) Harada, J.; Shimojo, T.; Oyamaguchi, H.; Hasegawa, H.; Takahashi, Y.; Satomi, K.; Suzuki, Y.; Kawamata, J.; Inabe, T. *Nat. Chem.* **2016**, *8*, 946.

- (22) Li, P.-F.; Tang, Y.-Y.; Wang, Z.-X.; Ye, H.-Y.; You, Y.-M.; Xiong, R.-G. *Nat. Commun.* **2016**, *7*, 13635.
- (23) Shi, P.-P.; Tang, Y.-Y.; Li, P.-F.; Ye, H.-Y.; Xiong, R.-G. *J. Am. Chem. Soc.* **2017**, *139*, 1319.
- (24) Tang, Y.-Y.; Zhang, W.-Y.; Li, P.-F.; Ye, H.-Y.; You, Y.-M.; Xiong, R.-G. *J. Am. Chem. Soc.* **2016**, *138*, 15784.
- (25) Ye, H.-Y.; Ge, J.-Z.; Tang, Y.-Y.; Li, P.-F.; Zhang, Y.; You, Y.-M.; Xiong, R.-G. *J. Am. Chem. Soc.* **2016**, *138*, 13175.
- (26) Akutagawa, T.; Koshinaka, H.; Sato, D.; Takeda, S.; Noro, S.-I.; Takahashi, H.; Kumai, R.; Tokura, Y.; Nakamura, T. *Nat. Mater.* **2009**, *8*, 342.
- (27) Fu, D. W.; Zhang, W.; Cai, H. L.; Zhang, Y.; Ge, J. Z.; Xiong, R.-G.; Huang, S. D. *J. Am. Chem. Soc.* **2011**, *133*, 12780.
- (28) Hang, T.; Zhang, W.; Ye, H.-Y.; Xiong, R.-G. *Chem. Soc. Rev.* **2011**, *40*, 3577.
- (29) Zhang, Y.; Ye, H.-Y.; Fu, D.-W.; Xiong, R.-G. *Angew. Chem. Int. Ed.* **2014**, *53*, 2114.
- (30) Horiuchi, S.; Tokunaga, Y.; Giovannetti, G.; Picozzi, S.; Itoh, H.; Shimano, R.; Kumai, R.; Tokura, Y. *Nature* **2010**, *463*, 789.
- (31) Horiuchi, S.; Kumai, R.; Tokura, Y. *Adv. Mater.* **2011**, *23*, 2098.
- (32) Horiuchi, S.; Kobayashi, K.; Kumai, R.; Ishibashi, S. *Nat. Commun.* **2017**, *8*, 14426.
- (33) Fu, D.-W.; Zhang, W.; Cai, H.-L.; Ge, J.-Z.; Zhang, Y.; Xiong, R.-G. *Adv. Mater.* **2011**, *23*, 5658.
- (34) Fu, D.-W.; Cai, H.-L.; Liu, Y.; Ye, Q.; Zhang, W.; Zhang, Y.; Chen, X.-Y.; Giovannetti, G.; Capone, M.; Li, J.; Xiong, R.-G. *Science* **2013**, *339*, 425.
- (35) Valasek, J. *Phys. Rev.* **1921**, *17*, 475.
- (36) Samara, G. A. *Ferroelectrics* **1973**, *5*, 25.
- (37) Matthias, B. T.; Miller, C. E.; Remeika, J. P. *Phys. Rev.* **1956**, *104*, 849.
- (38) Fatuzzo, E.; Merz, W. J. *Phys. Rev.* **1959**, *116*, 61.
- (39) Zhang, Y.; Ye, H.-Y.; Cai, H.-L.; Fu, D.-W.; Ye, Q.; Zhang, W.; Zhou, Q.; Wang, J.; Yuan, G.-L.; Xiong, R.-G. *Adv. Mater.* **2014**, *26*, 4515.
- (40) Pan, Q.; Liu, Z.-B.; Tang, Y.-Y.; Li, P.-F.; Ma, R.-W.; Wei, R.-Y.; Zhang, Y.; You, Y.-M.; Ye, H.-Y.; Xiong, R.-G. *J. Am. Chem. Soc.* **2017**, *139*, 3954.
- (41) Zhang, Y.; Liao, W.-Q.; Fu, D.-W.; Ye, H.-Y.; Liu, C.-M.; Chen, Z.-N.; Xiong, R.-G. *Adv. Mater.* **2015**, *27*, 3942.

- (42) Zhang, Y.; Liao, W. Q.; Fu, D. W.; Ye, H. Y.; Chen, Z. N.; Xiong, R. G. *J. Am. Chem. Soc.* **2015**, *137*, 4928.
- (43) Ye, H. Y.; Zhou, Q.; Niu, X.; Liao, W. Q.; Fu, D. W.; Zhang, Y.; You, Y. M.; Wang, J.; Chen, Z. N.; Xiong, R. G. *J. Am. Chem. Soc.* **2015**, *137*, 13148.
- (44) Cameron, T. B.; Hanson, H. N.; de la Fuente, G. F.; Huheey, J. E. *Phosphorus, Sulfur Silicon Relat. Elem.* **1993**, *78*, 37.
- (45) Bickley, J. F.; Copsey, M. C.; Jeffery, J. C.; Leedham, A. P.; Russell, C. A.; Stalke, D.; Steiner, A.; Stey, T.; Zacchini, S. *Dalton Trans.* **2004**, 989.
- (46) Sheldrick, G. M. *Acta Crystallogr. A* **2008**, *64*, 112.
- (47) Gupta, A. K.; Nicholls, J.; Debnath, S.; Rosbottom, I.; Steiner, A.; Boomishankar, R. *Cryst. Growth Des.* **2011**, *11*, 555.
- (48) Ballabh, A.; Trivedi D. R.; Dastidar, P. *Cryst. Growth Des.* **2005**, *5*, 1545.
- (49) Trivedi, D. R.; Dastidar, P. *Cryst. Growth Des.* **2006**, *6*, 1022.
- (50) Trivedi D. R.; Dastidar, P. *Cryst. Growth Des.* **2006**, *6*, 2114.
- (51) Ok, K. M.; Chi, E. O.; Halasyamani, P. S. *Chem. Soc. Rev.* **2006**, *35*, 710.
- (52) Li, Y.-H.; Qu, Z.-R.; Zhao, H.; Ye, Q.; Xing, L.-X.; Wang, X.-S.; Xiong, R.-G.; You, X.-Z. *Inorg. Chem.* **2004**, *43*, 3768.
- (53) Shamiryani, D.; Abell, T.; Iacopi, F.; Maex, K. *Mater. Today* **2004**, *7*, 34.
- (54) Law, C. W.; Tong, K. Y.; Li, J. H.; Li, K. *Solid-State Electronics* **2000**, *44*, 1569.
- (55) Srivastava, A. K.; Praveenkumar, B.; Mahawar, I. K.; Divya, P.; Shalini, S.; Boomishankar, R. *Chem. Mater.* **2014**, *26*, 3811.
- (56) Dong, X.-Y.; Li, B.; Ma, B.-B.; Li, S.-J.; Dong, M.-M.; Zhu, Y.-Y.; Zang, S.-Q.; Song, Y.; Hou, H.-W.; Mak, T. C. W. *J. Am. Chem. Soc.* **2013**, *135*, 10214.
- (57) Srivastava, A. K.; Divya, P.; Praveenkumar, B.; Boomishankar, R. *Chem. Mater.* **2015**, *27*, 5222.

End of Chapter 5

Chapter 6



Thesis Conclusion and Future Perspectives

In summary, this thesis presents a rational approach for the design, synthesis and characterization of metal-organic and simple-organic assemblies in non-centrosymmetric polar space groups by employing amino-P(V) motifs. The molecular components that constitute these self-assemblies have been looked closely with the view of imparting the required non-centrosymmetry and polar order in them. For this we utilized a series of isomeric flexible dipodal amino-P(V) ligands which on reaction with transition metal ions resulted in metal-organic assemblies with diverse structures in centrosymmetric as well as non-centrosymmetric space groups. Thus, it has been found that choice of counter anions such as nitrate and perchlorate anions can alter the structure and long-range order that are responsible for the ferroelectric polarization in a molecule (Chapter 2). Interestingly, we have also found that ferroelectric polarization can be tuned by host-guest interactions in metal-ligand cavitands. Thus, the Ni(II) and Co(II) based tetrameric cavitands not only can encapsulate hydrated alkali metal cations (in higher hydration spheres) but also shows significant variations in the ferroelectric polarization attributes such as remnant polarization, coercive field and fatigue tolerance (Chapter 3). Further, it has been found that subtle variations in the ligand backbone can alter the dimensionality of the obtained assemblies which again has a significant effect in tuning the polarization of the obtained assemblies (Chapter 4). Moreover, it is to be mentioned that the presence of guest solvates such as water and methanol in the framework lattice can influence the magnitude of polarization in these assemblies. Further, we have been successful in demonstrating ferroelectricity in polar organic salts that are stabilized by tetraanilino phosphonium cations (Chapter 5). The ferroelectric responses of some of the reported materials in this thesis are of great interest for academic researchers and are somewhat better in comparison with several reported supramolecular ferroelectric systems (Table 6.1). However, they still require further improvements in terms of their performance at higher frequencies and ability to form thin films to compete with the performance of traditional ferroelectrics and practical utility as ferroelectric devices. Nevertheless, the results demonstrated in this thesis can be of some help in developing rational approaches and design strategies for overcoming the major roadblocks to attain practically useful ferroelectric assemblies.

Table 6.1: Remnant Polarization (P_r) and Coercive Field (E_c) value of selected typical ferroelectric materials for comparison with the metal-organic and organic ferroelectric assemblies reported in this thesis.

S.No.	Materials	P_r (μCcm^{-2}); Temperature (K)	E_c (kVcm^{-1})	References
1.	Rochelle Salt	0.25; 276K	0.2	1,2
2.	Triglycine sulphate (TGS)	3.8; 220K	0.9	1,3
3.	KH_2PO_4 (KDP)	5	0.1	1,4
4.	Nylon-11	5; RT	600	1
5.	Guanidinium perchlorate	8.4; RT	8.7	5
6.	Guanidinium tetrafluoroborate	8.5; RT	11.4	5
7.	Diisopropylammonium Chloride	8.9; 440K	9	6
8.	NaNO_2	10; 140K	5	1
9.	Copolymer P(VDF-TrFE)	8; RT	500	1,7
10.	Vinylidene fluoride (VDF) oligomer	13; RT	1200	1,8
11.	Hdabco ReO_4	16; RT	>30	1
12.	Diisopropylammonium bromide	23; 426K	5	9
13.	Barium Titanate (BaTiO_3)	26; RT	10	1
14.	Croconic Acid	30; RT	14	10
15.	Helical 1D- $\{\text{Cu}^{\text{II}}\text{L}_2\}_n$ assembly	2.6; RT	16	11; Chapter 2
16.	Tetrameric Ni/Co- Cavitand and their host-guest systems	27 to 30.5; RT	8.6 to 16.7	12; Chapter 3
17.	2D- $\{\text{Cu}^{\text{II}}\text{L}_2\}_n$ assembly	28; RT	5.9	13; Chapter 4
18.	Tetraanilino phosphonium dihydrogen phosphate ($^{\text{ta}}\text{PDP}$)	30; RT	3.3	Chapter 5

REFERENCES

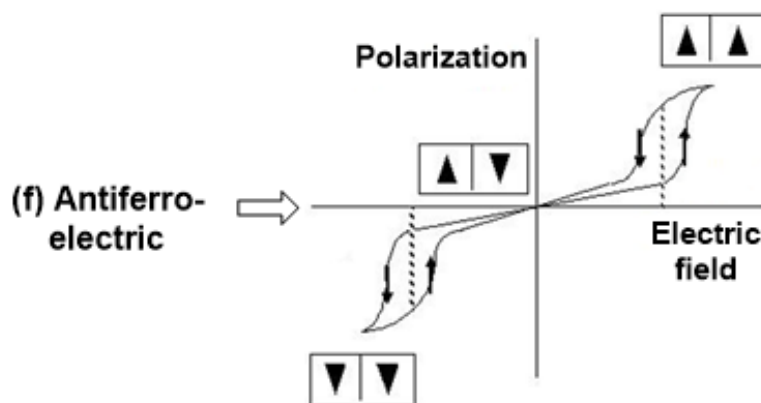
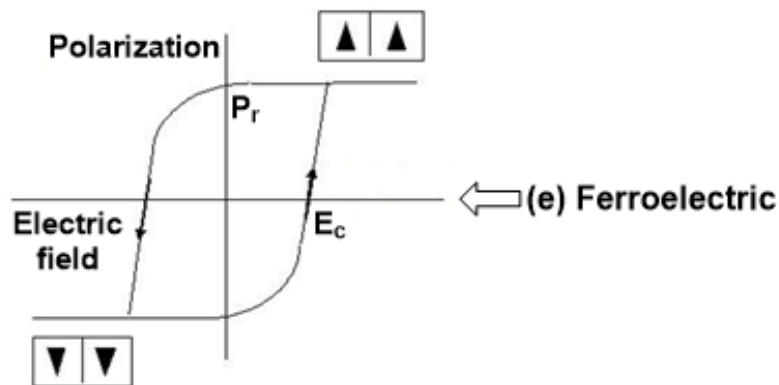
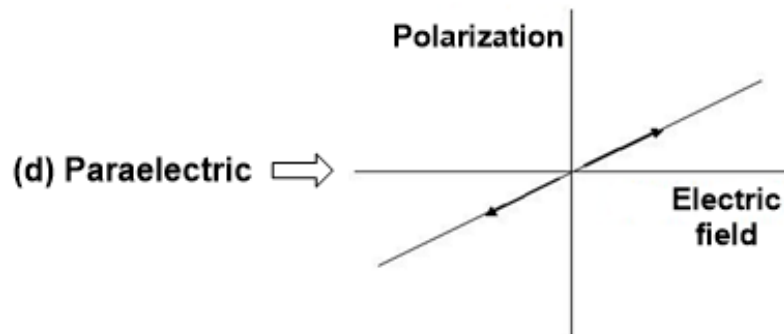
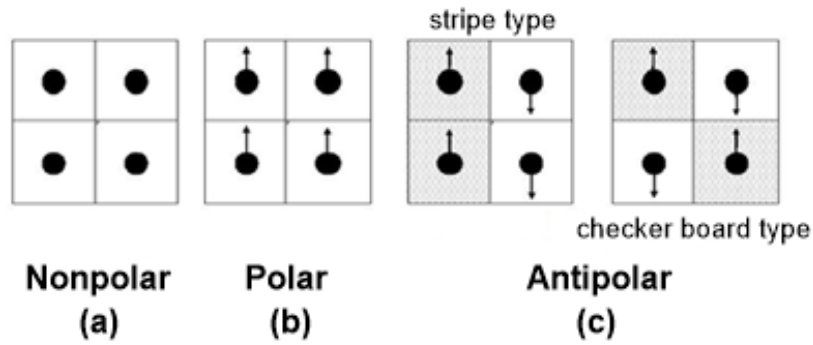
- (1) Horiuchi, S.; Tokura, Y. *Nat. Mater.* **2008**, *7*, 357-366.
- (2) Valasek, J. *Phys. Rev.* **1921**, *17*, 475-481.
- (3) Hoshino, S.; Mitsui, T.; Jona, F.; Pepinsky, R. *Phys. Rev.* **1957**, *107*, 1255.
- (4) Busch, G.; Scherrer, P. *Naturwissenschaften* **1935**, *23*, 737.
- (5) Szafranski, M. *J. Phys. Chem. B* **2011**, *115*, 8755.
- (6) Fu, D.-W.; Zhang, W.; Cai, H. L.; Ge, J. Z.; Zhang, Y.; Xiong, R. G. *Adv. Mater.* **2011**, *23*, 5658.
- (7) Noda, K.; Ishida, K.; Kubono, A.; Horiuchi, T.; Yamada, H.; Matsushige, K. *J. Appl. Phys.* **2003**, *93*, 2866.
- (8) Furukawa, T. *Phase Trans.* **1989**, *18*, 143.
- (9) Fu, D.-W.; Cai, H.-L.; Liu, Y.; Ye, Q.; Zhang, W.; Zhang, Y.; Chen, X.-Y.; Giovannetti, G.; Capone, M.; Li, J.; Xiong, R.-G. *Science* **2013**, *339*, 425.
- (10) Horiuchi, S.; Kobayashi, K.; Kumai, R.; Ishibashi, S. *Nat. Commun.* **2017**, *8*, 14426.
- (11) Srivastava, A. K.; Praveenkumar, B.; Mahawar, I. K.; Divya, P.; Shalini, S.; Boomishankar, R. *Chem. Mater.* **2014**, *26*, 3811.
- (12) Srivastava, A. K.; Vijayakanth, T.; Divya, P.; Praveenkumar, B.; Steiner, A.; Boomishankar, R. *J. Mater. Chem. C* **2017**, *5*, 7352.
- (13) Srivastava, A. K.; Divya, P.; Praveenkumar, B.; Boomishankar, R. *Chem. Mater.* **2015**, *27*, 5222.

End of Chapter 6

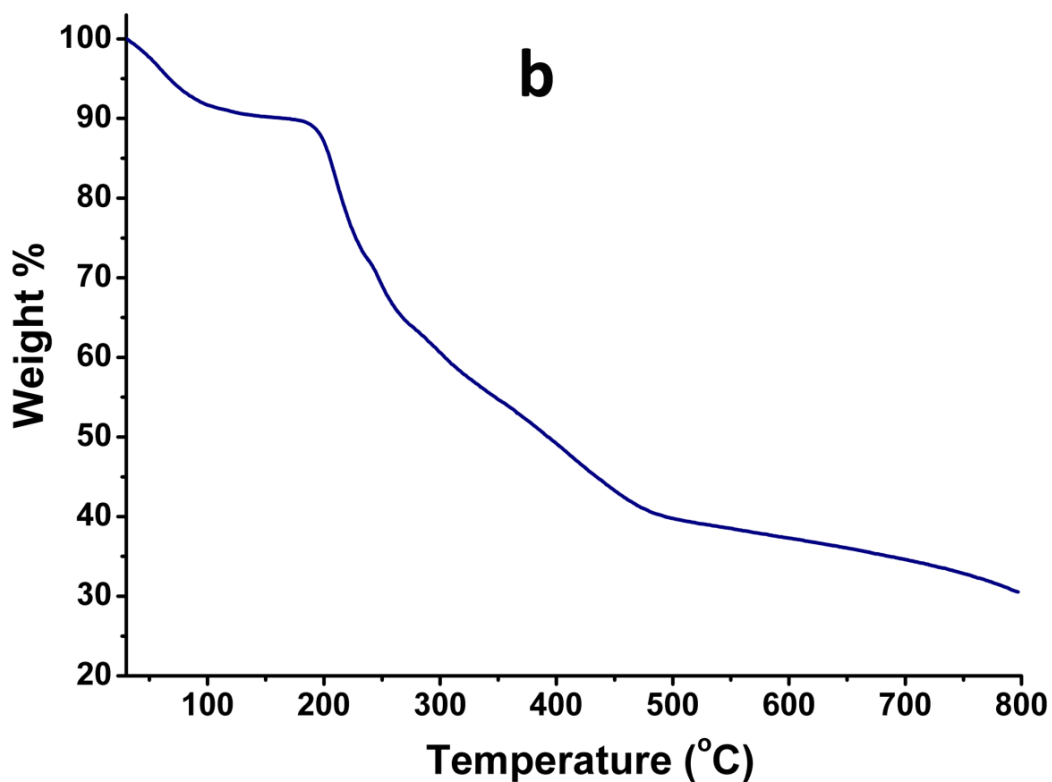
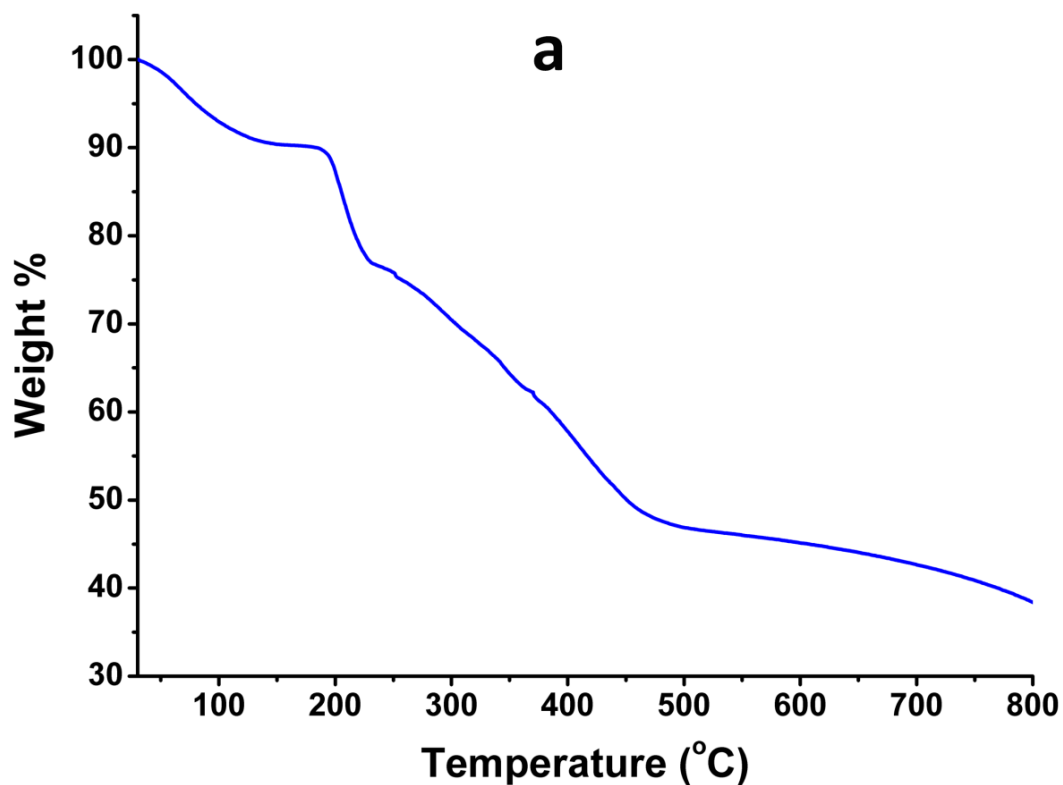


Appendix

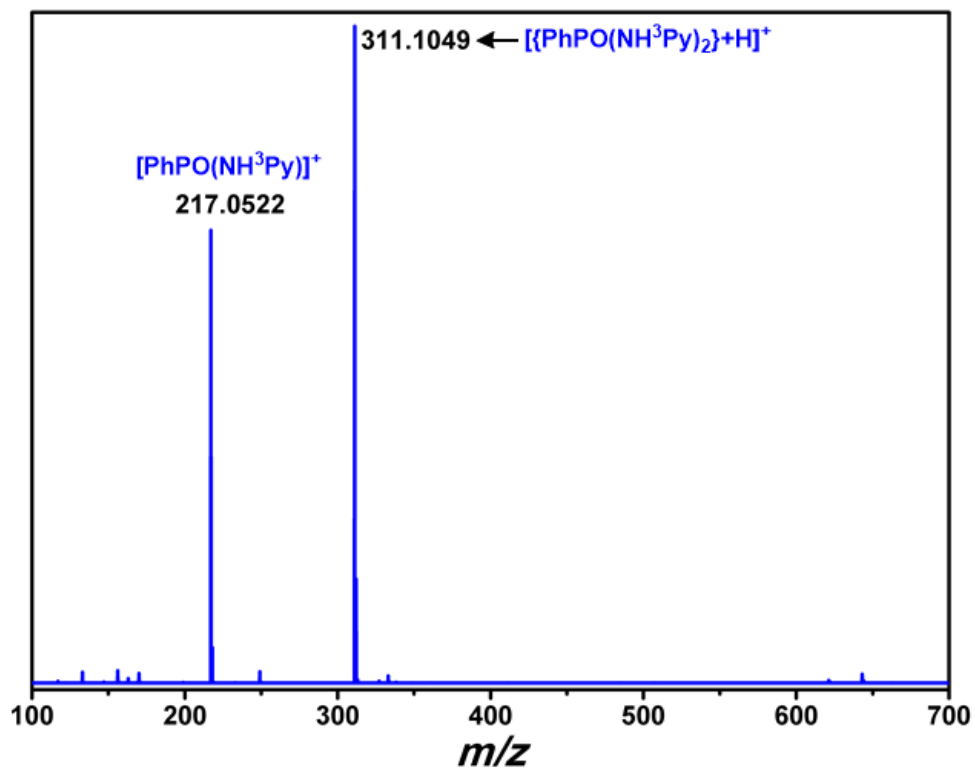
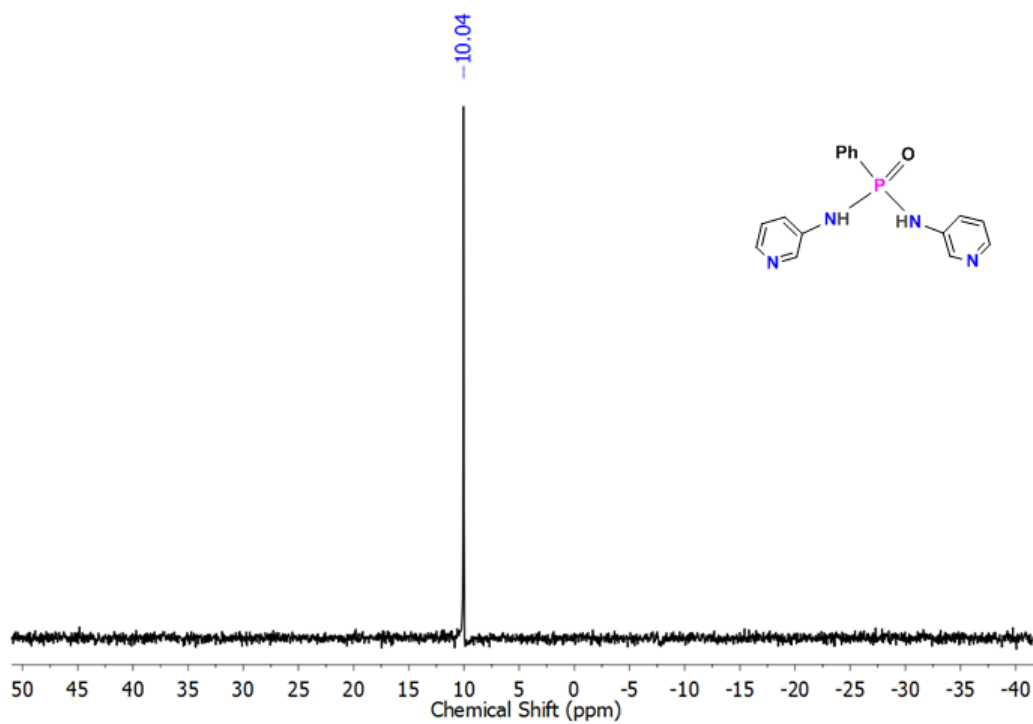


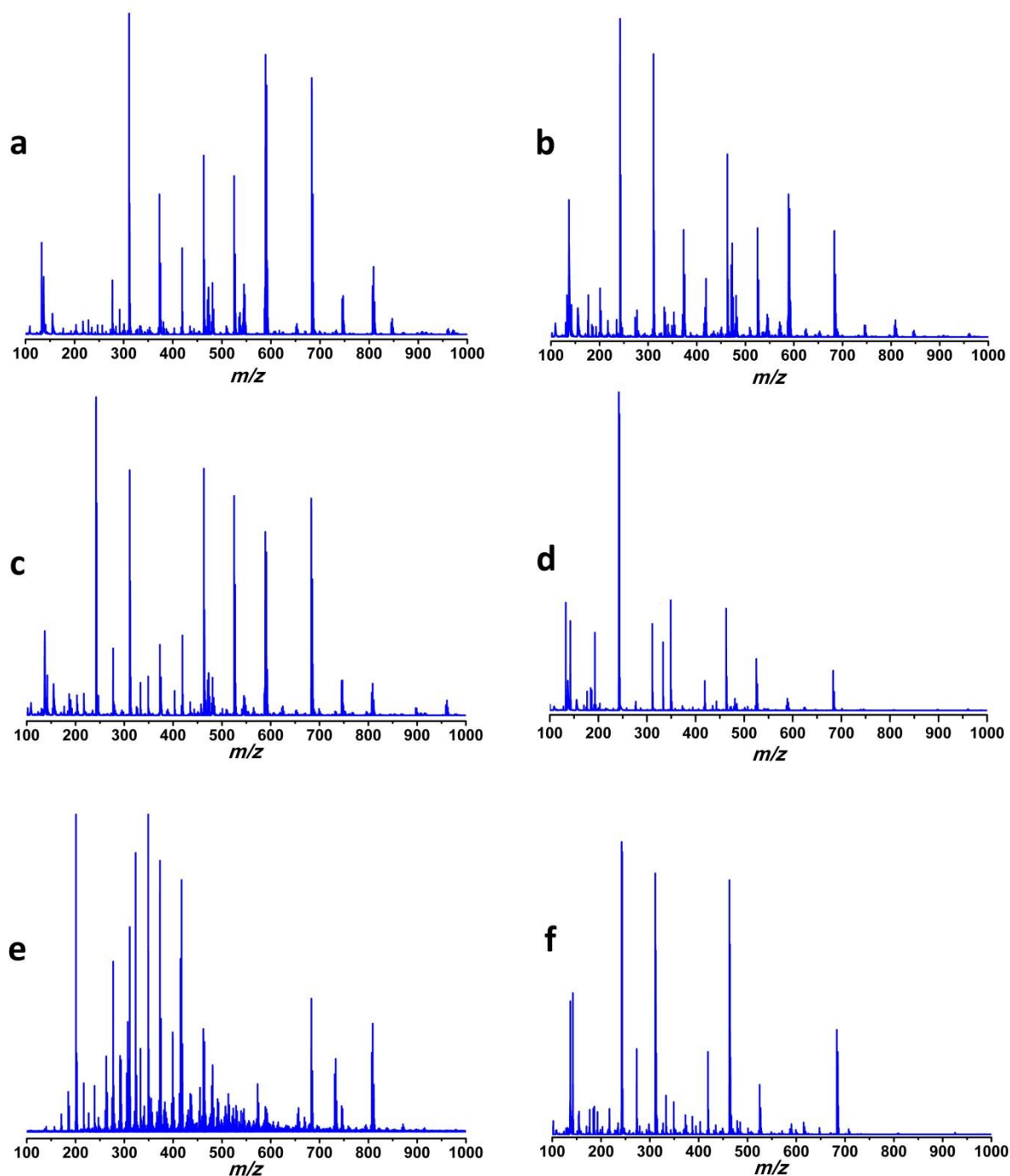


Appendix A1.1: Schematic of the arrangement of dipoles as (a) nonpolar, (b) polar, and (c) antipolar models for the crystalline materials. Polarization versus Electric field loops for (d) paraelectric, (e) ferroelectric, and (f) antiferroelectric materials. (Adopted from “Uchino, K. *Actuators* **2016**, 5, 11” © 2016 by the author)

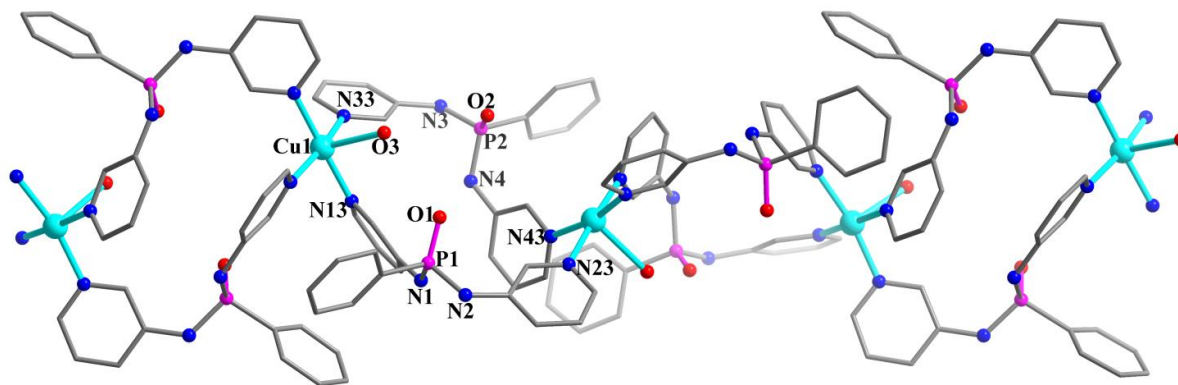


Appendix A2.1: Thermogravimetric analysis data for (a) **2** and (b) **2a**.

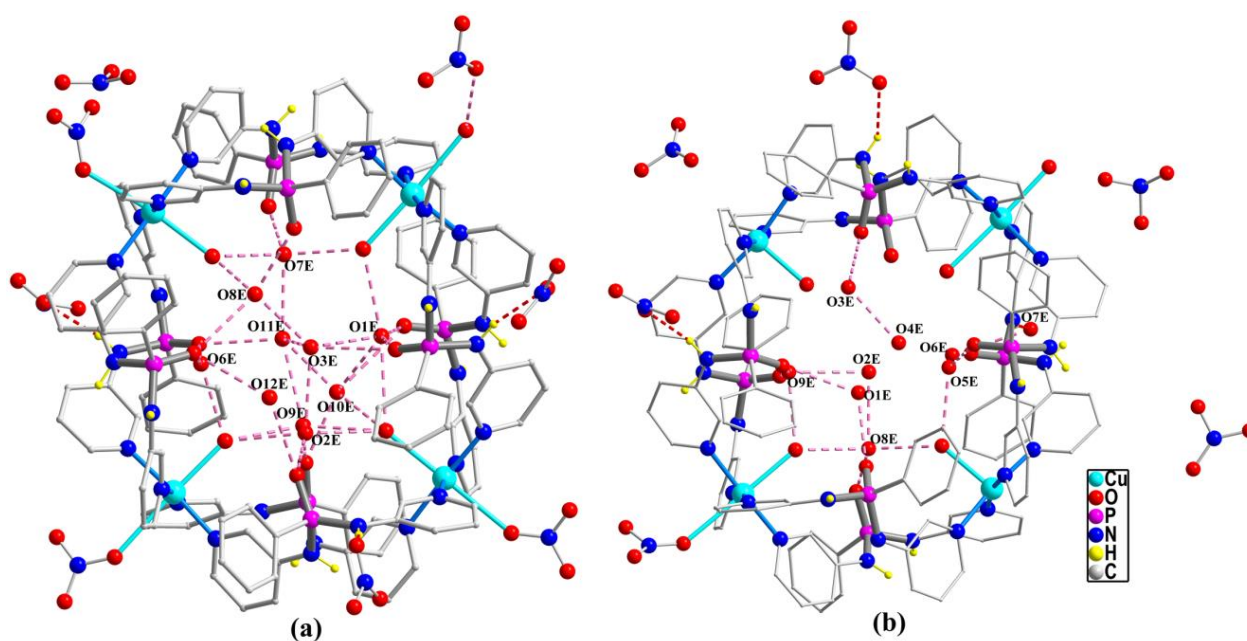
Appendix A2.2: ESI-mass spectrum of L¹.Appendix A2.3: ³¹P-NMR spectrum of L¹.



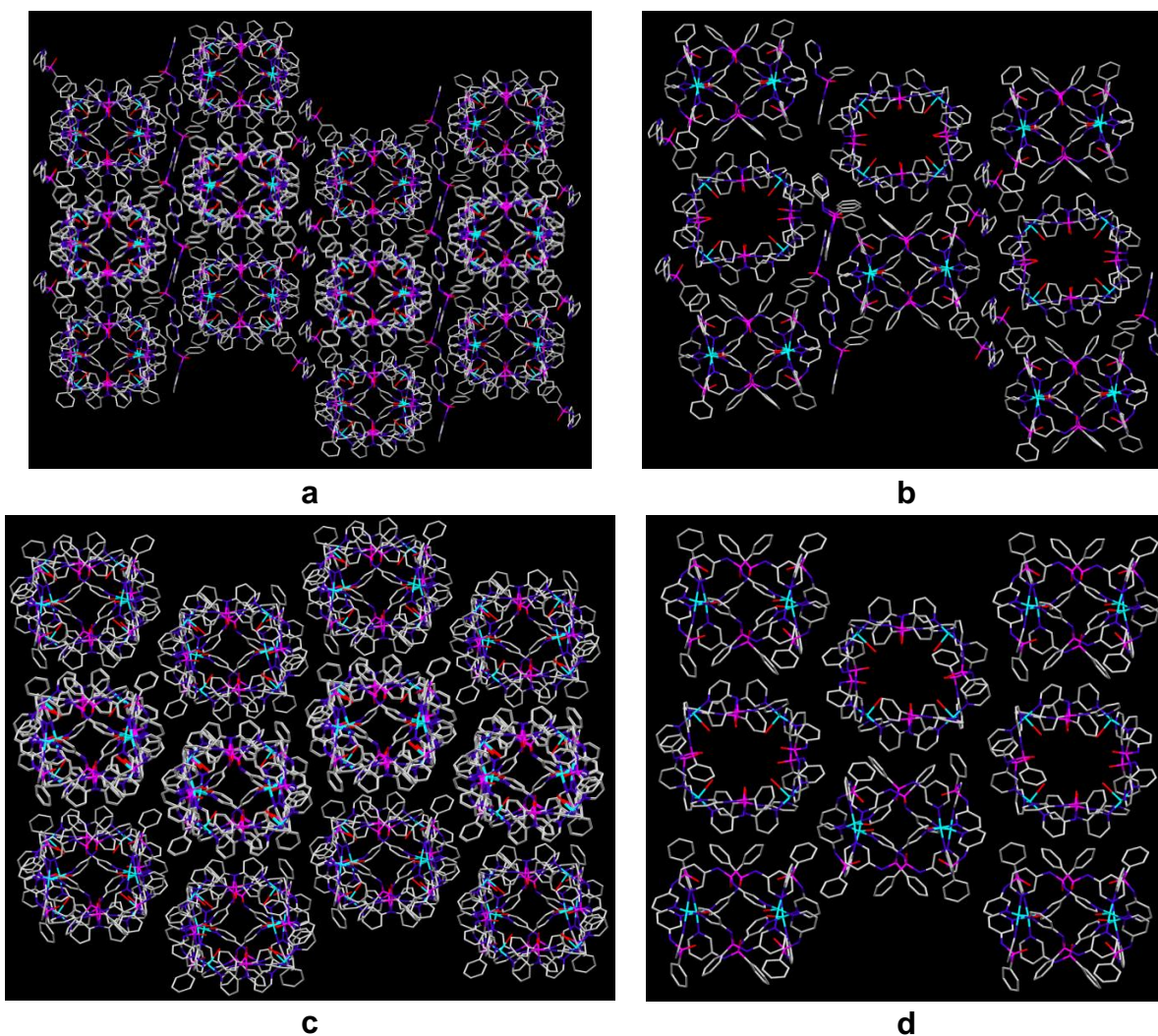
Appendix A2.4: MALDI-TOF mass spectrum of (a) **1**, (b) **1a**, (c) **2**, (d) **2a**, (e) **2**·[K(H₂O)₈], and (f) **3**. The peaks in the spectra suggest that all these assemblies are built from the same set of repeating units in their solution, which associate to form distinct assemblies under different conditions.



Appendix A2.5: Crystal structure of 1a.

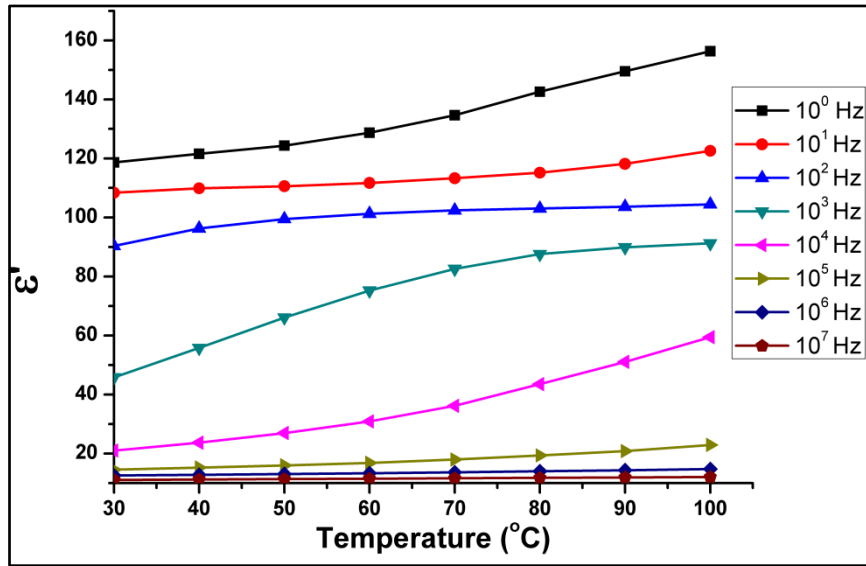


Appendix A2.6: Intrinsic pores in **2** and **2a** filled with disordered solvate water molecules. The molecular structure of **2** consists of 3.5 encapsulated H₂O molecules and **2a** consists of 5.5 H₂O molecules.

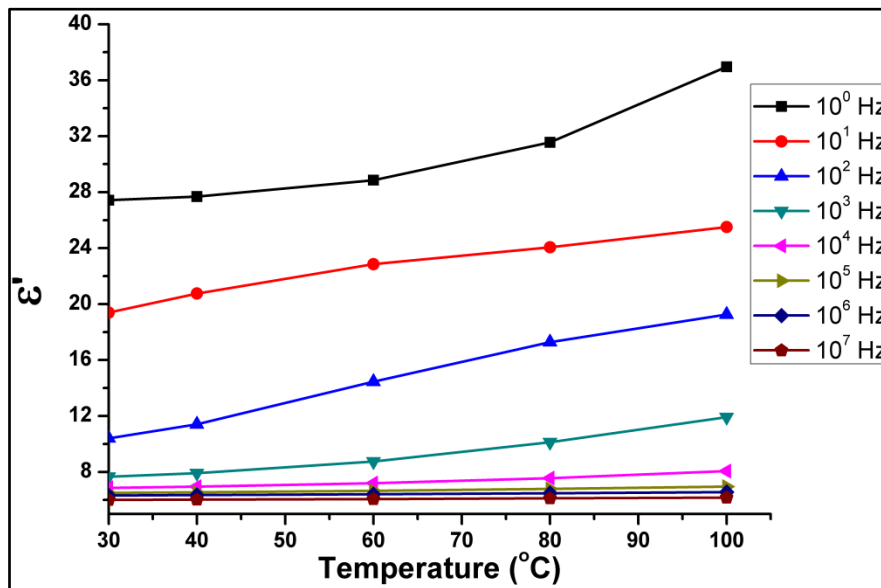


Appendix A2.7: Packing Diagram in (a) **2** and (c) **2a** showing the hindered access to their intrinsic cavities. View of a single sheet of the packing layers in (b) **2** and (d) **2a**.

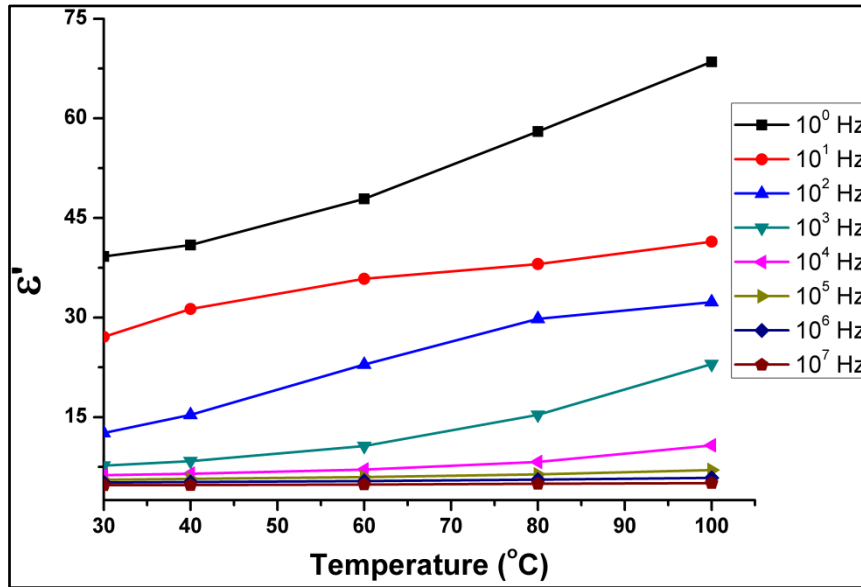
Dielectric and Ferroelectric Measurements



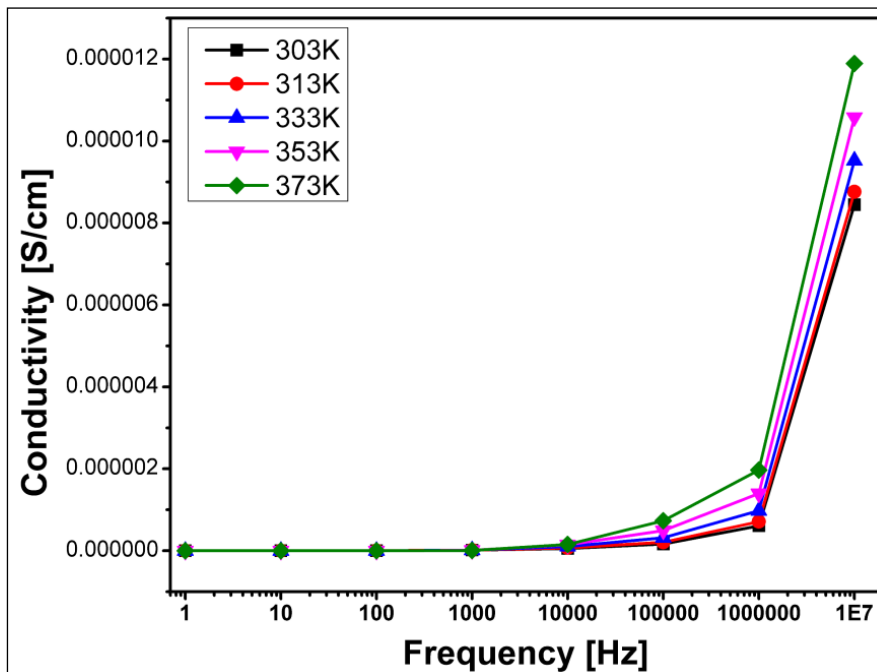
Appendix A2.8: Temperature dependence of dielectric constant for 1.



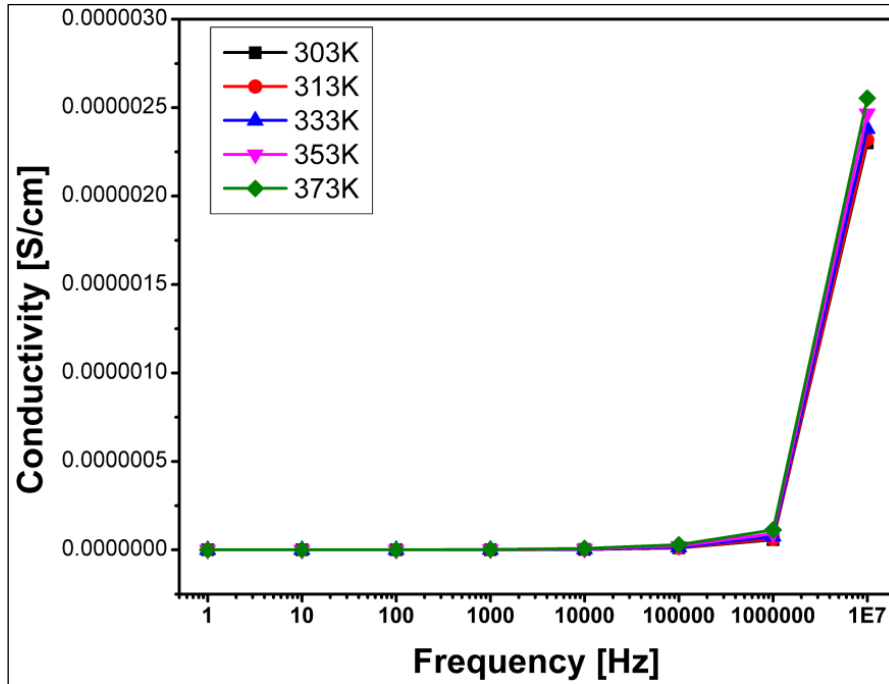
Appendix A2.9: Temperature dependence of dielectric constant for 1a.



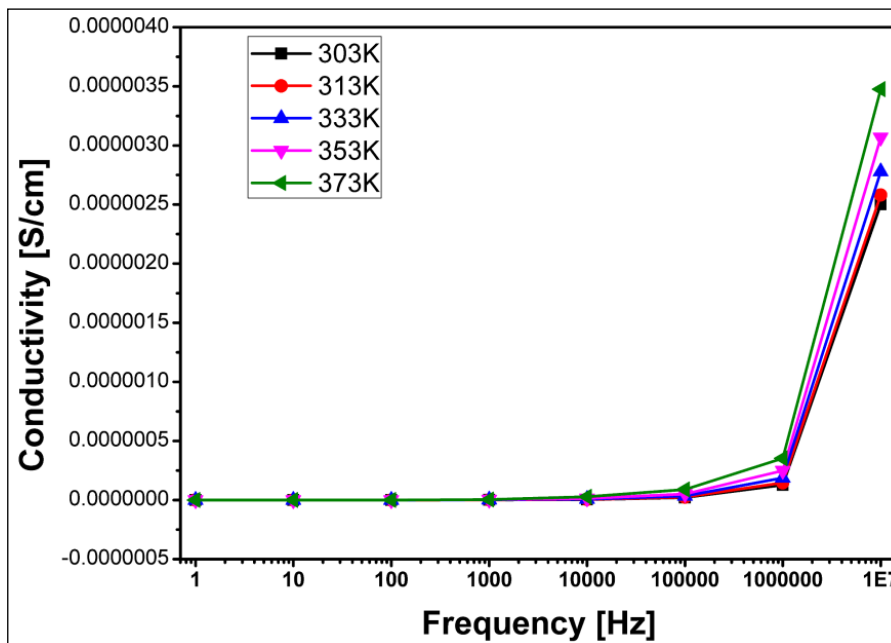
Appendix A2.10: Temperature dependence of dielectric constant for 2.



Appendix A2.11: Conductivity vs. frequency plot for 1.

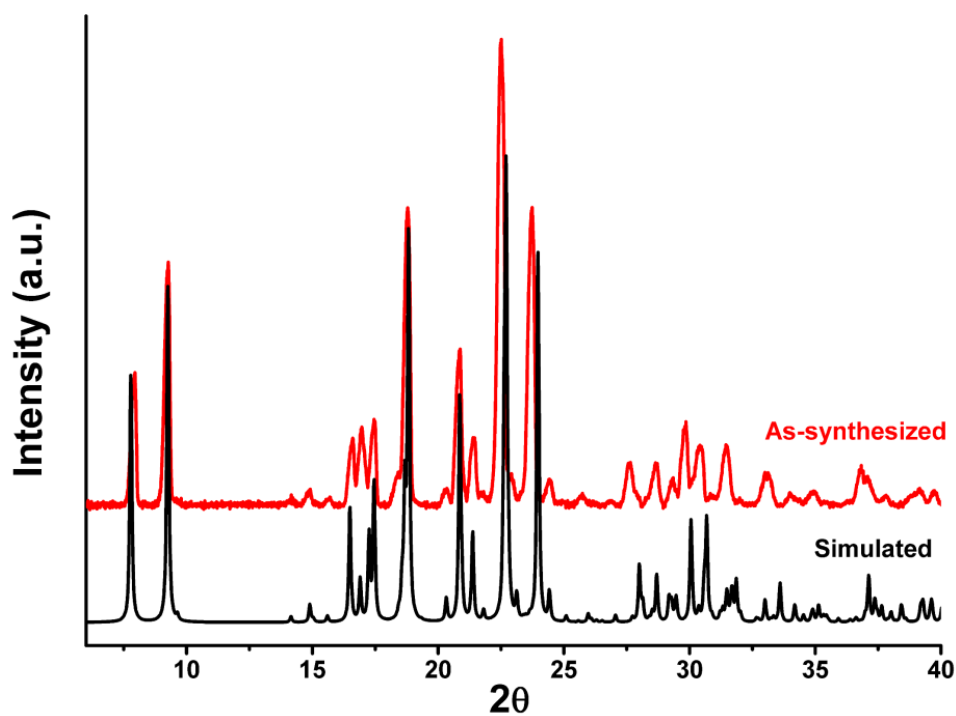
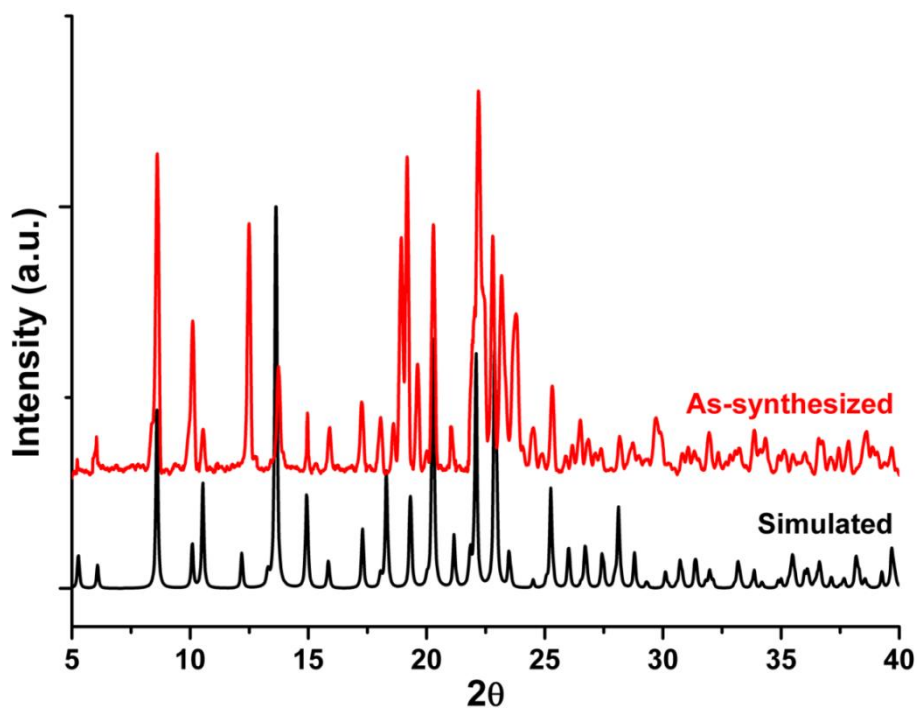


Appendix A2.12: Conductivity vs. frequency plot for 1a.

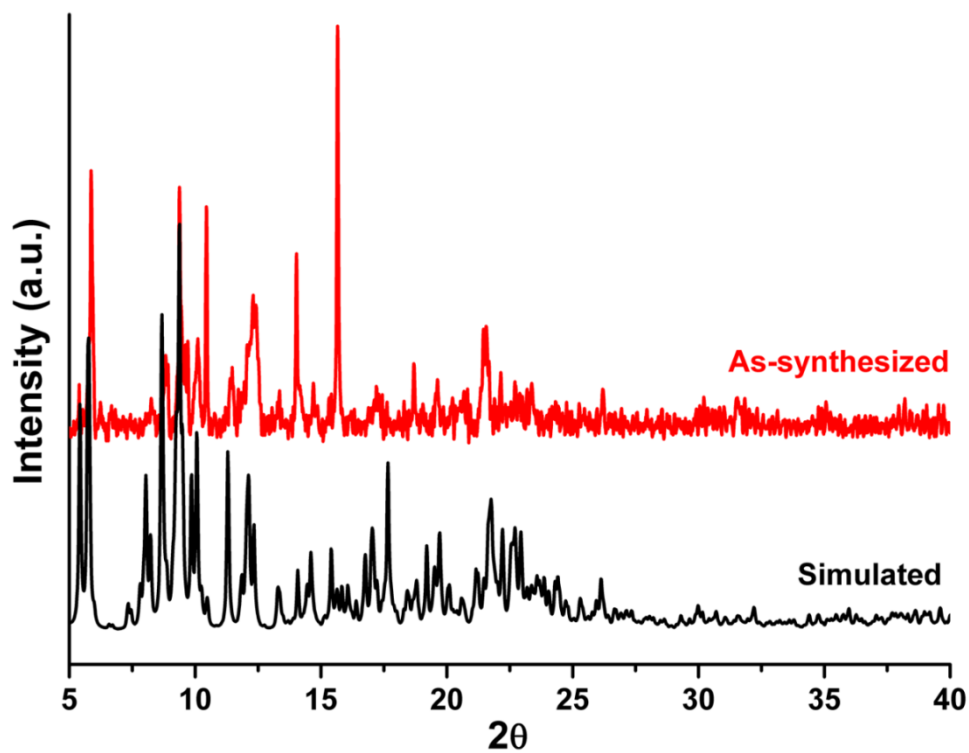


Appendix A2.13: Conductivity vs. frequency plot for 2.

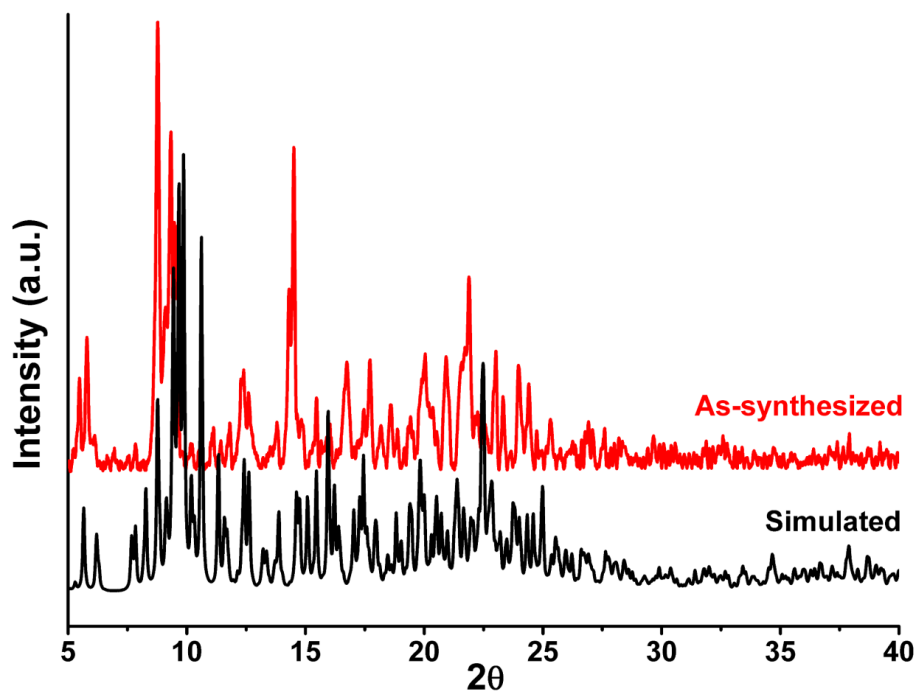
Powder X-ray Diffraction (PXRD) Analysis

Appendix A2.14: PXRD pattern of L¹.

Appendix A2.15: PXRD plot of 1.



Appendix A2.16: PXRD plot of 2.



Appendix A2.17: PXRD plot of 2a.

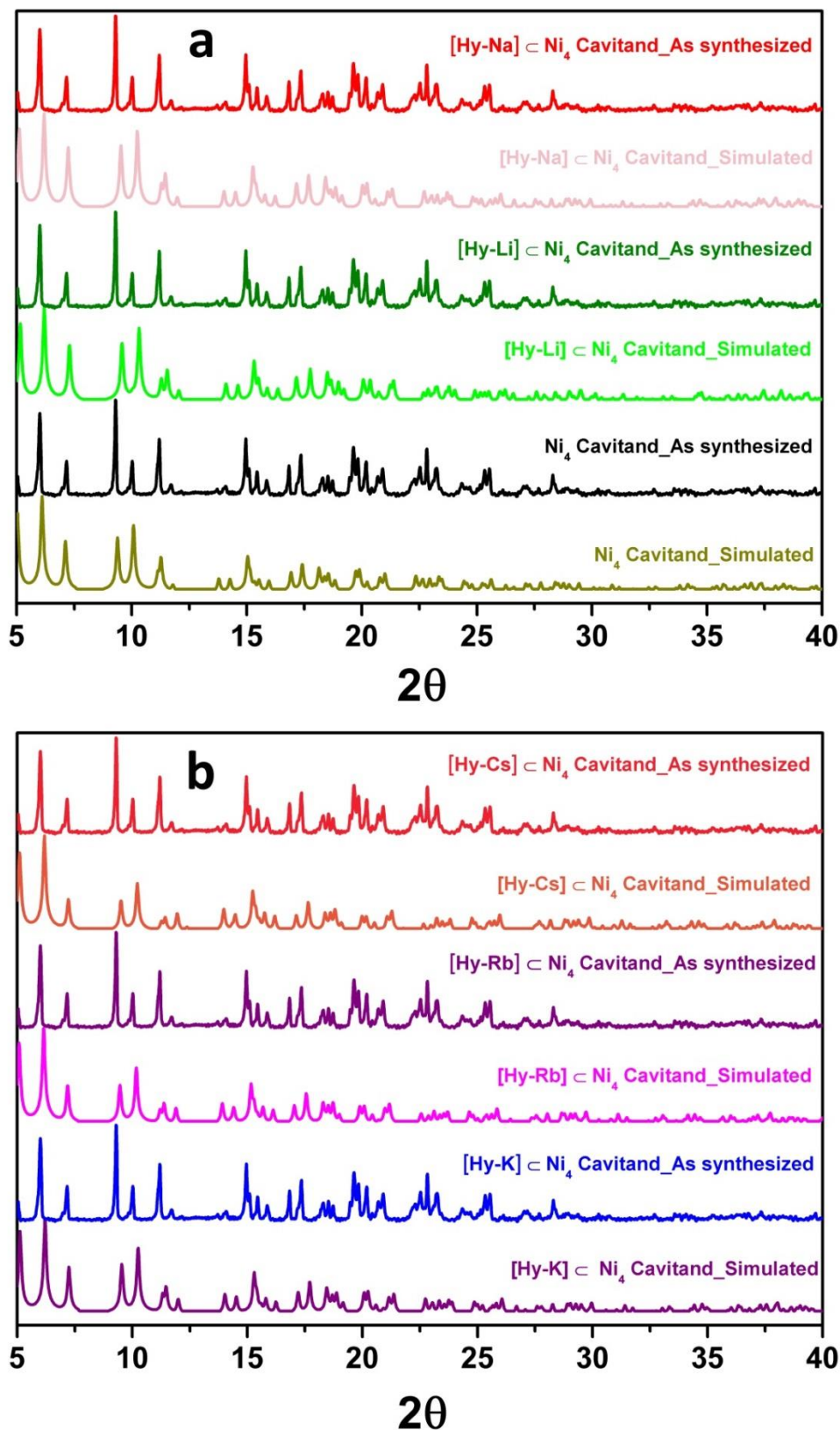
Appendix A2.18: Selected bond-lengths and angles for **L¹**, **1**, **1a**, **2**, **2a**, **2**⊃[K(H₂O)₈] and **3**.

Compound	Bond length	Bond angle
L¹	P(1)-O(1) : 1.488(3) P(1)-N(1) : 1.640(4) P(1)-N(2) : 1.651(4) P(1)-C(1) : 1.801(5)	N(1)-P(1)-N(2) : 105.45(18) O(1)-P(1)-N(1) : 116.40(19) O(1)-P(1)-N(2) : 108.61(17) O(1)-P(1)-C(1) : 112.0(2) N(1)-P(1)-C(1) : 104.2(2) N(2)-P(1)-C(1) : 109.9(2)
1	Cu(1)-N(13) : 2.006(5) Cu(1)-N(63)#1 : 2.009(5) Cu(1)-N(33) : 2.015(5) Cu(1)-N(83)#1 : 2.019(5) Cu(1)-O(5) : 2.403(6) Cu(2)-N(43) : 2.025(5) Cu(2)-N(53) : 2.024(5) Cu(2)-N(23) : 2.025(5) Cu(2)-N(73) : 2.027(5) Cu(2)-O(6)#2 : 2.436(5)	N(13)-Cu(1)-N(63)#1 : 89.3(2) N(13)-Cu(1)-N(33) : 90.37(19) N(63)#1-Cu(1)-N(33) : 167.6(2) N(13)-Cu(1)-N(83)#1 : 178.9(2) N(63)#1-Cu(1)-N(83)#1 : 90.9(2) N(33)-Cu(1)-N(83)#1 : 89.69(19) N(13)-Cu(1)-O(5) : 88.2(2) N(63)#1-Cu(1)-O(5) : 96.6(2) N(33)-Cu(1)-O(5) : 95.7(2) N(83)#1-Cu(1)-O(5) : 90.6(2) N(43)-Cu(2)-N(53) : 166.6(2) N(43)-Cu(2)-N(23) : 91.1(2) N(53)-Cu(2)-N(23) : 88.7(2) N(43)-Cu(2)-N(73) : 87.68(19) N(53)-Cu(2)-N(73) : 93.4(2) N(23)-Cu(2)-N(73) : 176.0(2) N(43)-Cu(2)-O(6)#2 : 94.4(2) N(53)-Cu(2)-O(6)#2 : 98.9(2) N(23)-Cu(2)-O(6)#2 : 89.8(2) N(73)-Cu(2)-O(6)#2 : 86.50(18)
1a	Cu(1)-N(33) : 2.003(4) Cu(1)-N(43)#1 : 2.011(4) Cu(1)-N(23)#2 : 2.027(5) Cu(1)-N(13) : 2.042(5) Cu(1)-O(3) : 2.428(4)	N(33)-Cu(1)-N(43)#1 : 168.23(18) N(33)-Cu(1)-N(23)#2 : 89.97(18) N(43)#1-Cu(1)-N(23)#2 : 89.67(18) N(33)-Cu(1)-N(13) : 89.03(19) N(43)#1-Cu(1)-N(13) : 92.17(18) N(23)#2-Cu(1)-N(13) : 175.64(19) N(33)-Cu(1)-O(3) : 95.68(17) N(43)#1-Cu(1)-O(3) : 96.08(16) N(23)#2-Cu(1)-O(3) : 90.45(17) N(13)-Cu(1)-O(3) : 85.44(17)
2_sq	Cu(1)-N(13) : 1.987(7) Cu(1)-N(133) : 2.008(7) Cu(1)-N(33) : 2.022(7) Cu(1)-N(153) : 2.046(7) Cu(1)-O(1C) : 2.277(6) Cu(2)-N(53) : 2.004(8) Cu(2)-N(73) : 2.019(8) Cu(2)-N(43) : 2.024(7) Cu(2)-N(23) : 2.045(8) Cu(2)-O(2C) : 2.391(7) Cu(3)-N(83) : 2.005(7) Cu(3)-N(113) : 2.030(7) Cu(3)-N(63) : 2.057(6) Cu(3)-N(93) : 2.064(7) Cu(3)-O(3C) : 2.318(7)	N(13)-Cu(1)-N(133) : 89.2(3) N(13)-Cu(1)-N(33) : 90.0(3) N(133)-Cu(1)-N(33) : 170.9(3) N(13)-Cu(1)-N(153) : 176.7(3) N(133)-Cu(1)-N(153) : 90.5(3) N(33)-Cu(1)-N(153) : 89.7(3) N(13)-Cu(1)-O(1C) : 92.9(2) N(133)-Cu(1)-O(1C) : 94.8(3) N(33)-Cu(1)-O(1C) : 94.3(3) N(153)-Cu(1)-O(1C) : 90.3(3) N(53)-Cu(2)-N(73) : 89.3(3) N(53)-Cu(2)-N(43) : 177.7(4) N(73)-Cu(2)-N(43) : 90.9(3) N(53)-Cu(2)-N(23) : 89.8(3) N(73)-Cu(2)-N(23) : 172.4(4)

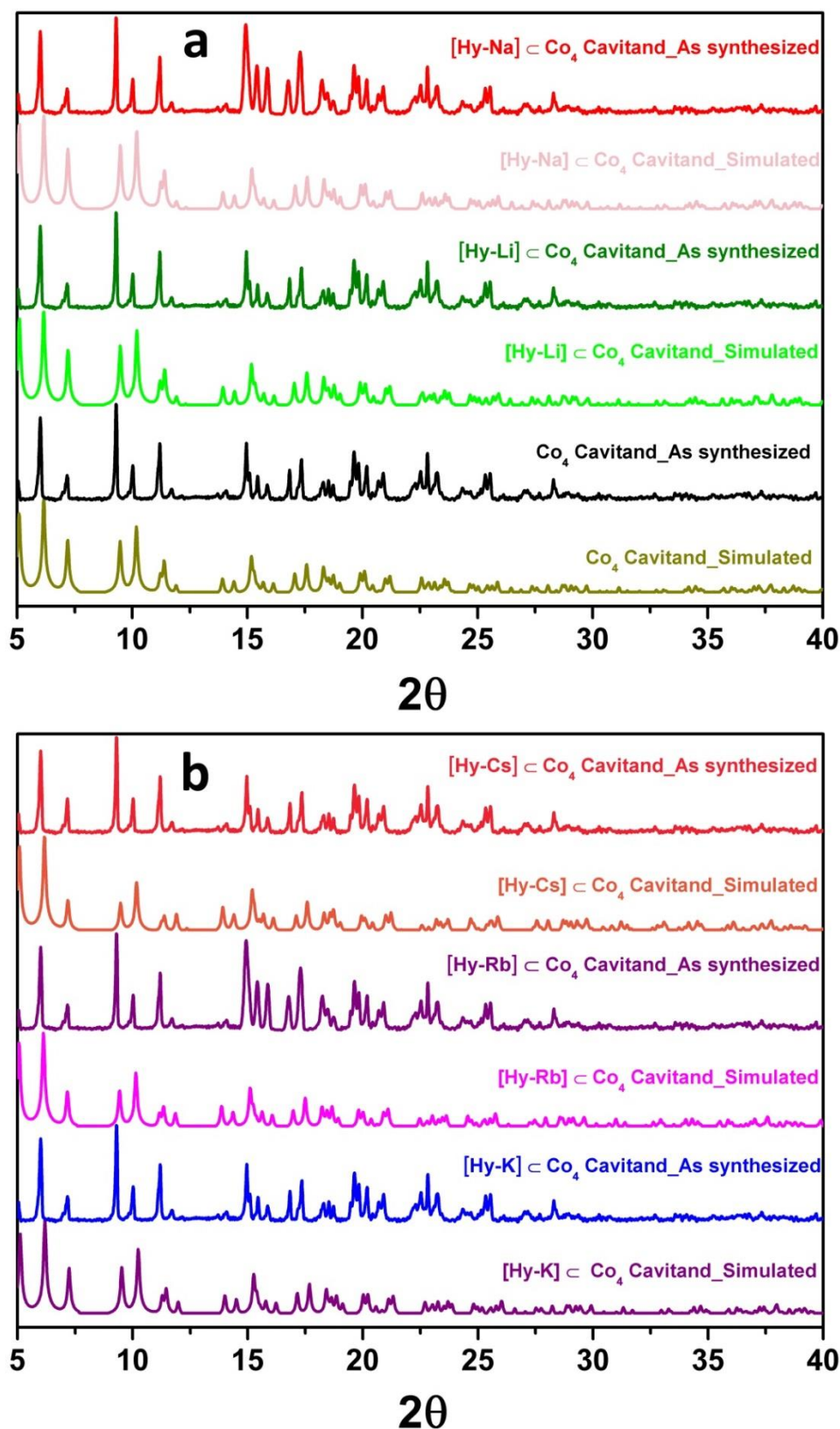
	Cu(4)-N(103) : 2.021(7) Cu(4)-N(143) : 2.022(7) Cu(4)-N(163) : 2.026(7) Cu(4)-N(123) : 2.047(7) Cu(4)-O(4C) : 2.347(7)	N(43)-Cu(2)-N(23): 89.7(3) N(53)-Cu(2)-O(2C): 90.6(3) N(73)-Cu(2)-O(2C): 92.7(3) N(43)-Cu(2)-O(2C): 91.7(3) N(23)-Cu(2)-O(2C): 94.8(3) N(83)-Cu(3)-N(113): 90.8(3) N(83)-Cu(3)-N(63): 89.6(3) N(113)-Cu(3)-N(63): 174.1(3) N(83)-Cu(3)-N(93): 173.8(3) N(113)-Cu(3)-N(93): 91.3(3) N(63)-Cu(3)-N(93): 87.8(3) N(83)-Cu(3)-O(3C): 92.4(3) N(113)-Cu(3)-O(3C): 95.5(3) N(63)-Cu(3)-O(3C): 90.4(3) N(93)-Cu(3)-O(3C): 93.2(3) N(103)-Cu(4)-N(143): 88.4(3) N(103)-Cu(4)-N(163): 173.0(3) N(143)-Cu(4)-N(163): 90.4(3) N(103)-Cu(4)-N(123): 91.9(3) N(143)-Cu(4)-N(123): 178.4(3) N(163)-Cu(4)-N(123): 89.2(3) N(103)-Cu(4)-O(4C): 94.1(3) N(143)-Cu(4)-O(4C): 90.8(3) N(163)-Cu(4)-O(4C): 92.8(3) N(123)-Cu(4)-O(4C): 90.8(3)
2a_sq	Cu(1)-N(13) : 1.992(3) Cu(1)-N(163) : 2.003(4) Cu(1)-N(33) : 2.007(4) Cu(1)-N(143) : 2.019(5) Cu(1)-O(1C) : 2.327(6) Cu(2)-N(43) : 1.995(4) Cu(2)-N(73) : 1.996(4) Cu(2)-N(53) : 1.997(3) Cu(2)-N(23) : 2.002(4) Cu(2)-O(2C) : 2.242(6) Cu(3)-N(83) : 1.997(4) Cu(3)-N(113) : 1.999(4) Cu(3)-N(93) : 2.001(3) Cu(3)-N(63) : 2.015(3) Cu(3)-O(5C) : 2.392(6) Cu(3)-O(3C) : 2.573(7) Cu(4)-N(133) : 1.973(5) Cu(4)-N(153) : 1.994(5) Cu(4)-N(103) : 2.006(5) Cu(4)-N(123) : 2.007(5) Cu(4)-O(4C) : 2.241(6)	N(13)-Cu(1)-N(163): 177.9(2) N(13)-Cu(1)-N(33): 92.0(2) N(163)-Cu(1)-N(33): 87.6(2) N(13)-Cu(1)-N(143): 90.4(2) N(163)-Cu(1)-N(143): 90.3(2) N(33)-Cu(1)-N(143): 171.6(2) N(13)-Cu(1)-O(1C): 87.6(2) N(163)-Cu(1)-O(1C): 90.4(2) N(33)-Cu(1)-O(1C): 94.6(2) N(143)-Cu(1)-O(1C): 93.6(2) N(43)-Cu(2)-N(73): 90.0(2) N(43)-Cu(2)-N(53): 170.1(2) N(73)-Cu(2)-N(53): 89.1(2) N(43)-Cu(2)-N(23): 90.1(2) N(73)-Cu(2)-N(23): 171.1(2) N(53)-Cu(2)-N(23): 89.29(19) N(43)-Cu(2)-O(2C): 94.2(2) N(73)-Cu(2)-O(2C): 94.7(2) N(53)-Cu(2)-O(2C): 95.7(2) N(23)-Cu(2)-O(2C): 94.3(2) N(83)-Cu(3)-N(113): 87.6(2) N(83)-Cu(3)-N(93): 175.0(2) N(113)-Cu(3)-N(93): 89.0(2) N(83)-Cu(3)-N(63): 92.0(2) N(113)-Cu(3)-N(63): 179.0(2) N(93)-Cu(3)-N(63): 91.4(2) N(83)-Cu(3)-O(5C): 91.2(2) N(113)-Cu(3)-O(5C): 91.4(2)

		N(93)-Cu(3)-O(5C): 92.6(2) N(63)-Cu(3)-O(5C): 87.7(2) N(83)-Cu(3)-O(3C): 86.7(2) N(113)-Cu(3)-O(3C): 90.9(3) N(93)-Cu(3)-O(3C): 89.6(2) N(63)-Cu(3)-O(3C): 90.0(3) O(5C)-Cu(3)-O(3C): 176.8(2) N(133)-Cu(4)-N(153): 89.8(3) N(133)-Cu(4)-N(103): 89.9(3) N(153)-Cu(4)-N(103): 169.5(3) N(133)-Cu(4)-N(123): 172.4(3) N(153)-Cu(4)-N(123): 91.1(3) N(103)-Cu(4)-N(123): 87.7(3) N(133)-Cu(4)-O(4C): 92.3(3) N(153)-Cu(4)-O(4C): 96.3(2) N(103)-Cu(4)-O(4C): 94.2(3) N(123)-Cu(4)-O(4C): 95.0(3)
$2\rightarrow[\text{K}(\text{H}_2\text{O})_8]_{\text{sq}}$	Cu(1)-N(143) : 2.008(5) Cu(1)-N(33) : 2.010(5) Cu(1)-N(13A) : 2.037(4) Cu(1)-N(163) : 2.049(5) Cu(1)-O(1C) : 2.291(4) Cu(2)-N(53) : 2.019(5) Cu(2)-N(43) : 2.034(5) Cu(2)-N(73) : 2.054(5) Cu(2)-N(23) : 2.062(5) Cu(2)-O(2C) : 2.251(4) Cu(3)-N(113) : 2.008(6) Cu(3)-N(83) : 2.022(5) Cu(3)-N(63) : 2.024(6) Cu(3)-N(93) : 2.053(5) Cu(3)-O(3C) : 2.299(5) Cu(4)-N(103) : 2.015(5) Cu(4)-N(133) : 2.020(5) Cu(4)-N(153) : 2.039(5) Cu(4)-N(123) : 2.040(5) Cu(4)-O(4C) : 2.258(6) K(1)-O(1K) : 2.772(8) K(1)-O(6K) : 2.782(6) K(1)-O(2K) : 2.789(7) K(1)-O(4K) : 2.797(5) K(1)-O(8K) : 2.883(8) K(1)-O(7K) : 2.976(7) K(1)-O(5K) : 2.992(6) K(1)-O(3K) : 3.193(8)	N(143)-Cu(1)-N(33): 177.31(19) N(143)-Cu(1)-N(13A): 89.90(17) N(33)-Cu(1)-N(13A): 89.35(18) N(143)-Cu(1)-N(163): 88.62(18) N(33)-Cu(1)-N(163): 91.89(19) N(13A)-Cu(1)-N(163): 174.59(19) N(143)-Cu(1)-O(1C): 90.37(17) N(33)-Cu(1)-O(1C): 92.23(18) N(13A)-Cu(1)-O(1C): 91.97(17) N(163)-Cu(1)-O(1C): 93.25(17) N(53)-Cu(2)-N(43): 173.3(2) N(53)-Cu(2)-N(73): 91.6(2) N(43)-Cu(2)-N(73): 92.28(19) N(53)-Cu(2)-N(23): 87.7(2) N(43)-Cu(2)-N(23): 87.41(19) N(73)-Cu(2)-N(23): 168.92(19) N(53)-Cu(2)-O(2C): 91.95(17) N(43)-Cu(2)-O(2C): 93.13(16) N(73)-Cu(2)-O(2C): 94.73(18) N(23)-Cu(2)-O(2C): 96.35(18) N(113)-Cu(3)-N(83): 92.2(2) N(113)-Cu(3)-N(63): 175.4(2) N(83)-Cu(3)-N(63): 90.1(2) N(113)-Cu(3)-N(93): 89.9(2) N(83)-Cu(3)-N(93): 170.2(2) N(63)-Cu(3)-N(93): 87.2(2) N(113)-Cu(3)-O(3C): 91.2(2) N(83)-Cu(3)-O(3C): 92.12(19) N(63)-Cu(3)-O(3C): 92.6(2) N(93)-Cu(3)-O(3C): 97.4(2) N(103)-Cu(4)-N(133): 91.19(19) N(103)-Cu(4)-N(153): 175.8(2) N(133)-Cu(4)-N(153): 87.86(19) N(103)-Cu(4)-N(123): 91.4(2) N(133)-Cu(4)-N(123): 174.0(2) N(153)-Cu(4)-N(123): 89.13(19)

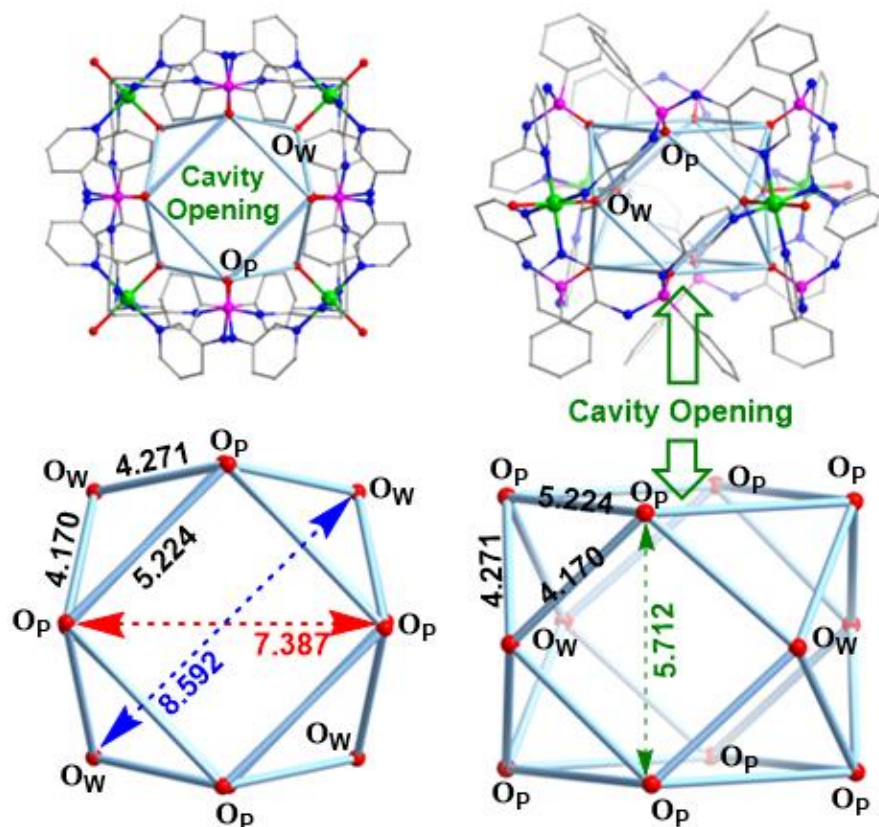
		N(103)-Cu(4)-O(4C): 88.7(2) N(133)-Cu(4)-O(4C): 95.5(2) N(153)-Cu(4)-O(4C): 95.5(2) N(123)-Cu(4)-O(4C): 90.0(2) O(1K)-K(1)-O(6K): 143.2(2) O(1K)-K(1)-O(2K): 95.7(3) O(6K)-K(1)-O(2K): 73.54(17) O(1K)-K(1)-O(4K): 134.7(3) O(6K)-K(1)-O(4K): 74.34(14) O(2K)-K(1)-O(4K): 67.4(2) O(1K)-K(1)-O(8K): 73.3(3) O(6K)-K(1)-O(8K): 70.0(2) O(2K)-K(1)-O(8K): 76.0(3) O(4K)-K(1)-O(8K): 134.5(2) O(1K)-K(1)-O(7K): 102.0(3) O(6K)-K(1)-O(7K): 70.11(16) O(2K)-K(1)-O(7K): 138.95(18) O(4K)-K(1)-O(7K): 118.50(16) O(8K)-K(1)-O(7K): 74.2(3) O(1K)-K(1)-O(5K): 116.3(2) O(6K)-K(1)-O(5K): 91.38(16) O(2K)-K(1)-O(5K): 140.0(2) O(4K)-K(1)-O(5K): 72.96(14) O(8K)-K(1)-O(5K): 134.0(2) O(7K)-K(1)-O(5K): 59.80(16) O(1K)-K(1)-O(3K): 70.0(2) O(6K)-K(1)-O(3K): 145.82(18) O(2K)-K(1)-O(3K): 120.74(18) O(4K)-K(1)-O(3K): 83.04(16) O(8K)-K(1)-O(3K): 140.7(2) O(7K)-K(1)-O(3K): 100.14(19) O(5K)-K(1)-O(3K): 57.14(17)
3	Cu(1)-N(33) : 1.992(8) Cu(1)-N(63)#1 : 2.010(8) Cu(1)-N(53) : 2.021(8) Cu(1)-N(13) : 2.026(8) Cu(1)-O(71) : 2.235(6) Cu(2)-N(23)#1 : 1.974(9) Cu(2)-N(23) : 1.974(9) Cu(2)-N(43)#1 : 2.045(8) Cu(2)-N(43) : 2.045(8) Cu(2)-O(11) : 2.625(14)	N(33)-Cu(1)-N(63)#1 : 176.2(3) N(33)-Cu(1)-N(53) : 89.0(3) N(63)#1-Cu(1)-N(53) : 88.9(3) N(33)-Cu(1)-N(13) : 91.8(3) N(63)#1-Cu(1)-N(13) : 89.2(3) N(53)-Cu(1)-N(13) : 161.0(3) N(33)-Cu(1)-O(71) : 95.3(3) N(63)#1-Cu(1)-O(71) : 88.1(3) N(53)-Cu(1)-O(71) : 97.3(3) N(13)-Cu(1)-O(71) : 101.5(3) N(23)#1-Cu(2)-N(23) : 175.8(6) N(23)#1-Cu(2)-N(43)#1 : 90.4(4) N(23)-Cu(2)-N(43)#1 : 89.9(4) N(23)#1-Cu(2)-N(43) : 89.9(4) N(23)-Cu(2)-N(43) : 90.4(4) N(43)#1-Cu(2)-N(43) : 171.5(5) N(23)#1-Cu(2)-O(11) : 80.4(4) N(23)-Cu(2)-O(11) : 95.5(4) N(43)#1-Cu(2)-O(11) : 86.3(5) N(43)-Cu(2)-O(11) : 102.1(5)



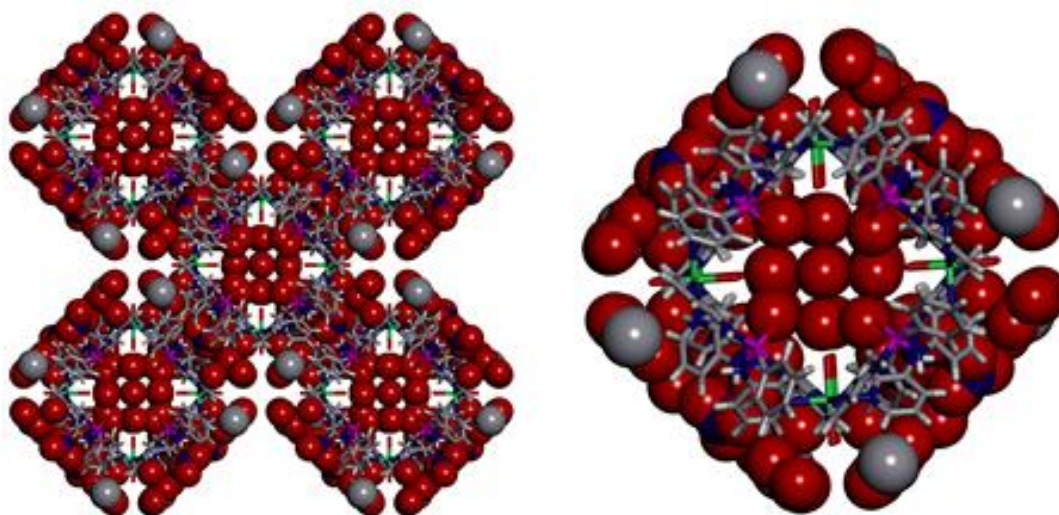
Appendix A3.1: Powder X-ray diffraction (PXRD) profiles of Ni_4 cavitant (4) and $\{[\text{Hy-A}]\subset 4\}$.



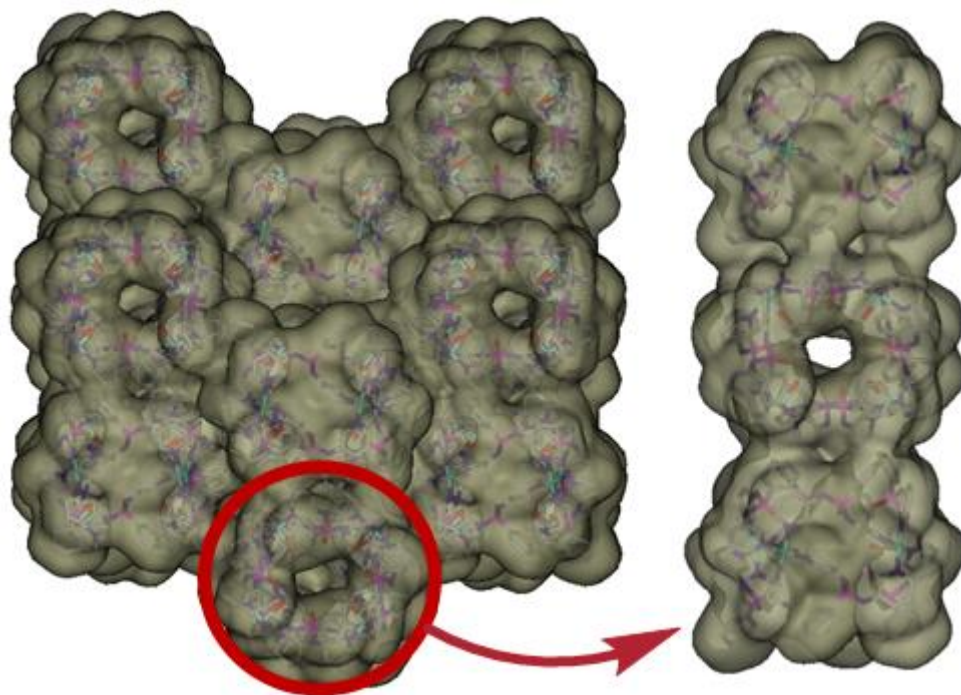
Appendix A3.2: Powder X-ray diffraction (PXRD) profiles of Co₄ cavitand (5) and {[Hy-A]⊂5}.



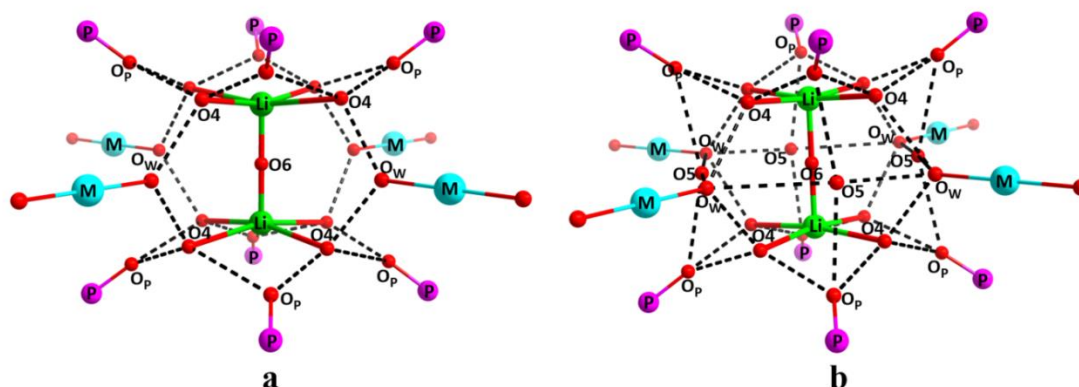
Appendix A3.3: View of the intrinsic void in **4** and the metric parameters associated with the cavity.



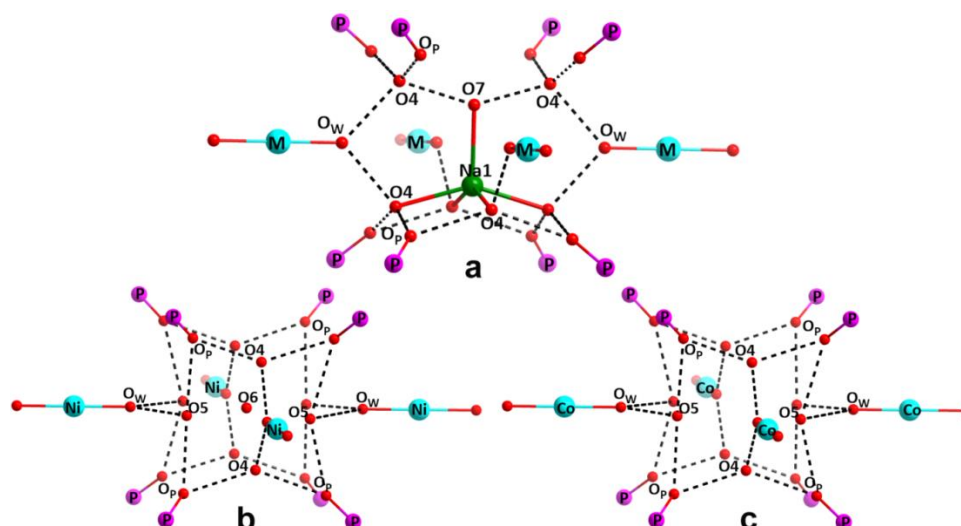
Appendix A3.4: Packing structure of **4**; the encapsulated polar guest solvents as well as the solvents and nitrate anions in the packing cavity were shown in the space-fill representation (colour code: C, grey; N, blue; O, red; P, purple; Ni, light-green; H, white).



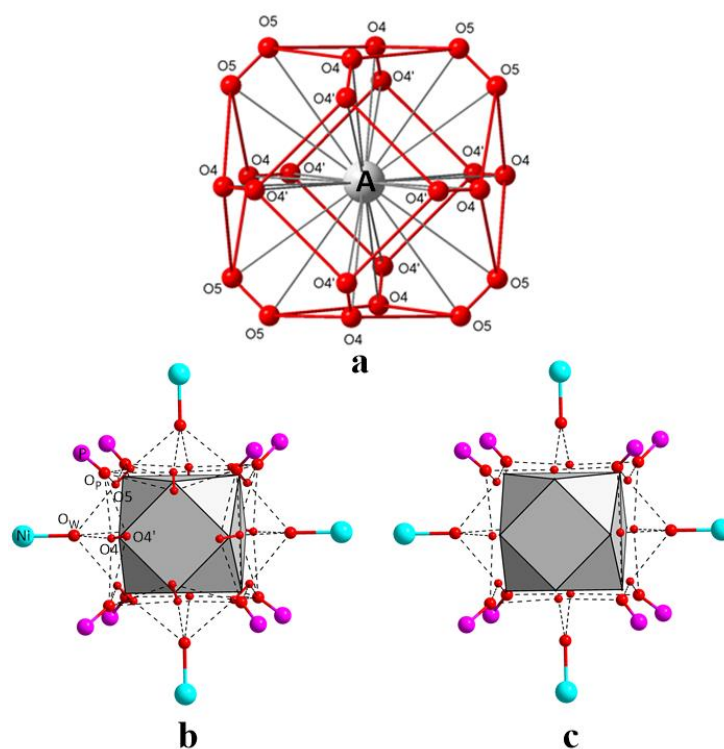
Appendix A3.5: Packing arrangement of the earlier reported Cu_4 cavitaand (compound **2**; discussed in chapter 2) and view of the interrupted channel along the c -axis.



Appendix A3.6: (a) View of the disordered $[\text{Li}(\text{H}_2\text{O})_5]^+$ motif in $[\text{Hy-Li}]<4$ and $[\text{Hy-Li}]<5$ alongwith its H-bonding interactions. (b) Location of the additional encapsulated water molecules (O5) in $[\text{Hy-Li}]<4$ and $[\text{Hy-Li}]<5$ and their interactions with the host framework. ($\text{M} = \text{Ni}^{2+}$ or Co^{2+})



Appendix A3.7: View of the two distinct guest environments in $[\text{Hy-Na}]c4$ and $[\text{Hy-Na}]c5$. (a) One of the disordered segment of the $[\text{Na}(\text{H}_2\text{O})_5]^+$ guest and its H-bonding with the host framework **4** or **5** ($\text{M} = \text{Ni}^{2+}$ or Co^{2+}). (b) View of the additional water cluster (made up of O4, O5 and O6) encapsulated inside $[\text{Hy-Na}]c4$. (c) View of the additional water cluster (made up of O4 and O5) encapsulated inside $[\text{Hy-Na}]c5$.



Appendix A3.8: View of the hydration sphere around the $\text{K}^+/\text{Rb}^+/\text{Cs}^+$ ions in $\{[\text{Hy-A}]c4\}$ and $\{[\text{Hy-A}]c5\}$. (a) The 24 vertex truncated cube made up of symmetry

equivalent O4, O4' and O5 atoms in the disordered state. (b) and (c) shows the formation of a cuboctahedral coordination around the alkali metal ion via the omission of one of the disordered sites of O4/O4' and O5 atoms.

Appendix A3.9: Refinements of {[Hy-A]₄ (A=K⁺, Rb⁺, and Cs⁺) complexes with varying coordination numbers

A	A(H ₂ O) _n	Occupancy factor			Isotropic displacement parameter (U)						R1	Sum of occupancy factors	
		O4	O4'	O5	U(O)	U(M)	U(Ni)	U(O1)	U(O2)	U(O3)		O4+O4'	O4+O5
K	6	0.53	0.03	0.19	0.049	0.078	0.054	0.070	0.055	0.082	0.055	0.562	0.716
	7	0.60	0.05	0.22	0.058	0.078	0.054	0.070	0.055	0.082	0.052	0.655	0.822
	8	0.68	0.07	0.25	0.067	0.078	0.054	0.070	0.055	0.082	0.050	0.749	0.927
	9	0.75	0.09	0.28	0.076	0.078	0.054	0.070	0.055	0.082	0.048	0.842	1.030
	10	0.82	0.12	0.31	0.084	0.078	0.054	0.069	0.055	0.082	0.048	0.935	1.133
	11	0.89	0.14	0.35	0.093	0.078	0.054	0.069	0.055	0.081	0.049	1.028	1.234
	12	0.96	0.17	0.38	0.101	0.078	0.054	0.069	0.054	0.081	0.051	1.123	1.333
Rb	6	0.44	0.12	0.19	0.027	0.057	0.055	0.063	0.054	0.086	0.069	0.560	0.626
	7	0.50	0.15	0.23	0.038	0.057	0.055	0.063	0.054	0.086	0.066	0.648	0.727
	8	0.56	0.17	0.26	0.048	0.057	0.055	0.063	0.053	0.085	0.064	0.737	0.827
	9	0.63	0.20	0.30	0.058	0.057	0.055	0.063	0.053	0.085	0.063	0.825	0.926
	10	0.69	0.22	0.34	0.067	0.057	0.055	0.063	0.052	0.085	0.062	0.914	1.025
	11	0.75	0.25	0.37	0.077	0.057	0.055	0.063	0.052	0.085	0.061	1.003	1.125
	12	0.82	0.27	0.41	0.087	0.057	0.055	0.063	0.052	0.084	0.061	1.091	1.227
Cs	6	0.39	0.17	0.19	0.020	0.043	0.048	0.054	0.047	0.072	0.058	0.564	0.577
	7	0.45	0.21	0.22	0.028	0.043	0.048	0.054	0.047	0.072	0.054	0.654	0.669
	8	0.51	0.24	0.26	0.036	0.043	0.048	0.054	0.046	0.072	0.050	0.744	0.764
	9	0.57	0.27	0.29	0.044	0.043	0.048	0.054	0.046	0.072	0.047	0.832	0.860
	10	0.63	0.29	0.33	0.052	0.043	0.048	0.054	0.046	0.071	0.045	0.919	0.956
	11	0.68	0.32	0.37	0.059	0.043	0.048	0.054	0.046	0.071	0.045	1.004	1.056
	12	0.74	0.34	0.41	0.067	0.043	0.048	0.054	0.046	0.071	0.047	1.088	1.156

This table lists refinements of K⁺, Rb⁺ and Cs⁺ complexes with varying coordination numbers of A (alkali metal ion) ranging from 6 to 12. This was done by fixing the sum of occupancy factors of O4, O4' and O5 and at the same time refine them with a combined isotropic displacement parameter *U*(O) (column highlighted in yellow) in

order to suppress correlations between occupancy factors and U -values. For comparison, U -values of A, Ni and other O-atoms are listed alongside R1. Columns O4+O4' and O4+O5 give the sum of occupancy factors of the two sites. These cannot exceed a value of 1.0, since this would bring two coordination sites into too close contact (values in excess of 1.0 are highlighted in red). Comparison of the resulting parameters of the various runs shows that the coordination number tends to increase from K^+ to Cs^+ . While it is difficult to extract definite numbers from these values, coordination numbers of 8, 9 and 10 for K^+ , Rb^+ and Cs^+ , respectively, appear to be in good agreement with listed values (rows highlighted in yellow).

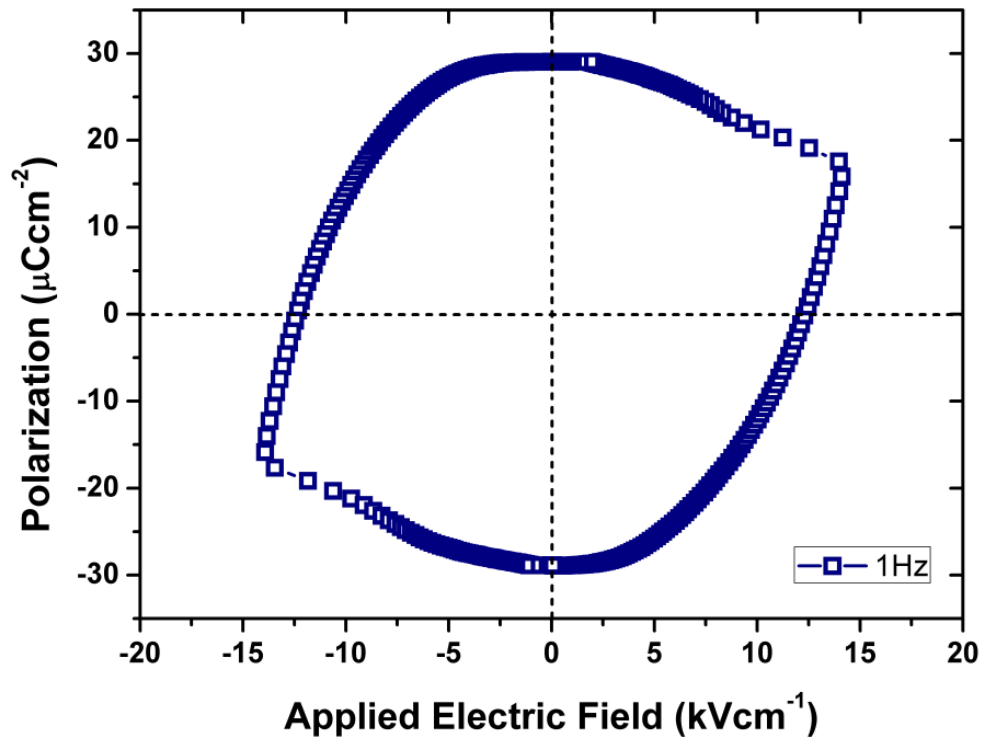
Appendix A3.10: Refinements of $\{[Hy-A]c5$ ($A=K^+$, Rb^+ , and Cs^+) complexes in their most suitable hydration numbers

A	$A(H_2O)_n$	Occupancy factor			Isotropic displacement parameter (U)						R1	Sum of occupancy factors	
		O4	O4'	O5	U(O)	U(M)	U(Co)	U(O1)	U(O2)	U(O3)		O4+O4'	O4+O5
K	8	0.65	0.10	0.25	0.067	0.069	0.050	0.059	0.068	0.097	0.067	0.747	0.899
Rb	9	0.34	0.48	0.31	0.054	0.042	0.046	0.053	0.048	0.093	0.054	0.818	0.643
Cs	10	0.59	0.27	0.39	0.050	0.032	0.031	0.047	0.034	0.035	0.040	0.857	0.985

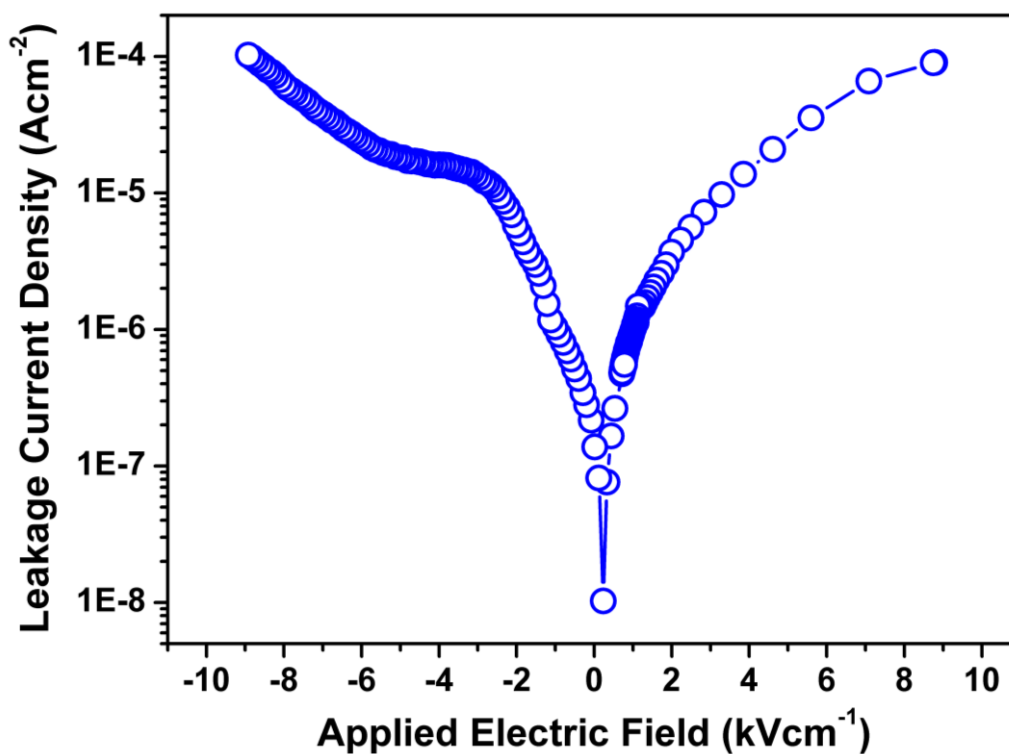
Appendix A3.11: List of A-O* distances and O-O distances between coordinated water and oxygen atoms of the $\{[Hy-A]c4$ ($A=K^+$, Rb^+ , and Cs^+) host-guest assemblies (in Å).

A	A-O4	A-O4'	A-O5	O _p -O4	O _p -O4'	O _p -O5	O _w -O4	O _w -O5
	K	3.05	3.12	3.09	2.73 2.81	2.72 2.80	2.86 2.89	2.64
Rb	3.18	3.27	3.29	2.73 2.80	2.66 2.87	2.81 2.87	2.71	2.63
Cs	3.27	3.29	3.35	2.77 2.79	2.70 2.89	2.78 2.89	2.69	2.66

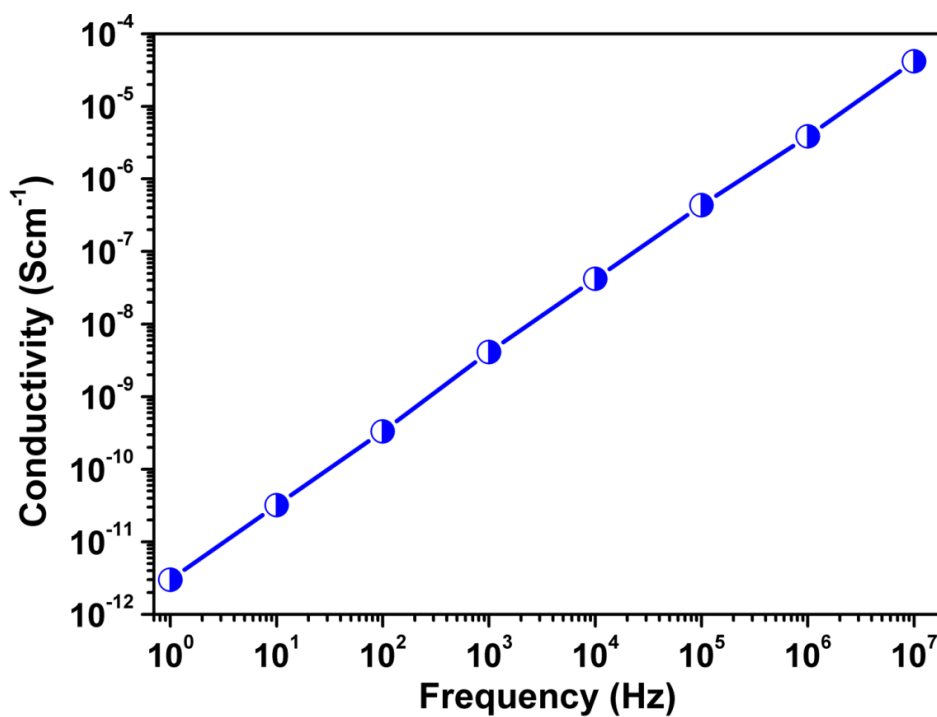
*The A-O distances show a slight increase from K^+ to Cs^+ , while O-O distances are fairly similar for the different hydrated guest, and are in the appropriate range for hydrogen bonding.



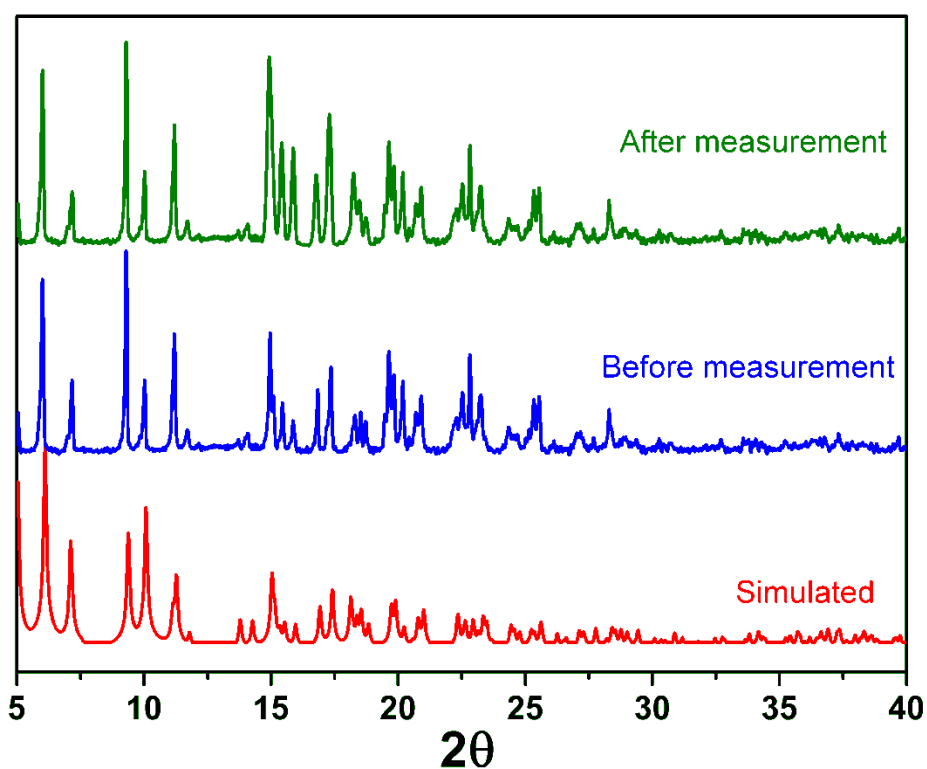
Appendix A3.12: Ferroelectric hysteresis loop of 4 at 1 Hz at room temperature.



Appendix A3.13: Plot of the Leakage current density vs applied electric field for 4.



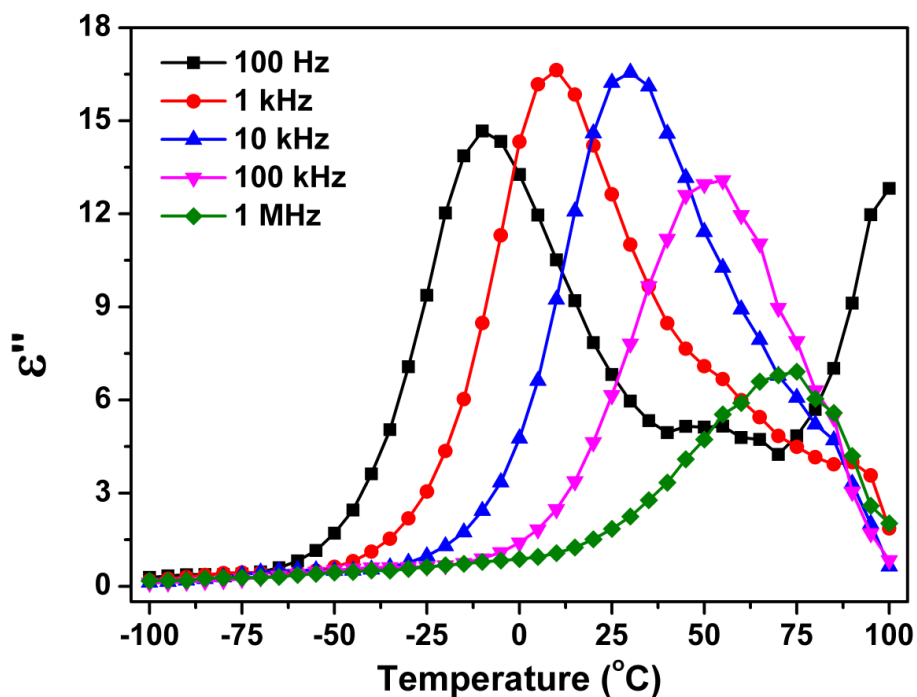
Appendix A3.14: Frequency dependent plot of the conductivity of 4 at 30°C.



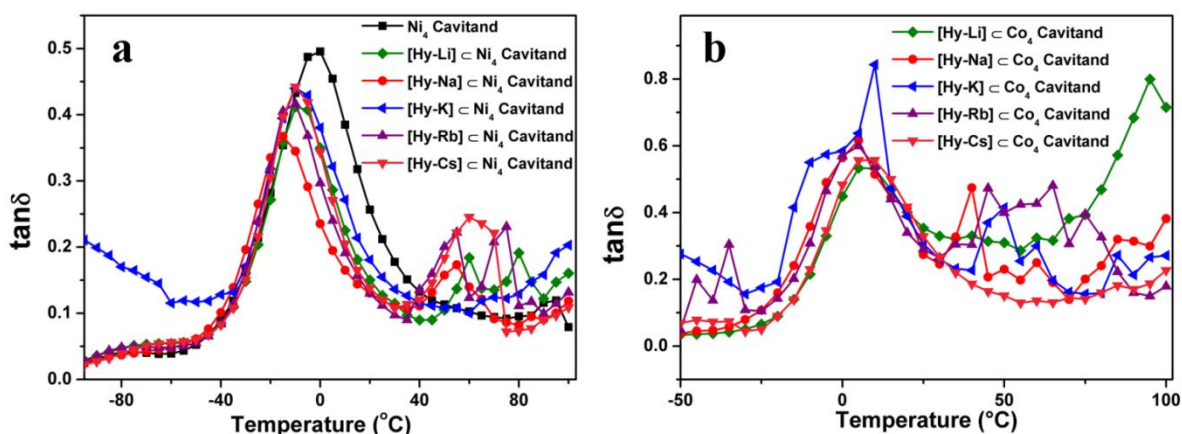
Appendix A3.15: Comparison of the PXRD patterns of the disc of 4 before and after ferroelectric measurements.

Appendix A3.16: Single-point ONIOM Calculation on **4** (using b3lyp/6-31g: hf/pm6 basis set).

System	Dipole Moment (Debye)
Cage+Anion+Solvent	66.3870
Cage+Anion	26.1042



Appendix A3.18: Temperature dependence of the imaginary part (ϵ'') of dielectric permittivity of **4**.

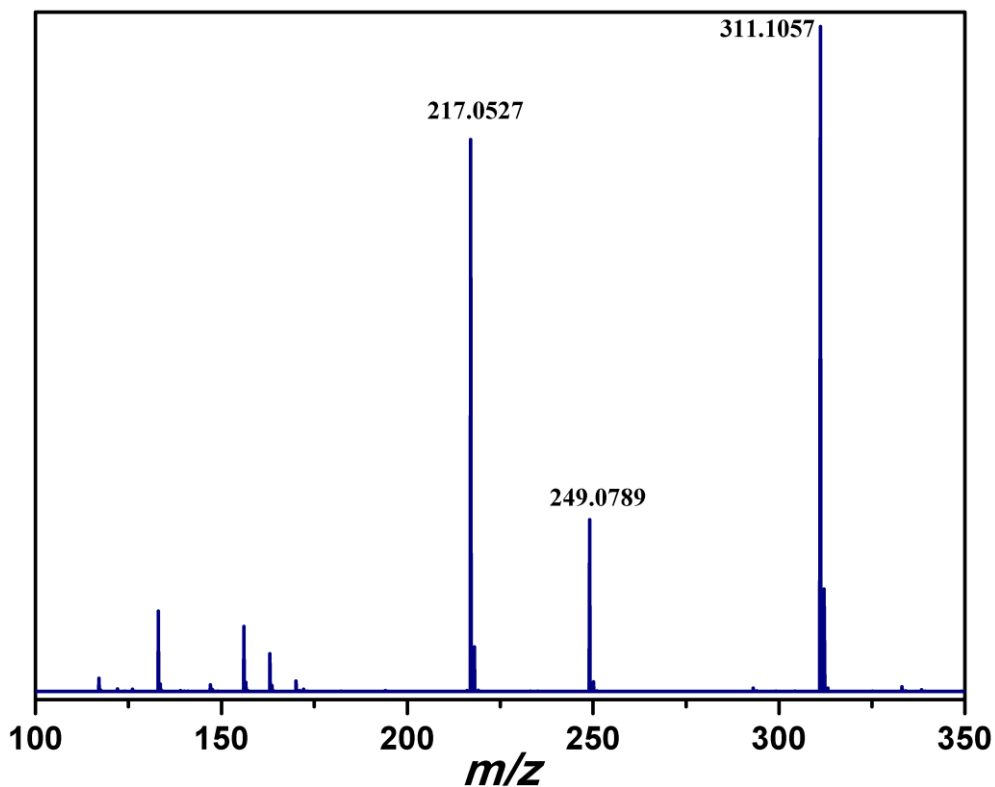
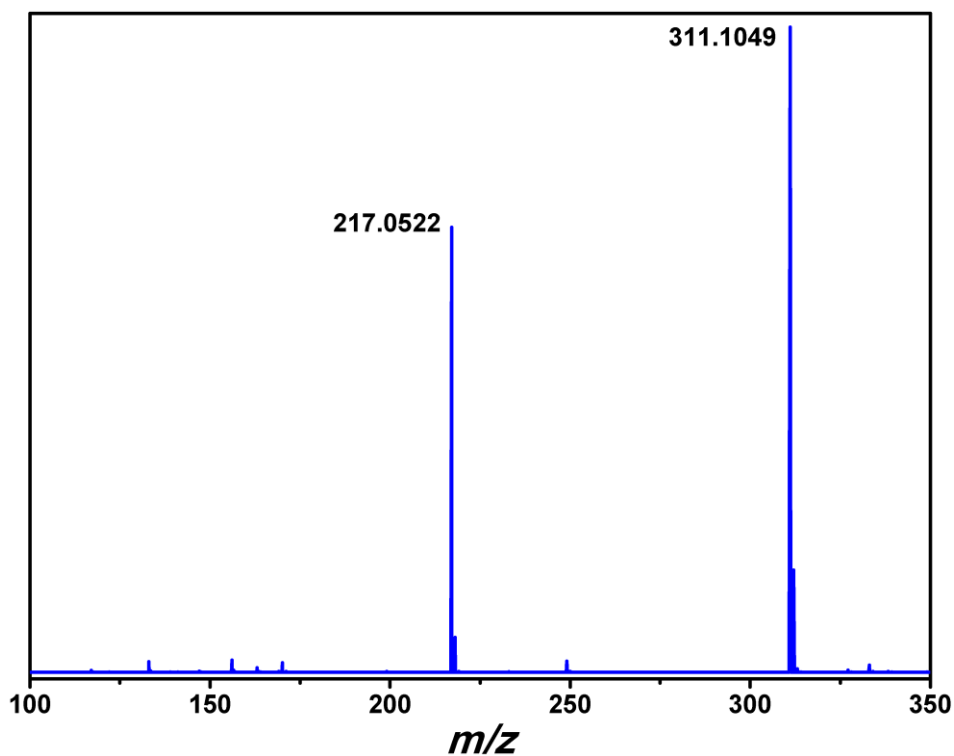


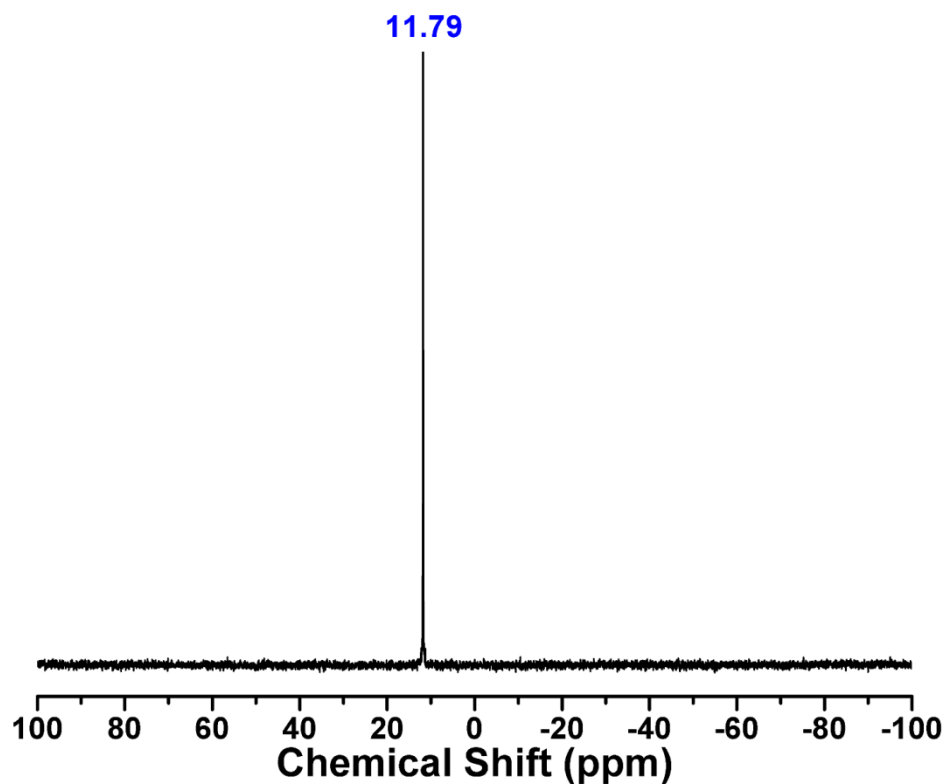
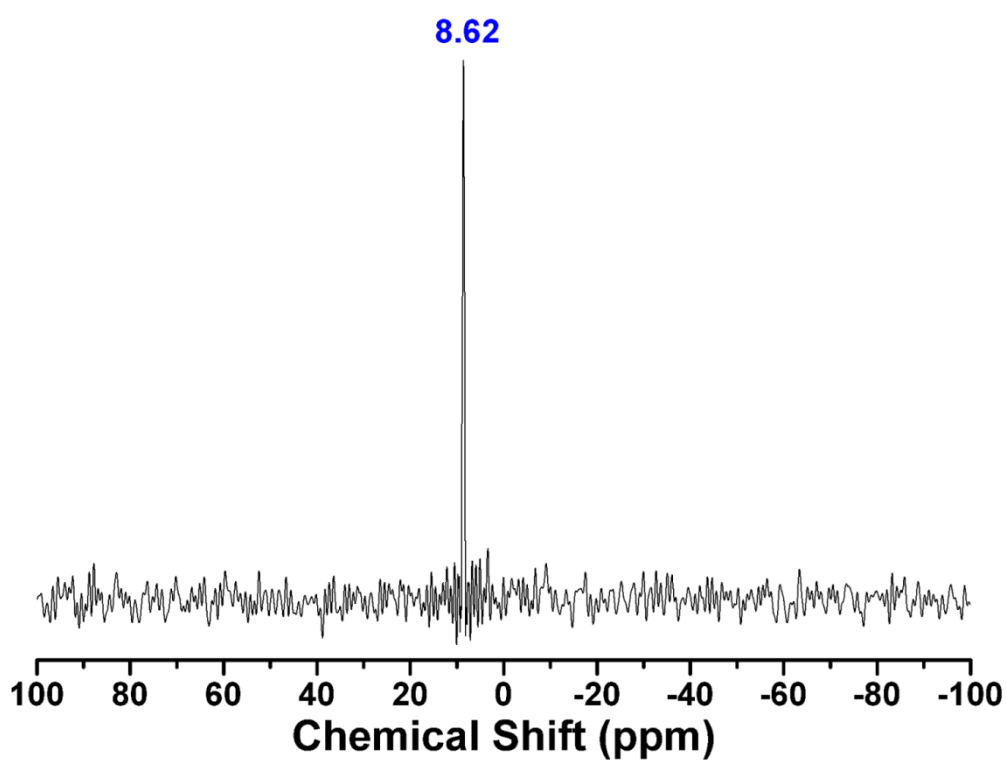
Appendix A3.19: Temperature dependence of the dielectric loss for (a) $\{[\text{Hy-A}]\subset\text{Ni}_4\}$ and (b) $\{[\text{Hy-A}]\subset\text{Co}_4\}$ at 1 kHz.

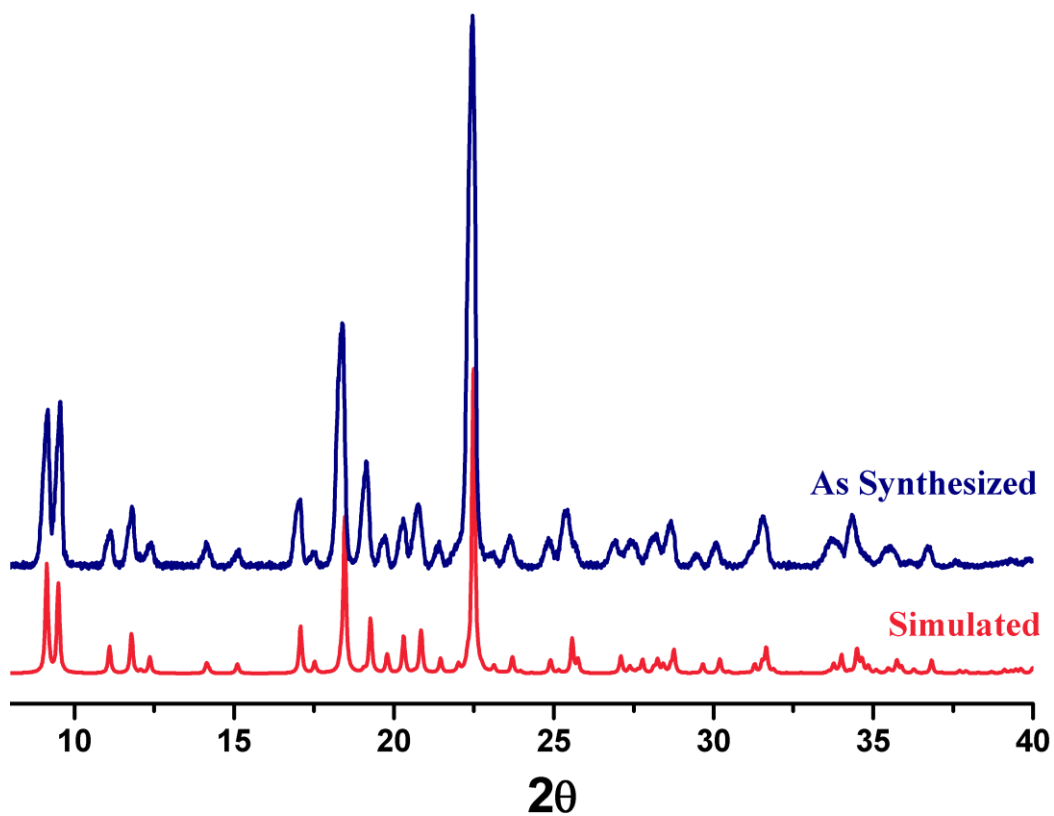
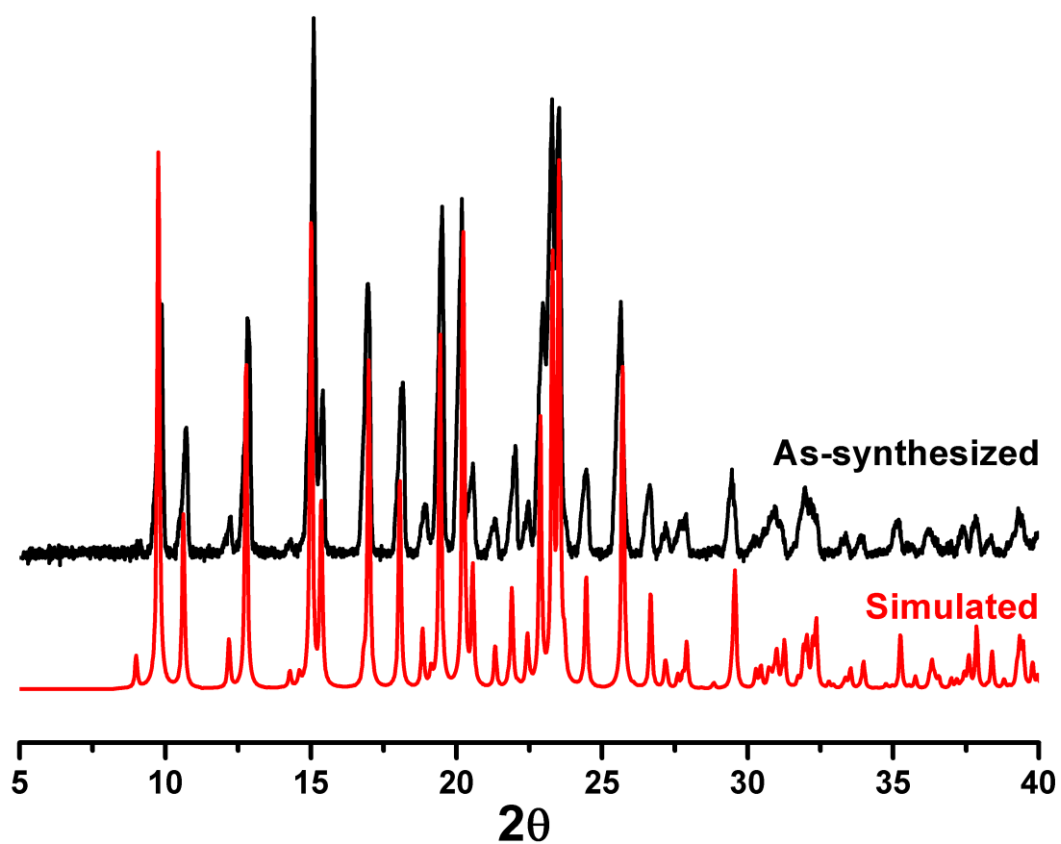
Appendix A3.20: The P_r loss (%) data obtained from ferroelectric fatigue measurement cavitands.

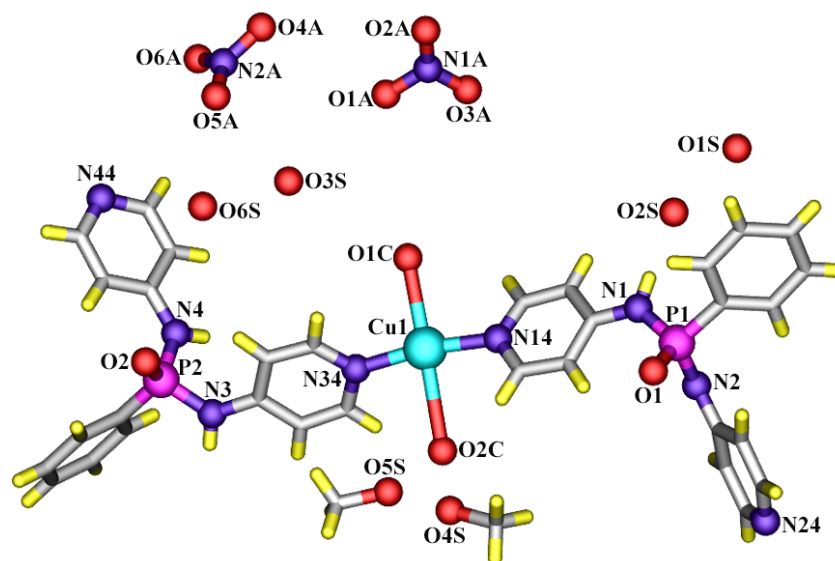
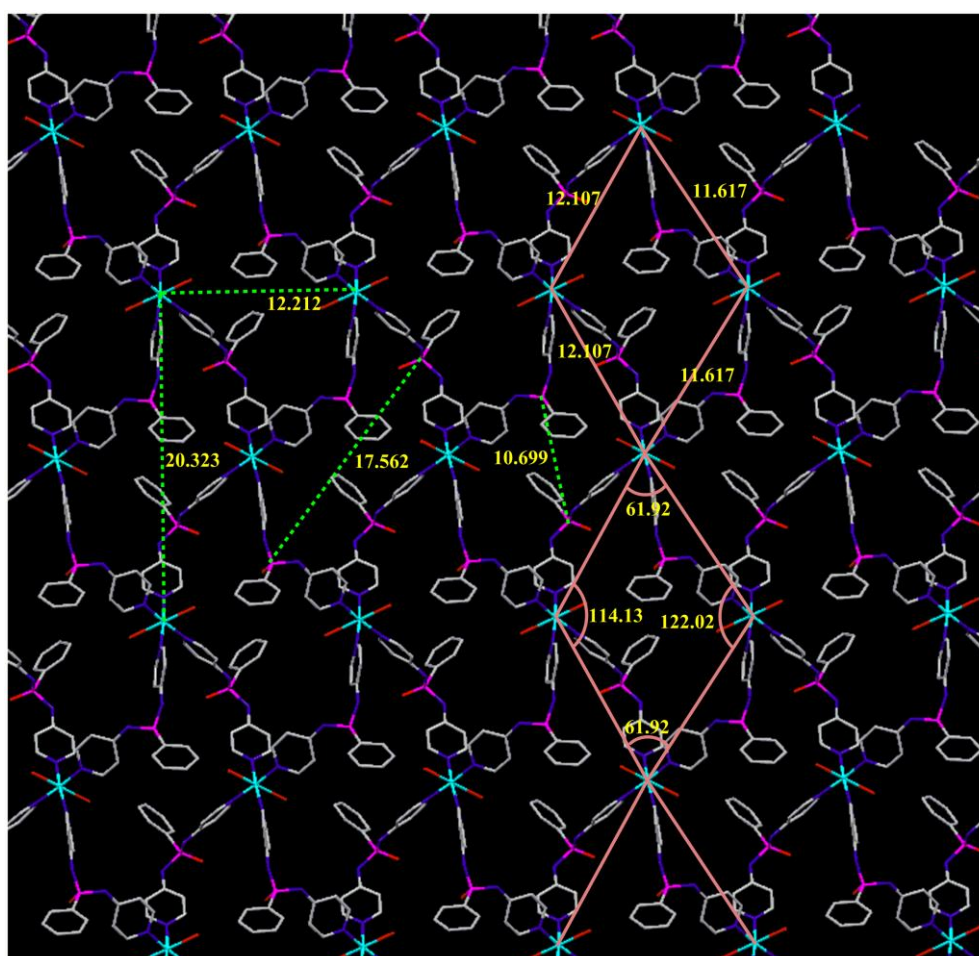
Host-Guest Assembly	P_r loss (in %) after 10^5 switching cycles	
	Ni_4 -series	Co_4 -series
M_4^*	6.423	--
$[\text{Hy-Li}]\subset\text{M}_4$	9.029	0.1858
$[\text{Hy-Na}]\subset\text{M}_4$	--	2.099
$[\text{Hy-K}]\subset\text{M}_4$	21.1102	0.7023
$[\text{Hy-Rb}]\subset\text{M}_4$	21.099	3.177
$[\text{Hy-Cs}]\subset\text{M}_4$	34.7173	12.5014

*For the sake of simplicity $(\text{H}_2\text{O})_9\subset\text{M}_4$ is given only as M_4 at many places in chapter 3 and appendix for chapter 3.

Characterization DataAppendix A4.1: ESI-mass spectrum of L^2 .Appendix A4.2: ESI-mass spectrum of L^3 .

Appendix A4.3: ^{31}P -NMR spectrum of L^2 .Appendix A4.4: ^{31}P -NMR spectrum of L^3 .

Appendix A4.5: PXR D pattern of L^2 .Appendix A4.6: PXR D pattern of L^3 .

Appendix A4.7: Asymmetric unit of **6**.Appendix A4.8: Bond distances and angles in **6**.

Appendix A4.9: Result of Topology Analysis for 6.

#####

Compound 6

#####

Topology for Cu1

Atom Cu1 links by bridge ligands and has

Common vertex with	R(A-A)				f
Cu 1	0.1643	0.4805	-0.4189	(-1 0-1)	11.617A 1
Cu 1	1.1643	0.4805	0.5811	(0 0 0)	11.617A 1
Cu 1	1.1643	-0.5195	0.5811	(0-1 0)	12.107A 1
Cu 1	0.1643	-0.5195	-0.4189	(-1-1-1)	12.107A 1

Structural group analysis

Structural group No 1

Structure consists of plane layers (1 0-1) with CuP2O5N8C33H33

Coordination sequences

Cu1: 1 2 3 4 5 6 7 8 9 10

Num 4 8 12 16 20 24 28 32 36 40

Cum 5 13 25 41 61 85 113 145 181 221

Rad 11.9(0.3) 20.0(5.0) 29.2(6.4) 38.5(8.0) 48.0(9.7) 57.4(11.4) 66.9(13.2)
76.3(14.9) 85.8(16.7) 95.3(18.4)

Cmp Cu4 Cu8 Cu12 Cu16 Cu20 Cu24 Cu28 Cu32 Cu36 Cu40

TD10=221

Vertex symbols for selected sublattice

Cu1 Point symbol:{4⁴.6²}

Plane net vertex symbol:[4.4.4.4]

Extended point symbol:[4.4.4.4.6(2).6(2)]

Vertex symbol: [4.4.4.4.*.*]

ATTENTION! Some rings * are bigger than 6, so likely no rings are contained in that angle

Point symbol for net: {4⁴.6²}

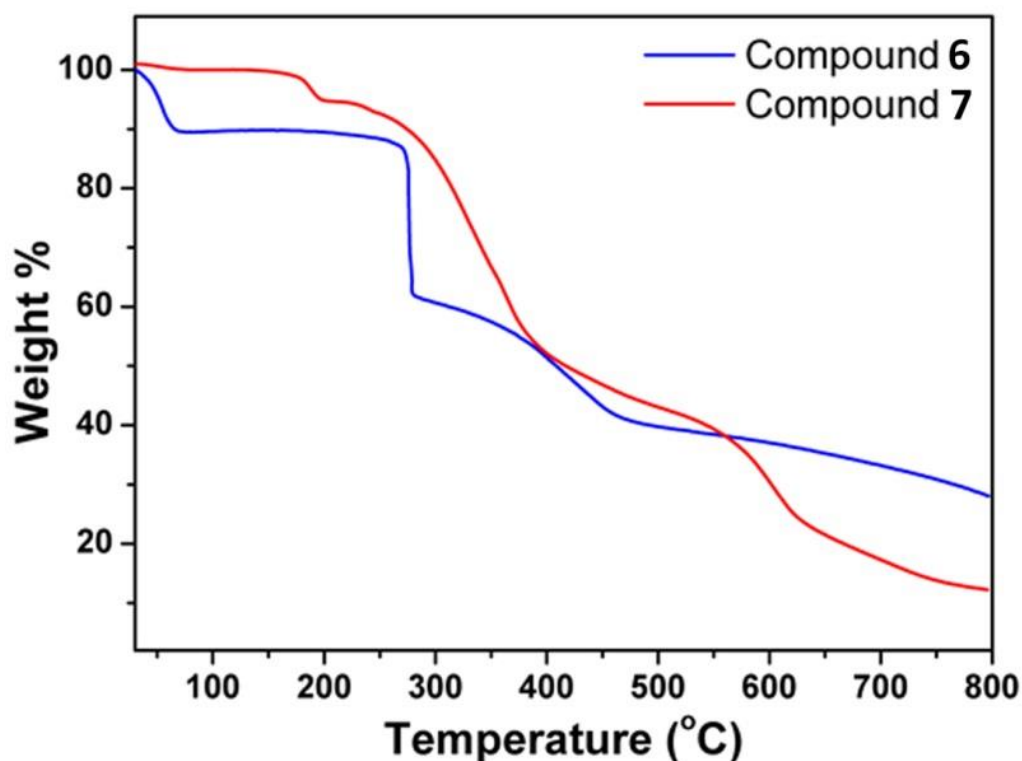
4-c net; uninodal net

Plane net tiling: [4]

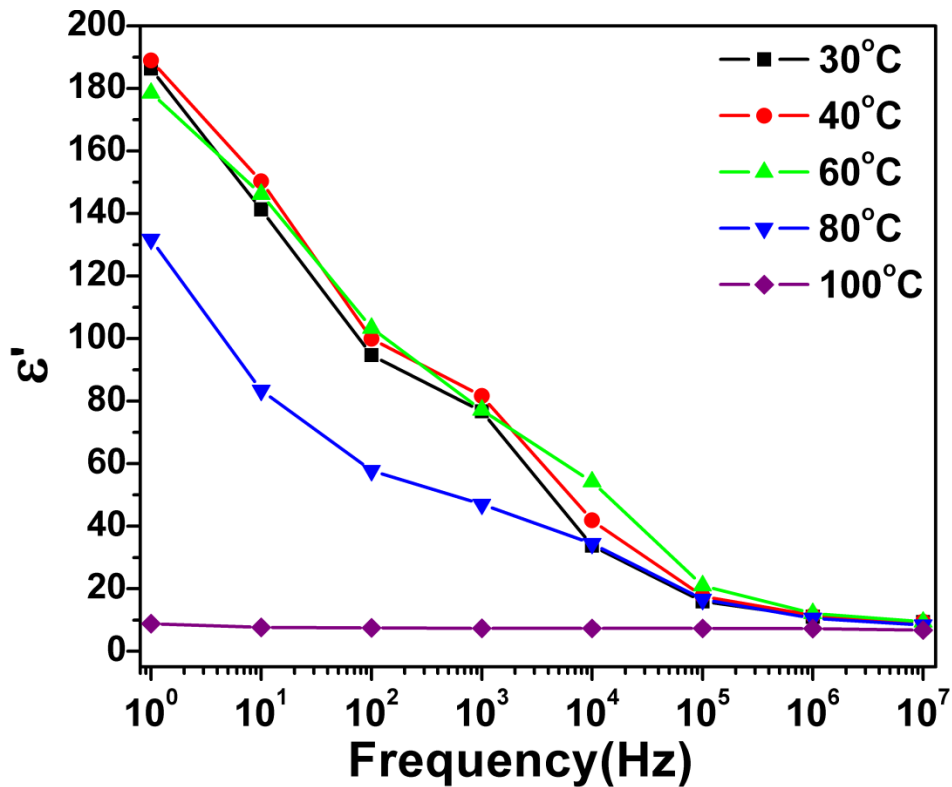
Plane net signature: [121](4)[4.4.4.4]

Topological type: sql/Shubnikov tetragonal plane net (topos&RCSR.ttd) {4⁴.6²} - VS [4.4.4.4.*.*] (76188 types in 11 databases)

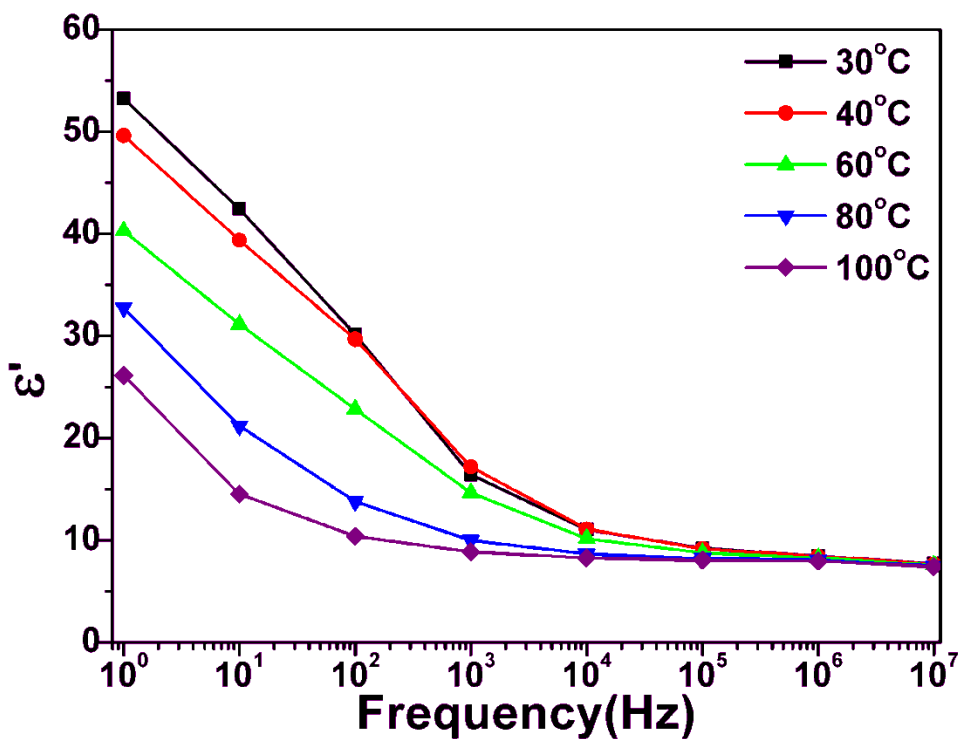
Elapsed time: 8.35 sec.



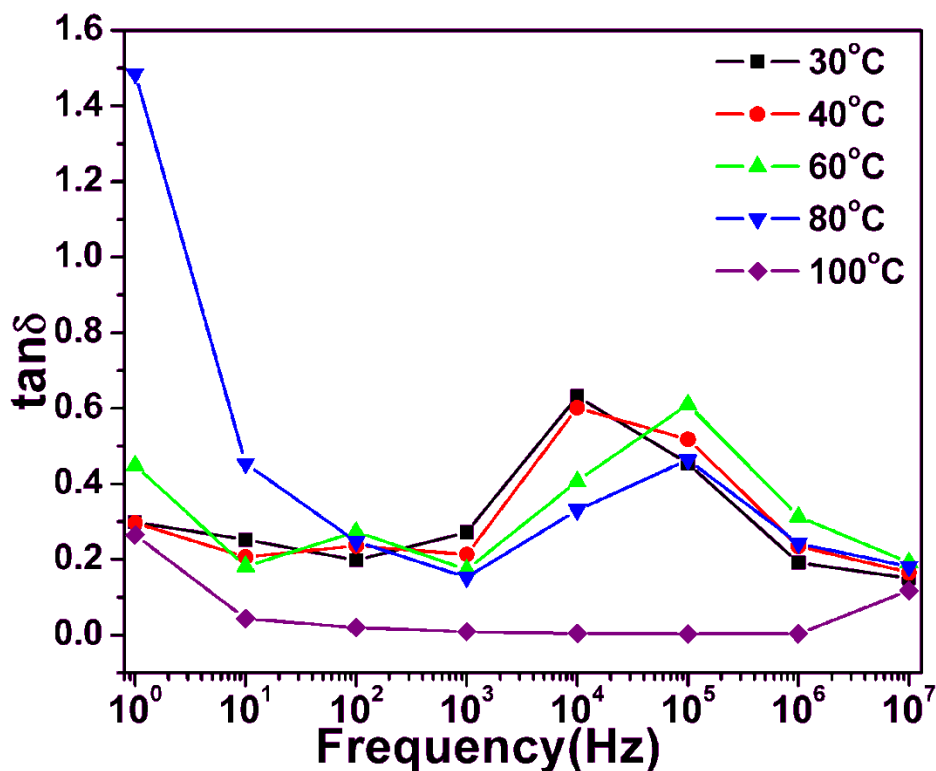
Appendix A4.10: TGA plots for 6 and 7.



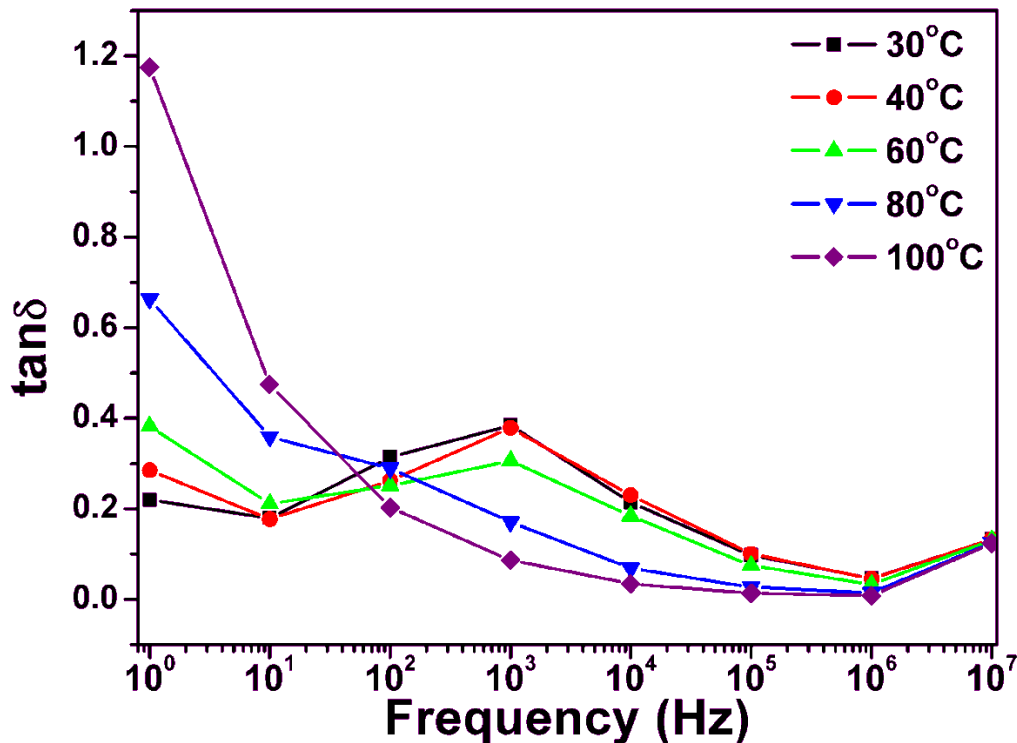
Appendix A4.11: Frequency dependence of the real part of dielectric constant (ϵ') for 6 at various temperatures.



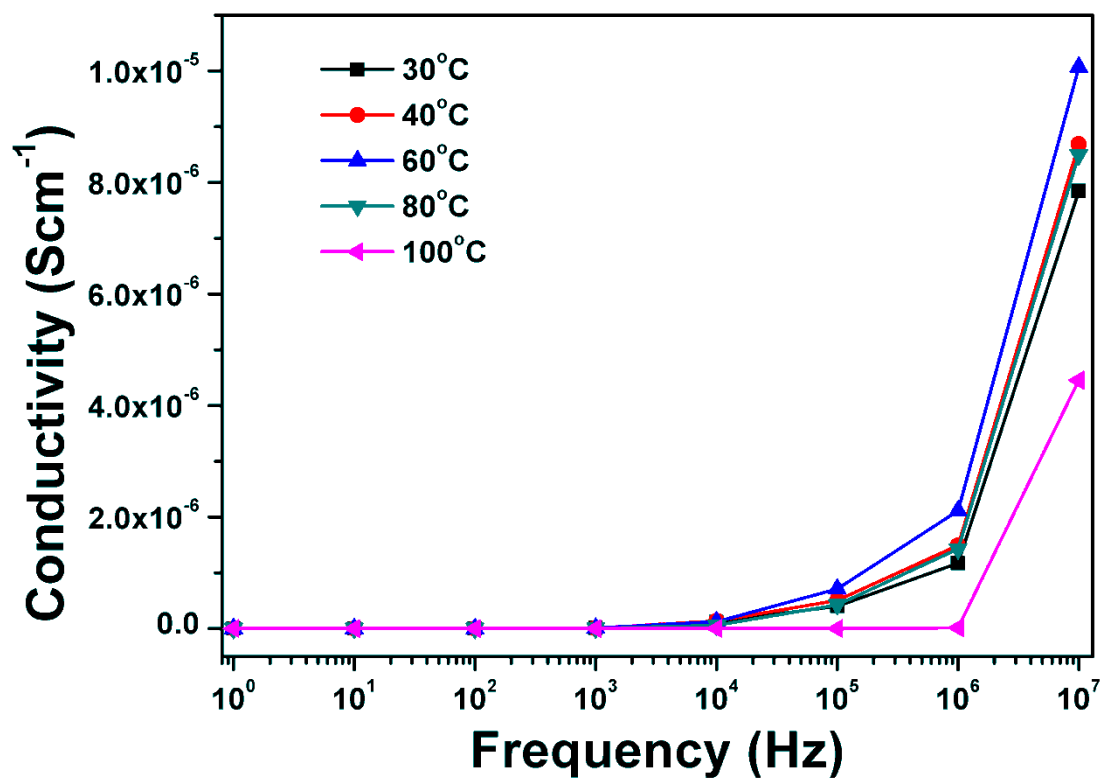
Appendix A4.12: Frequency dependence of the real part of dielectric constant (ϵ') for 7 at various temperatures.



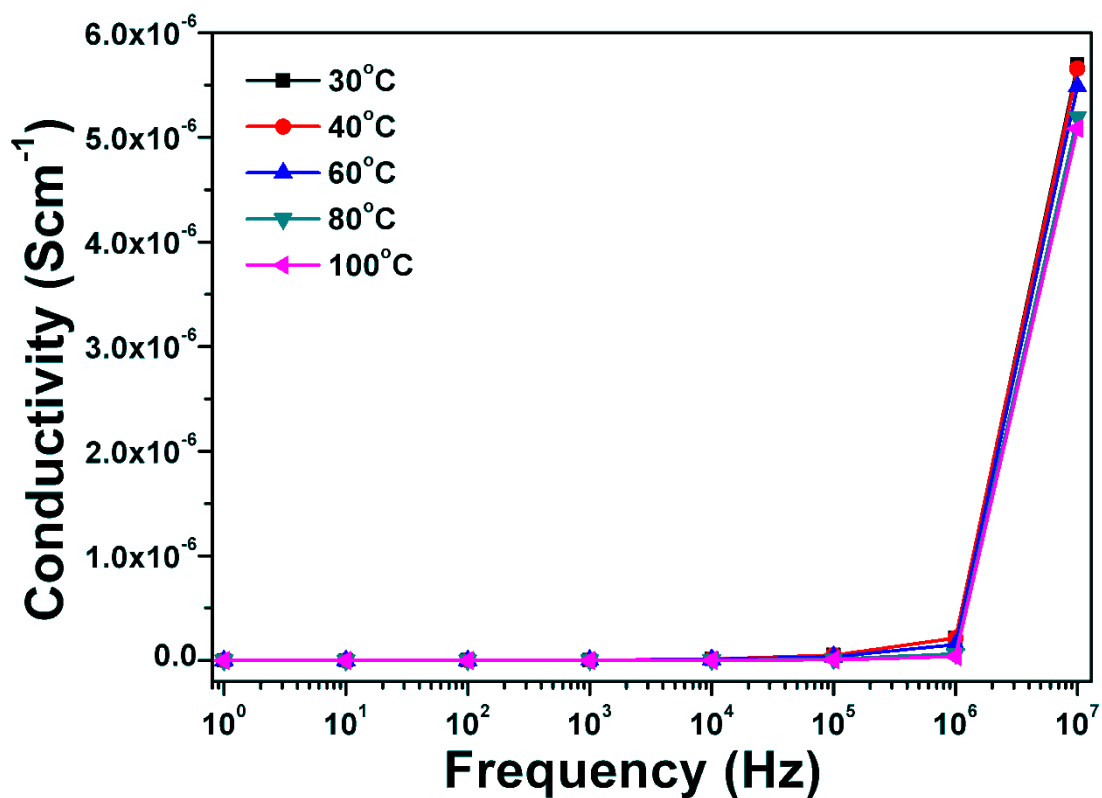
Appendix A4.13: Frequency dependence of the dielectric loss for 6 at various temperatures.



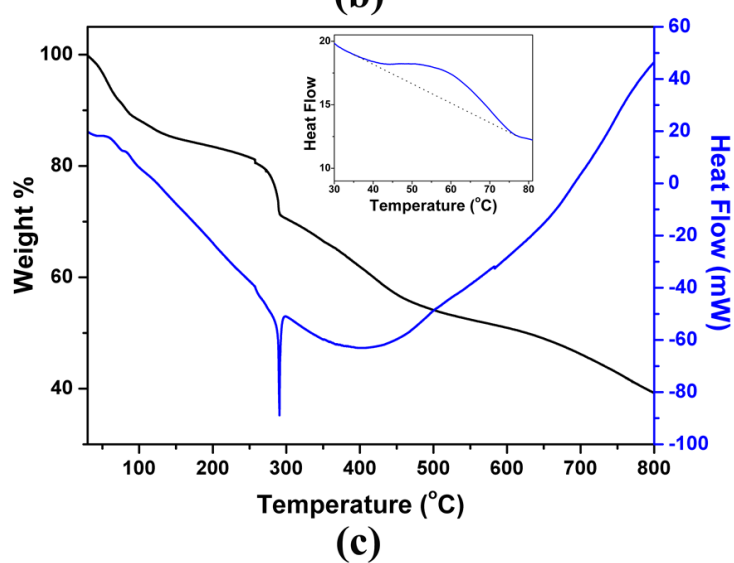
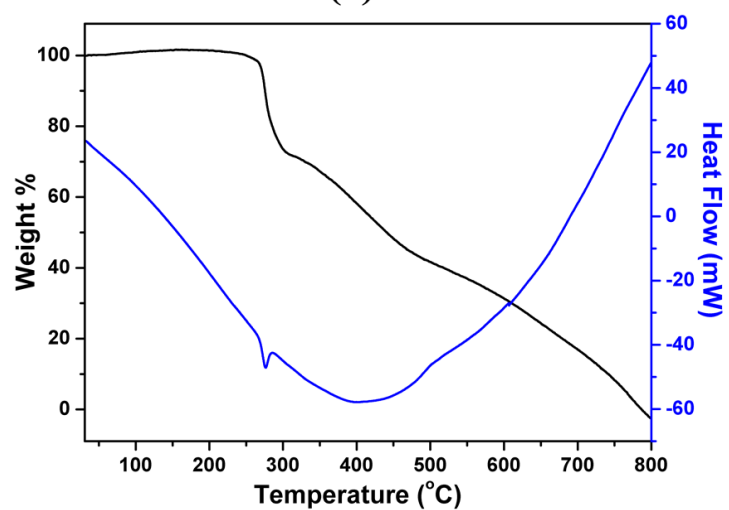
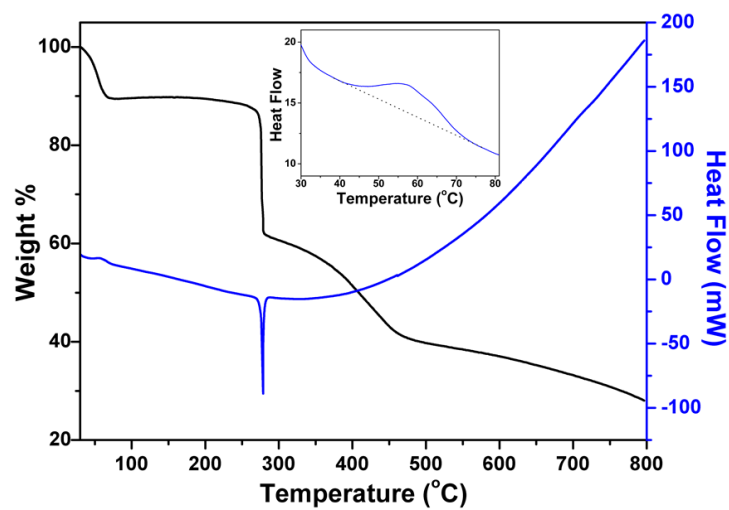
Appendix A4.14: Frequency dependence of the dielectric loss for 7 at various temperatures.

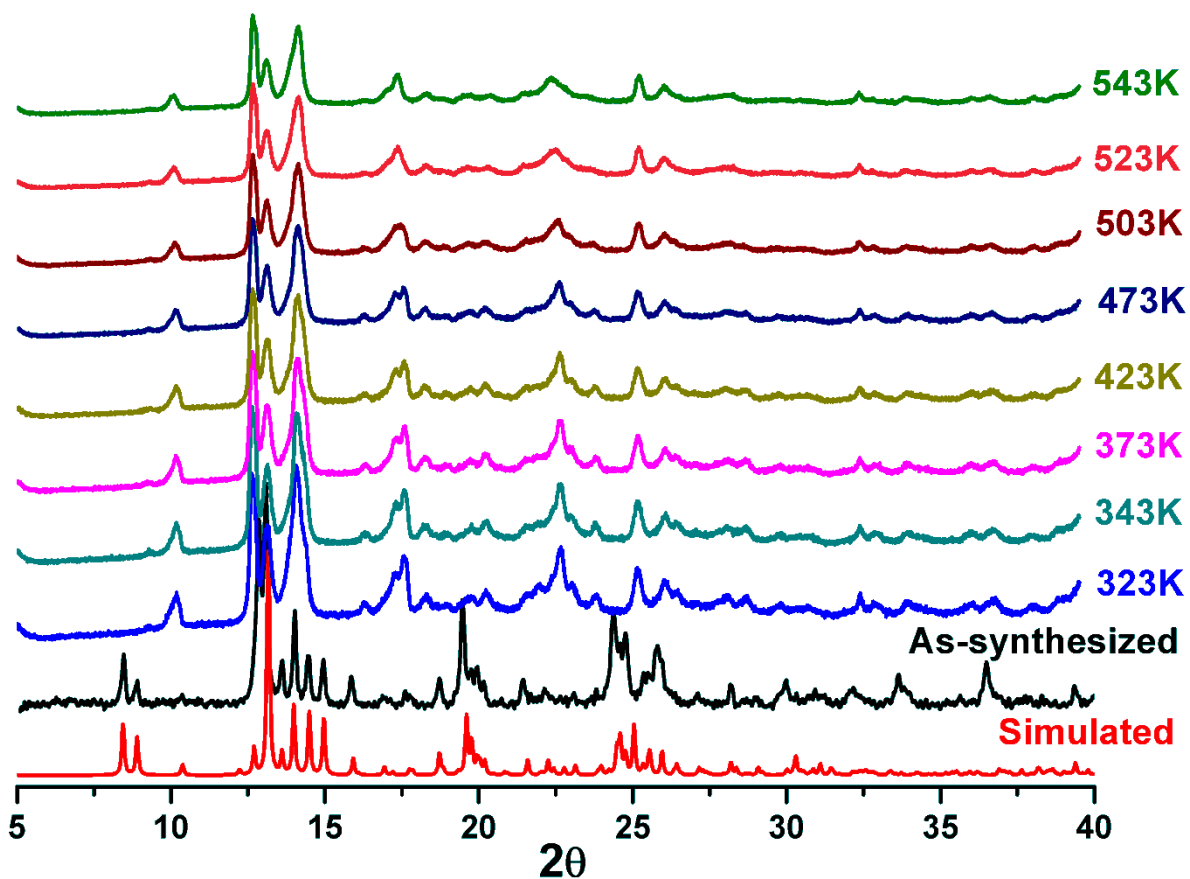


Appendix A4.15: Conductivity vs. frequency plot for 6.

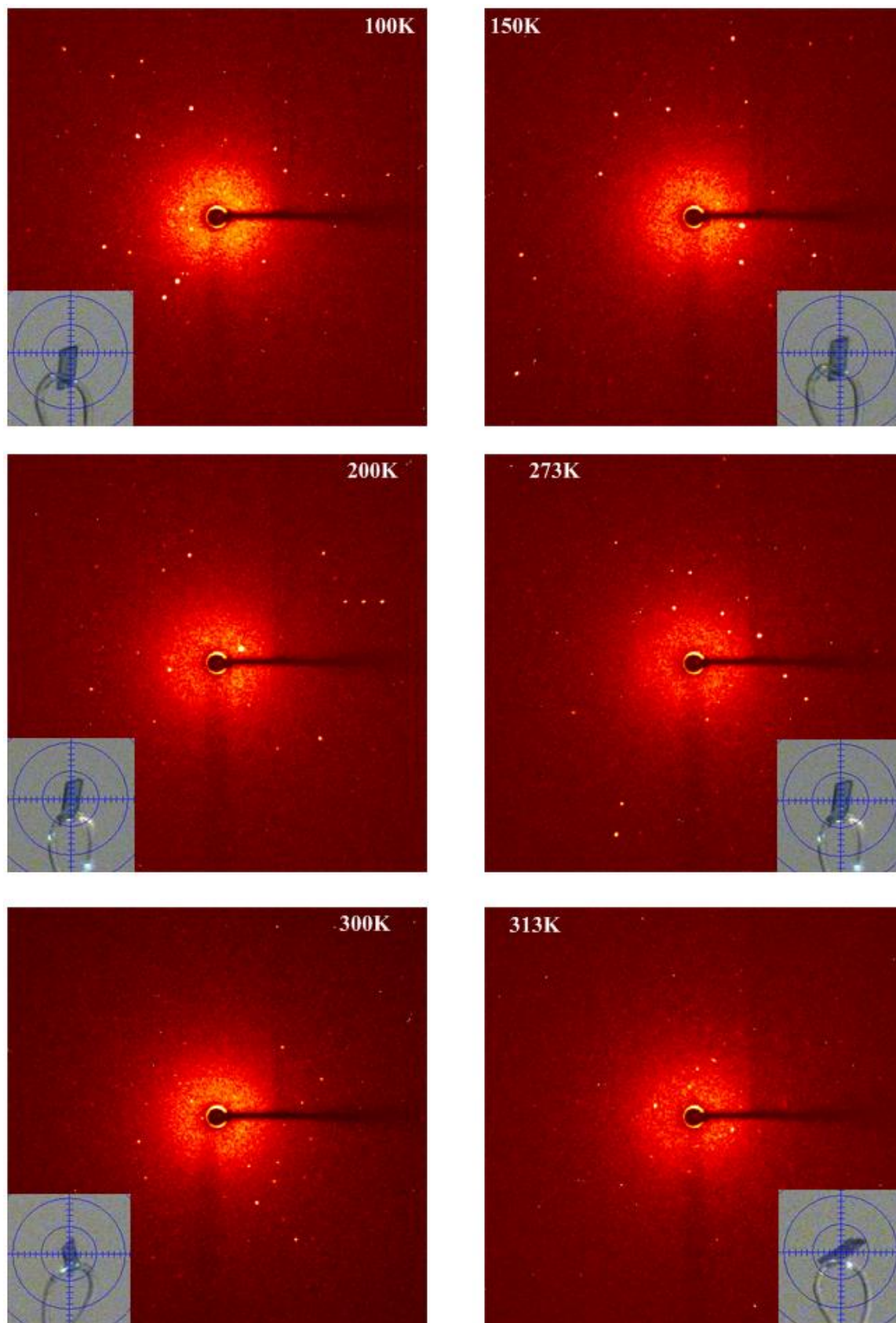


Appendix A4.16: Conductivity vs. frequency plot for 7.

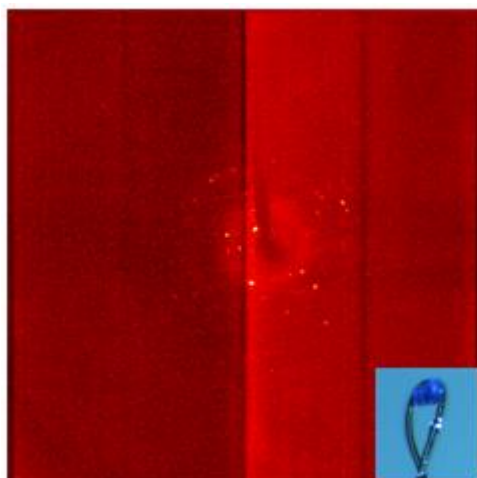
Additional studies supporting Desolvation assisted T_c in 6**Appendix A4.17: TGA-DSC data for (a) 6 (b) 6_{desolvated} and (c) 6_{resolvated}.**



Appendix A4.18: Variable temperature PXRD plots of 6.



Appendix A4.19: Diffraction spots for the single crystal of **6** at different temperatures.



Unit Cell Parameter at 40 °C after 24h heating under hot N₂ flow

$$a = 25.41(11) \text{ \AA}; b = 10.18(4) \text{ \AA}; c = 18.58(8) \text{ \AA}$$

$$\alpha = 90.00^\circ; \beta = 130.97^\circ(13); \gamma = 90.00^\circ$$

$$\text{Volume} = 3627.76 \text{ \AA}^3$$

Monoclinic Cc

Appendix A4.20: Unit cell parameter at 40 °C obtained on the single crystal of **6** after 24h heating under hot N₂ flow on a Bruker D8 Venture diffractometer with Microfocus X-ray source and photon detector. Due to poor data quality, only unit cell was indexed, as the weak reflections were not sufficient enough to yield an acceptable structure. The total potential solvent accessible void volume (459.1 Å³) in **6** (as obtained on squeezing all the solvents in **6**, except coordinated water), is nearby to the difference of the unit cell volume obtained at 40 °C and that obtained for **6** at 100K, suggesting the desolvation is not affecting the framework much.

Appendix A4.21: Comparison of unit-Cell parameters for **6** and **6**_{desolvated}.

6	6 _{desolvated} (derived from single-crystal data)	6 _{desolvated} (derived from PXRD data) ^a
$a = 25.688(5) \text{ \AA}; \alpha = 90^\circ$ $b = 12.212(3) \text{ \AA}; \beta = 127.862(3)^\circ$ $c = 17.076(7) \text{ \AA}; \gamma = 90^\circ$ Volume = 4229(2) Å ³	$a = 25.41(11) \text{ \AA}; \alpha = 90^\circ$ $b = 10.18(4) \text{ \AA}; \beta = 130.39(13)^\circ$ $c = 18.58(8) \text{ \AA}; \gamma = 90^\circ$ Volume = 3627.7(6) Å ³	$a = 26.40(4) \text{ \AA}; \alpha = 90^\circ$ $b = 10.316(20) \text{ \AA}; \beta = 129.77(6)^\circ$ $c = 18.61(3) \text{ \AA}; \gamma = 90^\circ$ Volume = 3894.9(17) Å ³

^a The PXRD patterns were indexed using TREOR90 algorithm from the Crysfire powder indexing suite¹¹ and refinements were carried out using Powder v2.0 software (Source: CCP14 site). A figure of merit > 20 for the refined data was obtained.

Appendix A5.1: Selected bond-lengths and angles for **8** and **9**.

Compound	Bond length		Bond angle	
8	P(1)-N(3)	1.595(10)	N(3)-P(1)-N(4)	102.0(5)
	P(1)-N(4)	1.628(10)	N(3)-P(1)-N(2)	117.1(5)
	P(1)-N(2)	1.637(10)	N(4)-P(1)-N(2)	111.2(5)
	P(1)-N(1)	1.642(11)	N(3)-P(1)-N(1)	111.6(5)
	P(2)-N(8)	1.609(10)	N(4)-P(1)-N(1)	116.8(5)
	P(2)-N(7)	1.618(10)	N(2)-P(1)-N(1)	98.8(5)
	P(2)-N(6)	1.633(11)	N(8)-P(2)-N(7)	115.9(5)
	P(2)-N(5)	1.636(10)	N(8)-P(2)-N(6)	112.7(5)
	P(3)-N(11)	1.611(10)	N(7)-P(2)-N(6)	102.0(6)
	P(3)-N(9)	1.612(10)	N(8)-P(2)-N(5)	99.1(5)
	P(3)-N(10)	1.623(11)	N(7)-P(2)-N(5)	113.0(5)
	P(3)-N(12)	1.630(10)	N(6)-P(2)-N(5)	114.7(6)
			N(11)-P(3)-N(9)	114.7(5)
			N(11)-P(3)-N(10)	112.4(6)
			N(9)-P(3)-N(10)	101.1(5)
			N(11)-P(3)-N(12)	100.9(5)
		N(9)-P(3)-N(12)	112.4(5)	
		N(10)-P(3)-N(12)	116.0(5)	
9	P(1)-N(1)	1.599(15)	N(1)-P(1)-N(3)	99.4(7)
	P(1)-N(3)	1.622(13)	N(1)-P(1)-N(2)	114.8(7)
	P(1)-N(2)	1.627(13)	N(3)-P(1)-N(2)	112.6(8)
	P(1)-N(4)	1.640(12)	N(1)-P(1)-N(4)	114.0(8)
	P(2)-N(5)	1.622(14)	N(3)-P(1)-N(4)	115.7(6)
	P(2)-N(6)	1.625(12)	N(2)-P(1)-N(4)	101.1(7)
	P(2)-N(7)	1.631(13)	N(5)-P(2)-N(6)	111.9(8)
	P(2)-N(8)	1.642(14)	N(5)-P(2)-N(7)	101.7(7)
	P(3)-N(11)	1.34(2)	N(6)-P(2)-N(7)	114.0(8)
	P(3)-N(9)	1.606(16)	N(5)-P(2)-N(8)	113.4(8)
	P(3)-N(12)	1.610(16)	N(6)-P(2)-N(8)	101.7(7)
	P(3)-N(10)	1.637(17)	N(7)-P(2)-N(8)	114.7(6)
	P(4)-N(15)	1.39(2)	N(11)-P(3)-N(9)	114.6(9)
	P(4)-N(14)	1.41(2)	N(11)-P(3)-N(12)	122.4(12)
	P(4)-N(16)	1.64(2)	N(9)-P(3)-N(12)	101.0(8)
	P(4)-N(13)	1.67(3)	N(11)-P(3)-N(10)	99.2(11)
	P(5)-N(18)	1.609(13)	N(9)-P(3)-N(10)	108.4(10)
	P(5)-N(19)	1.617(15)	N(12)-P(3)-N(10)	115.3(10)
	P(5)-N(17)	1.621(15)	N(15)-P(4)-N(14)	128(3)
	P(5)-N(20)	1.635(15)	N(15)-P(4)-N(16)	98.7(14)
	P(6)-N(23)	1.572(17)	N(14)-P(4)-N(16)	100.0(17)
	P(6)-N(21)	1.581(16)	N(15)-P(4)-N(13)	130(2)
	P(6)-N(24)	1.617(14)	N(14)-P(4)-N(13)	99.5(15)
	P(6)-N(22)	1.701(17)	N(16)-P(4)-N(13)	108.1(11)
	P(1A)-O(11)	1.467(10)	N(18)-P(5)-N(19)	100.3(8)
	P(1A)-O(12)	1.511(9)	N(18)-P(5)-N(17)	114.6(9)
	P(1A)-O(14)	1.559(14)	N(19)-P(5)-N(17)	117.1(8)
	P(1A)-O(13)	1.577(12)	N(18)-P(5)-N(20)	113.6(7)
	P(2A)-O(21)	1.529(11)	N(19)-P(5)-N(20)	111.6(9)
	P(2A)-O(22)	1.541(12)	N(17)-P(5)-N(20)	100.4(8)
	P(2A)-O(24)	1.561(15)	N(23)-P(6)-N(21)	119.5(8)
	P(2A)-O(23)	1.583(18)	N(23)-P(6)-N(24)	113.8(8)
	P(3A)-O(34)	1.36(2)	N(21)-P(6)-N(24)	101.8(8)
	P(3A)-O(32)	1.410(13)	N(23)-P(6)-N(22)	102.9(8)
	P(3A)-O(31)	1.477(14)	N(21)-P(6)-N(22)	106.8(8)
	P(3A)-O(33)	1.671(17)	N(24)-P(6)-N(22)	112.2(9)
	P(4A)-O(44)	1.462(16)	O(11)-P(1A)-O(12)	114.2(6)
	P(4A)-O(43)	1.494(13)	O(11)-P(1A)-O(14)	106.8(7)
	P(4A)-O(41)	1.501(13)	O(12)-P(1A)-O(14)	110.1(7)
	P(4A)-O(42)	1.601(14)	O(11)-P(1A)-O(13)	109.0(7)
	P(5A)-O(53)	1.476(15)	O(12)-P(1A)-O(13)	109.3(7)
	P(5A)-O(51)	1.486(14)	O(14)-P(1A)-O(13)	107.1(6)

P(5A)-O(52)	1.507(12)	O(21)-P(2A)-O(22)	109.9(6)
P(5A)-O(54)	1.653(13)	O(21)-P(2A)-O(24)	111.7(8)
P(6A)-O(63)	1.447(13)	O(22)-P(2A)-O(24)	109.4(8)
P(6A)-O(62)	1.519(12)	O(21)-P(2A)-O(23)	105.9(8)
P(6A)-O(61)	1.556(15)	O(22)-P(2A)-O(23)	110.8(9)
P(6A)-O(64)	1.583(14)	O(24)-P(2A)-O(23)	109.2(8)
		O(34)-P(3A)-O(32)	102.3(14)
		O(34)-P(3A)-O(31)	123.8(18)
		O(32)-P(3A)-O(31)	122.0(9)
		O(34)-P(3A)-O(33)	99.4(2)
		O(32)-P(3A)-O(33)	107.8(9)
		O(31)-P(3A)-O(33)	104.9(9)
		O(44)-P(4A)-O(43)	114.3(8)
		O(44)-P(4A)-O(41)	116.3(9)
		O(43)-P(4A)-O(41)	117.0(8)
		O(44)-P(4A)-O(42)	99.9(12)
		O(43)-P(4A)-O(42)	108.3(9)
		O(41)-P(4A)-O(42)	106.7(8)
		O(53)-P(5A)-O(51)	110.2(9)
		O(53)-P(5A)-O(52)	116.6(8)
		O(51)-P(5A)-O(52)	117.0(7)
		O(53)-P(5A)-O(54)	103.5(8)
		O(51)-P(5A)-O(54)	101.5(8)
		O(52)-P(5A)-O(54)	105.7(7)
		O(63)-P(6A)-O(62)	114.3(7)
		O(63)-P(6A)-O(61)	106.0(8)
		O(62)-P(6A)-O(61)	113.7(8)
		O(63)-P(6A)-O(64)	106.5(8)
		O(62)-P(6A)-O(64)	108.2(7)
		O(61)-P(6A)-O(64)	107.8(9)

Appendix A5.2: Hydrogen bond table for 8.

D-H...A	d(D-H)	d(H...A)	d(D...A)	<(DHA)
N(1)-H(1)...O(11T)	0.88	1.93	2.725(15)	149.8
N(2)-H(2)...O(11T)	0.88	1.85	2.697(14)	160.4
N(3)-H(3)...O(32T)#1	0.88	1.84	2.713(13)	170.8
N(4)-H(4)...O(31T)#1	0.88	1.92	2.782(13)	164.3
N(4)-H(4)...O(32T)#1	0.88	2.58	3.277(13)	136.5
N(5)-H(5)...O(1S)	0.88	2.03	2.873(13)	159.0
N(6)-H(6)...O(31T)#2	0.88	2.45	3.206(14)	144.8
N(6)-H(6)...O(2S)#2	0.88	2.60	3.365(14)	145.4
N(7)-H(7)...O(2S)#2	0.88	1.92	2.799(14)	177.0
N(8)-H(8)...O(1S)	0.88	1.92	2.781(13)	164.6
N(9)-H(9)...O(21T)	0.88	1.91	2.728(13)	154.0
N(10)-H(10)...O(22T)	0.88	1.87	2.739(13)	167.4
N(11)-H(11)...O(12T)#3	0.88	2.26	3.016(15)	143.8
N(12)-H(12)...O(12T)#3	0.88	2.00	2.698(14)	135.2
O(1S)-H(1S)...O(22T)	0.75	1.87	2.618(12)	173.7
O(2S)-H(2S)...O(31T)	0.84	1.86	2.654(13)	156.2

Symmetry transformations used to generate equivalent atoms:

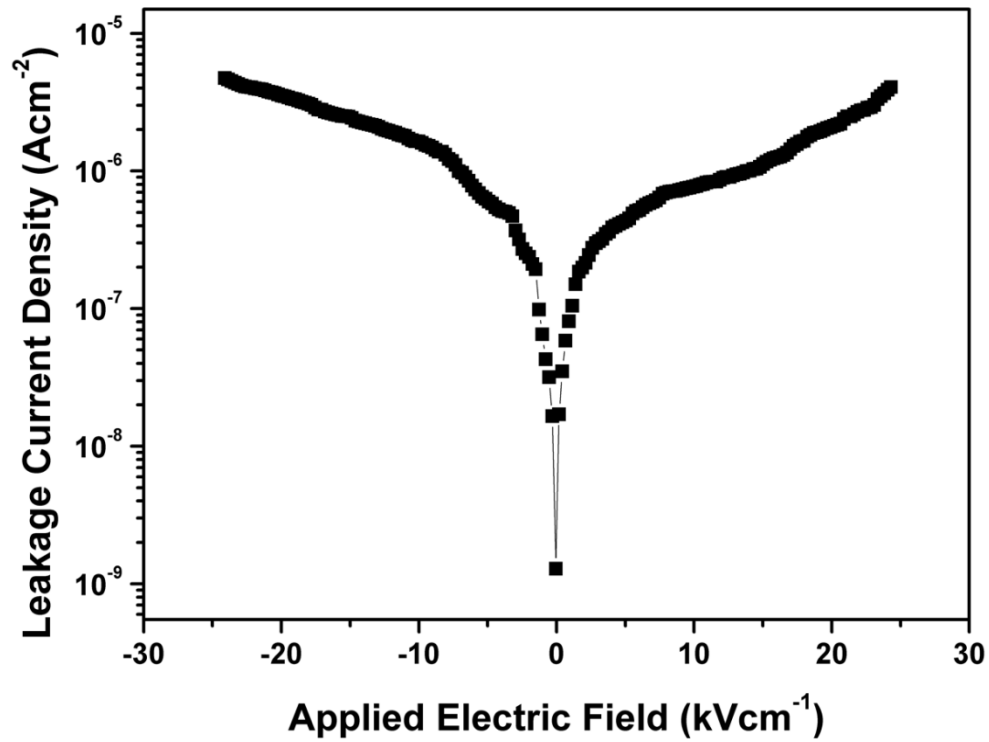
#1 $x+1/2, -y+2, z$ #2 $-x+1/2, y, z-1/2$ #3 $x-1/2, -y+1, z$

Appendix A5.3: Hydrogen bond table for 9.

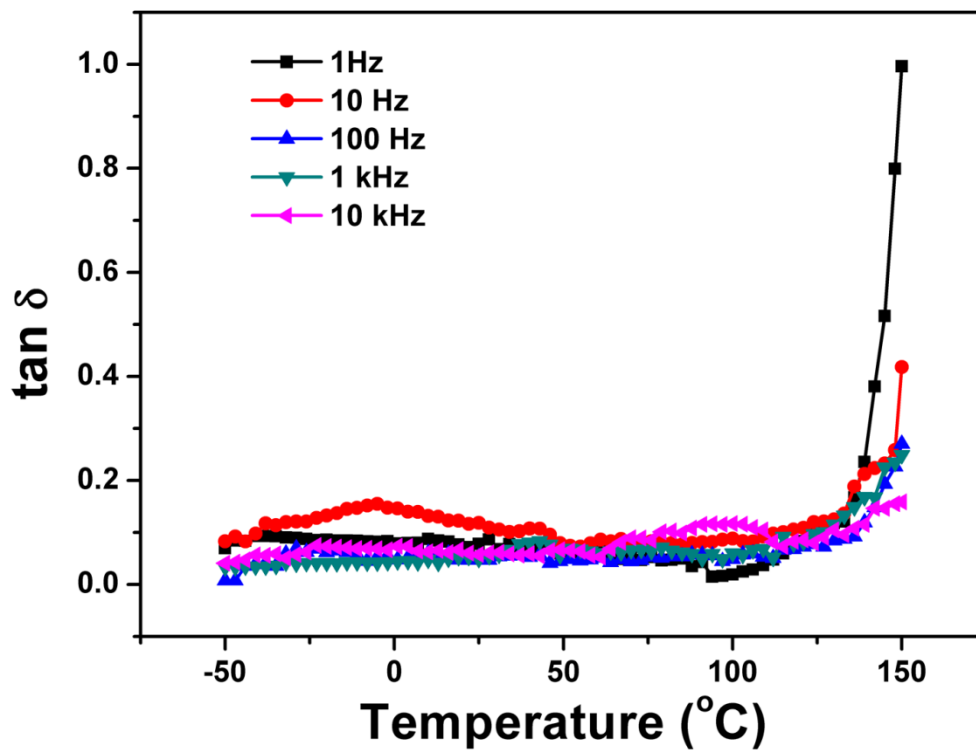
D-H...A	d(D-H)	d(H...A)	d(D...A)	<(DHA)
N(1)-H(1N)...O(11)	0.88	1.97	2.824(16)	164.8
N(2)-H(2N)...O(51)#1	0.88	2.04	2.873(17)	157.7
N(3)-H(3N)...O(11)	0.88	1.95	2.788(17)	158.2
N(4)-H(4N)...O(51)#1	0.88	2.03	2.872(18)	159.2
N(4)-H(4N)...O(53)#1	0.88	2.62	3.250(19)	129.3
N(5)-H(5N)...O(63)#2	0.88	1.96	2.797(19)	158.5
N(6)-H(6N)...O(11)#3	0.88	1.90	2.771(17)	167.6
N(7)-H(7N)...O(63)#2	0.88	2.04	2.865(14)	155.7
N(8)-H(8N)...O(12)#3	0.88	2.01	2.753(15)	141.3
N(9)-H(9N)...O(31)	0.88	2.12	2.89(2)	145.9
N(10)-H(10N)...O(1S)	0.88	2.07	2.897(19)	156.4
N(11)-H(11N)...O(1S)	0.88	2.15	2.93(2)	146.3
N(12)-H(12N)...O(31)	0.88	2.04	2.85(2)	153.1
N(13)-H(13N)...O(22)	0.88	2.04	2.79(2)	142.3
N(14)-H(14N)...O(21)	0.88	2.07	2.72(2)	129.3
N(15)-H(15N)...O(32)	0.88	2.36	3.20(3)	161.4
N(16)-H(16N)...O(31)	0.88	1.78	2.65(2)	167.2
N(17)-H(17N)...O(21)	0.88	1.96	2.785(17)	156.5
N(18)-H(18N)...O(43)#4	0.88	1.97	2.796(19)	155.0
N(19)-H(19N)...O(43)#4	0.88	2.10	2.936(18)	157.6
N(20)-H(20N)...O(21)	0.88	1.95	2.794(19)	159.3
N(21)-H(21N)...O(42)	0.88	2.07	2.90(2)	157.8
N(22)-H(22N)...O(52)	0.88	1.91	2.79(2)	177.1
N(23)-H(23N)...O(51)	0.88	2.13	2.922(19)	149.0
N(24)-H(24N)...O(43)	0.88	1.85	2.722(18)	168.4
O(13)-H(13A)...O(52)#5	0.84	1.87	2.620(15)	148.6
O(14)-H(14A)...O(62)#5	0.84	1.75	2.584(15)	173.0
O(23)-H(23A)...O(34)#2	0.84	1.75	2.54(2)	155.6
O(24)-H(24A)...O(44)#2	0.84	1.96	2.504(19)	121.6
O(32)-H(32A)...O(42)	0.84	1.69	2.46(2)	153.0
O(33)-H(33A)...O(41)	0.84	1.67	2.49(2)	166.2
O(41)-H(41A)...O(33)	0.84	1.98	2.49(2)	118.5
O(41)-H(41A)...O(34)	0.84	2.65	3.47(5)	166.5
O(44)-H(44A)...O(24)#6	0.84	1.72	2.504(19)	154.7
O(53)-H(53A)...O(62)	0.84	1.90	2.547(19)	132.5
O(54)-H(54A)...O(12)#3	0.84	1.79	2.600(17)	160.8
O(61)-H(61A)...O(52)	0.84	2.07	2.668(18)	127.8
O(64)-H(64A)...O(2S)	0.84	1.88	2.67(3)	155.7
O(1S)-H(1S)...N(10)	0.84	2.18	2.897(19)	143.2
O(1S)-H(1S)...N(11)	0.84	2.14	2.93(2)	155.4

Symmetry transformations used to generate equivalent atoms:

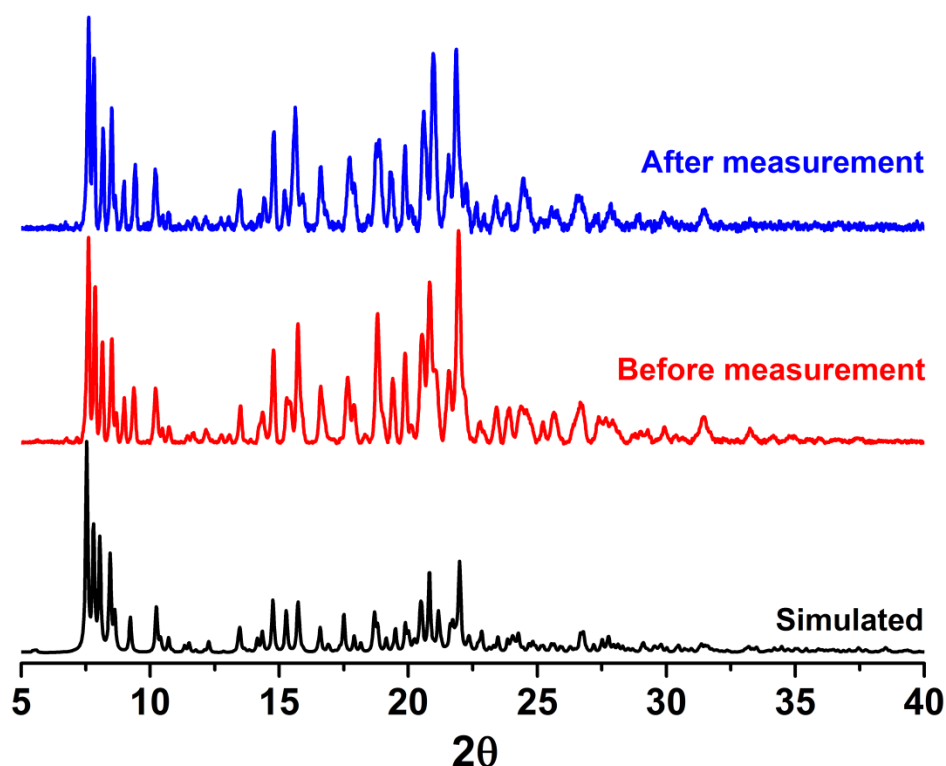
#1 $-x+1, y-1/2, -z+1$ #2 $x-1, y, z$ #3 $x, y, z-1$
 #4 $-x+1, y+1/2, -z+1$ #5 $x, y, z+1$ #6 $x+1, y, z$



Appendix A5.4: Unit cell parameters for 9.



Appendix A5.5: Temperature dependence of the dielectric loss of 8 measured at various frequencies.



Appendix A5.6: PXRD plots for pressed pellets of **9** before and after ferroelectric hysteresis loop measurements.

Appendix A5.7: Comparison of unit-Cell parameters of **9** at various temperatures.

Unit Cell Parameter	Temperature				
	100 K	150 K	300 K	325 K	353 K
a	13.24(2) Å	13.26(4) Å	13.29(5) Å	12.70(8) Å	12.74(5) Å
b	23.70(4) Å	23.71(6) Å	23.97(4) Å	24.09(9) Å	24.14(12) Å
c	24.81(4) Å	24.82(7) Å	24.97(5) Å	25.03(6) Å	25.12(11) Å
β	97.87°(5)	98.13°(5)	100.37°(6)	99.52°(4)	99.64°(9)
Volume	7711(2) Å ³	7736(8) Å ³	7781(7) Å ³	7549(12) Å ³	7514(13) Å ³
Space Group	$P2_1$	$P2_1$	$P2_1$	$P2_1$	$P2_1$